Development of Low-Cost Pressurisation System for Rocket Engines

Linas KARAVECKAS

Submitted for the degree of
Doctor of Philosophy
At the Kingston University

Supervisory Team:
Dr Adam Baker
Prof Andy Augousti
Dr Malcolm Claus

July 2019

linas.karaveckas@gmail.com

Abstract

Increasing demand for low-cost satellites requires new affordable launch vehicles. Rocket turbopump systems are deemed to be one of the most complex and expensive components of conventional rockets, thus cost reduction of these parts is essential to business success.

The aim of this research was to evaluate existing rocket turbopumps and identify options for significant cost reductions. Alternative pressurisation options were also considered which could meet low-cost targets for a small satellite launch vehicle.

Four pressurisation systems were identified which could meet the requirements for a low-cost launch vehicle were shortlisted for further studies. These were turbopumps, piston pumps, pressure-fed and pistonless pumps. A mass model was developed to estimate the Gross Lift off Mass (GLOM) of the launch vehicle and to carry out a mass sensitivity analysis.

Based on these findings, the feasibility of the piston pump was explored for a low-cost launch vehicle. To test the concept and to evaluate the manufacturing techniques, two prototypes were built. The first demonstrator (Mark I) was used to evaluate the feasibility of the valves and to optimise performance. To avoid the complexities associated with cryogenic and oxidising liquids, the tests were carried out with water.

Further trials were conducted on the Mark II to assess compatibility at cryogenic temperatures. The prototype has successfully demonstrated that selected components have functioned as intended at low temperatures.

Through the process of development, it was determined that the piston pump is a very simple system – only a few parts require a high precision of manufacturing, such as the piston bore and piston.

The project novelty and achievement are 1) Various modern pressurisation systems were critically evaluated and it was concluded that a piston pump could offer a low-cost alternative to the turbopump. 2) It was demonstrated that a piston pump could be used in a small launch vehicle, but further work is required to extend the validation. 3) Demonstrators were used to show which components and parts could be used with Liquid Oxygen in small launch vehicles.

Contents

Abbreviations

cP	Centipoise
cSt	Centistokes
CTE	Coefficient of Thermal Expansion
DAU	Data Acquisition Unit
FOS	Factor of Safety
GLOM	Gross Lift Off Mass
l	Litre
LEO	Low Earth Orbit
LN_2	Liquid Nitrogen
LOX	Liquid Oxygen
N_2	Nitrogen
NPSH	Net Positive Suction Heat
$NPSH_A$	Net Positive Suction Heat Available
$NPSH_R$	Net Positive Suction Heat Required
PTFE	Polytetrafluoroethylene
RPA	Rocket Propulsion Analysis
T/W	Thrust to Weight Ratio

Mathematical Symbols

A	Cross-Section Area of the Piston
A_c	Combustion Chamber Area
A_e	Nozzle Exit Area
A_t	Throat Cross-Section Area
A_{Tank}	*Surface Area of Tank*
b	Average Operation Speed
C	Pump Constant
C_{Sea}	Effective Exhaust Velocity at Sea Level
$C_{Optimum}$	Optimum Effective Exhaust Velocity
C_{Vacuum}	Effective Exhaust Velocity in Vacuum
c^*	Characteristic Velocity
C_p	Combustion Chamber Pressure
cP	Centipoise (Viscosity)
cSt	Centistokes (Viscosity)
D	Displacement
D_c	Chamber Diameter
D_{piston}	Piston Diameter
D_t	Throat Diameter
E	Modulus of Elasticity
F	Thrust
g_0	Gravitation Constant
H	Pressure Head (feet or metres)
H_{aa}	Acceleration Head (feet or metres)
H_d	Pressure head at the Discharge (feet or metres)
$H_{elevation}$	Vertical Surface Between Liquid in the Tank (feet or metres)
$H_{friction}$	Friction Losses in the Piping (feet or metres)
H_s	Pressure Head at the Suction (feet or metres)
H_{tank}	Head in the Tank (feet or metres)
H_p	Pump Total Head (feet or metres)
H_{vapour}	Vapour Pressure (feet or metres)
l	Rod Length
Isp	Specific Impulse
Isp_{Sea}	Specific Impulse at Sea Level
$Isp_{Optimum}$	Optimum Specific Impulse
Isp_{Vacuum}	Specific Impulse in Vacuum
K	Fluid Compressibility Constant
K	Kelvin
L	Actual Suction Pipe Length

L_c	Combustion Chamber Length
L_n	Nozzle Cylinder Length
L^*	Chamber Characteristic Length
L/D	Length to Diameter ratio
M	Mach Number
M_e	Mach Number at Exit
$M_{insulation}$	Mass of Insulation
$M_{Thrust\ Structure}$	*Thrust Structure Mass*
$\dot{m}$	Mass Flow Rate
m	Number of Pistons
m_o	Initial Total Mass
m_c	Combustion Chamber Mass
m_{inert}	Inert Mass
m_f	Final Mass
m_n	Nozzle Mass
$m_{payload}$	Payload Mass
m_{piston}	Piston Mass
$m_{propellant}$	Propellant Mass
m_{tp}	Turbopump Mass
n	Number of Pump Stages
n	Stroke Speed (RPM)
N	Shaft Rotation Speed
N_r	Pump's Rotation Speed
N_s	Specific Speed
N_{ss}	Specific Suction Speed
O/F	Oxidiser to Fuel Ratio
P	Pressure
P_a	Ambient Pressure
P_{ac}	Acceleration Head Pressure
P_{av}	Average Pressure
P_c	Combustion Chamber Pressure
P_d	Pressure at Discharge
P_e	Nozzle Exit Pressure
P_{min}	Minimum Pressure
P_{max}	Maximum Pressure
P_s	Pressure at Discharge
P_{req}	Required Pump Power
ΔP_{cool}	Pressure Drop in the Cooling System
ΔP_{feed}	Pressure Drop in the Feed System
ΔP_{inj}	Pressure Drop in the Injector
Q	Flow Rate

Q_a	Actual Flow Rate
Q_t	Theoretical Flow Rate
r	Radius
r_c	Chamber Radius
r_t	Throat Radius
s	Stroke of the Pump
$S1\ Split$	Stage 1 Split ratio
$S2\ Split$	Stage 1 Split ratio
$S3\ Split$	Stage 1 Split ratio
t	Time
t	Thickness
T	Temperature
T	Thrust of the Engine
T_{boil}	Boiling Temperature
TRL	Technology Readiness Level
t_w	Wall Thickness
T/W	Thrust to Weight Ratio
UTS	Ultimate Tensile Strength
V	Velocity
V	Volume
v_{flow}	Flow velocity
V_{piston}	Piston Velocity
x	Piston Motion from Piston Pin to Crank Centre
YS	Yield Strength
ρ	Density
ρ_{fuel}	Fuel Density
ρ_{oxi}	Oxidiser Density
ρ_w	Material Density of the Wall
μ	Coefficient of Friction
μ_s	Static Frictional Coefficient
σ_θ	Hoop Stress
σ_T	Thermal Stress
τ	Torque
η_v	Volumetric Efficiency
η_p	Pump Efficiency
γ	Specific Heats
θ	Crank Angle
θ_{cc}	Constant Contraction Half Angle
θ_{cn}	Nozzle cone half angle
ω	Angular Velocity
ω	Piston Angular Velocity
ψ	Velocity Factor

λ	Nozzle Efficiency
ε	Throat Cross-Section Area to Nozzle Exit Area Ratio

Acknowledgements

The Author of this project would like to acknowledge and thank the following people for their valued guidance and support throughout the duration of the project.

- The project supervisors Dr Adam Baker, Prof Andy Augousti and Dr Malcolm Claus
- Visiting project advisor: Dr Martin Heywood
- Laboratory technicians especially Martin Theobald, Cliff Searle, Dale Cooper and Neil Mehta.
- SealsCo: especially Claire Preece for providing some free seals and supplying other seals at a discounted rate.
- Saint-Gobain: especially Gino Stevenheydens, David Hudson, Steve Armstrong for providing advice on seals and providing dynamic seals at a discounted rate.

Introduction

1.1 Motivation of Research

A large business share of the space industry is dominated by the private sector and newly emerging competitors, such as SpaceX, Rocket Lab and Firefly.[1, 2]. Due to an increased demand for low-cost satellites, they aim to provide the low-cost launch services. SpaceX approached this challenge by developing a semi-reusable system to minimise manufacturing costs, while Rocket Lab focuses on much smaller expendable vehicles, that can be built on the assembly line and launched over 100 times a year [2]. To keep the launches affordable, their engines are created through 3D Printing and use an electric turbopump. According to Rocket Lab claims, this is the key to their business success [3]

To transfer some of this market share to the UK, the British government has developed a national space policy seeking the capability to launch small satellites into orbit by 2020. Companies such as Newton Launch Systems are aiming to fill in this market gap by developing a small sub 20 tonnes lift-off mass launch vehicle that can deliver around 50 kg payload to Low Earth Orbit (LEO). The 1st and 2nd stage of all the current available launch systems are usually powered by the turbopump-fed propulsion systems which are responsible for a large part of the launch vehicle cost. The cost of such systems must be significantly reduced, or a new low-cost approach must be developed to ensure vehicle is economically feasible.

1.2 Pressurisation System Design Requirements

Newton Launch System has specified the following requirements of the pressurisation system:

- Flow rates: 30kg/s
- Pressure (ΔP): 30bar
- Propellant: Liquid Oxygen and Liquid Propane
- Lifetime: 150s

1.3 Aim of the Research

The aim of the research is to evaluate the factors which lead to high development and manufacturing cost of rocket turbopumps, and then further assess if significant cost reductions could be made in these areas. It is understood that the majority of engineering challenges arise due to a requirement to deliver cryogenic and oxidising fluids at a high flow rate at high pressure, while retaining the inert mass of the system at a minimum.

Due to the small size of the launch vehicle, a feasibility study of alternative pressurisations systems shall be evaluated to determine if requirements as outlined in section **1.2** could be met.

The proposed cost reduction to the turbopump or alternative pressurisation system shall be experimentally evaluated to test feasibility.

1.4 Objectives

To meet the project aims, the following objectives must be completed:

- The propulsion system will run on LOX and propane with an oxidiser to fuel ratio (O/F) of 2.5, as outlined in section 1.2. Evaluate the compatibility with cryogenic, oxidising and low viscosity liquids of potential candidates. The properties of these propellants are compared against water.

Table 2-1: Properties Comparison Table [4-6]

	Water (at 293K)	**LOX (at 75K)**	**Propane (at 150K)**
T_{boil} **at 1 bar**	373K	90K	231K
ρ	998.24kg/m^3	1214kg/m^3	667.48kg/m^3
Viscosity	1cP (1cSt)	0.32cP (0.26cSt)	0.65cP (1cSt)

Where T_{boil} – Boiling Temperature and viscosity units: cP – centipoise and cSt - centistokes

- The direct development and manufacturing cost of rocket turbopumps cannot be obtained, thus this shall be assessed based on the complexity of the technology through literature review.
- The key areas for cost reductions for rocket turbopump shall be identified and how these changes would affect pump performance. Alternative pressurisation systems shall be further evaluated against requirements as stated in section 1.2, before they shall be compared against a turbopump.
- Numerically compare proposed pressurisations systems or changes to turbopump to evaluate the feasibility for a small low-cost launcher. Mass model shall be created to assess Gross Lift Off Mass (GLOM) of the vehicle.
- Fabricate a demonstrator pump for liquid oxygen to validate design assumptions, manufacturing costs and performance.
- Evaluate the proposed pressurisation system to determine if it is technically and economically feasible.
- Recommend a pressurisation approach for a small low-cost launcher.

Chapter 2

Literature Review

2.1 Introduction

2.1.1 Why is There a Need for a Turbopump?

All existing launch vehicles use a turbopump to pressurise and deliver propellant to the combustor chamber. The importance of a high-pressure propellant can explained using the Rocket thrust Equation 2-1 [7]. The specific heats (γ) in the equation are defined as "a factor in adiabatic engine processes and in determining the speed of sound in a gas" [8]. The only controllable variable in this equation is the combustion chamber pressure (p_c). Therefore, the only way to deliver sufficient thrust for lift-off is by either increasing combustion chamber pressure or increasing the mass flow, as indicated by Equation 2-4. The second option is the less preferred choice as it has an adverse effect on the Gross Lift-Off Mass (GLOM) of the vehicle. To prove that higher value of p_c leads to a greater thrust, Rocket Propulsion Analysis v2.2 software and Equation 2-2 were used to aid in calculating Mach Number at exit (M_e) and nozzle exit pressure (p_e), as listed in Table 2-1 [9]. The data shows that the value of p_e is unaffected by this change, while p_e/p_c declines at higher p_c values. Substituting this data back into Equation 2-1 proves that thrust is depended on the chamber pressure.

Specific impulse (Isp) also benefits by increases in the p_c value as shown in Equation 2-3 [7]. This term is used to measure how efficiently a rocket uses propellant. As seen in Equation 2-4, engines with a higher Isp would require a smaller amount of flow rate to deliver the same amount of thrust, resulting in a higher payload capacity.

$$F = \underbrace{A_t p_c \gamma \left\{ \frac{2}{\gamma - 1} \left(\frac{2}{\gamma + 1} \right)^{\frac{\gamma+1}{\gamma-1}} \left[1 - \left(\frac{p_e}{p_c} \right)^{\frac{\gamma-1}{\gamma}} \right] \right\}^{0.5}}_{\text{momentum change thrust}} + \underbrace{(p_e - p_a) A_e}_{thrust\ arising\ due\ to\ pressure} \tag{2-1}$$

where F – thrust (N), A_t - throat cross-section area (m²), A_e – nozzle exit area (m²), γ – ratio of specific heats, p_c – chamber pressure (Pa), p_e – nozzle exit pressure (Pa) and p_a – ambient pressure (Pa)

$$p_e = p_c \left[1 + \frac{\gamma - 1}{2} M_e^2 \right]^{\frac{\gamma}{1-\gamma}} \tag{2-2}$$

$$Isp = \frac{c^*}{g_0} \gamma \left\{ \frac{2}{\gamma - 1} \left(\frac{2}{\gamma + 1} \right)^{\frac{\gamma+1}{\gamma-1}} \left[1 - \left(\frac{p_e}{p_c} \right)^{\frac{\gamma-1}{\gamma}} \right] \right\}^{0.5} \tag{2-3}$$

where c^*– characteristic velocity (m/s), g_0 – gravitational constant (9.81 m/s²) and M_e – Mach number at exit

$$Isp = \frac{F}{g_0 \dot{m}} \quad (2\text{-}4)$$

where F thrust force (N) and $\dot{m}$ propellant mass flow rate (kg/s)

Table 2-1: Exit Pressures When P_a is at 1bar and γ is 1.176 (extracted from Rocket Propulsion Analysis v2.2)

p_c (bar)	M_e	p_e (bar)	p_e/p_c
10	2.1436	1.034	0.103
20	2.4957	1.078	0.054
30	2.7009	1.092	0.036
40	2.8496	1.090	0.027
50	2.9672	1.082	0.022
60	3.0646	1.072	0.018
70	3.1479	1.061	0.015
80	3.2206	1.050	0.013
90	3.2851	1.039	0.012
100	3.3431	1.029	0.010

To understand why turbopumps are exclusively used in orbital launch vehicles, the historic requirements were reviewed. Soyuz-2-1v is one of the smallest liquid powered rocket with a GLOM of 157,000 kg [10]. Based on this figure, it could require as much as 225kg/s of total propellant flow rate to produce sufficient thrust for lift-off [10]. Taking further into a consideration that the pump must deliver high-pressure and work in cryogenic and oxidising environment, there is no other system that could match performance of the turbopump. In the 1950s other pumps such as, piston, gear, screw, lobe and vane pumps, were considered, however these technologies have never matured [11]. This was due to either manufacturing complexities of the time or there was not enough evidence to prove feasibility of the system.

According to Newton Launch Systems requirements defined in section **1.2**, a pressurisation system for a small satellite launcher must deliver 30kg/s. It is 7.5 times less than required for Soyuz-2-1v, thus it opens an opportunity to explore alternative pump options and to investigate novel cost reductions for the existing rocket turbopumps. Before proceeding any further, the difference between positive and centrifugal pumps will be explained and terms such as Net Positive Suction Head (NPSH) and cavitation will be defined.

Pump systems are separated into two groups; positive displacement or centrifugal pumps. Piston, gear, screw, lobe and vane pumps are classified as positive displacement pumps, whereas the turbopump is classified as a centrifugal pump. Positive displacement pumps transfer liquid by expanding volume on the suction side and decreasing volume on the discharge side. The key difference between these two categories is that the performance of a centrifugal pump declines with increased viscosity and pressure, as illustrated in Figure 2-1 and Figure 2-2 respectively. Flow rates of the positive displacement pumps are almost unaffected by these factors and the material strength defines the maximum operating pressure in these pumps [12]. Positive displacement pumps do not have a shut-off head and therefore must not be operated without a relief valve on the discharge side. Two diagrams, shown in Figure 2-3 and Figure 2-4, were used to illustrate the effects of the shut-off head, in which fluid is transferred to a closed system. When the turbopump

system is full, the inlet and outlet pressures will equalise and flow will stop (Figure 2-3). The chamber volume in a positive displacement pump (Figure 2-4) will continue to shrink until there is a rupture in the system.

In a centrifugal pump, the pressure of the liquid is raised by transferring kinetic energy from the input power source to the fluid. Then At the diffusers, liquid is then expanded and kinetic energy is converted to pressure in accordance with the Bernoulli Equation 2-5 [13].

$$\underbrace{\frac{\rho v_1^2}{2} + p_1}_{\substack{\textbf{Inlet} \\ \textit{High dynamic pressure} \\ \textit{Low static pressure}}} = \underbrace{\frac{\rho v_2^2}{2} + p_2}_{\substack{\textbf{Outlet} \\ \textit{Low dynamic pressure} \\ \textit{High static pressure}}} = constant \qquad (2\text{-}5)$$

Where ρ – density (kg/m³), v_1 – upstream velocity (m/s), v_2 – downstream velocity (m/s), p_1 – upstream pressure (Pa) and p_2 – downstream pressure (Pa)

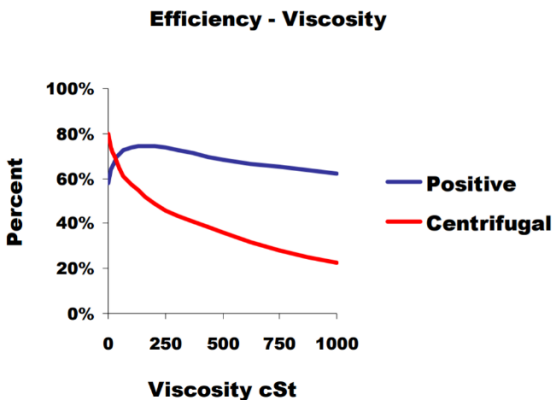

Figure 2-1: Efficiency vs Viscosity [14]

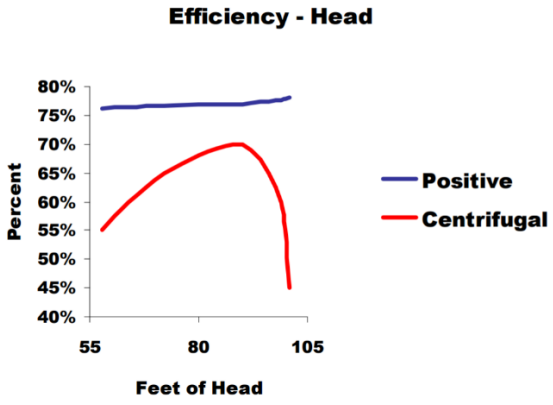

Figure 2-2: Efficiency vs Pressure Head [14]

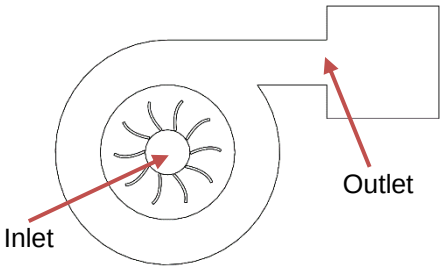

Figure 2-3: With Shut-off Head

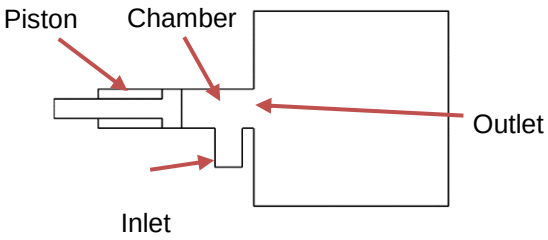

Figure 2-4: Without Shut-off Head

2.1.2 Net Positive Suction Head (NPSH)

All rocket turbopumps are affected by a phenomenon called cavitation and before going into more detail on this, the Net Positive Suction Head (NPSH) must be defined. NPSH is expressed via two terms: *NPSH required* ($NPSH_R$) and *NPSH Available* ($NPSH_A$). It should be noted that the pressure in the pumps is expressed in terms of feet or metres. This is known as a pressure head which can be converted from pressure via Equation 2-6 [15].

$$H = \frac{P}{\rho g} \quad (2\text{-}6)$$

Where H – pressure head (m), P – pressure (Pa), ρ – density (kg/m^3) and g – gravitational field (9.81m/s^2).

$NPSH_R$ is the minimum head required at the suction port to keep the pump from cavitating [16]. More details on this is explained in the next section **2.1.3 Cavitation.** The value of $NPSH_R$ is defined by the system, therefore it must be obtained experimentally.

$NPSH_A$ is defined as a head available at the suction port of the pump and calculated from Equation 2-7 [16]. Factors which determine the head at the inlet are defined in Figure 2-5. It should be noted, that to minimise the intensity of cavitation, the $NPSH_A$ must always be greater than $NPSH_R$.

$$NPSH_A = H_{tank} + H_{elevation} - H_{friction} - H_{vapour} \quad (2\text{-}7)$$

Where H_{tank} – absolute pressure in the tanks, $H_{elevation}$ – vertical surface between liquid in the tank and the centreline of the pump and $H_{friction}$ – friction losses in the piping, H_{vapour} – vapour pressure [16].

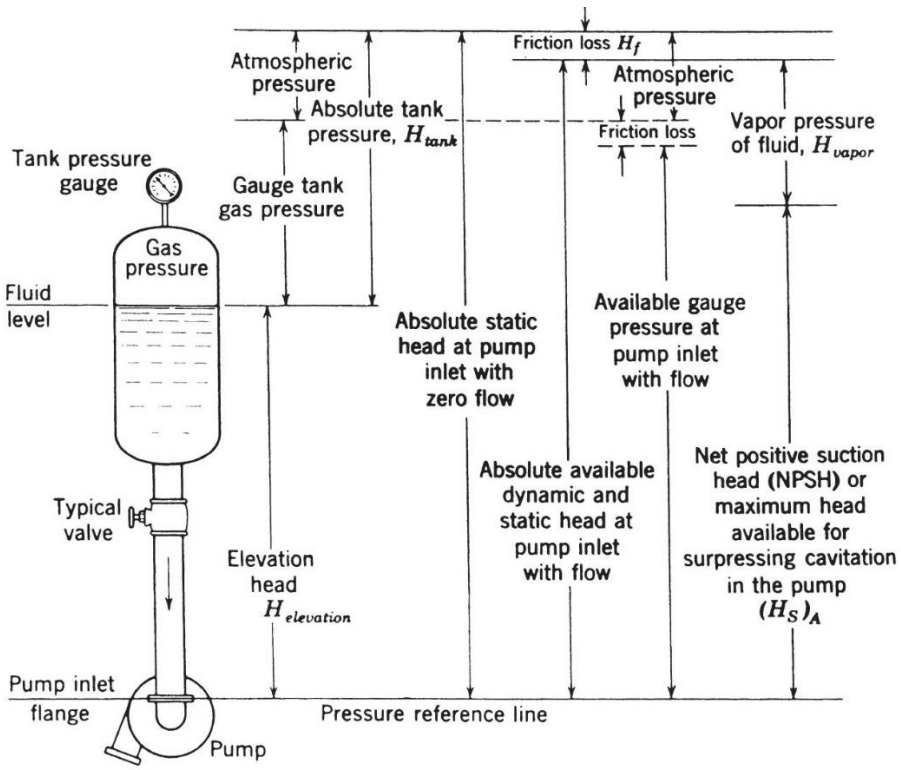

Figure 2-5: Definition of Pump Suction Head [16]

2.1.3 Cavitation

The cavitation phenomenon occurs when the localised pressure in liquid falls below its vapour pressure, resulting in gas bubble formation and implosion. This phenomenon is likely to occur when fluid is accelerated in a control valve or on the low-pressure side of an impeller blade. A constricted area in the piping or where a sudden change in the direction of fluid flow occurs can also cause cavitation, but this case is uncommon.

The graph in Figure 2-6 shows the pressure variation in the pump. As the liquid enters the eye, fluid acceleration causes the pressure to drop. If $NPSH_A$ is insufficient, the pressure of the fluid falls

below the vapour pressure line (between point A and point B), as illustrated in Figure 2-6. At point A, vapour bubbles are formed and sustained in this form until it reaches point B, where it is no longer able to continue in the vapour state and it implodes. The process between vapour cavity formation and implosion takes only a fraction of a second. This creates pressure fluctuation and flow instabilities, which results in reduction of efficiency, increased vibration levels and potential damage [15].

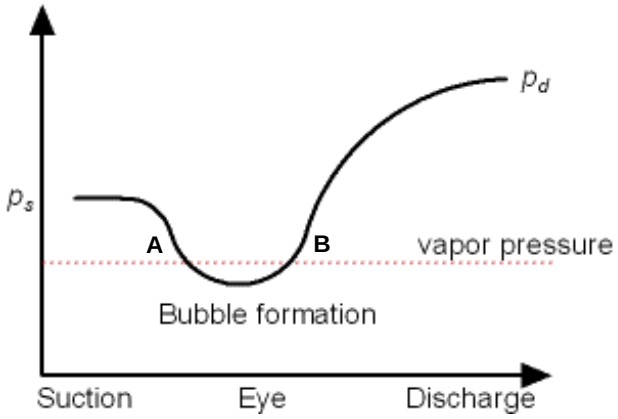

Figure 2-6: Cavitation Graph [17]

Figure 2-7 illustrates cavitation pitting damage. It should be noted that bubbles themselves do not cause any damage, but the collapse of the gas bubbles does. After a vapour cavity is formed, the liquid exerts pressure on the bubble and vice versa. During this process, the pressure of the liquid increases to the point where the vapour bubble is no longer able to withstand it and it collapses on itself. This occurs at point B, as previously described.

The collapse of the gas bubble results in high velocity micro jets and a localised shock wave, which by some estimates generates pressures of several hundreds of atmospheres [18, 19]. When the cavitation occurs close to the surface, pressures in this range are capable of plastically deforming metals. Over time, this repetitive process over the same area can cause erosion of the surface, as illustrated in Figure 2-8, and this reducing the life expectancy of the component and efficiency of the pump.

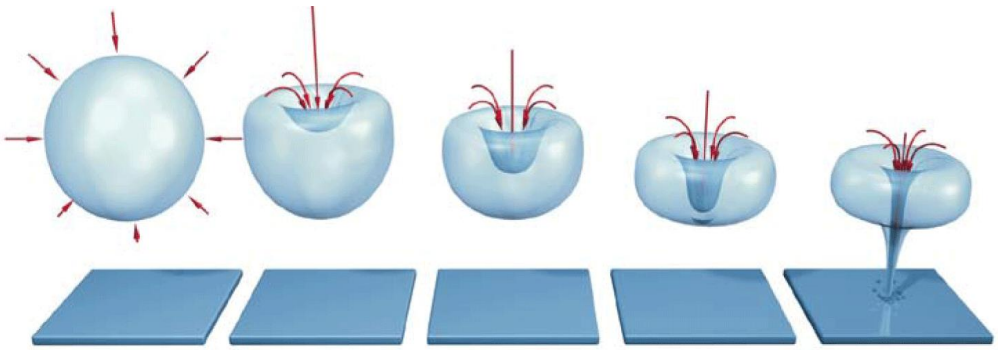

Figure 2-7: Vapour Bubble Implosion [20]

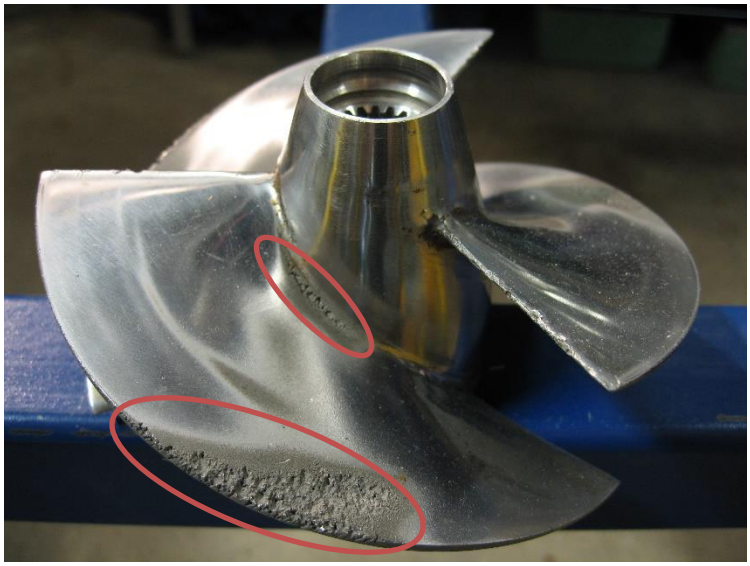

Figure 2-8: Cavitation Damage [21]

2.2 Turbopump

Launch vehicles primarily uses turbopumps to deliver pressurised propellant to the combustor chamber, however it is highly complex and expensive. A cut-away of typical rocket turbopump is illustrated in Figure 2-9. The pump is comprised of two sections: a centrifugal pump and a driving gas turbine, normally mounted on the same shaft, or in some cases geared together.

At the pump inlet, an inducer is used to raise the pressure head of the propellant to prevent significant cavitation. This process reduces $NPSH_R$, therefore propellant can be stored at lower pressures and the pump can operate at higher speeds. At the impeller, energy is transferred to the fluid by acceleration outwards from the centre of the rotor. Fluid then enters the stator vanes (not shown in this graph) and it goes through a diffusion process, where the kinetic energy of the fluid is converted to the pressure. For multi-staging, this process can be repeated several times, until a desirable pressure head is achieved, however it results in higher complexity, weight and cost.

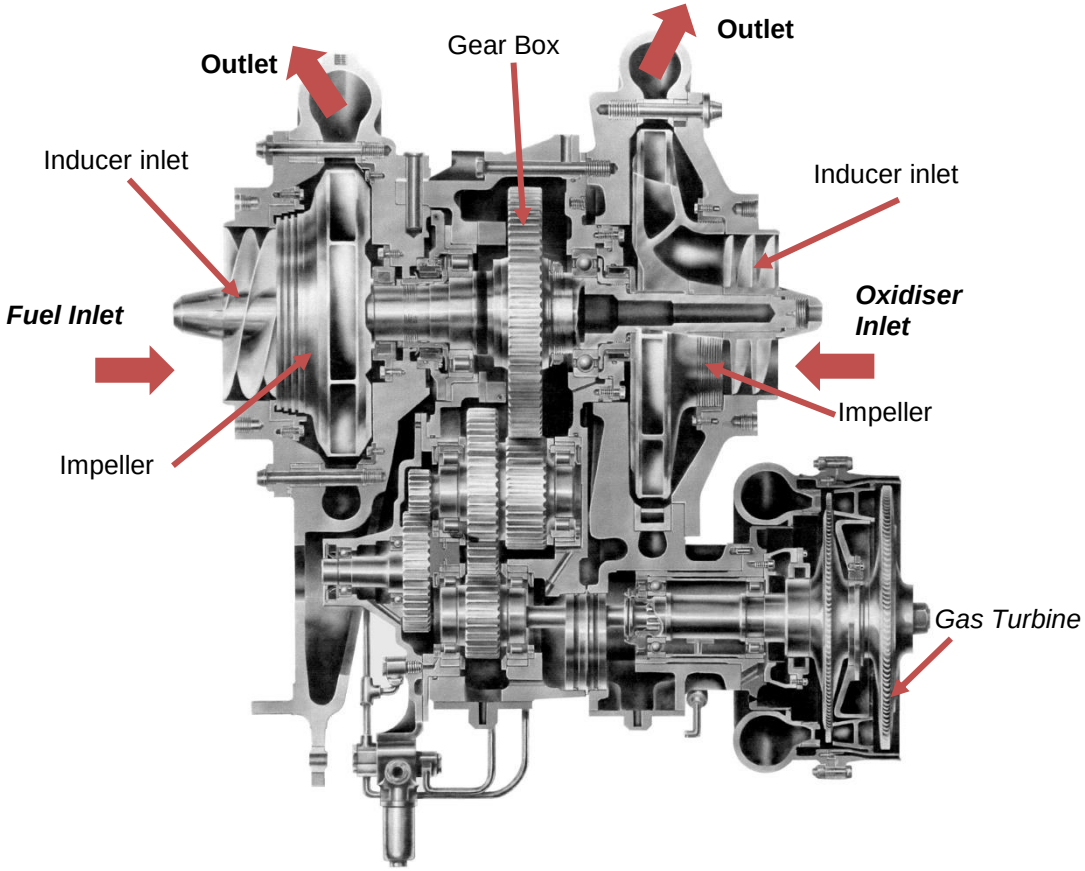

Figure 2-9: Cut-away of the Turbopump [22]

The turbopump provides a higher power to weight ratio than any other form of rotary machinery and this is essential for maximising the payload capacity [23]. As stated in **2.1** section, the current launch vehicles have to produce flow rates of over 200kg/s To meet the thrust level demands turbopumps are the only systems which can provide an acceptable mass fraction for this size of vehicle. Due to its technology readiness level, this system also been used in smaller vehicles, such as Black Arrow [24]. Development of a rocket turbopump is a very difficult and costly process, which can take up to 2 years and cost several million dollars apiece [25, 26]. To address all of the challenges associated with the turbopump, engineers with a background in hydrodynamics, aerodynamics, mechanical engineering, structural engineering, structural dynamics, rotordynamics, thermal design and engineering, materials, manufacturing, testing and instrumentation are essential [27].

Speed selection is a critical part in pump design which requires a trade-off selection between performance and cost. The design is more complicated if the selected speed is too low, the inert mass will be too high, resulting in inadequate performance. If the speed is too high, the turbopump might not meet reliability and life expectancy requirements [28]. The result of any of these failure modes will lead to very costly and time-consuming modifications.

Specific speed (N_s) is another important parameter that should be considered when designing a rocket turbopump. It is used to select the most efficient impeller geometry which is based on existing designs and collected data. The value of N_s is calculated in terms of rotational speed,

volume flow rate and head raised for that stage, as expressed in Equation 2-8 [7]. It should be noted, specific speed is typically calculated based on imperial units.

$$N_s = \frac{N_r\sqrt{Q}}{\left(\frac{H_p}{n}\right)^{0.75}} \tag{2-8}$$

Where N_s – stage specific speed (dimensionless), N_r – Pump's rotation speed (RPM) Q – Flow rate (USgpm), H_p – pump total head (ft) and n – number of pump stages.

The diagram in Figure 2-10 shows that for low specific speeds (500 – 1,500) a radial-vane impeller should be considered, while for high speeds (9000+) an axial-flow impeller. The radial-vane impeller displaces fluid perpendicularly to the inlet port, which results in pressure development due to centrifugal force. This type of impeller has the highest ratio between exit (d_o), and inlet (d_i) diameter ports. The d_o/d_i ratio decreases with increased specific speed, and for a truly axial-flow impeller, the outlet diameter becomes equal to the inlet diameter. For an axial impeller, pressure is developed by accelerating the propellant along the axis of rotation of the pump. Specific speed can also be used to estimate efficiency, pressure head, and power requirements, as seen in Figure 2-10.

The graph in Figure 2-11, shows how efficiency is affected by specific speed at various flow rates. At a low value of specific speed, the inlet passage is relatively small compared to the outlet. This results in high friction losses, which translate to low efficiency, as seen in Figure 2-11 at N_s = 500 [7].

To optimise the design, a trade-off analysis between power, efficiency and pressure head must be carried out when selecting the geometry of the rocket turbopump. The requirement of very high flow rates at very high pressures would make the radial or Francis impellers the most suitable shapes, however low specific speed would result in a low rotation speed, thereby high inert mass. According to Sutton and Biblarz, centrifugal pumps should be designed for the highest efficiency [16]. This efficiency is achieved at the highest capacity and when the specific speed is around 2,500 (refer to Figure 2-11). However, most of the pumps operate at efficiencies between 30% and 70% due to fluid losses from the surface roughness of the casing and impeller, bearing, seals and leakages [16].

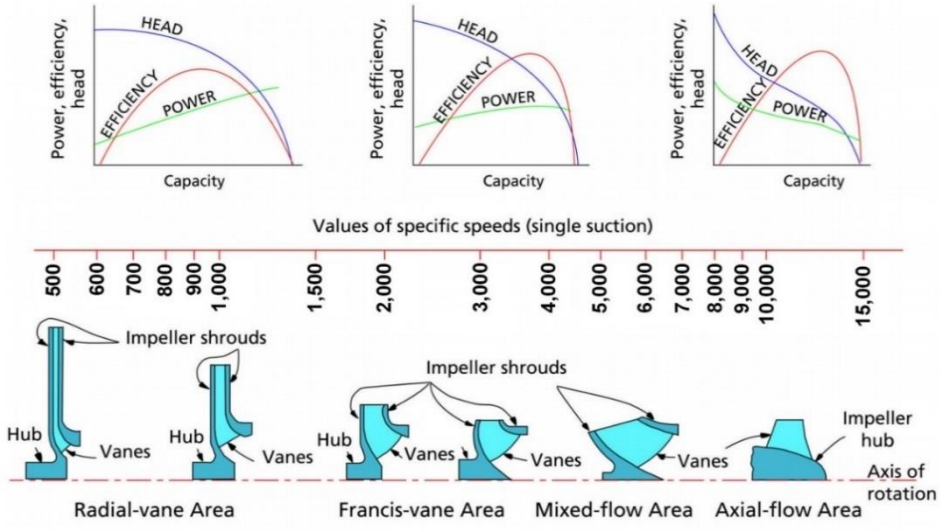

Figure 2-10: Impeller profiles vs Specific Speeds [15, 29]

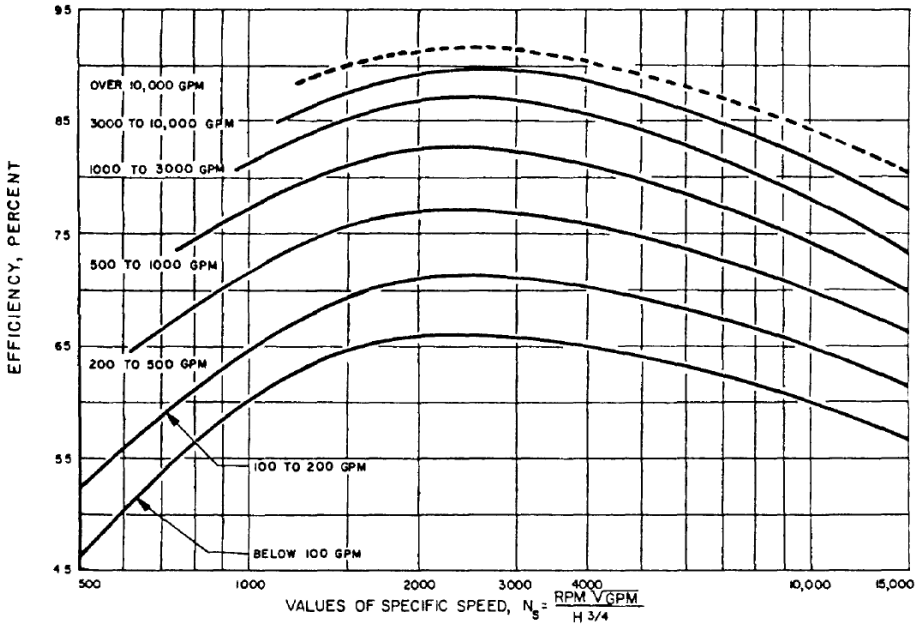

Figure 2-11: Efficiency vs Specific Speed [28]

Suction Specific Speed (N_{ss}) is another significant parameter which characterises a pump's suction performance. As previously defined, the $NPSH_A$ must always be greater than $NPSH_R$ to prevent significant cavitation in the system. The required suction vapour pressure can be calculated from the suction specific speed using Equation 2-9 [15].

$$N_{ss} = \frac{N\sqrt{Q}}{NPSH_R^{0.75}} \tag{2-9}$$

Where N_{ss} – suction specific speed (unitless), N – shaft rotation speed (RPM), Q – flow rate (USgpm) and $NPSH_R$ (ft)

According to Sutton and Biblarz, the suction specific speed is dependent on specific speed and quality of the design [16]. A pump has poor suction characteristics when the N_{ss} value is around 5,000, no cavitation is expected when values range between 1,000 and 25,000, and controllable local cavitation has values above 40,000[16]. The current generation of rocket inducers has a very

high N_{ss} value of over 80,000 [16]. This capability allows turbopumps to operate under some cavitation. This decreases the value of the $NPSH_R$, thus propellant can be stored under lower pressures in lighter tanks.

2.2.1 Bearings

A turbopump shaft is supported by two or more bearings, which are designed to transmit radial and axial loads from the rotary assembly on the housing [28]. These loads may result due to the weight of the parts, inertia, non-uniform pressure distribution and unbalanced axial thrust [28]. The bearing must also provide adequate radial stiffness and damping to retain adequate clearance between the inducer impeller and the housing. Most importantly, bearings must be capable of operating directly in cryogenic and corrosive environments. The cryogenic propellant must therefore provide lubrication to reduce wear of the parts at high speeds, since lubricating oil or grease would freeze at these temperatures.

Rolling element bearings are most commonly used in rocket turbopumps, due to their high load capability, stiffness and their ability to start and shut down reliably. However, these bearings are speed limited. This limit is expressed as a DN factor, defined as the product of the inner bore diameter D (mm) and shaft rotation speed N (RPM). Rolling element bearing limits typically range between 1.6 million and 2.1 million in rocket turbopumps [30].

To overcome the speed limitation of rolling element bearing, hydrostatic bearings are gradually gaining popularity in rocket turbopumps. These bearings operate on a thin layer of highly pressurised fluid, which is diverted from the pump discharge. As the contact between housing and rotor assembly is eliminated, such bearings offer almost unlimited speed and damping of the turbopump rotor [30]. The drawback of this approach is that under transient conditions, such as engine start up and shut down there is the potential for a rubbing contact.

2.2.2 Dynamic Seals

Turbopump dynamic seals are another critical part of the turbopump assembly which serves two main functions: to keep the oxidiser, fuel and hot turbine gas apart, and to minimise propellant leakage and thus to improve the efficiency. Due to propellant compatibility issues, seal failure can cause propellant ignition in the pump compartment, which would lead to a catastrophic pump failure. To prevent the propellants from mixing, multiple seals are used with purge and drainage passages that safely remove any propellant that passes the first seal layer. This arrangement is shown in Figure 2-12. As an additional safety measure, helium is used to provide an effective separation medium in the case of a single seal failure.

The turbopump commonly uses five types of dynamic seal: face contact, segmented shaft-riding, hydrostatic, floating ring and labyrinth seals [30]. The sealing selection option is dependent on seal pressure capability, temperature limits, wear life, speed limits, leakage, space requirements and cost [30]. The primary turbopump seal is a face contact seal due to its very good sealing characteristics. The seal is maintained by rubbing the sealing face on a rotating mating ring attached to the shaft. These seals are surface speed limited due to the heat generated by friction and the ability to extract this heat. This limit is given as a PV factor, where P is the contact load

(psi) and V is the rubbing velocity (ft/s) [30]. The high value of rubbing velocity, required for rocket turbopumps, would lead to higher development costs, in order to meet the reliability and life requirements. This system is furthermore complicated by extreme temperature gradients as seals must provide a barrier between very high temperatures (650°C – 930°C) on the turbine side and very low temperatures (-185°C – -270°C) on the pump side [30].

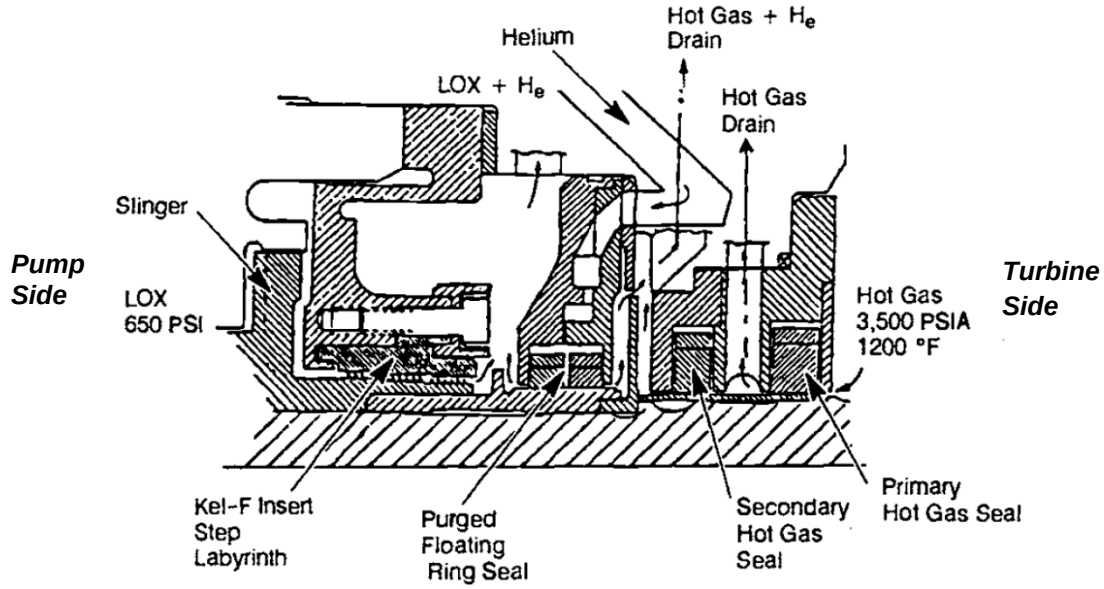

Figure 2-12: Turbopump Sealing System [30]

2.3 Other Pressurisation Options

As previously explained, the flow rate requirements of a small satellite launcher are significantly smaller, thus other pressurisation options have been explored. This includes Screw, gear, vane, lobe and piston pumps and some pressure-fed systems.

2.3.1 Screw Pump

The screw pump is a rotary positive displacement pump, as previously described. It is typically used with viscous fluids that a turbopump is unable to handle. In the screw pump, the fluid enters gaps between screws which then displace the fluid axially as the screw rotates and meshes (see Figure 2-13). Because of relatively low inertia of the rotating components, it can operate at over 10,000 RPM to allow higher flow rates [15].

This type of system does not normally generate high pressures due to labyrinth seals being the primary seal, hence to accommodate higher pressures, a larger number of threads and longer screw is required. The screw pump becomes a less practical option as the pressures increases due to the diminished efficiency and large length of the pump. Furthermore, the manufacturing complexity is somewhat similar to the turbopump, due to the requirement for high precision screws.

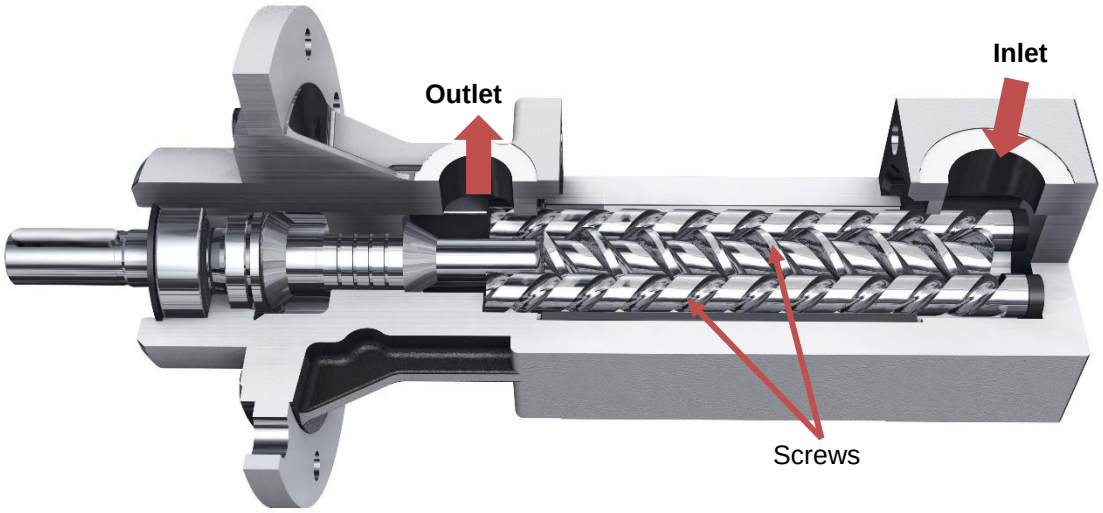

Figure 2-13: Screw Pump [31]

2.3.2 Gear, Vane and Lobe Pumps

As illustrated in Figure 2-14 and Figure 2-15, these rotary positive displacement pumps consist of gears, vanes or lobes closely fitted in the casing. Similarly to the screw pump, gears and vanes must mesh very accurately to provide an adequate barrier between the inlet and outlet sides. In addition, all faces are sealing faces, therefore very accurate fitting is required to minimize the leakage rate.

As the gear, vanes or lobes rotate, cavities are created at the pump inlet and progress through the pump to a point where it is no longer open. As illustrated in previous figures, the number of cavities formed at any one time depends on the pump type. There is a short transition where these cavities are completely isolated from the pump inlet and outlet. As the pump rotates, fluid fills these voids and moves along from inlet to outlet. At the pump outlet, meshing teeth gradually decrease the size of the cavities, and as a result of that, liquid is forced out at the outlet. As this is happening, new cavities are simultaneously formed at the inlet and the process continues.

2.3.2.1 Gear Pumps

Gear pumps are the most common rotary pressurisation system due to their wide range of applications. They are classified as external or internal, as Figure 2-14 illustrates.

Flow rates and the pressure head of external gear can range up to 95l/s and 34.5bar respectively [15]. The pump usually consists of two identical toothed gears of which one of them is a driver. Each gear is supported by a shaft with the bearings on each side of the gear [32].

Internal gear pump flow rates and pressures typically do not exceed 69l/s and 15.5bar respectively [15]. This pump consists of outer driving and smaller inner idle gears.

Gear pumps are mainly used for high viscosity applications but also have successfully pumped very low viscosity liquids, such as propane and ammonia [32]. According to the National Institute of Standards and Technology (NIST), the viscosity of LOX is temperature dependent and ranges between 0.2cP and 0.86cP [5]. Propane viscosity falls in the same range as LOX at a temperature between -135°C and -45°C [6].

The amount of fluid slippage is determined by both the viscosity of the fluid and the pressure differential between the inlet and outlet. A low viscosity liquid can squeeze through the gaps more easily than a more viscous liquid. A high outlet pressure can also force less viscous liquid through the gaps, causing further slippage. This reduces pump performance, so other types of pumps are preferred for low viscosity fluids.

Smaller gear pumps can operate at speeds up to 3,450RPM and larger versions up to 640RPM [32]. At higher speeds, centrifugal forces and lack of time prevents the liquid from filling cavities sufficiently, which determines these operational speed limits.

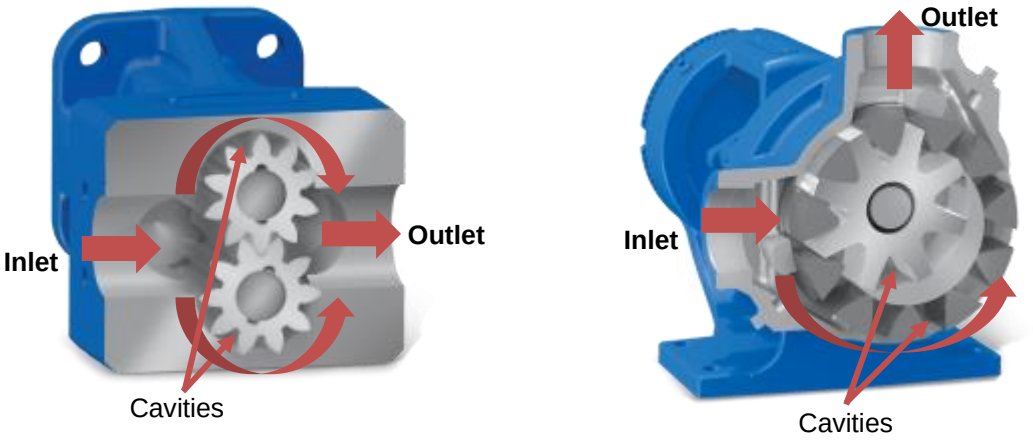

External Gear Pump [33] *Internal Gear Pump [34]*

Figure 2-14: Gear Pump – (a) Internal Gear Pump & (b) External Gear Pump

2.3.2.2 Lobe Pumps

Lobe pump operation is comparable to gear pumps, except that the lobes do not make any contact with each other, which is prevented by external timing gears [32]. Unlike gear pumps, these pumps can handle small solids without suffering any damage. However, lobe pumps are very inefficient at pumping low viscosity liquids due to the large gaps between lobes and the reduced sealing capabilities. The limitation placed on the operation speed is even greater than that of gear pumps, due to centrifugal forces and inter-lobe cavity filling rates.

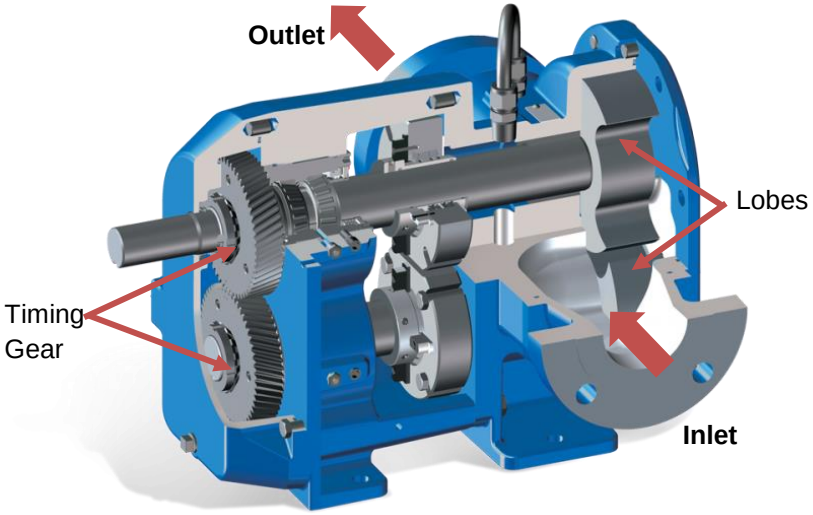

Figure 2-15: Lobe Pump [35]

2.3.2.3 Vane Pumps

Unlike gear or lobe pumps (Figure 2-16), vane pump does not consist of closely meshed components. Instead, pump inlet and outlet are separated by sliding vanes, which are attached to a rotor positioned off centre. As the rotor rotates, this configuration creates expanding and contracting cavities, which shifts fluid from pump inlet to outlet.

For the pump to function correctly, the vanes must always contact the wall to provide adequate sealing. To ensure the contact is always retained, centrifugal forces themselves are not sufficient, as hydraulic forces exerted by the liquid tend to push the vanes back to the rotor [36]. To counteract these forces, the discharged pressure is often redirected under the vanes [36].

Vane pumps are mostly used for low viscosity applications, offering flows at up to 63l/s and pressures at up to 8.6bar [15]. As the pressure gets higher, it becomes increasingly difficult to retain the rigidity of the vanes and thus maintain good sealing characteristics. Of course, thicker vanes can be considered, but this becomes less practical at higher pressures and other systems are more favourable.

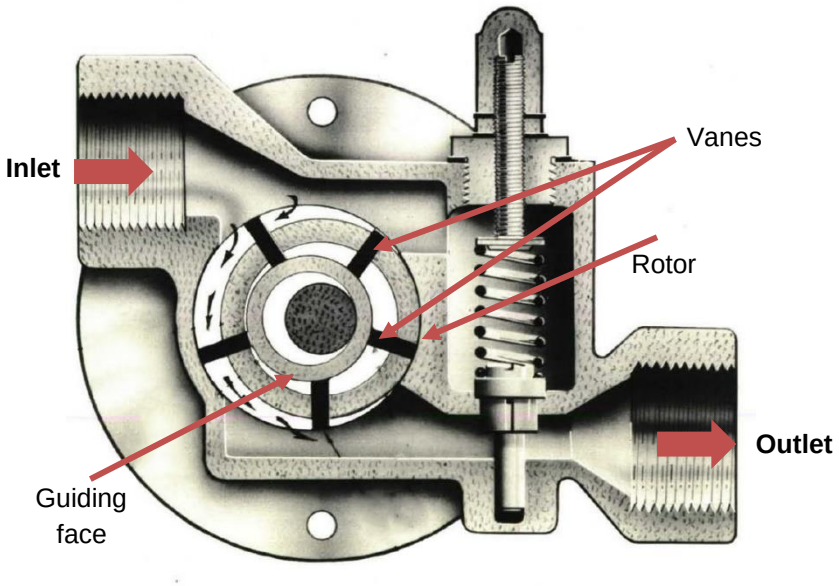

Figure 2-16: Vane Pump [11]

2.3.3 Piston Pump

The piston pump is a reciprocating displacement pump consisting of one or more cylinders, each containing a piston (Figure 2-17). The pistons are coupled to the connecting rod which is driven by a flywheel or crankshaft linked to an external power source. The flow rate is controlled by the rotation speed of the crankshaft or flywheel.

The reciprocating pump is classified as either single-acting or double-acting, differences are illustrated in Figure 2-18 and Figure 2-19. Each cylinder of the single-acting piston pump consists of one inlet and one outlet port. In the first half of the cycle it draws fluid in and the other half discharges. The double-acting piston pump consists of an inlet and outlet port mounted on both sides of the cylinder. This allows drawing the fluid in on one side while simultaneously discharging at the other end and vice versa. This configuration eliminates any period of zero flow rate but imposes extra complexity.

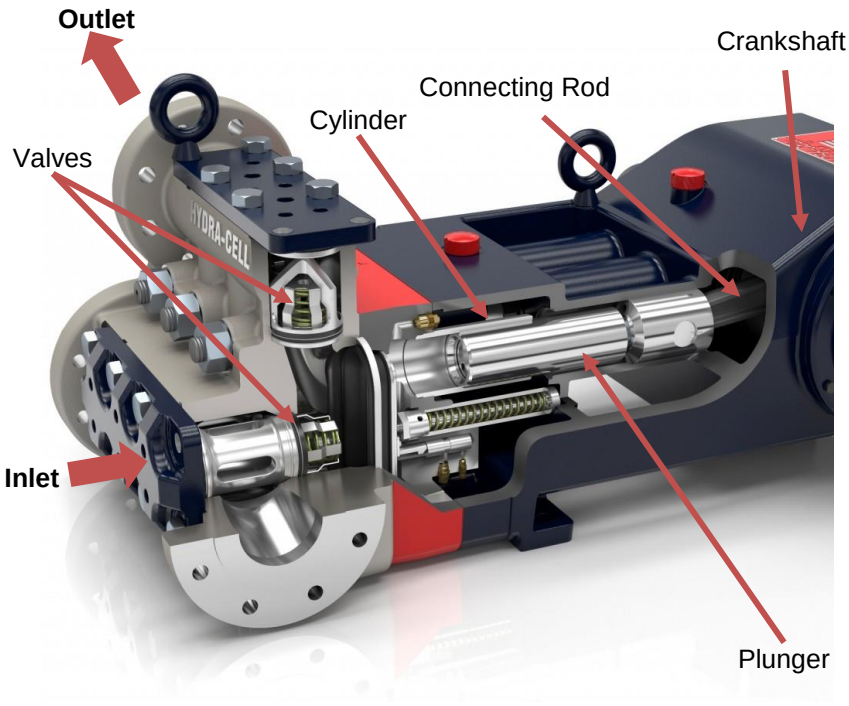

Figure 2-17: Triplex Piston Pump Cutaway [37]

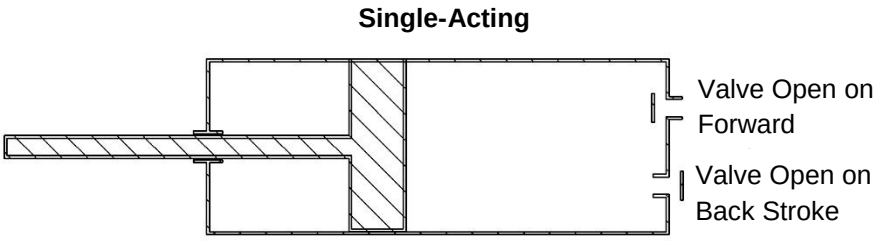

Figure 2-18: Schematics of Single-acting Pump

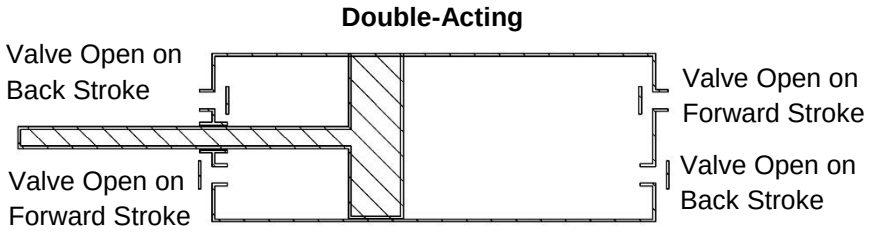

Figure 2-19: Schematics of Double-acting Pump

Piston pumps come in several configurations; linear as seen in the previous example, radial and axial types, as shown in Figure 2-22 and Figure 2-21 respectively. In radial piston pumps, pistons are positioned eccentrically to the shaft. As the shaft rotates one side of the pump sucks fluid (blue) and the other displaces (orange). An axial piston pump works in a very similar way – all pistons are mounted on the swashplate which is offset by an angle. This angle determines the stroke length of the piston. When the shaft rotates around its axis, the position of the piston changes inside the rotating barrel. Unlike previous types of reciprocating pumps, an axial piston pump does not require valves, which means it could operate at a higher speed. A benefit of radial and axial piston pumps over a single linear piston pump is that the flow is less intermitted due to the multiple-piston configuration.

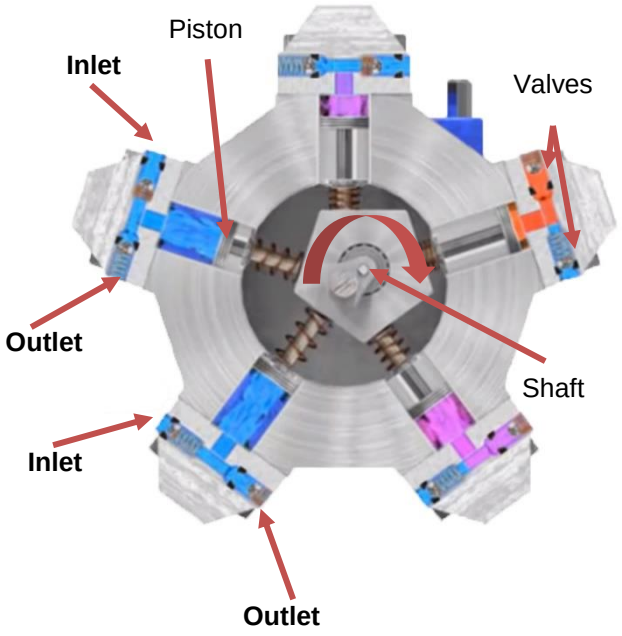

Figure 2-20: Radial Piston Pump [38]

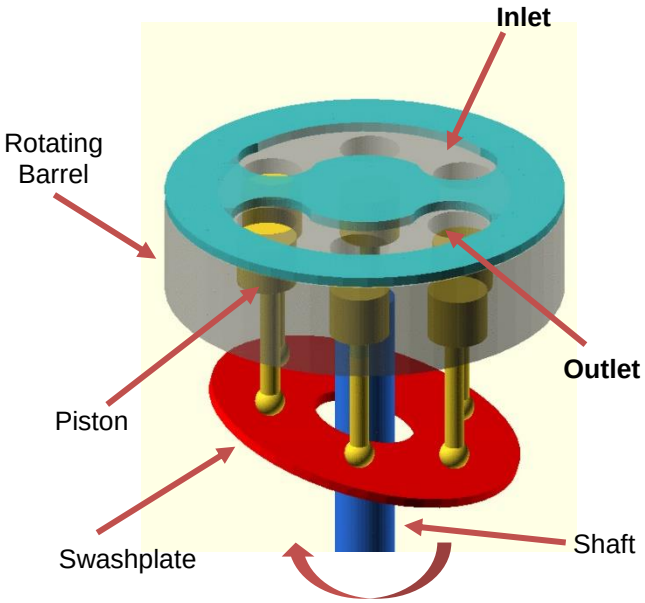

Figure 2-21: Axial Piston Pump Valve [39]

Unlike a turbopump, which generates pressure by converting kinetic energy of the fluid into the pressure, in reciprocating pumps pressure is generated by resistance in the piping and the system [15]. Thereby, a constant flow rate can be maintained regardless of the discharge pressure. Piston pumps are typically used in high-pressure applications, and in most cases, the pressure limit is constrained by the materials and not the system itself.

One advantage over rotary displacement pumps is that piston pumps are widely used with cryogenic liquids, such as Nitrogen (N_2), LOX and in some cases Hydrogen [40]. Commercially available cryogenic reciprocating pumps are able to operate at pressures up to 690bar, significantly higher than a turbopump could produce [41]. Another advantage is that none of the rotary components are required to operate directly in the cryogenic environment.

To increase life expectancy, reciprocating pumps typically operate at relatively low crank speeds. In this case, to satisfy the demands of a higher flow rate, the overall system size would have to be increased. This makes the pump bulky and heavy, which is undesirable for rockets. It should be noted that the life expectancy of most ground based pumps are years, and not minutes which are required for rocket stages.

Pump speed is the most critical selection criterion for the piston pump, and depends on piston life expectancy, NPSH, pulsation, valve and pump type. The design speeds are often capable of twice that of the actual rated speed [15]. The operational lifetime of the rocket pump is significantly shorter, which enables it to operate close to its design speed.

A study conducted by NASA in 1974 suggested that piston pumps become more attractive options for lower thrust rocket propulsion than a turbopump [23]. XCOR Aerospace has developed a rocket piston pump (Figure 2-22) for a reusable suborbital launch vehicle. Each pump is powerful enough to deliver the LOX to two engines and a second pump delivers fuel for the same two engines [25]. Each engine can produce ≈13.3kN of thrust or ≈4.5kg/s at an Isp of 300s [25].

By comparison with a high-performance turbopump, a piston pump requires no exotic materials or manufacturing process, and the parts can be readily built using high-precision machining shops [25]. The company has fabricated all their pumps using automotive manufacturing techniques developed over past 120 years [42]. Most importantly, XCOR Aerospace claims that this type of pump is an order of magnitude cheaper than a turbopump with a similar capability [25]. They made further claims, that the piston pump can outperform a turbopump for smaller thrust levels below 267kN to 445kN (90kg/s to 151kg at an Isp of 300s), depending on the propellant type [25]. However, the disadvantage of the system is that it produces pulsation.

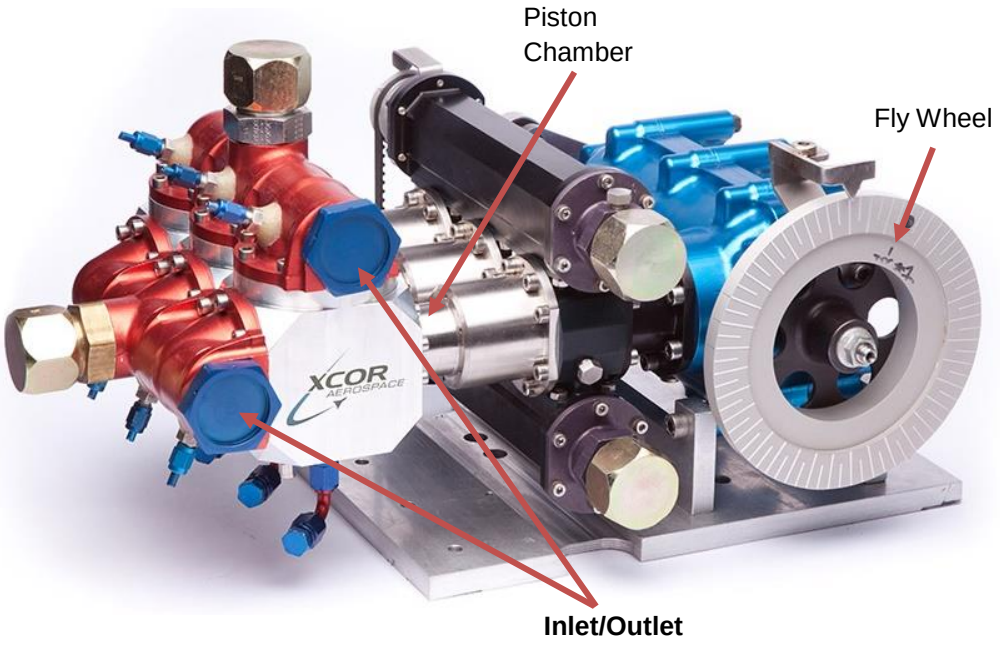

Figure 2-22: XCOR Triplex Piston Pump [43]

2.3.3.1 Pulsation

A reciprocating piston motion produces irregular flow rates, causing the fluid's velocity and pressure to fluctuate with respect to crankshaft angle. As fluid is constantly accelerated and decelerated at the suction pipe, this requires an additional energy to keep the fluid from falling below vapour pressure. This phenomenon is called an acceleration head and it must be compensated by increasing the $NPSH_A$ margin. It should be noted, that a higher value of $NPSH_A$ does not necessary reduces the effects of pulsation, it just moves the generated waveform away from the vapour pressure region. By some estimates, the acceleration head can be encountered up to 10 times higher than any other losses in $NPSH_A$ [15]. The magnitude of the acceleration head can be calculated from Equation 2-10 [44]. To compensate for the changes, the $NPSH_A$ for the piston pump can be redefined as expressed in Equation 2-11.

$$H_{acc} = \frac{LVnC}{gK} \tag{2-10}$$

Where H_{acc} – acceleration head (m), L – actual suction pipe length (m), V – average flow velocity (m/s), n – stroke speed (RPM), C – Pump Constant (see Table 2-2), g – Acceleration due to gravity 9.81 m/s^2 and K – fluid compressibility constant: 1.5 for water.

$$NPSH_A = H_{tank} + H_{elevation} - H_{acceleration} - H_{friction} - H_{vapour} \tag{2-11}$$

A high reciprocating speed is paramount to minimise the inert mass fraction of the launch vehicle. However, the speed of the pump affects the acceleration head by a factor C. The pulsation can be minimised by reducing the length of the pipe, installing a large diameter pipe, which consequently results in smaller velocity changes, incorporating damping and most importantly choosing the right pump type. As shown in Table 2-2, the pump constant varies from 0.4 to 0.022 and this has a significant influence on the pulsation; a larger number of cylinders would lead to a smaller C factor, and as a result, pulsation would be less. Figure 2-23, shows how the flow rate varies across different pump configurations. Vertical and horizontal axis refers to flow rate and crack angle respectively. A continues black line indicates the total flow and dotted lines flow of each cylinder. The flow rate for a duplex double-acting pump can vary between minimum and maximum values by 46%, while the flow variation for a nonuplex single-acting one falls to 2.1%. This suggests that pulsation between cycles can be reduced by installing a larger number of cylinders. For the most efficient flow distribution per cycle, an odd number of cylinders should be considered. An even number of cylinders will result in flow overlap of two or more pistons, which in turn results in emphasised peaks that generate greater pulsation [44]. For example, the four-cylinder single-acting pump flow rate profile is similar to the duplex double-acting one, as seen in Figure 2-23. This will have a total flow variation of 46%. To satisfy rocket propulsion requirements, a high number of cylinders is desirable to minimise the thrust fluctuation. The benefits of using a large number of cylinders diminishes due to the higher inert mass, hence it is unlikely that a large number of cylinders, such as septuplex or nonuplex pumps can provide enough benefit to justify the additional mass. Moreover, it should be taken into consideration that higher values of the acceleration head would result in a larger value of $NPSH_R$, which directly affects the mass of the propellant tanks. In addition, if a low number of cylinders is found to be the most effective option, a high pump speed can minimise the intermittent flow, resulting in more acceptable conditions for the launch vehicle.

Table 2-2: Pump Type Constants [44, 45]

Pump Type	No. Cylinders	Crank Angle	C
Simplex SA	1	360	0.4
Simplex DA	1	180	0.2
Duplex SA	2	180	0.2
Duplex DA	2	90	0.115
Triplex SA	3	120	0.066
Triplex DA	3	120	0.066
Quintuplex SA	5	72	0.04
Sextuplex SA	6	60	0.55
Septuplex SA	7	51.4	0.028
Nonuplex SA	9	40	0.022

SA = Single-acting; DA = Double-acting

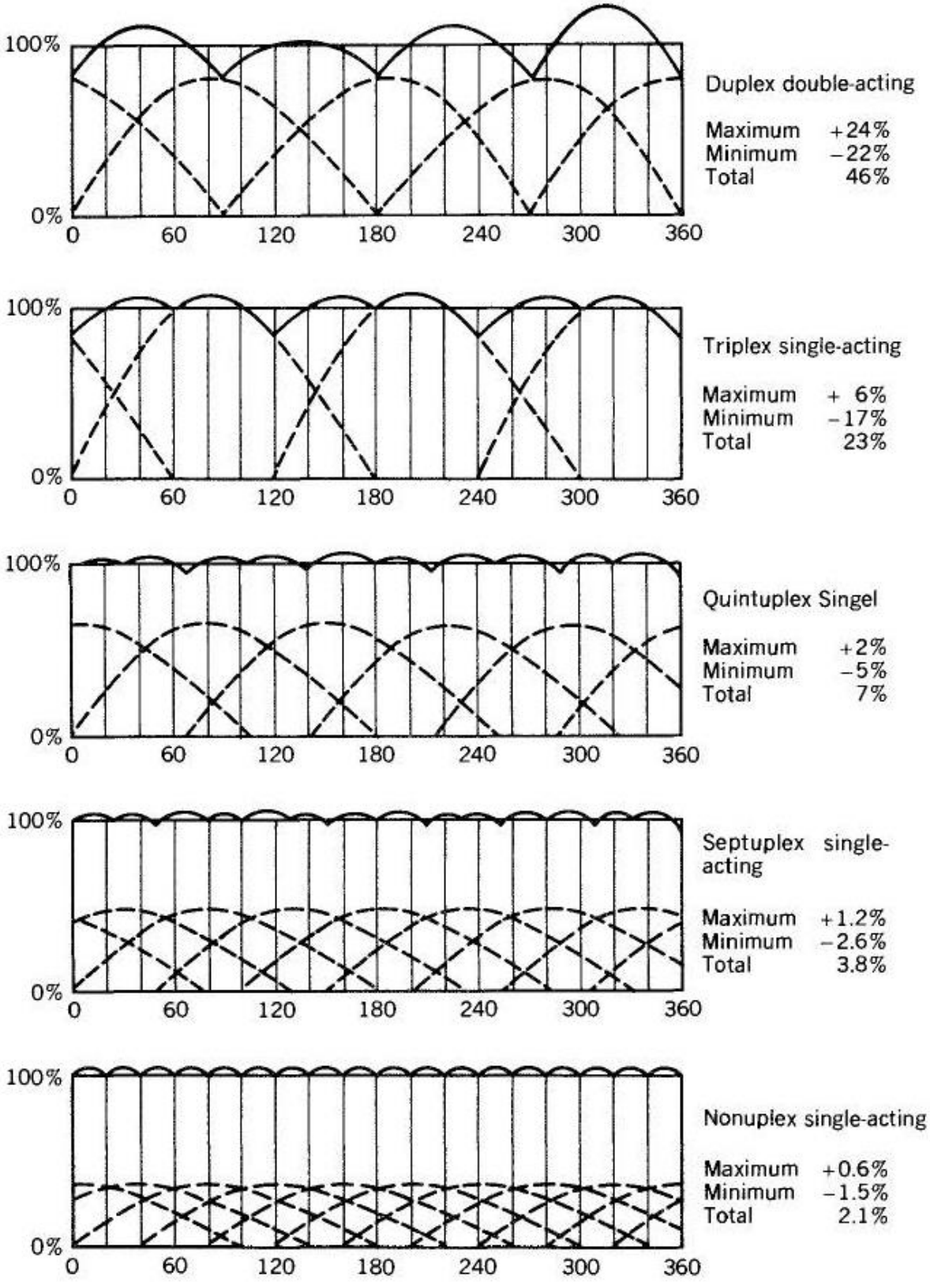

Figure 2-23: Flow Variations for Multi-Cylinder Pumps [15]

2.3.3.2 Valves

Valves are another critical part of the reciprocating pump which requires attention for the feasibility study. The primary function of a valve is to control the flow direction in the system. Self-acting check valves are the simplest and cheapest type of valve. They operate automatically and do not require any external controls, such as an electric input. When the upstream pressure drops below a certain value valve opens, allowing the fluid to flow. The pressure at which a valve opens is known as a cracking pressure [46]. This factor affects the inlet pressure requirements. The operating speed of self-acting valve tends to be restricted by a hydraulic limit, therefore for greater speeds, other valves such as actuated valves must be considered but these result in a higher complexity and cost [44]. For the feasibility study, the following valves were considered:

2.3.3.2.1 Poppet Valve

Poppet valves are most commonly used to control air flow in car engines as shown in Figure 2-24. A stiff spring is fitted around the poppet, which aids the poppet to return to its original closed position, and thus decrease the response time. This type of valves require an external driver, such as the camshaft, to control the motion of the valve. Hence, the additional components add extra complexity and mass to the system, but it is well developed technology. There are no known applications for cryogenic liquids or reciprocating pumps, but poppet valves should perform as expected under these conditions, as long as materials are compatible with cryogenic and oxidiser liquids.

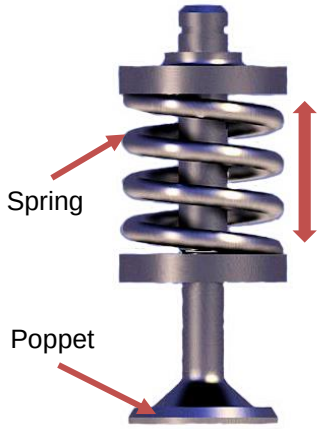

Figure 2-24: Poppet valve [47]

2.3.3.2.2 Check Valves

Check valves comes in many types, such as tilting, butterfly, poppet and ball valves. Tilting and butterfly valves are less relevant thus they were not considered. Several configurations of poppet and ball valves are illustrated in Figure 2-25 and Figure 2-26. These valves tend to be self-acting and they are mainly used to control the fluid flow in only one direction. Unlike previously described poppet valves, self-acting valves do not require an external driving mechanism to operate them; the pressure differential between the inlet and outlet side dictates the position of the valve. At the cracking pressure, the ball/poppet moves out of its original position, allowing fluid to flow around it. A spring can be installed for a faster response time and to ensure a tight seal. The spring stiffness will lead to higher cracking pressure requirements; therefore, it must be sized correctly to ensure severe cavitation is avoided.

These valves are often used in reciprocating pumps to pump fluids at low flow rates and high pressures. The operational speeds of these valves are low, which are likely to be limited by weight of the ball/poppet; a heavier object would lead to a higher inertia which restricts the movement.

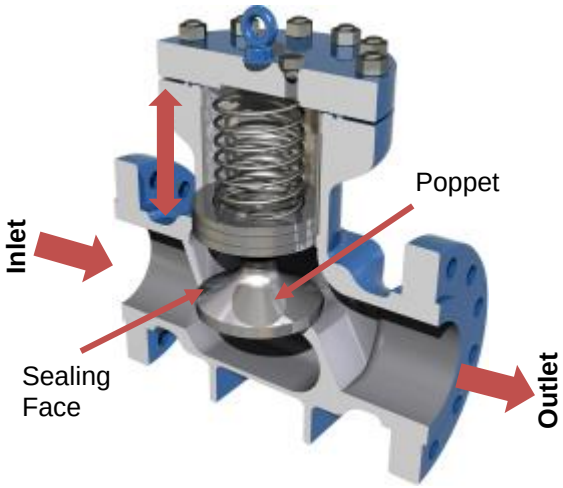

Figure 2-25: Poppet Check Valve [48]

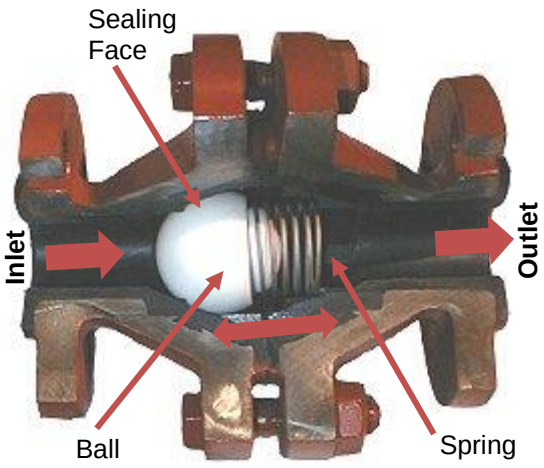

Figure 2-26: Ball Check Valve [49]

2.3.3.2.3 Sleeve Valve

The sleeve valve consists of a piston and sleeve mounted insider the piston cylinder. Figure 2-27 illustrates the sleeve valves used in the Bristol Centaurus Mark 175 engine. There are two or more cut outs in the sleeve for the inlet and outlet. The sleeve itself moves in reciprocating and rotation motions which are synchronised with the piston using gears. As the piston moves down, the cut out in the sleeve is matched with the inlet pipe to allow gases to enter the piston cylinder and vice versa for ejecting gases out of the cylinder.

However, this design was very shortly abandoned as poppet valves offered a lighter solution. In addition, it is heavily dependent on lubrication and good sealing is very difficult to achieve due to the number of moving parts.

There is no evidence that such a valve has ever been tested with cryogenic liquids. The large contact area between the sleeve and piston cylinder would cause significant heat generation, especially when operating at high speeds and high pressures. Special lubrication techniques would have to be implemented as standard lubrication will not work at low temperatures.

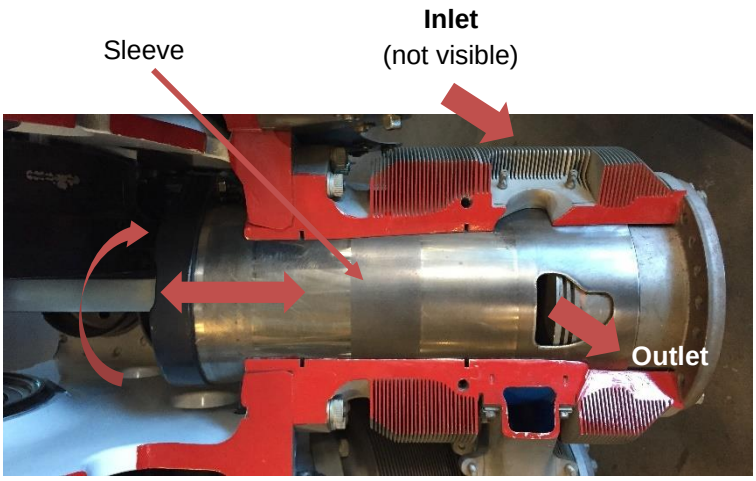

Figure 2-27: Sleeve Valve [50]

2.3.3.2.4 Reed Valve

A reed valve is a self-acting valve which works due to a pressure differential, similarly to the ball/poppet valves described previously. The reed valve comes in many shapes and forms, which consist of reed petals mounted on the reed base. An example is shown in Figure 2-28. At the cracking pressure, the petal flexes away from the reed block, resulting in fluid flow. A stop plate is fitted to prevent the material of the petal yielding beyond its elastic limit. When the flow is reversed, the petal elastically returns to its original position, closing the valve.

Petals are often made of a thin sheet of metal or composite material to enhance performance. The fibre orientation of composite materials allows the adjustment of the fibre orientation to make the petal stiffer and stronger [51, 52].

The low mass of petals allows them to operate at very high speed. In karting two stroke engines, this type of valve operates from 7,000 to 20,000RPM [51]. Due to the size and thickness of the petal, two stroke engine reed valves can only handle relatively low pressures. But in a modular configuration (Figure 2-29), reed valves are known to handle much greater pressures than required for two stroke engines. This is covered in more detail in **2.3.3.2.5 Plate/Ring Valve** section.

It is unclear whether reed valves have ever been tested under cryogenic conditions, but there is sufficient evidence indicating that they have been considered. XCOR Aerospace has patented a high-speed reed valve for application with cryogens and high reverse pressures, but the information on the design is very limited [53].

Figure 2-28: Reed Valve [54]

2.3.3.2.5 Plate/Ring Valve

Cut outs of the plate/ring valve are shown in Figure 2-29 and Figure 2-30. The valve plate sits between two valve seats, suspended on springs (not visible in this figure) to keep it in a closed position. At the cracking pressure, the spring plate moves away from the valve seat, resulting in flow through it.

This type of valve is often used with gas reciprocating compressors and the design can range from CT valves (Figure 2-30) to a modular reed valve configuration (Figure 2-29). Some plate valves can operate at speeds of over 3,600 RPM and pressure differentials up to 250bar [55, 56].

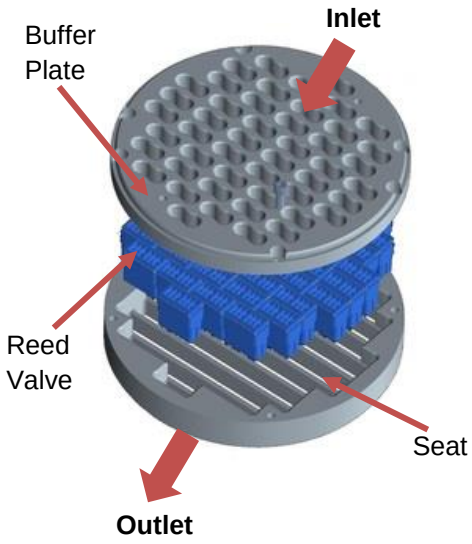

Figure 2-29: Plate Reed Valve [56]

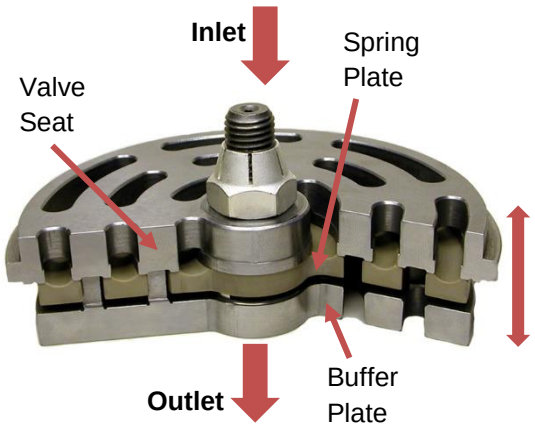

Figure 2-30: Plate/ring Valve [57]

2.3.4 Pressure-Fed System

The pressure-fed system is the simplest and cheapest pressurisation option, which relies entirely on the tank pressure for pressurisation. A schematic of this type of system is illustrated in Figure 2-31. When the control valves are opened, the pressure differential forces propellant into the combustion chamber where it is burned and ejected through the nozzle. To maintain the propellant tanks at a constant pressure as the propellant is consumed, high pressure gas flow to the propellant tanks is regulated. To reduce weight, helium is often used as a pressurising gas.

The major drawback of the system is that it cannot supply propellant to the combustion chamber at higher pressures than the propellant tank pressure. The requirement of higher pressures will result in adverse effects on the weight of the launch vehicle, due to increased propellant tank mass. This becomes an especially important factor as the size of the launch vehicle becomes greater. In general, the pressure-fed system gives a superior motor performance over the pump-fed system when the total specific impulse or mass flow rate is low, chamber pressure is low, the thrust to weight ratio is low (typically 0.6) and it is used for repeated short duration bursts [16].

This system is the most developed and the one most often used in spacecraft for manoeuvring attitude corrections. However, no launch vehicles have ever been developed and flown with a pressure-fed system. The thickness of the propellant tanks can be calculated by using hoop stress (Equation 2-12), which shows that by increasing propellant tank pressure or radius, the tank thickness will increase by a factor. Hence, storing propellant at high pressures on a large vehicle would result in a high inert mass. In addition, to retain a constant propellant tank pressure would require gas tanks and this adds more weight. Thus, the practically of such a system diminishes with the size of the vehicle.

$$\sigma_\theta = \frac{Pr}{t_w} \tag{2-12}$$

Where σ_θ – Hoop stress (Pa), P – internal pressure (Pa), r – mean radius of cylinder (m), t_w – wall thickness (m)

These weight issues can be mitigated by preheating the pressurised gas before injecting it into the propellant tanks. This will cause the gases to expand, resulting in higher pressures and thus less pressurant would be required. The advantage of this option is that the pressurant gas can be stored at lower pressures, resulting in lower inert mass. The combustion chamber pressure also can be lowered, which would lead to a thinner wall and lighter tanks, but this will lead to a decline in performance. Despite these challenges, several companies such as such as Firefly Space Systems are exploring pressurisation-fed system option for smaller launch vehicles, using light weight but high-pressure propellant tanks.

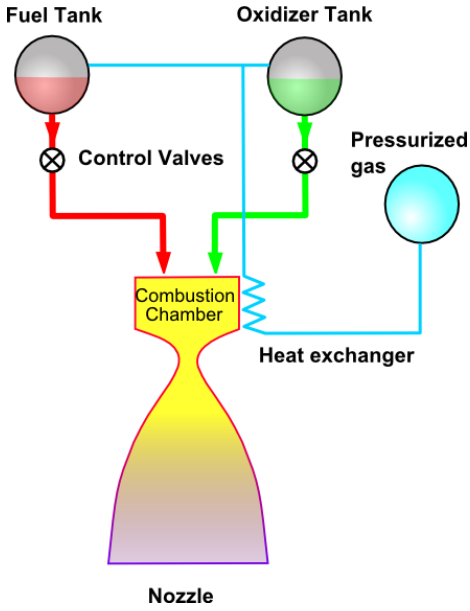

Figure 2-31: Pressure-fed system [58]

2.3.5 Pistonless Pump

The pistonless pump is an advanced version of the pressure-fed system with schematics shown in Figure 2-32. Each oxidiser and fuel tank consists of a large, low pressure tank, two or more pump chambers and one or more high-pressure tanks. The advantage of this system is that the propellant is stored at a relatively low pressure in the main tanks but pressurised in the smaller pump chambers. This helps to retain a relatively low mass of the tanks responsible for feeding the propellant directly to the engines. In fact, the main tank mass will be the same as for a turbopump, but the pistonless pump system will be slightly heavier due to the additional pump chamber and pressurisation tanks [59].

Unlike a turbopump which is very difficult to scale up or down without having to redesign the pump, the pistonless pump can be optimised at various scales [59]. A rocket which uses a turbopump must be started carefully to avoid engine pressure and flow fluctuation during ignition, which can be caused by cavitation. As Harrington claims, the pistonless pump can be started at full pressure and maximum flow rate. He further claims that the pistonless pump is less expensive than the turbopump, as it offers low development risk, manufacturing tolerances not need be tight, no exotic materials are required, and it is easier to integrate and easy to test [59]. In addition, further estimates showed that such a system uses less than 1% of its propellant's mass to run the system, whereas the turbopump can consume between 2.5% to 5% [59].

There are also some drawbacks of this system. Helium is a very scarce element, and in 2008 it was estimated that 78% of world helium reserves are based in the United States [60]. Helium might have to be imported from other countries or an alternative, heavier pressurisation gas must be used.

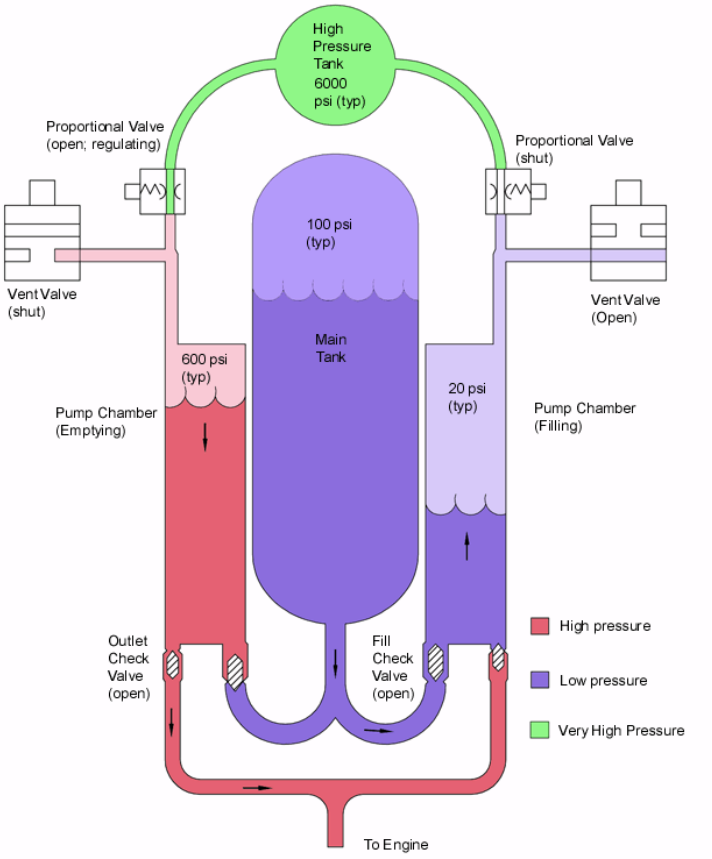

Figure 2-32: Pistonless Pump [61]

2.4 Pressurisation Options Summary

To narrow down the list of potential pressurisation options, all the systems were compared against the mission requirements and the less likely candidates were excluded from further evaluation. There are three major requirements, which the pressurisation system must meet.

- The system must be compatible with cryogenic and oxidising liquids. Properties of these fluids are listed in Table 2-1.
- Must supply high flow rates at high pressures
- Must be a lightweight and a reasonably sized solution.

2.4.1 Turbopump

Turbopumps enable high flow rates and pressures independent of tank pressures. High specific suction speed capacities allow tank pressures to be pressurised between 0.7 bar and 3.4 bar, resulting in a low inert mass [16]. It is evident that this system can meet the mission performance requirements, but the development and manufacturing costs of a high-performance turbopump may not be economically feasible for a small low-cost launcher.

The design and manufacture processes are very complex and time consuming. Any modification to the hardware can also lead to detailed design modifications and high costs. Some of the cost could potentially be reduced by incorporating new manufacturing techniques, such as 3D printing, for fabricating complex parts. A gas turbine creates many engineering challenges due to the large temperature gradient, thus replacing it with an electric power source and high-power density

batteries, it might further reduce the costs. Alternatively, pump performance can be traded with the cost.

Complex flow modelling or testing would be still necessary for the secondary flow paths, such as bearings and seals, to ensure the leakage is kept to a minimum and adequate separation is maintained between oxidiser and fuel [62]. Furthermore, currently accurate cavitation modelling data for high performance is not available, at least to the level required to provide useful information for engineers [63]. These and other key challenges for turbopumps are summarised in Table 2-3.

Table 2-3: Challenges of Turbopump

	Challenges
Specific Suction Speeds	• Choosing a desirable N_{ss} value for optimum performance, power and pressure. • Experimentally verify pump performance.
Bearings	• Cryogenic and corrosive environment. • High operating speed at high pressures (large DN factor). • Lubrication. • Provide adequate radial stiffness and damping. • Able to start and shut down reliably.
Seals	• Must work at extremely large temperature gradient. • Must work at high pressures and high speeds (large PV factor). • Oxidiser and fuel must be kept separate.

Based on the proposed cost reduction options, the cost could be reduced to some degree, however there is little supporting evidence that cost can be reduced enough to be suitable for a low-cost launcher. Based on this information for potential research and Technology Readiness Level (TRL), the turbopump is a strong candidate which requires further investigation.

2.4.2 Screw Pump

The screw pump can be used for high flow rates at high pressures, however there are no known examples of it being used for cryogenic applications. Due to all faces being sealing faces and material shrinkage at low temperatures, it could be extremely challenging to achieve high tolerances for low temperature applications. An increased cavity size would compromise the sealing performance, resulting in a higher leakage rate, especially when dealing with low viscosity fluids at high pressures. In addition, the system relies on a labyrinth seal to separate inlet and outlet sides, and therefore high pressures requires longer screws and a larger number of threads, which adds extra weight and complexity. The manufacturing processes can be as difficult as building a turbopump due to the requirement of tight tolerances.

Due to the requirement of high pressures, this type of pump is unlikely to provide a practical pressurisation system for launch vehicles. A very long pump can make it difficult to store, without compromising the length to diameter ratio of the launcher. The disadvantages of the screw pump outweigh all potential advantages that it could offer for a small launch vehicle. Based on this data alone, the screw pump was deemed unsuitable and therefore excluded from future studies.

2.4.3 Gear, Vane and Lobe Pumps

While gear and lobe pumps have a wide range of applications, there are no known applications pumping cryogenic liquids as well. Lobe and gear pumps are limited in such applications, due to cryogenics having a low viscosity. Similarly, the screw pump, due to all faces being sealing faces, retaining high tolerances at very low temperatures poses difficult engineering challenges. While the gear pump is not affected by low viscosity to the same extent as the lobe pump, tolerances can also be an issue.

Incompatibility with low viscosity media and difficulty retaining tight tolerances at cryogenic temperatures makes the lobe pump an unlikely candidate for a rocket pressurisation system. Moreover, this type of pump uses external timing gear to ensure that the lobes are synchronised. This can further complicate the system, especially if they must be chilled to reduce thermal stress. There is very little potential that such system can meet rocket pressurisation requirements, therefore it was excluded from further study.

While gear pumps have a higher tolerance to low viscosity fluids than vane pumps, the compatibility with LOX at high pressures is questionable. At low viscosities, efficiency is diminished which directly affects the pressure head obtainable. At cryogenic temperatures, the cavity tolerances are further reduced, resulting in additional inefficiencies. Similarly to the lobe pump, the gear pump is considered to offer very little potential, hence it was ruled out as a technology of interest.

Vane pumps are used in some cryogenic applications, but mostly other systems such as turbopumps are the preferred option [64]. This type of pump is typically used when pressure requirements are relatively low, due to constraints placed on the vanes. A larger pressure differential between the inlet and outlet sides would result in thicker vanes and higher friction losses. Furthermore, it could pose serious challenges to ensure vanes at cryogenic temperatures do not freeze in their initial position. This for sure would require a considerable amount of time and effort to find a reliable technique to overcome this issue. A frozen vane or vane with a restricted movement can cause significant efficiency losses, pump damage or even catastrophic failure. Moreover, the contact areas between vanes and wall must not produce friction at heat points, as this can ignite LOX inside the pump. This could become increasingly important when running the pump at high speeds.

Based on the information obtained, it was concluded that the vane pump complexity outweighs all the advantages for its use as a low-cost pressurisation system. In addition, the system cannot deliver the required high pressures, and therefore, similarly to the lobe pump, it was deemed unsuitable for a small satellite launcher.

2.4.4 Piston pump

The piston pump is a relatively new technology in the space industry, which has been built and tested by XCOR Aerospace, however the architecture of this pump is a closely guarded secret. This system has been tested in small light aircraft, it has never been flown in a launch vehicle [65]. Often piston pumps are designed to operate at relatively low flow rate capacities and at high

pressures. Most piston pump lifetimes are measured in years not minutes, hence they tend to operate at relatively low speeds to minimise wear and tear. When the operational lifetime is measured in minutes, the operational speed can be drastically increased. The advantage of the piston pump, unlike a turbopump, is that it does not have a shut-off pressure. Hence, it can operate at very high pressures and normally the pressure requirement is limited by the materials and not the pump itself.

It is evident that the piston pump can meet the pressure requirements and is compatible with a cryogenic propellant. However, it is unclear what power to weight ratio it can achieve when operating at high reciprocating speeds and a high flow rate, due to limited information available in the literature review. As stated previously, XCOR Aerospace claims that the piston pump can outperform turbopumps for thrust levels below 267kN to 445kN. The thrust required level for sub 20 tonne launch vehicles does not exceed this given thrust margin.

Given XCOR Aerospace's claims and the progress they had made with this pump, the piston pump is a strong candidate for the future evaluation of this technology. Furthermore, not much research has been carried out on this type of pump regarding its application to small launch vehicles, which provides even more reason for this investigation.

2.4.5 Pressure-Fed System

The literature review has shown that pressure-fed systems can be used for high flow rates at high pressures and are suitable for use with cryogens. However, it becomes less efficient and practical as the size of the system increases due to the increasing size of the tank and the pressurant mass. Nonetheless, this type of pressurisation system costs a small fraction of the rocket turbopump, due to its simplicity, hence further studies must be carried out to investigate it's benefits for small launchers.

2.4.6 Pistonless Pump

The pistonless pump is a relatively new rocket pressurisation technology which offers reduced complexities similar to the pressure-fed system, but matches the mass savings of the turbopump [59]. This technology has been tested under lab conditions but it has not been flight tested. Taking into a consideration the claims made by Harrington, it can potentially offer an alternative pressurisation system, hence further investigation is required [59].

Chapter 3

Mass Model

3.1 Introduction

In the previous chapter four pressurisation options; turbopump, piston pump, pressure-fed system and pistonless pump were selected for further evaluation. To aid in a further selection process, the GLOM of a small satellite launcher was compared for a turbopump, pressure-fed and a pistonless pump. Due to limited data, it was not possible to construct an accurate mass model for the piston pump system, therefore it was not included in this evaluation. However, based on the previous claims made by XCOR Aerospace that a rocket piston pump can outperform a turbopump for thrust levels below 267kN to 445kN, the GLOM of a launcher with a piston pump was assumed to be equivalent to that calculated for a turbopump. It should be noted that this assumption is valid for small satellite launchers only.

To estimate GLOM, a mass model was developed based on some historic data and some other system estimates. The model also made it possible to run a sensitivity analysis to determine how the mass changes of other systems would affect the GLOM. In this instance, key parameters, such as payload capacity, stored propellant pressure, combustion chamber pressure etc., were altered to understand the effects on GLOM of the vehicle. Furthermore, the optimum operation conditions of each system were identified based on this mass model. The next section explains how the mass model was derived.

3.2 Methodology

3.2.1 Fixed Parameters & Assumptions

Based on historic data and Newton Launch System instructions, several baseline parameters were established:

- Vehicle should be made of three stages;
- it's length-to-diameter (L/D) ratio shall not be exceed 15 to retain structural rigidity.
- To keep the cost at a minimum, a modular stage 1 and stage 2 shared the same engines, but the 1st stage had a cluster or three engines to provide the required T/W ratio.
- The acceleration of the 3rd and 2nd stages shall not exceed 5g's and 1st stage should provide a T/W ratio of 1.2.
- To compensate for any discrepancies, a stage reserve mass percentage of 20% for the 3rd stage and 15% for the 1st and 2nd were added. The reserve mass percentage of the 1st stage and 2nd stage is lower as these stages are heavier, hence the error percentage would be lower.
- Delta-v of 10km/s. Each stage must deliver a specified amount of impulse for the launch vehicle to reach orbital velocity. A measure of impulse in rocketry is expressed as change in velocity or else known Delta-v. To optimise thrust requirements as stated above, the delta-v was split across the stages and the split varied to obtain an optimal solution.

The mass model uses a set of fixed parameters, as highlighted in red in Figure 3-1 to provide baseline data for each stage. Through an iteration process, highlighted in blue, the mass of the tanks, propellant, turbopump, thrust chamber etc., were estimated for each stage and the GLOM mass was obtained. Twenty-five iteration steps proved to be enough to estimate mass to the nearest 1kg. The process below explains how a single integration step has been constructed. For a closer look at the mass model refer to **Appendix A: Mass Model**.

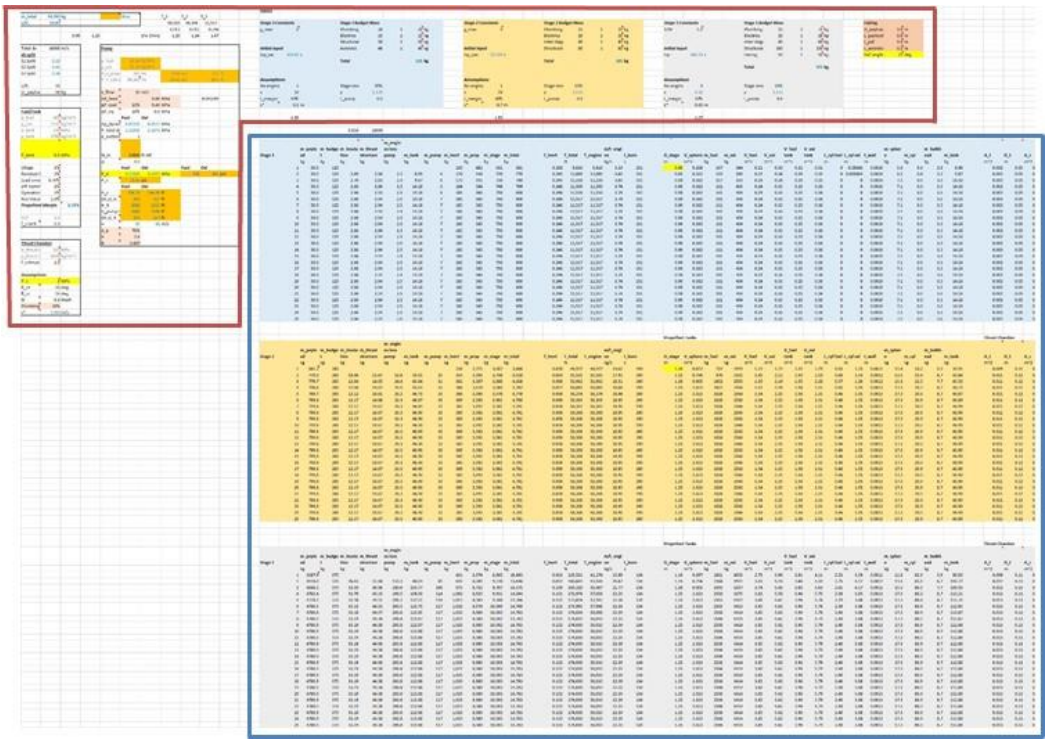

Figure 3-1: Mass Model

3.2.2 Thrust Chamber Mass Estimate

To estimate the mass of the turbopump and thrust chamber, the methodology outlined in Space Propulsion Analysis and Design was used, which was developed based on historic data [7]. The combustion chamber mass is expressed in Equation 3-1 [7]. The thrust chamber is normally made of high temperature resistant material such as Nickel. For the estimation, the properties of Nickel were taken from the Solidworks 2016 database for the calculations and a Factor of Safety (FOS) of 2.5 was assumed. A nozzle cone half angle (θ_{cn}) and constant contraction half angle (θ_{cc}) are shown in Figure 3-2 and Figure 3-3. A value of θ_{cn} typically ranges from 12° to 18° but the usual compromise is a half angle of 15°, thus this value was used in the mass model [7]. The range for constant contraction half angle (θ_{cc}), was not given, hence it was assumed to be the same as for the nozzle cone half angle.

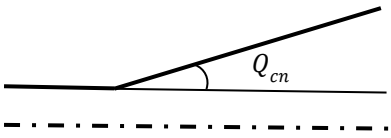

Figure 3-2: Nozzle Half Angle

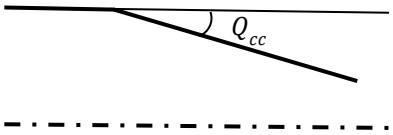

Figure 3-3: Constant Contraction Half Angle

$$m_c = \pi \rho_w t_w \left(2 r_c L_c + \left(\frac{(r_c^2 - r_t^2)}{\tan \theta_{cc}} \right) \right) \tag{3-1}$$

Where m_c – combustion chamber mass (kg), ρ_w – wall density (kg/m³), t_w – wall thickness, r_c – chamber radius (m), L_c – combustor cylinder length (m) and r_t – throat radius (m).

To complete the combustion chamber mass estimate, remaining unknowns, such as combustor cylinder length (L_c), chamber radius (r_c) and throat radius (r_t), were calculated using Equations 3-2 – 3-5. The remaining parameters such as the characteristic velocity (c^*) and Ips, were obtained from Rocket Propulsion Analysis V2.2 (RPA) software [9]. The optimum chamber pressure varied from system to system, thus changes in the resultant Isp were considered. The design requirements outlined in section **1.2**, were inputted into Rocket Propulsion Analysis. Using this software, these parameters were obtained for combustion pressures ranging from 1MPa to 5MPa at increments of 0.5MPa, as shown in Table 3-1 and Table 3-2. For the 1st stage and remaining stages, the data at sea level (Table 3-1) and in vacuum (Table 3-2) were used respectively.

$$L_c = \frac{L^* A_t}{A_c} \tag{3-2}$$

Where L – combustion chamber length (m) and L^* – chamber characteristic length

$$A_c = \frac{A_t}{M} \left[\left(\frac{2}{\gamma + 1} \right) \left(1 + \frac{\gamma - 1}{2} M^2 \right) \right]^{\frac{\gamma+1}{2(\gamma-1)}} \tag{3-3}$$

Where A_c – chamber cross-section area (m), M – Mach number in the combustion chamber (typical range 0.2-0.4) and γ –ratio of specific heats.

$$A_t = \frac{\dot{m}c^*}{p_c} \quad (3\text{-}4)$$

Where A_t – throat cross-section area (m), $\dot{m}$ – mass flow rate (kg/s), c^* – characteristic exhaust velocity (m/s) and p_c – chamber pressure (Pa).

$$A=\pi r^2 \quad (3\text{-}5)$$

Where A –cross-section area and r – radius

Table 3-1: Propulsion Data at Sea Level for Propane (C_3H_8) and Oxygen (O_2)

When Pe = 0.1MPa										
P_c	**MPa**	1	1.5	2	2.5	3	3.5	4	4.5	5
C*	**m/s**	1745	1760	1770	1777	1784	1789	1793	1797	1801
Isp	**s**	219	237	249	257	264	269	273	277	280
γ		1.172	1.172	1.172	1.172	1.172	1.173	1.173	1.173	1.173

Table 3-2: Propulsion Data in Vacuum for Propane (C_3H_8) and Oxygen (O_2)

When ε = 10										
P_c	**MPa**	1	1.5	2	2.5	3	3.5	4	4.5	5
Isp	**s**	308	310	312	313	314	314	315	315	316
γ		1.172	1.172	1.172	1.172	1.172	1.173	1.173	1.173	1.173

Moreover, the thrust chamber is comprised of other components such as the ablative layer, nozzle and injector. To take into account the additional weight, Equations 3-5 – 3-8 were used to estimate the nozzle mass and ratios from the "average" column in Figure 3-4 were used to calculate the remaining mass. It should be noted that the data in the figure is based on historic data.

$$m_n = \pi\rho t_w L_n (r_e + r_t) \quad (3\text{-}6)$$

Where m_n – nozzle mass (kg), L_n – cylinder length and r_e – nozzle exit radius (m).

$$\varepsilon = \frac{A_e}{A_t} \quad (3\text{-}7)$$

Where ε – nozzle expansion ratio.

$$L_n = \frac{(D_e - D_t)}{2\tan\theta_{cn}} \quad (3\text{-}8)$$

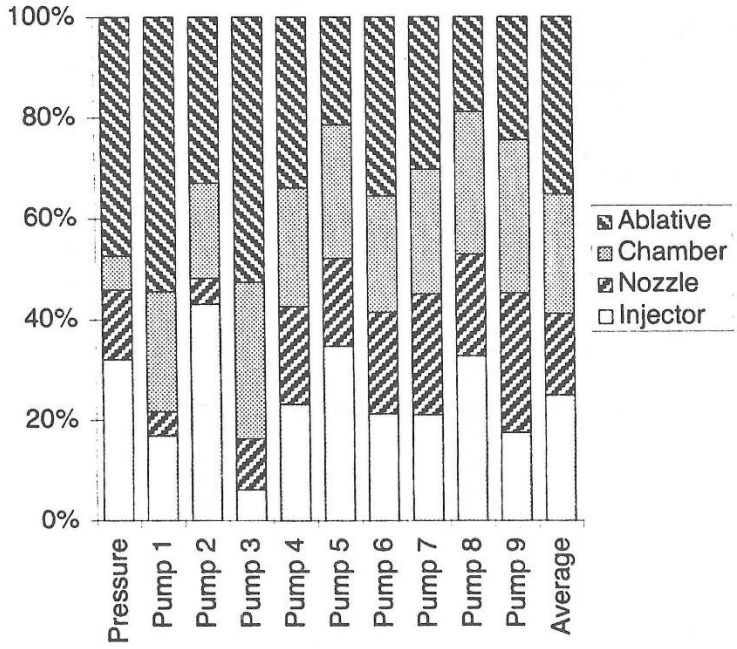

Figure 3-4: Thrust Chamber Mass Fractions [7]

3.2.3 Propellant and Tank Mass Estimates

For estimating propellant mass, Equations 3-10 and 3-11 were substituted into the Tsiolkovsky Rocket Equation 3-9, and then rearranged to give Equation 3-12

$$\Delta V = Isp \times g_o \times ln\left|\frac{m_o}{m_f}\right| \quad (3\text{-}9)$$

$$m_o = m_{inert} + m_{propellant} \quad (3\text{-}10)$$

$$m_f = m_{inert} \quad (3\text{-}11)$$

$$m_{propellant} = \left(e^{\frac{\Delta V}{Isp \times g_o}} \times m_{inert}\right) - m_{inert} \quad (3\text{-}12)$$

where m_f – final total mass (kg) and initial total mass (kg) and m_o – initial total mass (kg)

By calculating the propellant mass and using densities as outlined in Table 2-1, the total volume of fuel and oxidiser were calculated. This provided enough data to estimate the size of the propellant tanks. It is known that the O/F ratio is 2.5 and based on these two factors, the size of each tank was estimated. For the first iteration, a diameter of 0.8m was assumed, but if the L/D ration exceeded 15, the stage diameter was increased by an increment of 0.05 metres until L/D was reduced to the desired value. For simplicity, it was assumed that the stage diameter is equal to the propellant tank diameter and further assumptions were made that the Factor of Safety is 1.5, the tanks were made from aluminium 2024-T361, and the top and bottom parts of the tank were spherical [7]. Properties of aluminium were taken from the SolidWorks 2016 database and used for further calculations. Other uncertainties, such as ullage and a residual propellant, were used to determine a propellant margin [7, 16, 59].

The mass of spherical and cylindrical parts of the tank were then calculated using Equations 3-13 and 3-14. Wall thicknesses were estimated using Hoop Stress Equations 3-15 and 3-16 which were required to make mass estimates. To reduce the manufacturing complexity, a minimum wall thickness of 1mm was set.

$$m_{spherical\ section} = \frac{4}{3}\pi\rho_w\left(\left(\frac{D_{stage}}{2} + t_{wall}\right)^3 - \left(\frac{D_{stage}}{2}\right)^3\right) \quad (3\text{-}13)$$

Where $m_{Spherical\ section}$ – mass of spherical section (kg) and ρ_w – Material Density of the Wall (kg/m³)

$$m_{cylindrical\ section} = \pi\rho_w L_{cylinder}\left(\left(\frac{D_{stage}}{2} + t_{wall}\right)^2 - \left(\frac{D_{stage}}{2}\right)^2\right) \quad (3\text{-}14)$$

Where $m_{cylindrical\ section}$– mass of cylindrical section (kg) and $L_{cylinder}$ – length of cylinder (m)

$$t_{wall\ of\ sphere} = \frac{Pr}{2\sigma_\theta} \quad (3\text{-}15)$$

$$t_{wall\ of\ cylinder} = \frac{Pr}{\sigma_\theta} \quad (3\text{-}16)$$

Where σ_θ – Hoop stress (Pa), P – internal pressure (Pa), r – mean radius of cylinder (m), t – wall thickness (m)

Cryogenic liquids also require insulation to minimise heat transfer to the tanks. The insulation of each stage was estimated using Equation 3-17 [66]. For estimating the thrust structure mass, Equation 3-18 was used. The masses of the engines and tanks were based on the thrust chamber size and the size of the tanks [66].

$$M_{insulation} = 1.123A_{tank} \quad (3\text{-}17)$$

where $M_{insulation}$ – mass of insulation (kg) and A_{tank} – surface area of tank (kg/m²).

$$M_{Thrust\ Structure} = 2 \times 10^{-4}T \quad (3\text{-}18)$$

where $M_{Thrust\ Structure}$ – thrust structure mass (kg) and T – thrust of the engines (N)

3.2.4 Turbopump Mass Estimates

Finally, to estimate mass of the turbopump, recommended assumptions by Humble, Henry and Larso and the relationship between the mass of the turbopump and the pump shaft torque were used. The assumptions are listed in Table 3-3 and this relationship is expressed in Equations 3-19 and 3-20 [7]. In most cases, the middle value of the range was used for assumptions, however to obtain the mass for the worst case, the highest values of the empirical coefficient and empirical exponent were selected. By taking into consideration the pressure losses, the total delivery pressure was calculated in order to achieve targeted pressure in the combustor chamber. This pressure value was then converted in terms of head, measured in feet.

Further assumptions were made that each stage will have separate turbopumps for oxidiser and fuel.

$$m_{tp} = A\tau^B \quad (3\text{-}19)$$

$$\tau = \frac{P_{req}}{N_r} \quad (3\text{-}20)$$

Where m_{tp} – mass of the turbopump (kg), P_{req} – required pump power (W), τ – pump shaft torque ($N \cdot m$) and N_r – pump rotational speed (rad/s).

Table 3-3: Table 6 Assumptions [7]

Flow velocity (v_{flow})	10m/s
Pressure drop in the feed system (ΔP_{feed})	35,000Pa to 50,000Pa
Pressure drop in the cooling system (ΔP_{cool})	10% to 20%
Pressure drop in the injector (ΔP_{inj}) (unthrottled)	20%
Empirical coefficient (A)	1.3-2.6
Empirical exponent (B)	0.6-0.667

To estimate required power and pump rotation speed for the turbopump, another six steps had to be followed as expressed in Equations 3-22 – 3-26. To estimate the mass flow rate, the total thrust had to be calculated and values substituted into Equation 3-21. The thrust levels of the 2nd and 3rd stages are limited by the maximum G-Force, thus they were estimated using Equations 3-22. The 1st stage thrust is limited by the thrust to weight ratio, hence Equation 3-23 was used.

The pump rotation speed was calculated from suction specific speed as expressed in 3-24. A typical value for the suction specific speed (N_{ss}) is between 10,000 and 25,000ft-lbf for the designs with little cavitation [16]. To keep the pump complexity as low as possible, the smallest value was selected as a baseline parameter. The pump efficiency of 70%, was based on the pump efficiency diagram in Space Propulsion Analysis and Design [7].

$$Isp = \frac{T_{total}}{\dot{m} g_0} \tag{3-21}$$

$$T_{total} = g_{max} m_{inert} m_{payload} \tag{3-22}$$

$$T_{total} = m_{total} \left(\frac{T}{W}\right) g_0 \tag{3-23}$$

Where T_{total} – total thrust (N), g_{max} – maximum g-loading and g_0 – gravitational constant (9.81m/s²)

$$Q = \frac{\dot{m}}{\rho} \times 35.3146667 \tag{3-24}$$

Where Q – volumetric flow rate (ft³/s), ρ – density of media.

$$N_{ss} = 21.2 N_r \sqrt{\frac{Q}{(H_s)_R^{\frac{3}{4}}}} \tag{3-25}$$

Where N_{ss} – suction specific speed and $(H_s)_R$ – head suction required (ft).

$$P_{req} = \frac{g_0 \dot{m} H_p}{\eta_p} \tag{3-26}$$

Where H_p – pump's head pressure rise (ft), η_p – pump efficiency.

3.2.5 Pressure-fed and Pistonless Pump Mass Estimates

To estimate the mass of the pressure-fed and pistonless pump the same methodology as above was used, however these pressurisation options do not use a pump. Instead it requires a pressurant tank to keep the propellant tanks at a constant pressure. To keep the mass of the pressurant tank as low as possible, a spherical tank was assumed and using the Hoop Stress Equation 3-15, the tank thickness was calculated and then mass was estimated using Equation

3-13. The lowest pressurant tank pressure which allows the pressurant tank radius to be equal to or less than the launch vehicle radius was selected.

The pressurant mass was estimated based on the Ideal Gas Law (Equation 3-27) [67].

$$PV = mRT \tag{3-27}$$

Where P – pressure of gas (Pa), V – volume of gas (m^3), m – mass of gas (kg), R – gas constant (J/(kg·K) and T – temperature of gas (K). R for N_2 is 297(J/(kg·K) [68]

For the pistonless pump a few additional calculations were made to estimate the mass of the auxiliary/combustion tanks using the hoop stress Equations.

3.3 Phase 1: Combustion Chamber Optimisation

The initial parameters state that the pressure of the propellant must be raised by 30bar (3MPa), however this value was based on a launch vehicle with a turbopump. 3MPa might not provide the lowest GLOM for the overall system, thus the mass model was used to optimise the chamber pressure of all pressurisation options.

The graphs for each system, as shown in Figure 3-5 - Figure 3-7, were plotted to find a relationship between GLOM and Combustion Chamber Pressure. The results for the turbopump (Figure 3-5) indicate that a lower GLOM can be achieved by delivering a higher pressure to the combustion chamber. However, the benefits exponentially decrease as the pressures goes higher. For example, a pressure increase from 1MPa to 3MPa could lead to approximately 2,400kg reduction, while an increase from 3MP to 5MPa could lead to 700kg saving. However, optimising for high pressures is a less attractive option for a small low-cost launch vehicle as small mass savings could lead to significantly higher costs.

For pressure-fed and pistonless pump, as shown in Figure 3-6 and Figure 3-7, higher combustion chamber pressures have a negative influence on the GLOM. This is due to the requirement of thicker storage tanks and this offsets all mass benefits provided by a higher combustion chamber pressure. The model showed that the optimum chamber pressure for both of these systems is 1MPa. Nonetheless, the GLOM can be further minimised by installing a heat exchanger on the rocket nozzle, which expands the gases before injection into the main tanks. Harrington claims that the pressurant temperature must be raised to 310-810K [59]. To evaluate the temperature effects on the GLOM, the simulation was re-run with preheated pressurant gas at 810K and the results were recorded in Figure 3-8. The mass model showed that preheated gas can reduce the GLOM under optimum conditions by as much as 29% and 38% for pistonless and pressure-fed systems respectively. Furthermore, the optimum combustion chamber pressure for the pistonless pump rose from 1MPa to 1.5MPa. As seen in Figure 2-31, the heat exchanger is a simple design which only requires extra plumbing to reroute pressurant gases to the heat exchanger before the pressurant is delivered to the propellant tanks.

Based on all optimisations, the GLOM of the pressure-fed system, pistonless pump and turbopump (at 3MPa) were recorded in at their optimum design point in Table 3-4. The model showed that the GLOM of the vehicle with the pistonless pump system and pressure-fed system was 15% and 31%

respectively heavier than a vehicle with a turbopump. In addition it was noted that the GLOM of the launcher with pressure-fed and pistonless pump is mass sensitive - a slight increase in any sub system can significantly impact the overall mass of the vehicle. Therefore, further sensitivity analyses were carried out in the next section **3.4** to understand further effects on GLOM.

Table 3-4: Pressurisation System Comparison

	Turbopump	Pressure-fed**	Pistonless pump**
Propellant mass (kg)*	113	568	155
Pressurant tank mass (kg)*	N/A	460	410
GLOM (kg)	14,785	19,371	16,991

* 1st stage ** C_p= 10 bar

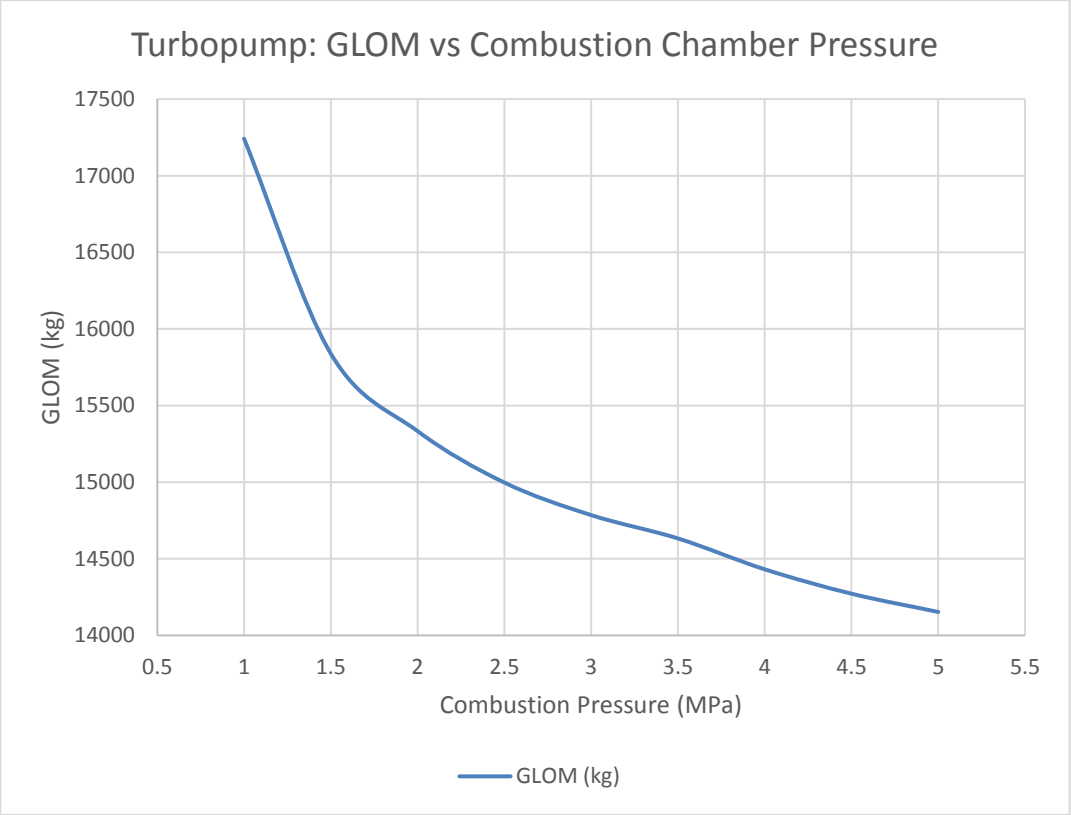

Figure 3-5: GLOM vs Combustion Chamber Pressure Graph of the Turbopump

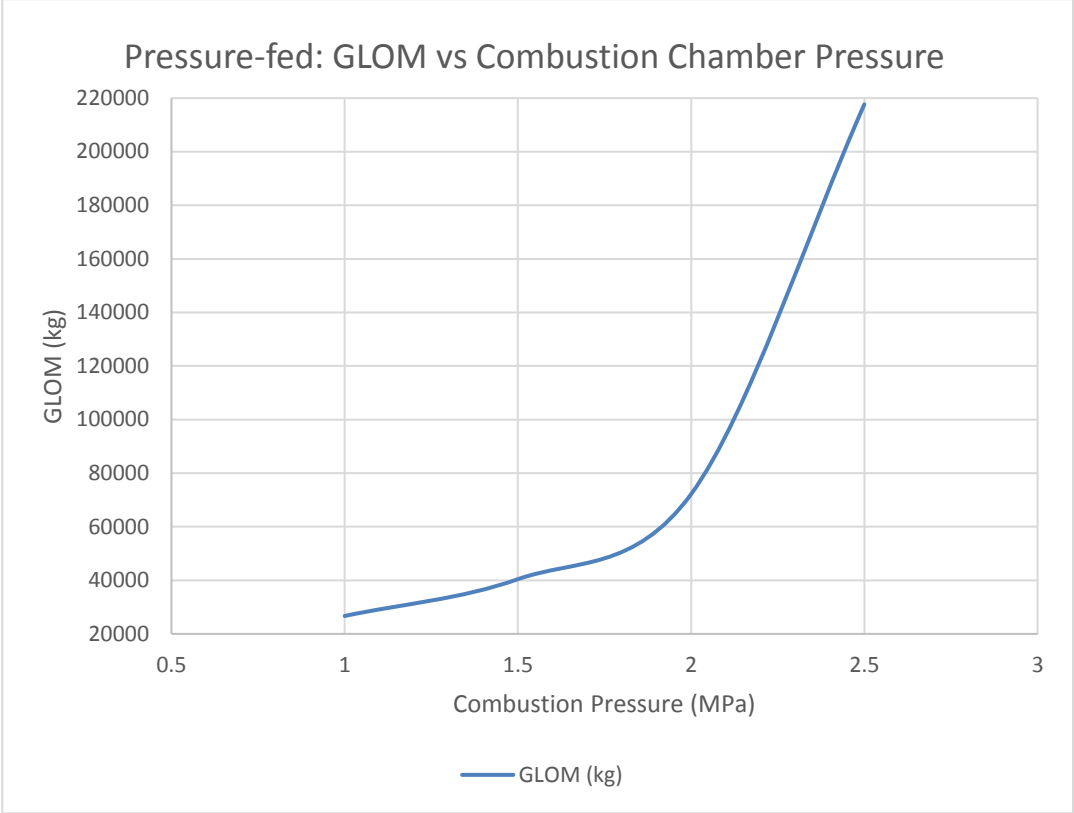

Figure 3-6: GLOM vs Combustion Chamber Pressure Graph of the Pressure-fed System

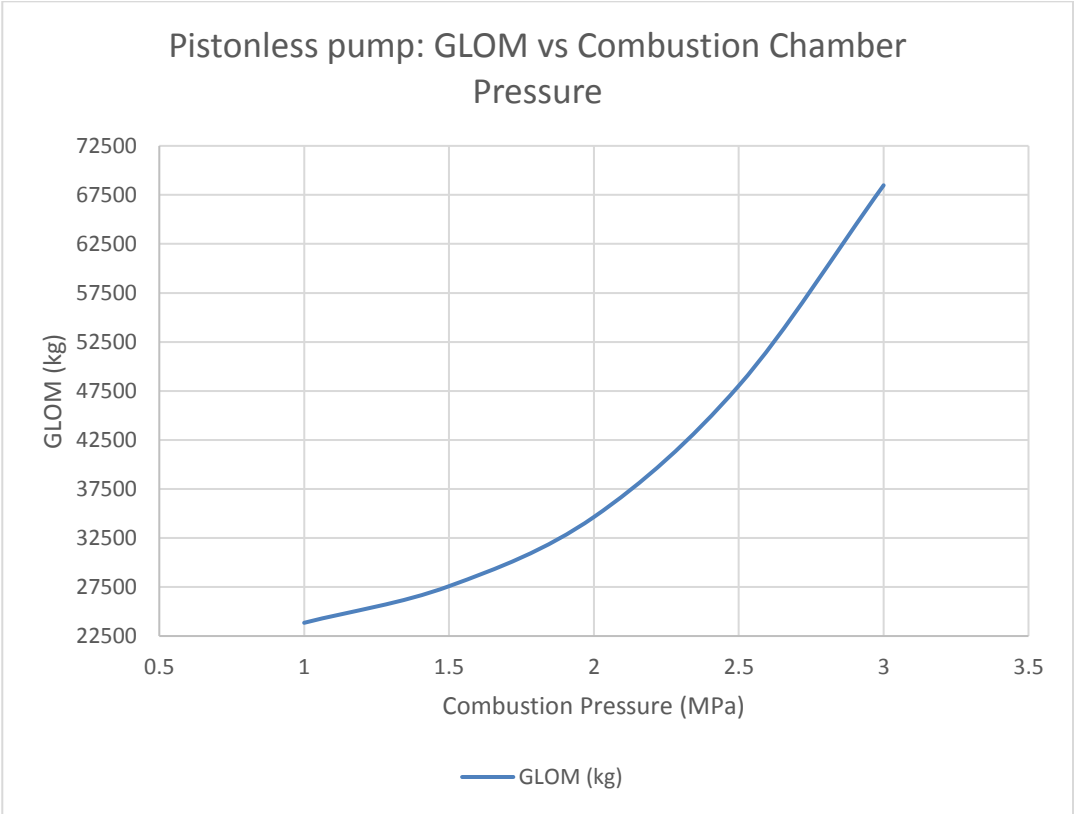

Figure 3-7: GLOM vs Combustion Chamber Pressure Graph of Pistonless Pump

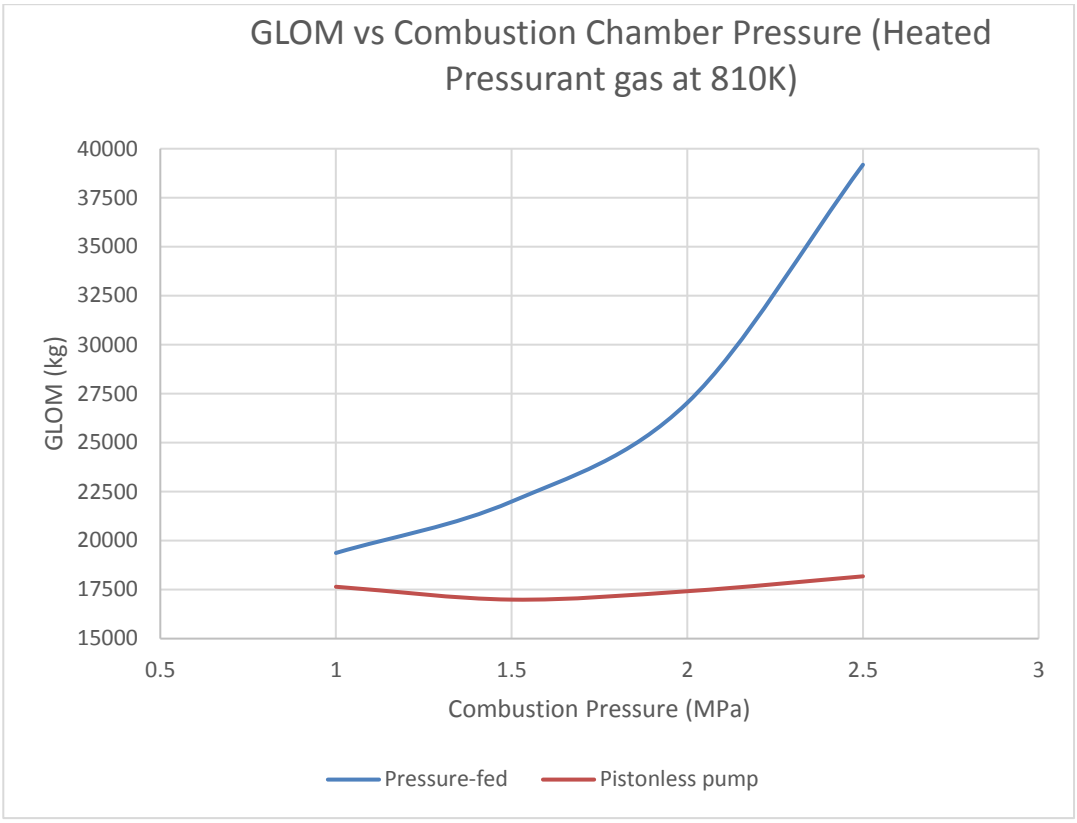

Figure 3-8: GLOM vs Combustion Chamber Pressure Graph at Heated Pressurant Gas 810K

3.4 Phase 2: Sensitivity Analysis

If a small low-cost launcher proved to be a success, there might come a need to expand the payload capacity, thus the pressurisation system must be scalable. Based on the previous data, a further comparison has been carried out to determine how the capacity affects the GLOM of the vehicle. In Figure 3-9 GLOM vs payload was plotted for all three systems to determine the effects. As expected, the GLOM of the vehicle powered by a turbopump will be less affected by these changes, followed by the pistonless pump and the pressure-fed system. Furthermore, the graph indicates that the payload capacity of a sub 20,000kg vehicle with a turbopump can be expanded to 150kg, whereas the payload of a pistonless pump can be expanded to 100kg max. It would be unlikely for a sub 20,000kg vehicle with a pressure-fed system to deliver a payload higher than 50kg.

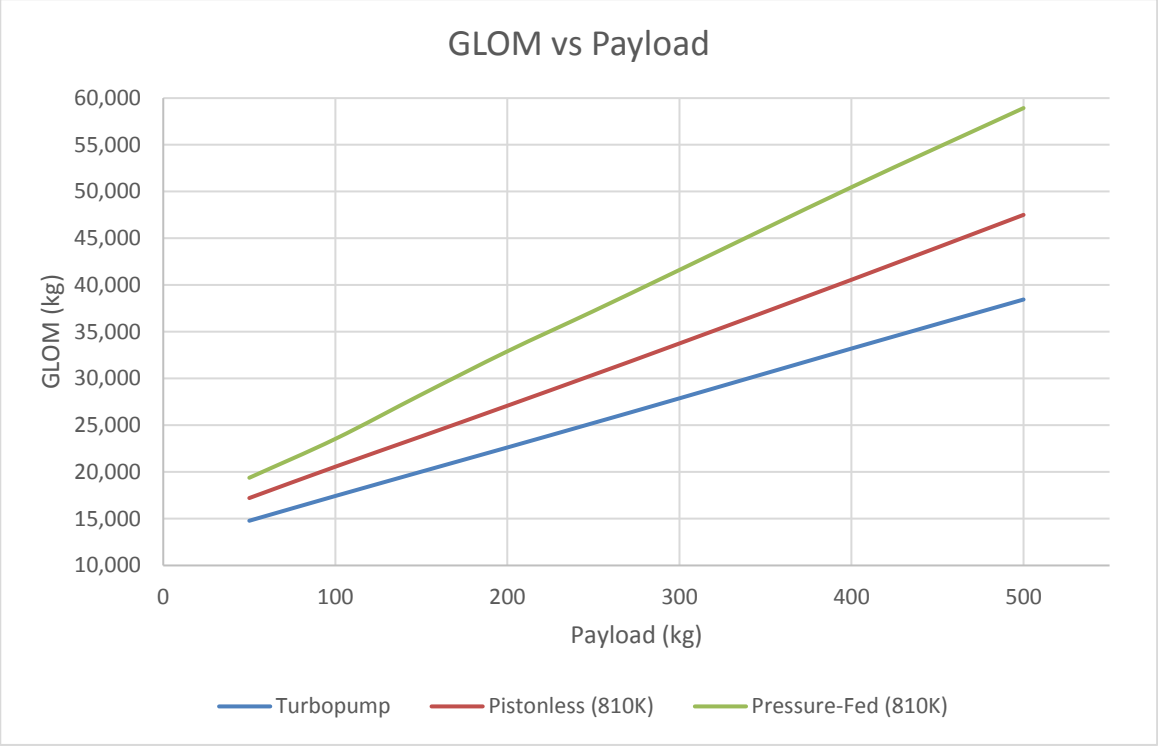

Figure 3-9: GLOM vs Payload for Different Types of Pressurisation

Despite the higher inert mass of the pistonless pump and pressure-fed system, these systems might still offer a cheaper alternative than the turbopump. Previously, the highest temperature of 810K for pressurant was selected but this top limit could be difficult to achieve. Therefore, the lower and middle limits of the proposed temperature range were evaluated and the effects on the GLOM were recorded in Figure 3-10 and Figure 3-11. Figure 3-10 indicates it is might not be possible to build a sub 20,000kg pressure-fed launcher unless pressurant temperature can be raised to 810K.

The GLOM of the launcher powered by the pistonless pump is also affected significantly by the temperature of the pressurant, as seen in Figure 3-11. Given that the pressure-fed system and pistonless pump are similar in complexity, the pistonless pump is more likely to offer a more attractive solution due to a lower inert mass. Furthermore, it was not possible to verify claims made by Harrington that this system can match performance that of the turbopump – it is only possible if the mass of the pressurant tank can be significantly reduced.

Specific suction speed (N_{ss}) characterises the pump's suction performance and typically this value ranges between 10,000 and 25,000 for turbopumps in rockets [16]. In the previous cases, the worst-case scenario was assumed, hence the lowest value was selected.

To avoid cavitation, the N_{ss} for the turbopump must not exceed 8,500 – 9,000 [69]. However, rocket turbopumps operate within constant cavitation to minimise the inert mass, but this results in a higher complexity, as explained in section **2.2 Turbopump**. The low-cost turbopump can be too expensive to be built to the current standard, hence the N_{ss} might have to be reduced below 10,000. To investigate this further, the N_{ss} vs GLOM for the 50kg payload was plotted in Figure 3-12. The graph shows that the pump performance can be greatly increased if an N_{ss} value greater than 5,000 is selected. Moreover, the graph indicates that increasing the N_{ss} value from 10,000 to 25,000 offers a very small reduction in GLOM.

To understand how the N_{ss} affects overall performance, the GLOM vs payload mass was plotted in Figure 3-13. This graph shows that reducing the N_{ss} value from 15,000 to 5,000 has a very small impact on the GLOM of the vehicle. Based on the theoretical data, running the turbopump below N_{ss} 8,500 could reduce the risk of cavitation significantly. In this case, complex cavitation simulations or tests may no longer be required, and as a result, would lead to a lower development cost. The mass model suggests, that a small vehicle could have a lower value of N_{ss} without resulting in significant mass penalties. This is especially applicable for smaller payload capacities.

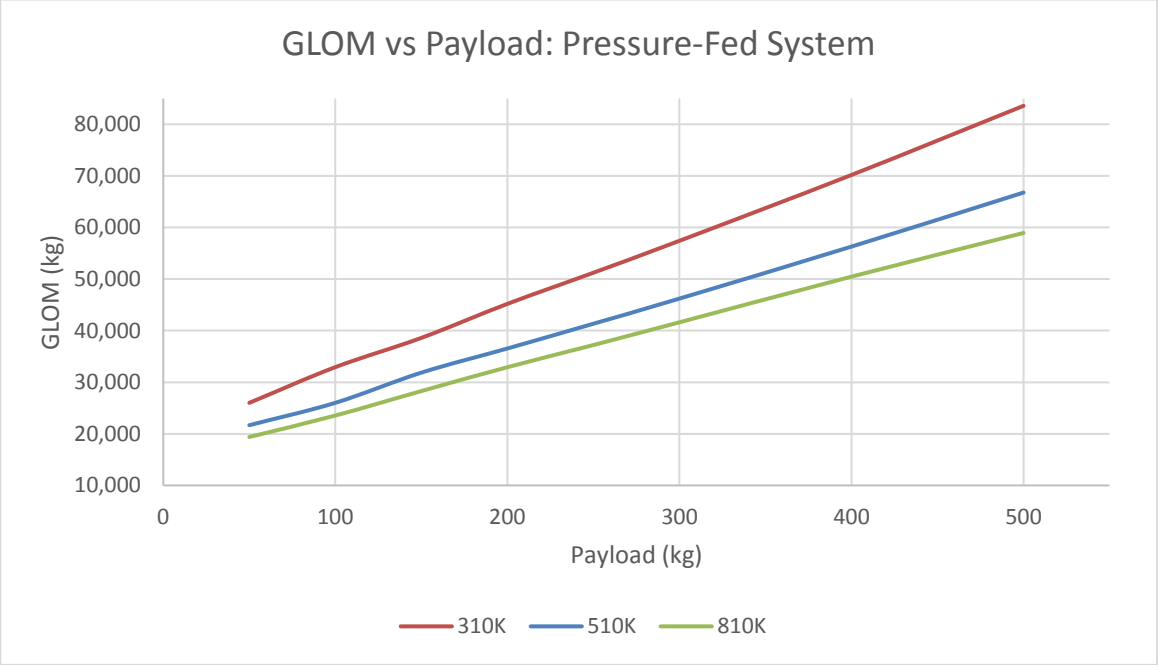

Figure 3-10: GLOM vs Payload of Pressure-Fed System

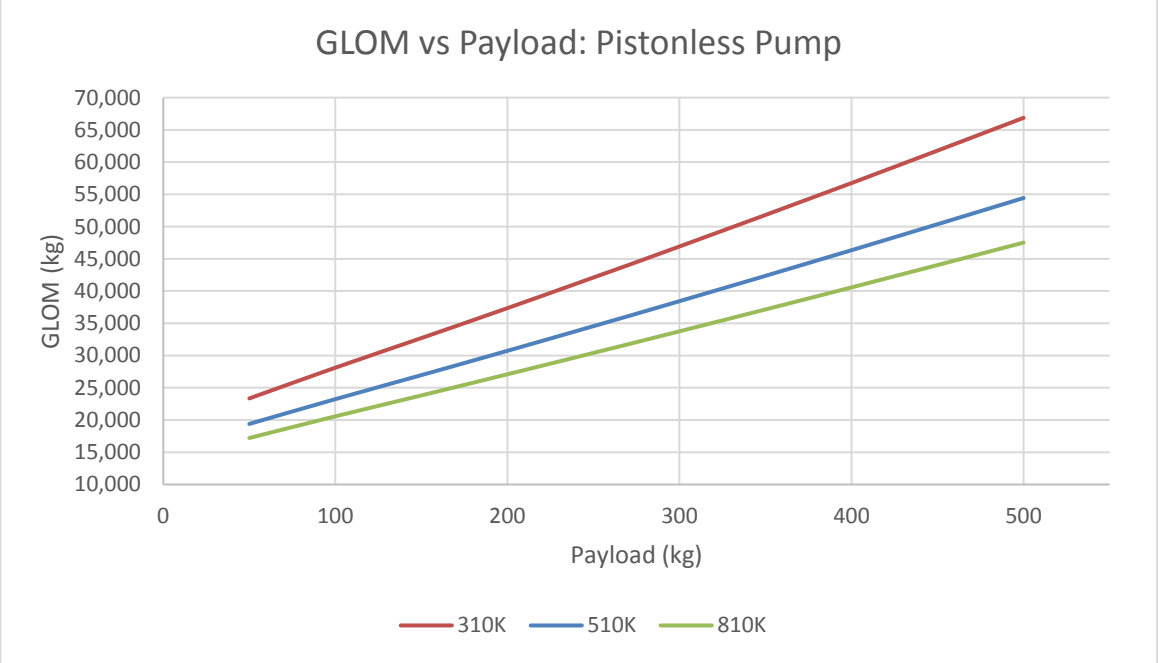

Figure 3-11: GLOM vs Payload of Pistonless Pump

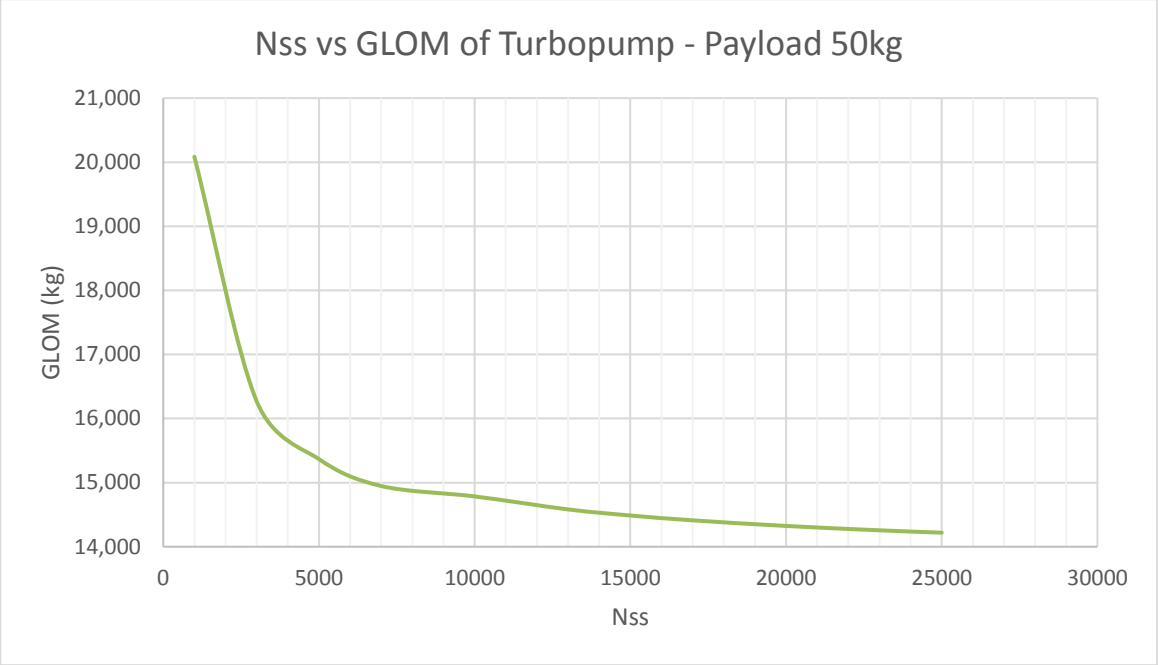

Figure 3-12: N_{ss} Vs GLOM of Turbopump with a 50kg Payload

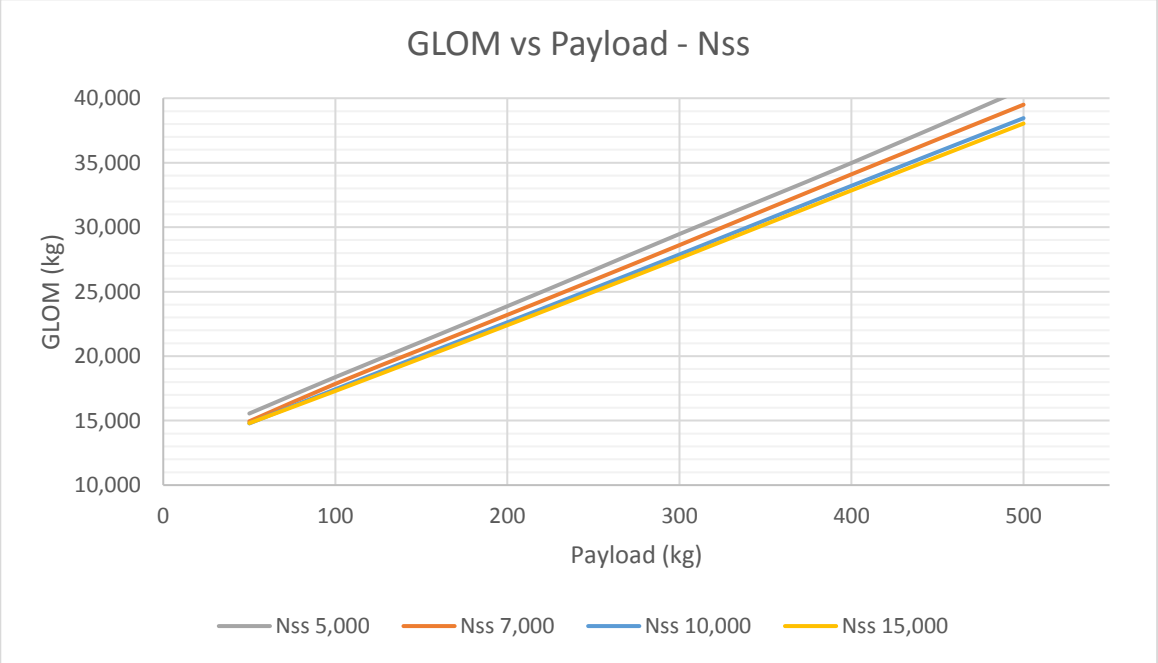

Figure 3-13: GLOM vs Payload – N_{ss} Graph

3.5 Technology Selection

The mass model has supported evidence obtained in the literature review that a turbopump outperforms both pressure-fed system and pistonless pumps. This was particularly evident at a heavier payload capacity. However, by heating the pressurant, the pressure-fed system and pistonless pump could potentially be used for a small capacity launch vehicle. Unlike the turbopump, pistonless pumps are not as well developed and the TRL stands at 3. As reported by Harrington the pistonless pump shares the same complexity as the pressure-fed system, but the mass model has shown that it can offer a 10% - 25% mass saving over a pressure-fed system for payloads up to 500kg [59]. Hence, if it comes to these two technologies, given the mass advantage

of the pistonless pump, it shall be favourable over the pressure-fed system. In addition, if this technology fails to mature, it can be changed to the pressure-fed system with some minor design changes.

Moreover, the model showed that the GLOM of the turbopump-fed vehicle is the least sensitive to sub-system mass changes (Figure 3-9). The simulation further showed that the payload capacity can be extended to 150kg without exceeding the GLOM limit of 20,000kg.

To keep the cost low, the simplicity that comes with the pistonless pump is desirable, however a turbopump powered vehicle provides a much higher performance, even at a low N_{ss} value, It is also a mature technology with a proven track record.

The pistonless pump is a very new technology which is ideal for a research project to determine its usefulness for a small launch vehicle. Given that this technology is at TRL 3, it may not be possible to fully compare its technical feasibility within this project's scope. The pump-fed systems are a more developed technology, which can also offer a research project to determine if a low-performance turbopump can be practically developed for a small low-cost launcher.

Taking into a consideration the complexity of the turbopump, it may not offer sufficient cost saving for a low-cost launcher. Due to insufficient data, the piston pump could not be directly evaluated using the mass model, but if the XCOR Aerospace claims are accurate, it has a similar performance as the turbopump for a GLOM below 30,000kg. The 1st stage of the launch vehicle with a payload of up to 150kg would require a total thrust of 240kN, which is within the defined piston pump 445kN limit.

The XCOR Aerospace 4K14 engine is fully developed with TRL 9, which has run a total of 529 times over 2 hours and been installed on the X-Race vehicle which completed 40 flights including seven in one day [70]. The technology readiness level is the same as for the turbopump, but it has never been flown in a launch vehicle. Furthermore, it is difficult to ignore the XCOR claims that the piston pump could be an order of magnitude cheaper than a turbopump with the same performance.

Taking into consideration the results obtained from the mass model, the turbopump has outperformed the pressure-fed and pistonless pumps by a large margin. A pressurisation system that could offer performance similar to the turbopump and at a fraction of the cost, is highly desirable, and based on the previous findings the piston pump can offer just that. In addition, lack of technical data for such a system to verify XCOR Aerospace claims makes it an ideal PhD project. Given that the piston pump has been around for hundreds of years, the technology is mature enough to enable a comprehensive evaluation. Based on all the findings, the piston pump was deemed to be the most favourable option and was selected for further evaluation to determine the suitability for small launch vehicles.

Chapter 4

Piston Pump – Mark I Demonstrator

4.1 Introduction

To assess the feasibility of a piston pump for a small-low cost launch vehicle, the prototype (Mark I) was designed and tested. Therefore, the XCOR Piston pump was further evaluated to give an insight into their design, although data about the system was very limited. After completing the assessment, the piston pump dynamics were assessed in order to understand the instantaneous pressure variation as this will influence the pump configuration. Upon completion of the study, a valve design was selected and experimentally tested to determine the feasibility of using the valve for this application. Volumetric efficiency and flow rates were measured against pump operating speed to determine how efficient the pump is and the range of the flow rates that can be achieved. The valve design was then optimised in order to achieve higher volumetric efficiencies and flow rates. In addition to these trials, the valve speed was tested to ensure it can operate at high-speeds and to identify design improvements for the Mark II technology demonstrator.

4.2 XCOR Piston Pump Design Overview

As previously explained, due to the ITAR restrictions information on the XCOR piston pump is limited. To understand how the pump is made and works, it was examined based on limited information and compared with existing reciprocating pumps. Figure 4-1 shows the side view of the XCOR piston pump, and by comparing it with a regular triplex piston pump, shown in Figure 2-17 (pg.18), they are almost identical. The main difference between these systems is that the XCOR pump has the additional chambers and a timing belt, as highlighted in blue. After closer inspection, inscriptions on the gears appear to show that the belt system is used to control the orientation of valves. Later models of the XCOR pump are shown in Figure 4-2, which has an additional inscription. The image on the left appears to show intake and exhaust chambers. The exhaust is usually associated with waste gas and the potential needs for this chamber include:

- Purging the system with inert gas, such as N_2, to remove water vapour to ensure the sealing face is not compromised.
- Cryogenic liquids, such as LN_2, are used to cool down the piston chamber to LOX temperatures.

It could also refer to the pumped liquid outlet, meaning the XCOR piston pump is a double acting pump. It can be noted that these chambers are much smaller than the main chamber, but given that the connecting rod runs through the piston chamber (Figure 2-19), it can explain the difference in size due to smaller volumetric flow.

The other difference between these designs is that the other version, seen in Figure 4-1, only consists of two smaller chambers, whereas the later version has four and the timing belt and gears were removed. By comparing the design in Figure 4-1 with Figure 2-17 it is evident that the valves in the main chamber are fitted between the fluid cylinder and manifolds. This suggests that the pump uses some type of self-acting valves, whereas valves in the smaller chambers are driven by the gear system (see **2.3.3.2 Valves** in **Chapter 2** for more details). If this pump is double acting, the reasons are unclear why two different types of valves were used. As future models no longer have the timing belt, perhaps XCOR were experimenting with various valve designs and valve control mechanisms.

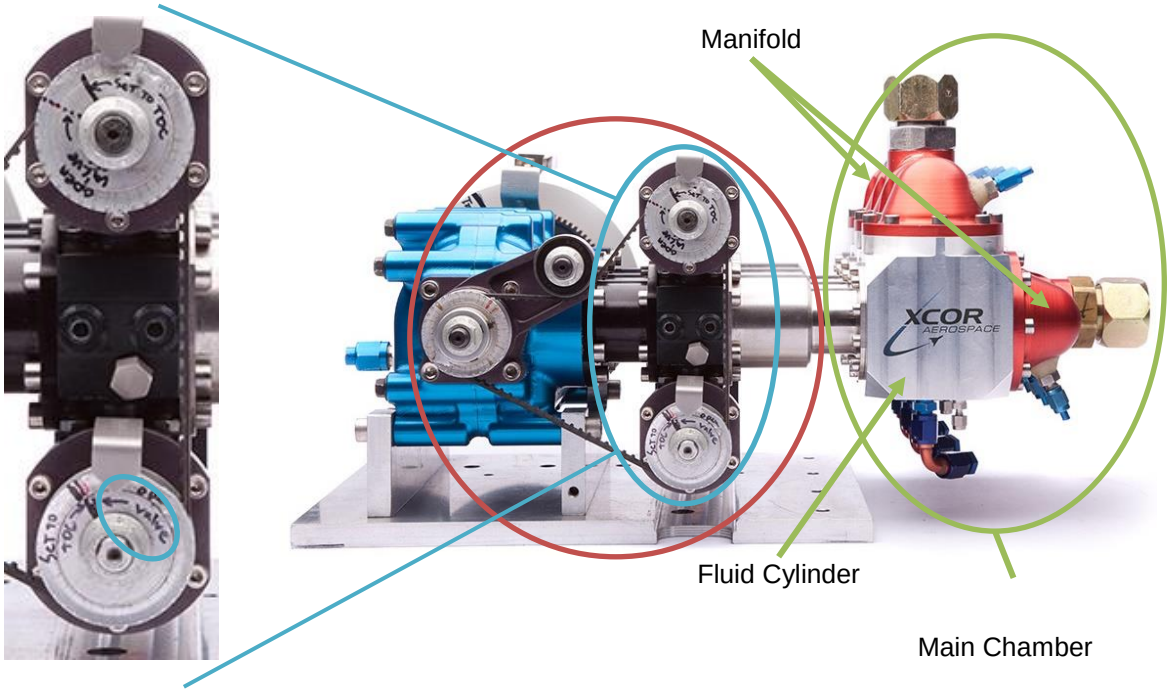

Figure 4-1: XCOR Piston Triplex Pump – Side View [71]

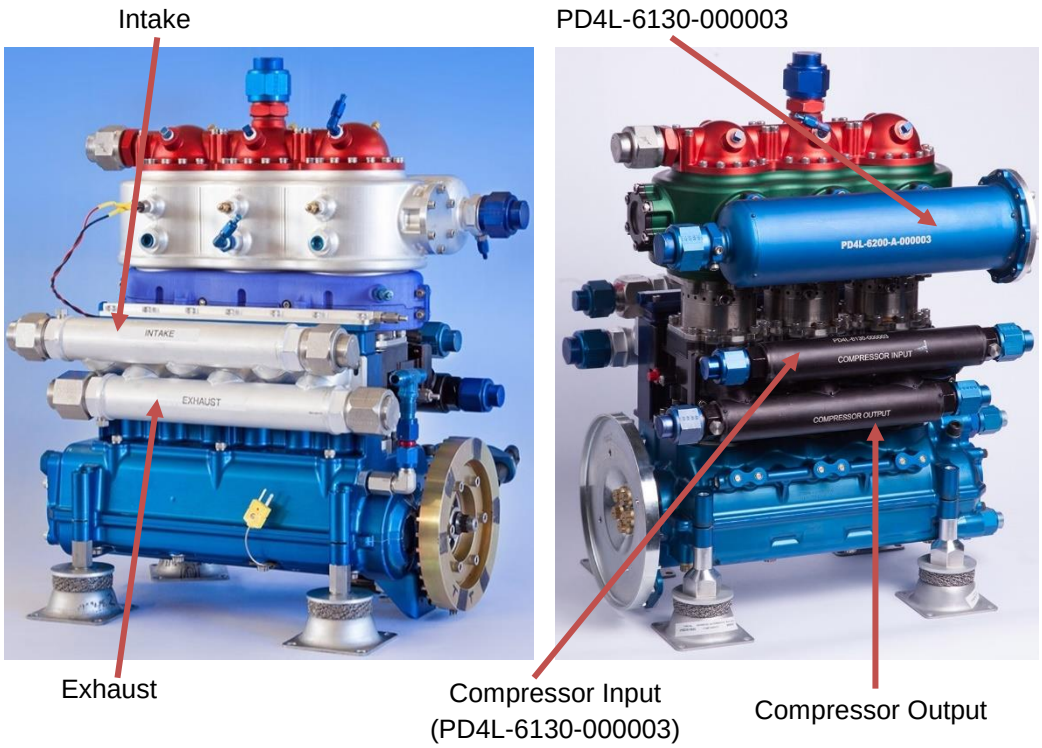

Figure 4-2: XCOR Piston Triplex Pump Future Models [71]

Based on the existing pump design, the manifolds are used to transfer fluid to each piston at the suction side emerging at the discharge. After further inspection, it is apparent that smaller cylinders are bolted to the main assembly (Figure 4-3). These cylinders can be removed to allow the installation of the valves, similarly as in the main chamber. The concern is that the lack of space could restrict the type of valves that can be installed in this area. It is possible that sensitive components were not shown in the display model. In Figure 4-4, the piston pump is installed in the flight vehicle and a longer manifold used, as highlighted in this figure. The large manifold provides more space; hence a wide range of valves can be used. The photo (Figure 4-3) also shows that a similar diameter pipe as attached on the main manifold is used for the smaller cylinders. This suggests that high flow rates are expected, and to justify the need for such flow rates, it further provides evidence that the pump could be double acting. This picture further shows that the older version of the piston pump is installed, as the gears are clearly visible.

Based on existing pump designs, the single acting piston pump can be fitted with either a piston or plunger. The main difference between these systems is that the seals for the plunge system are fitted in the housing, whereas seals for the piston are fitted on the piston itself. As shown in Figure 2-19, the plunger diameter is the same, thus this system cannot be used for a double acting pump. As shown in Figure 4-5, a double acting pump would require a piston type compressor to be installed.

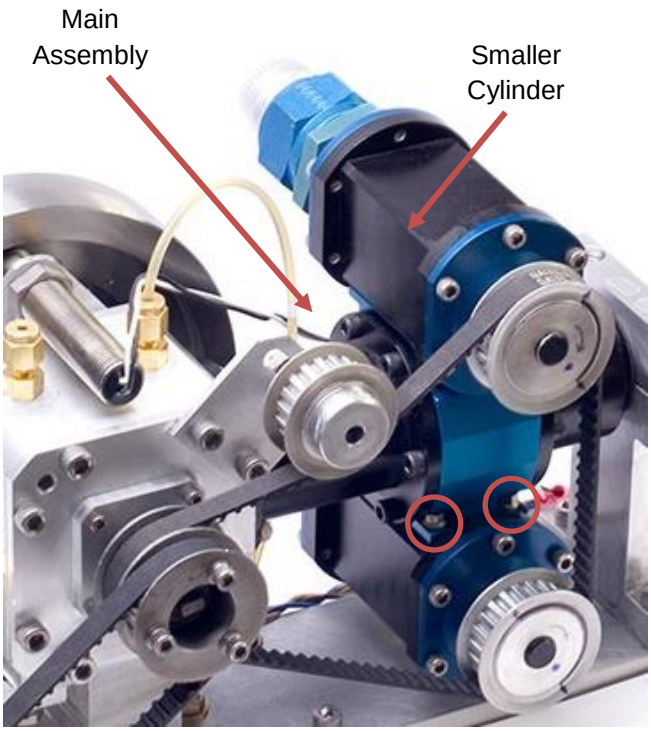

Figure 4-3: XCOR Piston Triplex Pump Other Models [71]

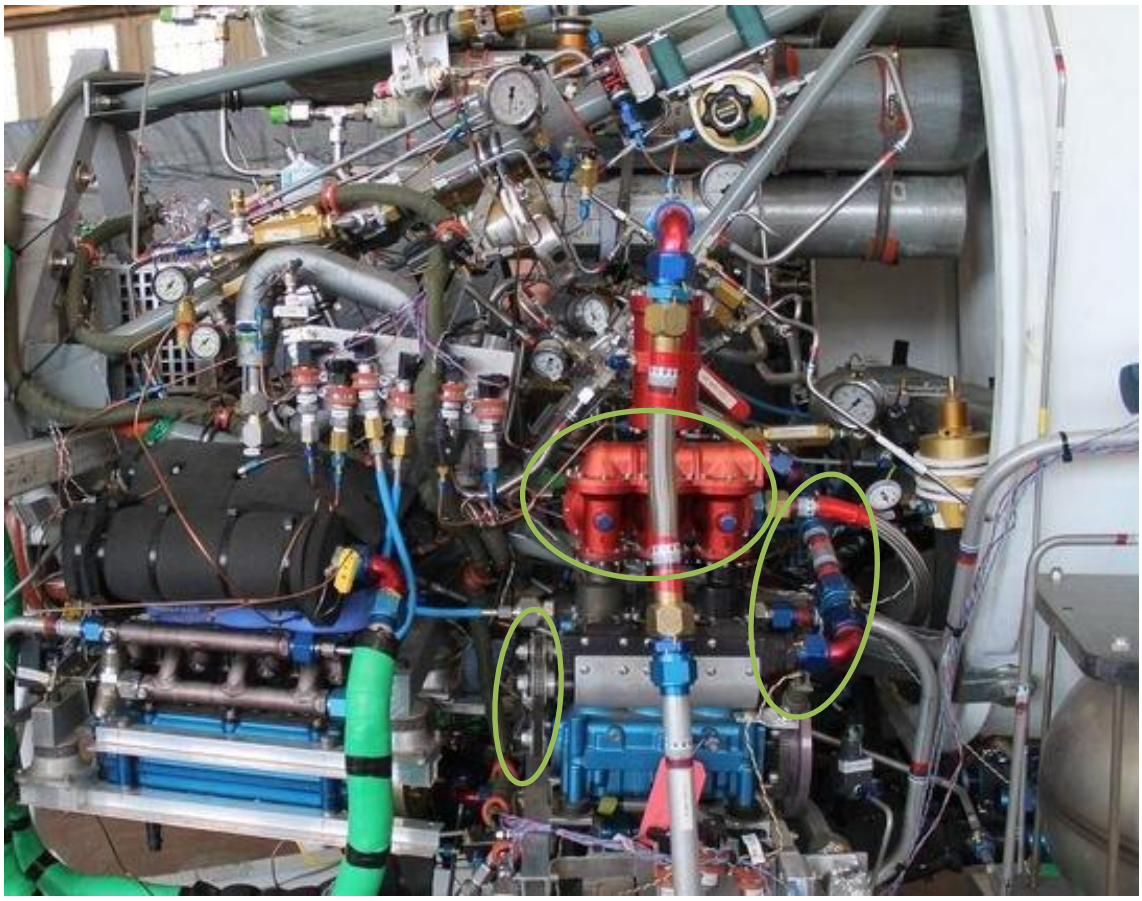

Figure 4-4: XCOR Piston Triplex Pump Other Models [71]

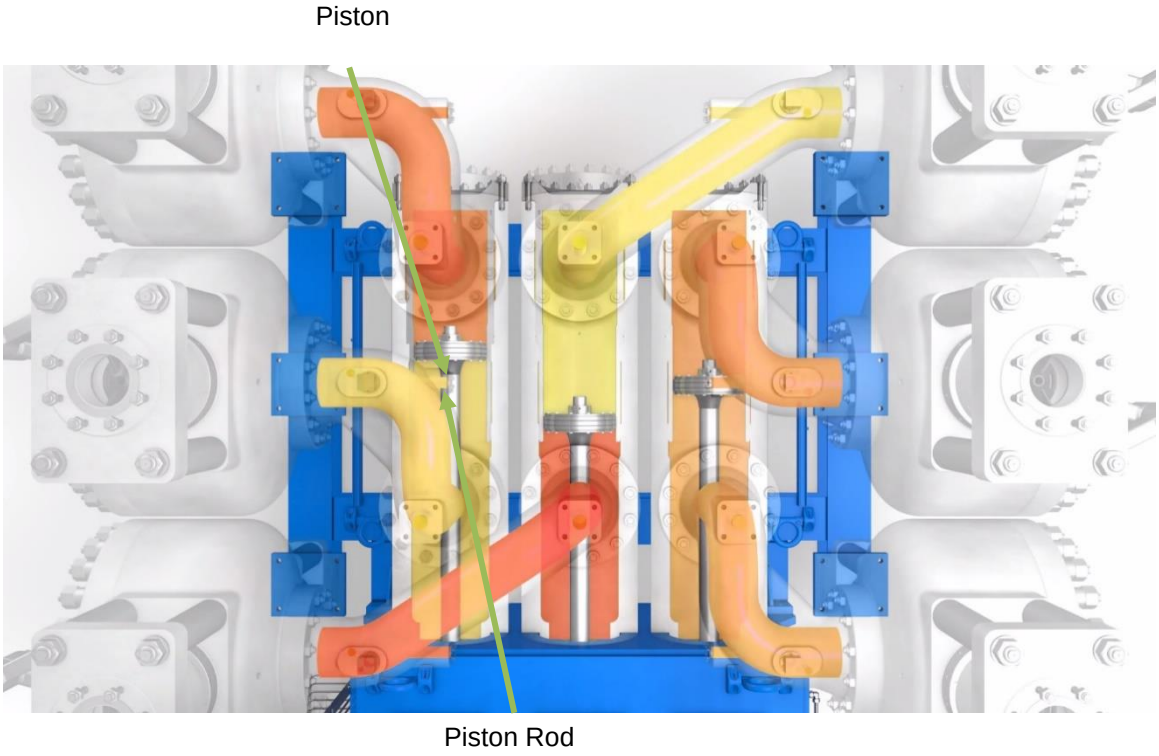

Figure 4-5: Triplex Double Acting Pump [72]

4.3 Development & Tests

4.3.1 Preliminary Design

To verify the XCOR cost claims and technology feasibility for a low-cost piston based pump, several technology demonstrators were manufactured and tested. The mark I demonstrator was developed to evaluate the basic concept of a rocket piston pump. This demonstrator allowed the exploration of various manufacturing techniques, identification of the challenges posed and observation of the operation in progress. The first demonstrator was tested using water only. This allowed low-cost transparent acrylic and PVC pipes to be installed at key locations to monitor the flow characteristics. These materials are easy to work with and available at very low-cost off-the-shelf. Most importantly, water did not pose complexities such as those associated with cryogenic temperatures.

Before proceeding to the manufacturing stage, some design parameters were established by carrying out further evaluation and a piston pump flow simulation was developed. The size of the pump, flow rate capacity, and acceleration head depend on the number of pistons installed, explained in **2.3.3.1 Pulsation** section. Using multiple cylinders, the total required flow rate is divided between all cylinders, which consequently led to a smaller piston volume or lower pump operating speed. The flow rate capacity can be further increased by the use of double-acting cylinders. Furthermore, as shown in Figure 2-23, the acceleration head decreases with the larger number of cylinders, but this results in a higher system mass and more complex hardware. To optimise the system, sizing and acceleration head a model was used to approximate the operation

speed, acceleration head, volume size of the piston cylinder and piston pump type (e.g. Simplex, Duplex, Triplex).

4.3.2 Piston Pump Sizing & Analysis

The mass flow rate is one of the factors which determine the size of the pump. Previously it was estimated that the GLOM of the launch vehicle carrying a 50kg payload is ≈15,000kg. The piston pump is a novel technology and it is unknown if it can offer the same potential at lift-off mass saving as the turbopump. To allow for any mass uncertainties, a launch vehicle with a GLOM of 20,000kg was assumed as a baseline. To launch a vehicle of this size, the engines would have to produce ≈235,400N of thrust ($F \approx 1.2(GLOM)go$). Assuming an Isp of 265s from the mass model (pg.144), a mass flow rate can be calculated using Equation 2-4 (pg.4). This gives a total mass flow rate of ≈90kg/s or 30kg/s for each engine.

The operating speed is another factor which defines the size of the piston pump. At higher RPMs, more fluid is displaced in a given time which results in a smaller pump size. By varying the piston cylinder volume, the operating speed can be optimised.

Before developing this model, the difference between flow rate and displacement must be understood. The flow capacity (Q), is defined as the mass flow delivered per unit time [15]. The displacement (D), is defined as the capacity of the pump with no slip losses and is expressed in Equation 4-1 and Equation 4-2 for single acting and double acting pumps respectively. When the density is known and the working fluid is incompressible, these equations can be used to estimate the theoretical flow rate. However, internal leakage is always going to occur, which will affect the volumetric efficiency (η_v). The actual flow rate can be estimated from Equation 4-3 when η_v is known [15]. The mass flow rate is given in Equation 4-4.

$$D = A \times m \times n \times s \times \frac{1}{6 \times 10^{10}} \tag{4-1}$$

$$D = (2A - a)m \times n \times s \times \frac{1}{6 \times 10^{10}} \tag{4-2}$$

Where: D – displacement (m^3/s), A – cross-section area of the piston (mm^2), m – number of pistons, n – speed of the pump (RPM), s – stroke of the pump (mm) and a – is the cross-section area of the piston rod (mm^2).

$$\eta_v = \frac{Q_a}{Q_t} \tag{4-3}$$

Where: η_v – volumetric efficiency, Q_a – actual flow rate (kg/s) and Q_t – theoretical flow rate (kg/s)

$$Q = D \times \rho \tag{4-4}$$

Where: ρ density of fluid (kg/m^3)

Based on the NIST data, raising the pressure of LOX (at 75K), propane (at 150K) and water (at 293.15K) from 1bar to 51bar would result in a volume reduction of 6%, 4% and 2% respectively [73]. It should be noted that the design combustion chamber pressure is 30bar, but higher values pressures were chosen, just in case the pressure requirements are raised. These low percentile compressibility factors are unlikely to have a substantial effect on the preliminary results, therefore flows were assumed incompressible.

A total of 8.6kg/s and 21.4kg/s of propane (fuel) and LOX (oxidiser) respectively must be delivered by the pumps at an oxidiser-to-fuel ratio (O/F) of 2.5. Assuming a volumetric efficiency of 90% i.e. some moderate losses, the operating speed was optimised for 1,000RPM by varying the piston cylinder volume. The XCOR piston pump runs below 900RPM but it can be turned up faster to supply more propellant [74]. Based on this existing model, the decision was made to use 1,000RPM as a baseline to measure pump performance. This speed may vary depending on the data output.

This model was then used to understand how the pump configuration affects the acceleration head. To carry out these calculations, further assumptions were made:

- Inlet pipe diameter - 100mm
- Inlet pipe length for Propane and LOX is 4m and 1m respectively.
- Pressure is proportional to flow.
- Flow is unaffected by pressure.
- Ideal valve timing.

The length of propane tank will be installed above the LOX tank, hence the higher length value was selected. This value was taken based on the size of the LOX tank from the mass model. For more details about this model, see **Appendix B: Sizing and Acceleration Head Model**.

Table 4-1 shows how the acceleration head and volume of the piston changes in various configurations. Referring to Equation 2-10 and pump constants in Table 2-2 (pg.22), it shows that the acceleration head is higher for a pump with fewer pistons, consequently simplex and duplex piston pumps exhibit high levels of pulsations. To minimise cavitation caused by this phenomenon, the inlet pressures will have to be greater than 5.8 bar and 11.6bar for duplex and simplex pumps respectively. Storing propellant at the high pressures will result in a high inert mass, which will deny the purpose of the pump. Furthermore, high fluctuations will cause a high intensity of vibrations which would introduce higher stresses on the parts. Of course, flow rates can be reduced to minimise the pulsation by incorporating several pumps, but then triplex, quintuplex or septuplex configuration becomes a more attractive option due to a lower "C" value (see Table 2-2). The triplex pump reduces the acceleration head considerably, and it is not unreasonable to store the propellant at pressures of 3bar, which should be sufficient to overcome the acceleration head.

If the pump configuration results in an unacceptable level of acceleration head, from a launch vehicle perspective the pump operating speed or the pump type can be changed. However, both options result in a higher pump mass. Alternatively, a double-acting pump can achieve these flow rates at a lower operating speed giving a lower acceleration head.

Referring to Table 4-1, the quintuplex or septuplex configuration offers little benefit over a triplex pump, and it may not provide enough justification to overcome the additional complexities and weight associated with extra pistons. The sizing and acceleration head calculated suggest that the triplex pump configurations offer the optimum solution.

Table 4-1: Acceleration head and Piston Volume

	Propane				LOX			
	Single-acting		Double-acting		Single-acting		Double-acting	
	P_{ac} (bar)	V (mm³)	P_{ac} (bar)	V (mm³)	P_{ac} (bar)	V (mm³)	P_{ac} (bar)	V (mm³)
Simplex	11.66	855,299	11.66	447,677	7.29	1,247,684	7.31	651,880
Duplex	5.86	425,293	5.90	229,729	3.65	623,213	3.64	330,810
Triplex	1.94	283,415	1.96	153,938	1.21	413,512	1.21	221,168
Quintuplex	1.19	167,415	1.18	98,520	0.73	249,380	0.74	136,848
Septuplex	0.83	120,763	0.83	73,544	0.52	175,929	0.53	98,960

* At Pump Speed of ≈1,000RPM

4.3.3 Dynamics

4.3.3.1 Instantaneous Displacement, Velocity & Acceleration

The instantaneous piston displacement, velocity and acceleration were calculated in order to determine the instantaneous pressure and maximum piston velocity. The position of the piston (x) with respect to time was calculated using Equation 4-5, which was derived from the cosine rule. Hence, the stroke length can be obtained from Equation 4-6. For more information on how to derive these equations, see **Appendix C: Dynamics** (pg.162). By taking the first derivative of Equation 4-6, Equation 4-7 was derived to obtain the instantaneous velocity (v), and by taking the second derivative – Equation 4-8 was derived to obtain the instantaneous acceleration (a). Refer again to the **Appendix C: Dynamics** for more details.

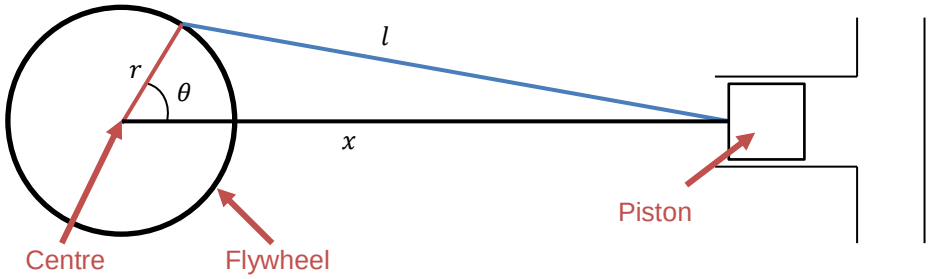

Figure 4-6: Geometric Layout of the Piston, Crank Shaft and Crank Radius

Where r – crank radius, l – rod length, x – piston motion from piston pin to crank centre and θ – crank angle

$$x = r\cos(\omega t) + \sqrt{l^2 - r^2\sin^2(\omega t)} \tag{4-5}$$

$$s = (r + l) - \left(r\cos(\omega t) + \sqrt{l^2 - r^2\sin^2(\omega t)}\right) \tag{4-6}$$

$$v = -\frac{r^2\omega\sin(2\omega t)}{2\sqrt{l^2 - r^2\sin^2(\omega t)}} - r\omega\sin(\omega t) \tag{4-7}$$

$$a = -\frac{r^2\omega^2\cos(2\omega t)}{\sqrt{l^2 - r^2\sin^2(\omega t)}} - \frac{r^4\omega^2\sin^2(2\omega t)}{4(l^2 - r^2\sin^2(\omega t))^{\frac{3}{2}}} - r\omega^2\cos(\omega t) \tag{4-8}$$

Initially it was expected that the piston would travel half of the stroke length when the crank angle is 90°, Assuming the piston crank radius is 0.5m and the rod length is 1m, using Pythagoras theorem It can be proven that at 90°, the piston would travel 0.634m, which is more than half of the stroke length (see below).

$$x = \sqrt{l^2 - r^2} = \sqrt{1^2 - 0.5^2} = 0.866m$$

$$s = (l + r) - x = (1 + 0.5) - 0.866 = 0.634m$$

The half stroke length for this configuration occurs at 68°. This peak can be moved closer to 90° by installing a longer rod, however, it can never reach 90°. This also means that the velocity minima and maxima do not occur at a crank angle of 90°.

The mark I prototype was tested with an 88mm rod and at a crank radius of 15mm, 22.5mm and 30mm. 15mm offered the smallest radius that provides sufficient clearance between the crank pin and rod which is mounted through the centre of the flywheel. To understand better how these changes affect the stroke length, velocity and acceleration, the graphs were plotted as shown in Figure 4-7, Figure 4-8 and Figure 4-9. For more details see **Appendix D: Dynamics – Graphs** (pg.164).

The stroke length graph (Figure 4-7) shows that the piston has moved half of the stroke at 81°, 76° and 73° at the crank radius of 15mm, 22.5mm and 30mm respectively. This indicates that at shorter stroke lengths (higher connecting rod length:crank radius ratio) the peak is moved towards 90°. Figure 4-8 shows that velocity minima occur at the crank angles as stated before.

As seen in Figure 4-7 between crank angles 0° and 180°, the piston is travelling back in the cylinder (creating suction) and between 180° and 360° moves back up (discharging). Referring to Figure 4-8, negative velocity indicates the suction cycle. The fastest change of velocity occurs between 0° and minima at the suction cycle and between maxima and 0° at the discharge cycle. The deceleration between the minima and 180° and the acceleration between 180° and the maxima is much lower between these intervals. However, by increasing the connecting rod length:crank radius, i.e. when r = 15mm, the difference between these intervals can be reduced.

In addition, by changing the crank radius from 15mm to 30mm, the maximum velocity at which the piston travels almost doubles which must be taken into the consideration when selecting dynamic seals. In the ideal situation for the largest lifetime, the maximum velocity and acceleration must be reduced to minimise wear and tear on the seals.

The piston acceleration graph (Figure 4-9) supports the previous statement that the greatest acceleration occurs at the start of suction and at the end of the discharge cycles. Referring to a crank radius of r=30mm, the highest acceleration is -441m/s^2 and the rate gradually declines until it reaches a point of maximum velocity. Furthermore, due to the cosine rule, the maximum piston acceleration is 229m/s^2. It also should be noted that the maximum acceleration is reached at a crank angle of 136° and from this point it decelerates and accelerates back up to 229m/s^2 at 224°. This phenomenon is caused due to the low connecting rod:crank radius ratio, and by increasing this ratio, the dip in acceleration can be reduced. As shown for r = 22.5mm, acceleration at the peak levels out and for r = 15mm, the acceleration curve is completely smooth.

In terms of operation, it is more desirable for the acceleration to be slower for the first half of the suction cycle because the energy transfer from the piston to the pumped medium is not instantaneous. This would cause the propellant to travel at a slightly slower rate than the piston,

and at very high piston speed, will result in the formation of voids. These voids can potentially reduce the propellant pressure, which can create cavitation or result in lower efficiency.

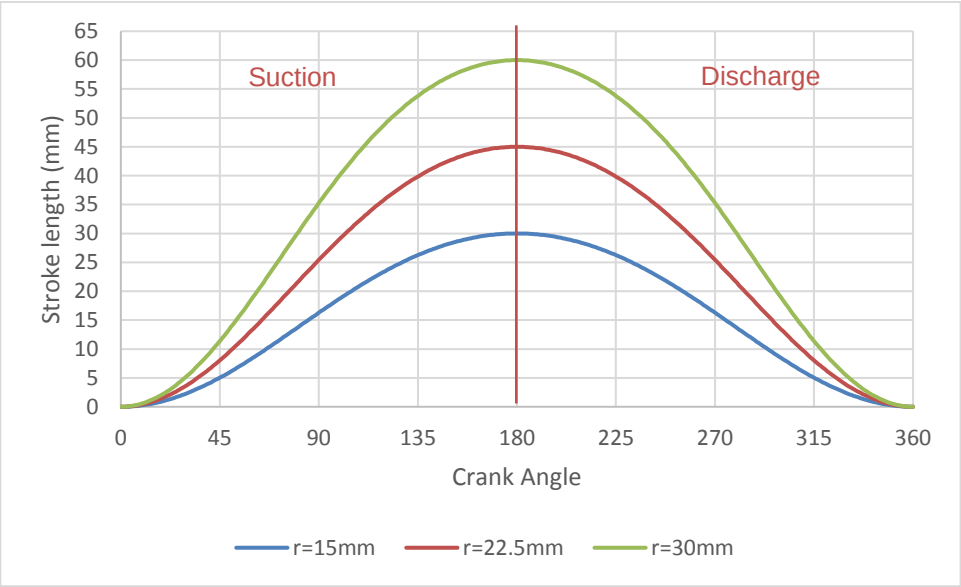

Figure 4-7: Stroke Length vs Crank Angle

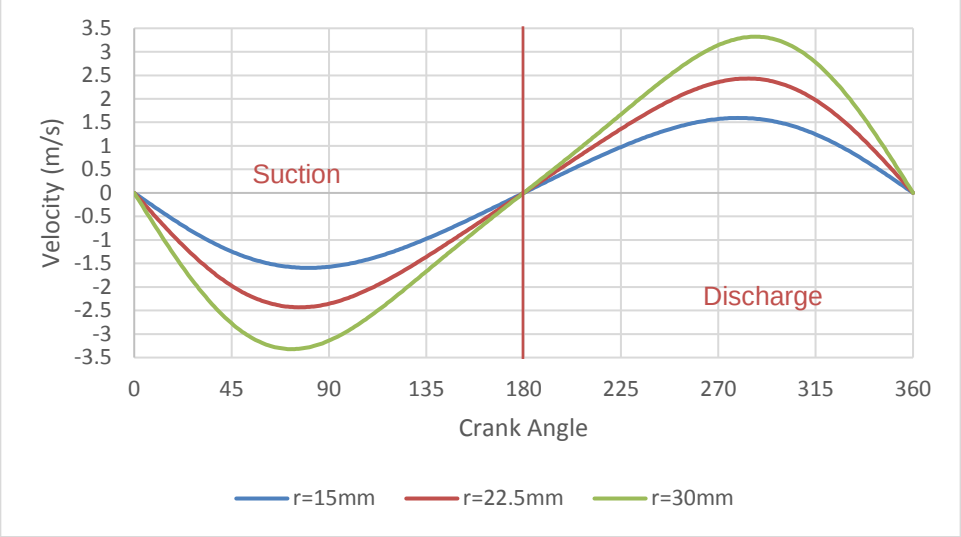

Figure 4-8: Velocity vs Crank Angle

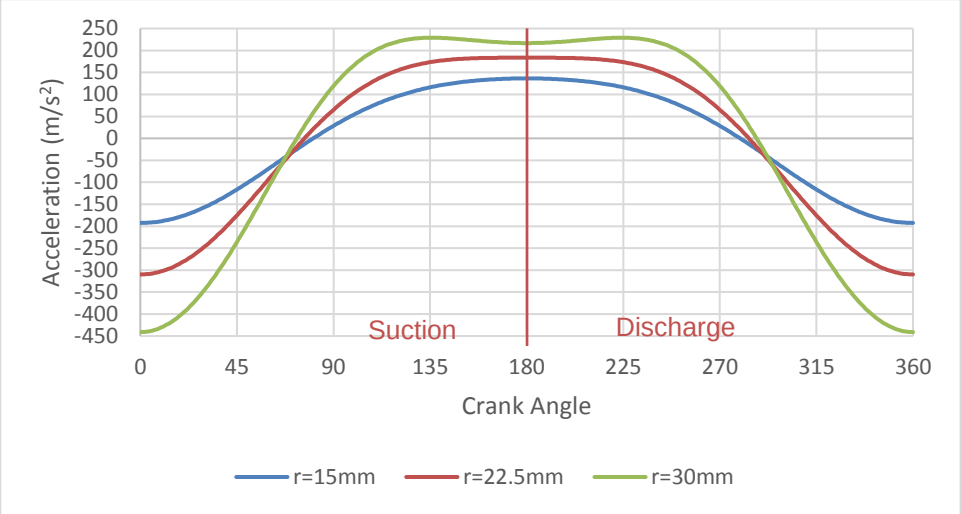

Figure 4-9: Acceleration vs Crank Angle

4.3.3.2 Instantaneous Pressure

To estimate instantaneous pressure, the following assumptions have been made:

- maximum pressure of the system is 30bar.
- Maximum pressure occur at the maximum flow rate as the fluid total pressure (static + dynamic) is the highest at this point.
- Propellant travels at the same speed as the piston (ideal valve timing)
- Fluid is incompressible.
- Pressure is proportional to the flow rate.
- Flow unaffected by pressure.

Based on these assumptions the diagram was drawn to estimate the average pressure of the cycle, as shown in Figure 4-10. For more details, refer to **Appendix E: Pressure Graph** (pg.165). As seen in this figure, for the first half of the cycle, no discharge pressure is produced and other half shows the predicted pressure profile. The pressure profile graph was plotted for all three crank radii and apart from slight side-shifts due to crank length:rod ratio, the graph profiles are similar. As defined in section **1.2,** the pump must deliver 30bar pressure, but the average pressure between 180° and 360° is 18bar. This was calculated by calculating the pressure at each crank angle and then taking the average value. If taking into consideration the full cycle, the average pressure drops to 9bar, and to achieve the average pressure of 30bar, the maximum instantaneous pressure must be increased to 100bar. High-pressure fluctuations would not only cause extreme vibration but also components will have to be designed to withstand these stresses. This further complicates the design of the seal and valves, which will result in higher development costs. Based on this statement alone, it is proven again that a single acting pump would not be suitable for a launcher.

Two more graphs in Figure 4-11 and Figure 4-12 were plotted for the duplex and triplex pumps for comparison. As the pressure values varied by a very small amount, the graphs were plotted for just r=30mm.

The graph in Figure 4-11 indicates that with the duplex system the pressure will fluctuate from 0bar to 30bar, with an average pressure over a complete cycle of 18.5bar. To achieve an average

pressure of 30bar or above, the pump must deliver a maximum pressure of 49bar. This again is a very inefficient design, as all components must be certified for 49bar pressure to accommodate a much lower average pressure.

Figure 4-12 shows that a triplex pump does not have a region with zero pressure – the minimum pressure is 18.5bar, which occurs three times in a cycle. The triplex pump would deliver an average pressure of 27.7bar and to boost the average pressure to 30bar, the maximum pump pressure must be raised to 33bar. This offers a more efficient design, as the design challenges would be similar to the pump with the pressure of 30bar. This brief analysis confirms that the triplex pump offers the most balanced configuration.

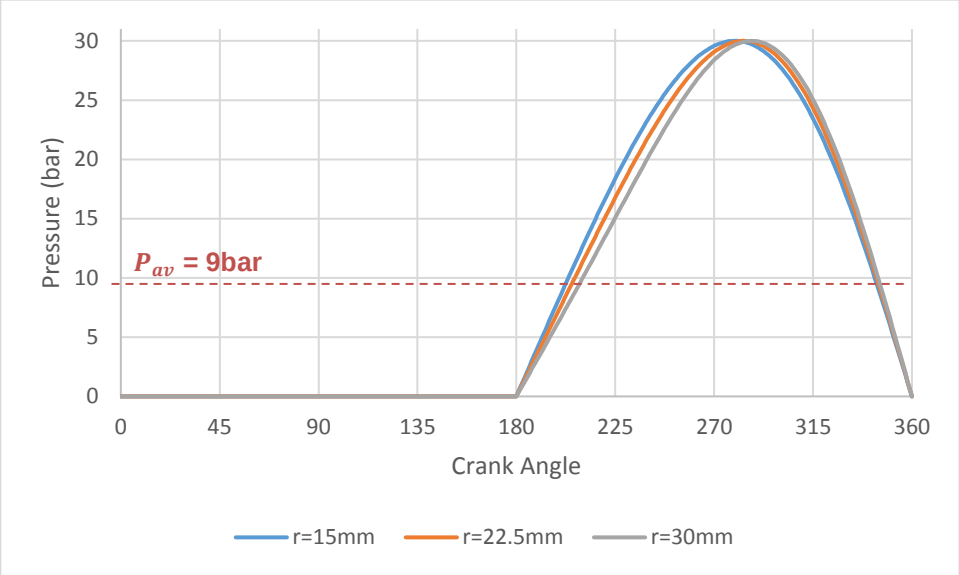

Figure 4-10: Simplex – Discharge Pressure vs Crank Angle

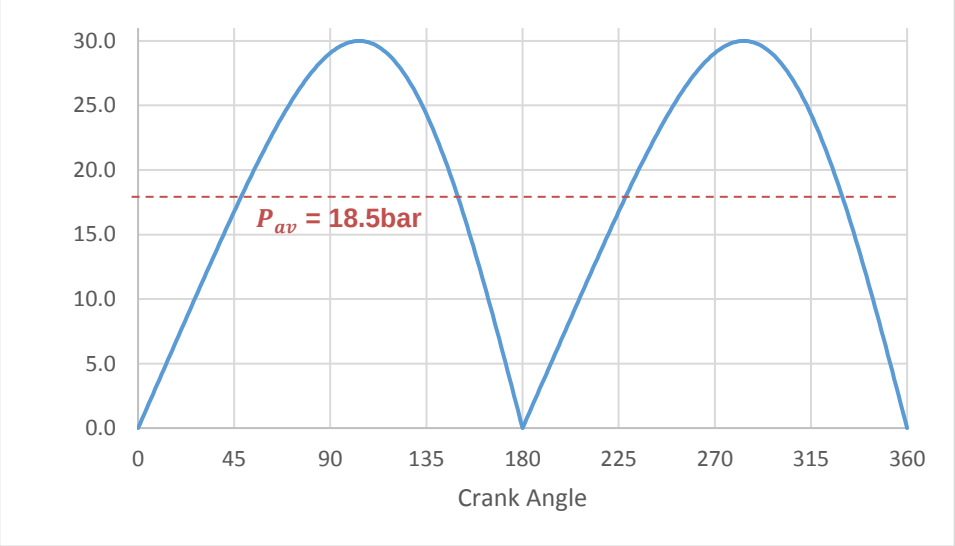

Figure 4-11: Duplex – Discharge Pressure vs Crank Angle

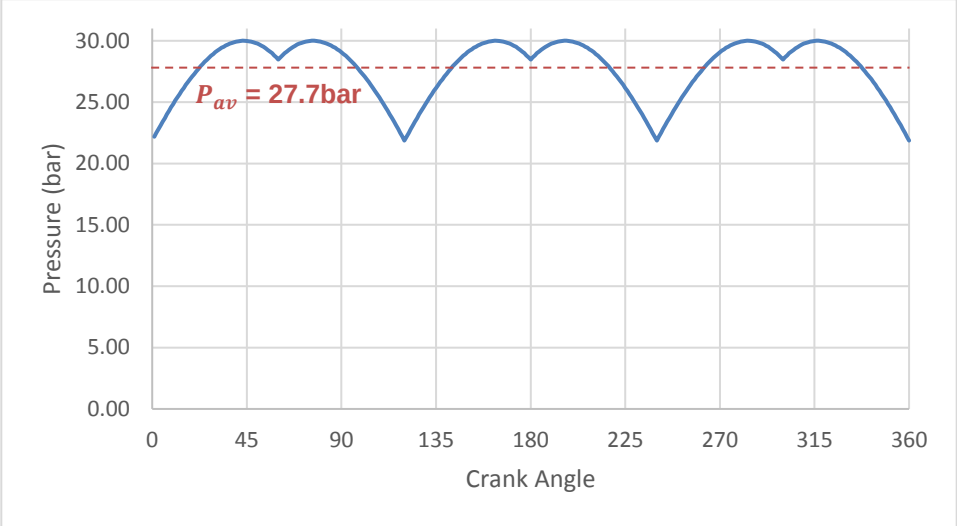

Figure 4-12: Triplex – Discharge Pressure vs Crank Angle

4.3.4 Valve Selection & Concept Design

Valves are the most critical part of the reciprocating pump and due to the high requirements of the rocket pump, it is vital to select the correct type. The valves must be selected according to operating speed, pressure rating, flow capacity and cryogenic compatibility. Table 4-2 shows the requirements of the system vs potential valve options. A score was given from 1 to 5, where 1 is least suitable and 5 the most suitable. While some valves scored very high in some areas but low in others, they were automatically excluded from further evaluation if the score was 2 or below. The valves which passed the initial scoring selection process were poppet valves, reed valves and plate/ring valves. As described in section **2.3.3.2.1** (pg.24), poppet valves require an external driver, such as a camshaft, when operating at high speeds. External drivers add extra complexity and cost, hence this option will not be considered unless the other two options are deemed inadequate. Unlike poppet valves, both reed valves and plate/ring valves are self-acting valves. The major drawback of plate/ring valves is that they are heavy, bulky and mostly used for gas. The triplex pump inlet diameter can be as little as 70mm, and this poses a major challenge for a design based on these geometrical constraints for high-flow applications. In contrast, a reed valve design is very simple and easy to implement, and like plate/ring valves, they are mostly used with gas. The applications for reed valves were examined and it was noted, that these valves are often used at operating speeds of over 1,000RPM. At low speeds, the contact between the petal and hard surface of the base would lead to poor sealing performance, and as a result, would increase the internal leakage. Current reciprocating pumps operate at speeds below 300RPM, and thus under these operating conditions, other valves, such as ball valves, are more desirable due to good sealing performance. This explains the reasons why reed valves were not considered with fluids. Despite their poor sealing capability, reed valves could be used with fluids, but the valve geometry must be optimised. Thus, the decision was made to explore this option further.

Table 4-2: Valve Comparison Table

	Suitability for:				
Valve Type	**High operating Speed**	**High Pressures**	**High Capacity**	**Cryogenics**	***Total***
Ball valve	2	5	3	3	***13***
Sleeve valve	5	3	4	2	***14***
Poppet valve	5	4	4	4	***17***
Reed valve	5	3	4	3	***15***
Plate/ring valve	3	5	4	3	***15***

* 1 = least suitable 5 = most suitable

The mark I demonstrator was built from standard acrylic and PVC pipes with an inner diameter of 53mm, hence the reed valve concept designs were designed based on this constraint. Figure 4-13 and Figure 4-14 Illustrates two initial designs which were examined. These designs were not optimised for high flow rates at high pressures. The concepts were used to explore the manufacturing techniques and technical feasibility.

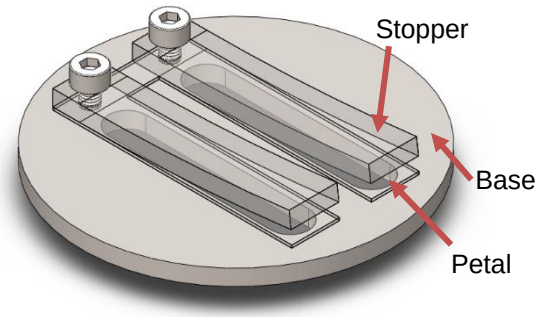

Figure 4-13: Reed Valve Concept 1

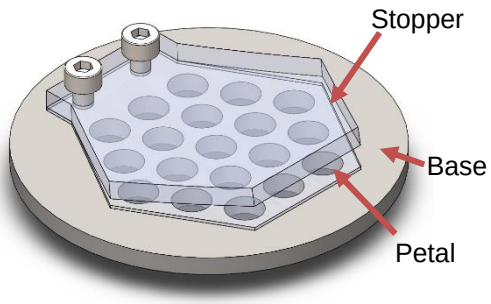

Figure 4-14: Reed Valve Concept 2

Before manufacturing valves, basic CFD analyses were carried out using SolidWorks Education Edition 2016 SP4.0 to predict the most favourable valve design. These CFD results were used for the observation purpose only. The cavitation is most likely to occur in the low-pressure region, thus the conditions of the inlet valve were simulated with an average flow rate of 1kg/s. More details of the setup are covered in **Appendix F: CFD Setup of Concept Reed Valves.**

Velocity profiles for each design were generated as shown in Figure 4-15 and Figure 4-16. Based on the velocity profiles and results, it can be concluded that concept design 1 is more efficient than design 2 due to lower velocities. Higher flow velocities are an indication that passages are more restricted, hence the pressure drop is expected to be higher in these regions. The CFD analysis further shows that a design with fewer but larger openings is more efficient than having many smaller openings evenly distributed across the base.

Nonetheless, both valve designs were manufactured and tested. During the initial trials it was apparent that a slight deformation of the petal created large gaps when the petal was fully shut, causing some difficulties priming the pump. This was especially noticeable in concept 2 as a large contact area between the petal and surface of the base led to a very poor sealing performance. The concept 1 experienced similar issues, however it was relatively small when compared with

concept 2 due to the contact area between petal and base being much smaller. Thus, based on the CFD results and sealing complications, concept 2 was rejected from further evaluation.

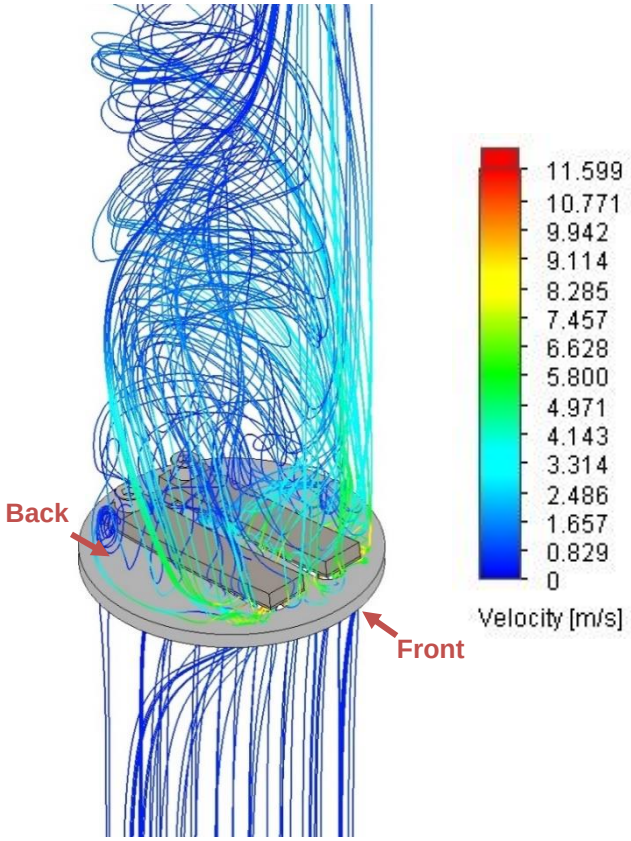

Figure 4-15: CFD Velocity Profile of Reed Valve Concept 1

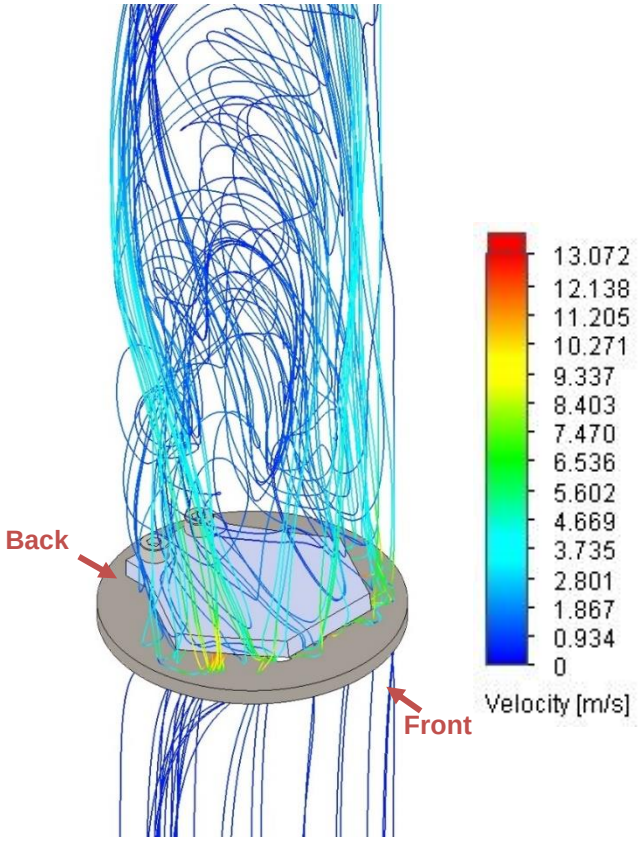

Figure 4-16: CFD Velocity Profile of Reed Valve Concept 2

4.3.5 Mark I Concept Assembly

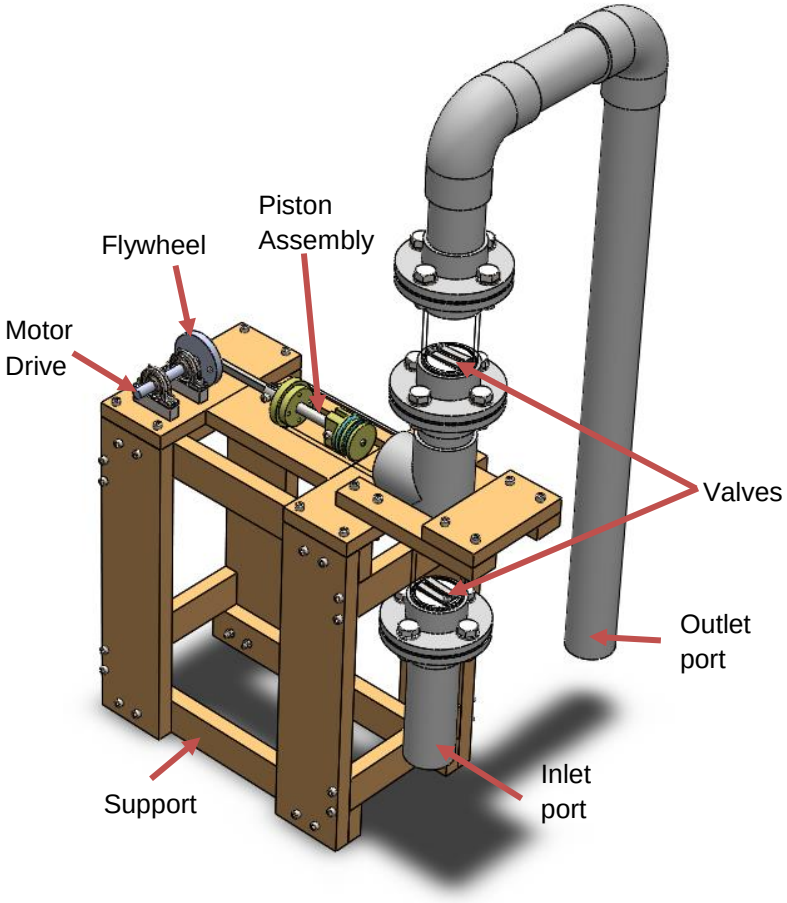

Figure 4-17: Mark I Full Assembly

Figure 4-17, illustrates the full CAD assembly of the Mark I demonstrator with the concept 1 reed valves. As previously described, to minimise manufacturing costs and time, off-the-shelf PVC pipes were used. The piston chamber and pipes at the valve positions were made from transparent PVC tubing. The primary functions of the transparent tubing were to observe the piston sealing performance and flow trajectory through the reed valves. In addition, reed operation can be monitored.

For stability reasons, the piston is connected to the crankshaft via the piston rod and connecting rod, as shown in Figure 4-18. The connecting rod translates circular motion to linear motion, ensuring the piston only travels along the axis of the cylinder, as this action may affect the sealing performance. To reduce the force between the end of the connecting rod and the piston, a nylon support was installed. Two pillow blocks were used to support the flywheel via the shaft, which was directly connected to the motor.

Dynamic seals are another critical part which can either be mounted on the piston or bore side (in Figure 4-19 the piston side mounting is shown). The difference between these two systems is covered in **Chapter 5**. The dynamic seals in the Mark II were mounted on the piston side as it was easier to make modifications to the piston than to the bore. C. Preece from SEALCO has supplied the seals in a similar style to that shown in Figure 4-19. Cryogenic conditions cannot be replicated

with water, such as material differential shrinkage, therefore the seal material was not taken into the consideration at this stage of the project. Instead, the industry standard polyurethane seal was used.

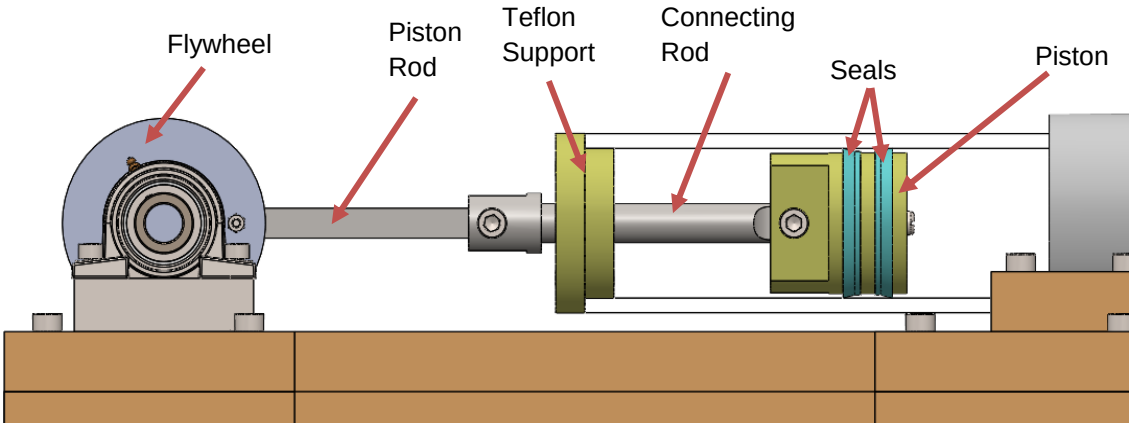

Figure 4-18: Piston Assembly

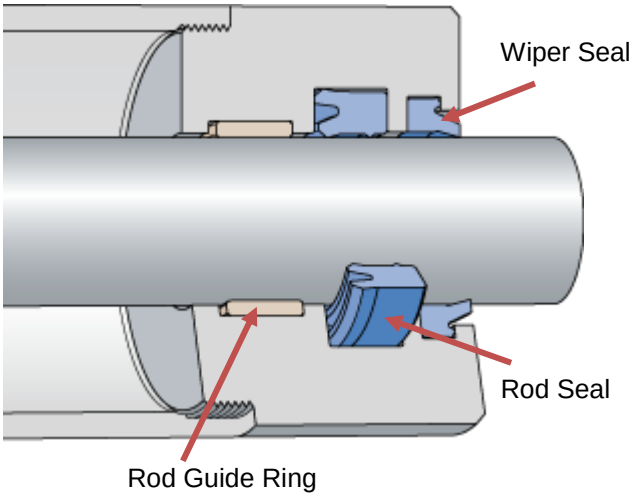

Figure 4-19: Seal on the Bore Side [75]

4.3.6 Test Setup 1

4.3.6.1 Overview & Methodology

Test 1 was used to measure the performance of the reed valve concept 1 (Figure 4-13). The reed valve performance data under the conditions required for rocket pressurisation system have never been published, hence these results would be novel. To evaluate the reed valve concept, the following data were compared:

- Volumetric efficiency (η_v) vs RPM
- Flow rate vs RPM

It should be noted that pressure sensors were not integrated into this model, as flanges or material were not suitable for pressure tests. Furthermore, the experimental aim was to test the basic concept of the reed valves and the Data Acquisition Unit (DAU) with pressure sensors were not available at that time.

To power up the pump, the flywheel was directly connected to an electric washing machine motor via a shaft. To control the pump speed, the motor was then connected to a Variac power supply (Figure 4-20) which allowed the output voltage to vary. The voltage was varied by increments of 10V and a minimum of 3 readings were taken in the same configuration.

To examine the effect of changing the stroke length, the flywheel was modified with a series of holes which were placed 7.5mm apart. This provided a capability to run experiments at stroke lengths of 30mm, 45mm and 60mm.

Initial experiments were conducted for a short duration until approximately 8.5kg of water were delivered. Pump speed was the major factor which affected the duration of the experiment – this ranged from 7s to 47s. The total mass delivered by the pump was recorded using a Travi Blue digital scale.

Two cameras then were used to record the experiment. One camera was positioned at the piston cylinder and the other at the outlet or inlet valve. This allowed determination of the precise running time and the total number of cycles. Camera data was processed in Adobe Premiere Pro CS6, which allowed extraction of the necessary footage and frame analysis to count pump cycles. Using this information, the average pump speed and average flow rates were calculated.

This information was then added to the spreadsheet where the average flow rates, speed of the pump and volumetric efficiencies were calculated. For more information, refer to Section **G: Piston Pump Mark I – Test Data** (pg.170)

Figure 4-20: Test 1 Apparatus Setup

4.3.6.2 Experimental Data and Analysis

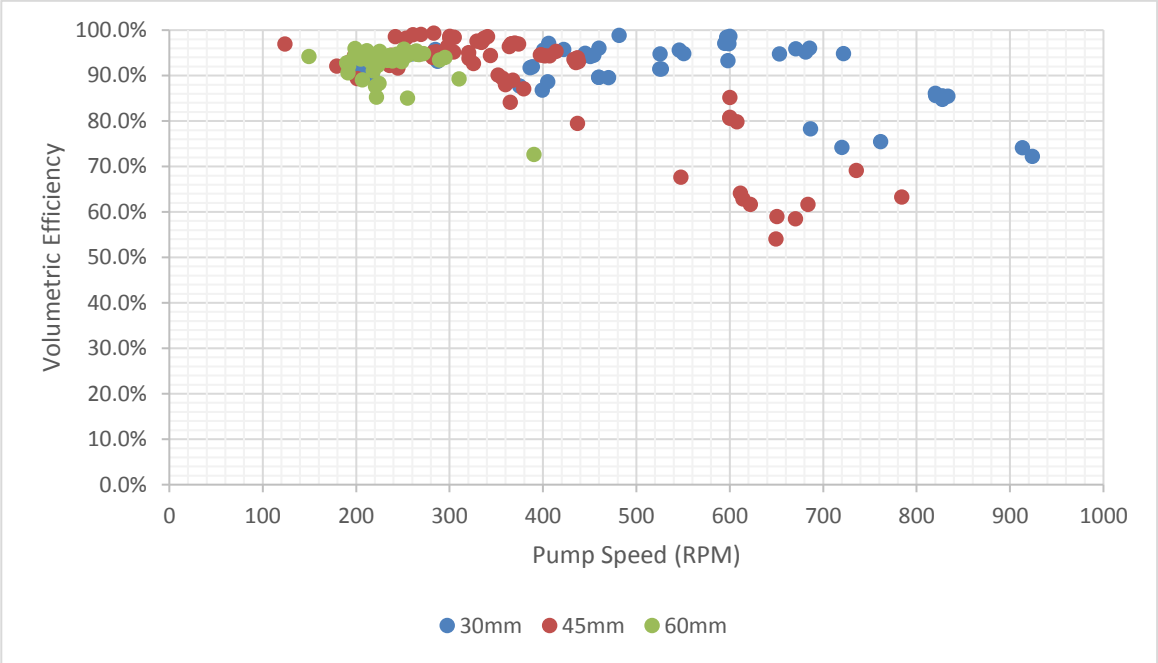

Figure 4-21: Volumetric Efficiency vs Pump Speed – Test 1

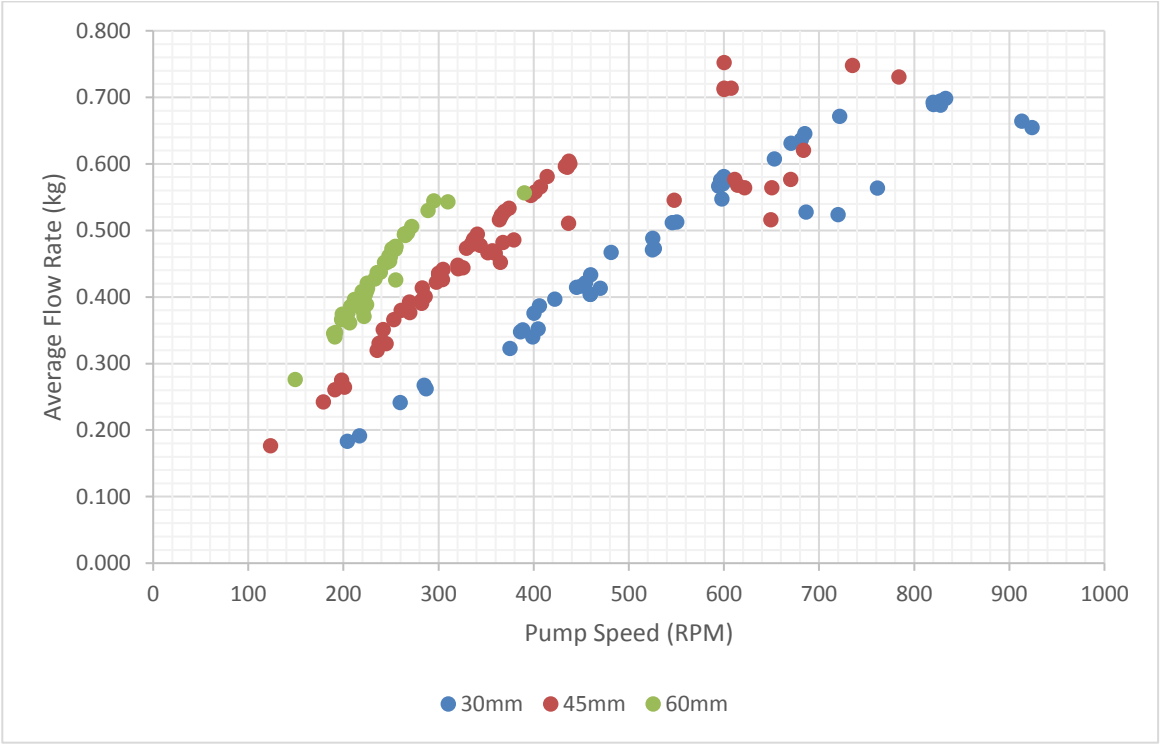

Figure 4-22: Average Flow Rate vs Pump Speed – Test 1

Two graphs, in Figure 4-21 and Figure 4-22, shows how volumetric efficiency and flow rate vary with the pump speed at stroke lengths of 30mm (blue), 45mm (red) and 60mm (green). Referring to results in Figure 4-21, in most of cases volumetric efficiency is above 80%. However, in a few instances when running at higher speeds (above 600RPM) the volumetric efficiency declines considerably at stroke lengths of 30mm and 45mm. Below 600RPM the volumetric efficiency stays relatively constant.

In some cases, at higher speeds, the efficiency is diminished considerably, which seems to be caused by the high gas content in the chamber, as shown in Figure 4-23. This time-lapse shows the outlet valve at an interval of 0.033s. At 0.067s bubbles are clearly visible, suggesting high gas content is being pumped. After further inspection, the root cause was narrowed down to poor dynamic seal performance and cavitation. Figure 4-24 shows the piston cylinder before and after the experiment, water droplets are clearly visible on the dry side. This suggests that the dynamic seals did not provide adequate sealing.

In addition, the valves were not optimised for the highest performance, as this initial experiment was intended to be used for proof of concept only. Inefficient valve design causes the fluid to change its momentum vector at several locations, as indicated by the red arrows in Figure 4-25. This leads to a pressure drop below the vapour pressure of the water across these areas, hence causing cavitation to form.

As seen in Figure 4-21, the setups with the stroke length of 60mm were tested below 400RPM. Running at higher pump speeds compromised the sealing performance which was caused by the high piston velocity. Furthermore, the motor struggled to perform under these conditions, therefore the flywheel and motor had to be equipped with gears to increase the torque on the flywheel shaft.

Based on the data shown in Figure 4-22, there is a linear correlation between average flow rate and pump speed, but this relationship is broken at higher speeds. As previously mentioned, these results are likely to be affected by the poor sealing performance and the poor valve design. Despite these issues, the graph shows the same flow rate can be achieved at lower speed but at a larger stroke length.

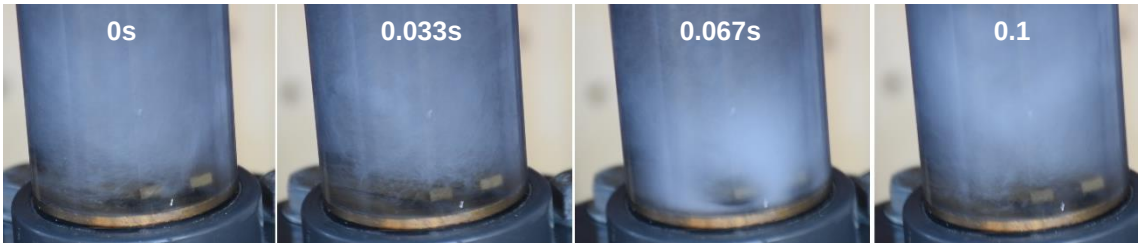

Figure 4-23: Outlet valve; Stroke Length – 45mm, Speed – 649RPM

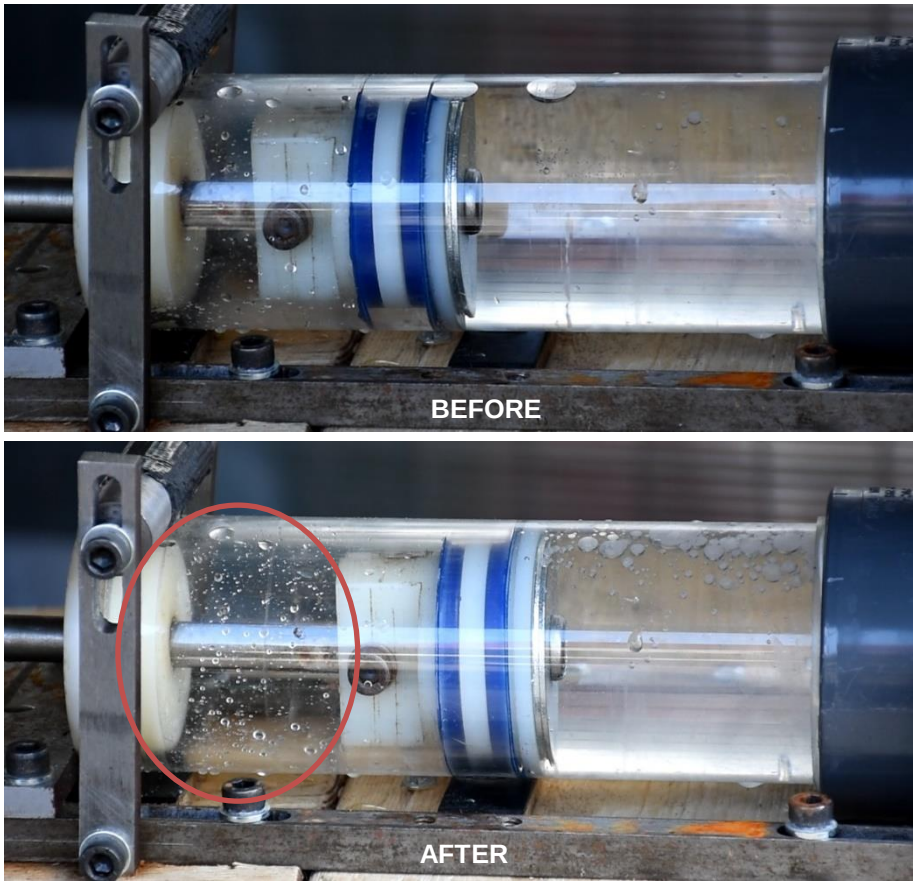

Figure 4-24: Piston Rocking

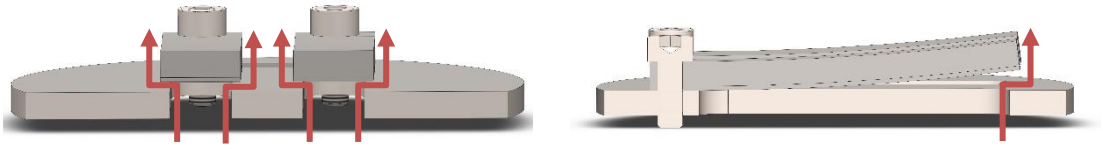

Figure 4-25: Valve Flow Direction

4.3.7 Test Setup 2

4.3.7.1 Overview & Methodology

After further investigating video footage of the initial test, it was concluded that rotatory motion of the flywheel caused the piston to rock, leading to poor sealing performance. To rectify this issue, the distance "A" between two seals was increased from 5mm to 40mm (Figure 4-26) to allow better stability. In addition, the sealing grooving diameter was changed from 40.5mm to 41mm and the piston was machined to higher tolerances to reduce the water contact area with the seals.

The same process as previously was carried out to evaluate the volumetric efficiency and mass flow rate vs pump speed.

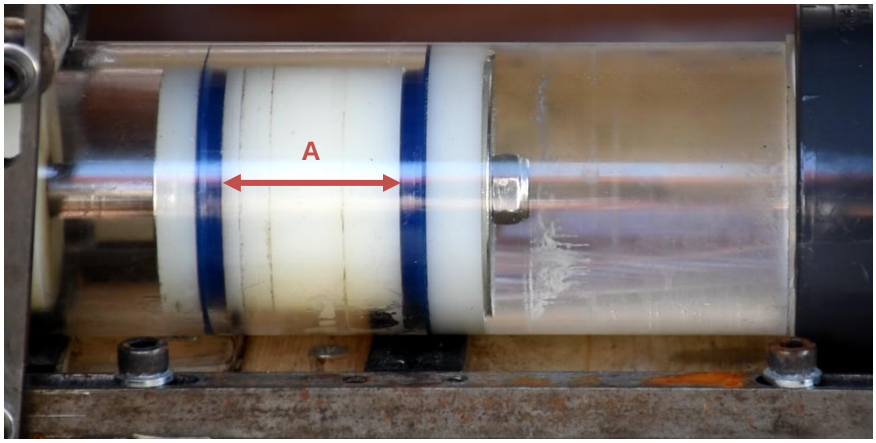

Figure 4-26: Improved Piston Design

Additional experiments were conducted to ensure that the valves can operate at pump speeds of over 1,000RPM. The test has shown that the reed valves can open and close in less than 0.032s, which is equivalent to ≈1,930RPM, almost double the target speed. To record this measurement, a GoPro Hero 3 Black Edition camera was used to record at 240fps (≈0.004s/frame). This footage was then slowed down in Adobe Premiere Pro CS6, where the number of close/open cycles were counted and the pump speed was determined from Equation 4-9.

$$N_{pump} = \frac{n_{cycles}}{t} \quad (4\text{-}9)$$

Where N_{pump} – pump speed (RPM), n_{cycles} – number of close/open cycles and t – duration of experiment (s).

4.3.7.2 Experimental Data and Analysis

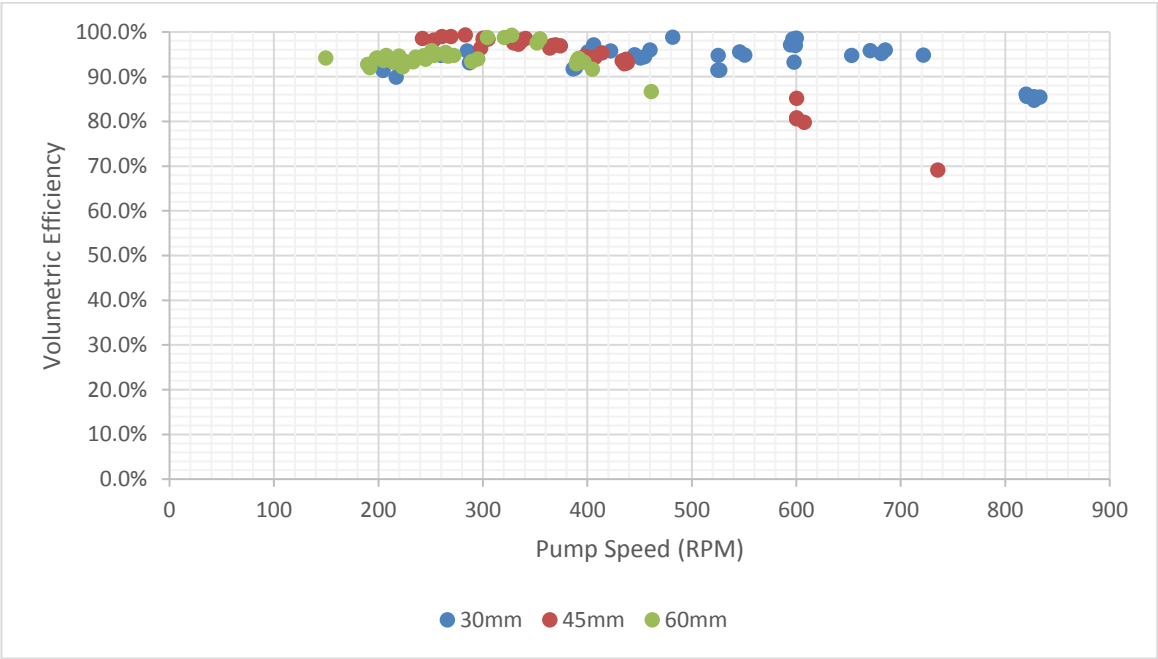

Figure 4-27: Volumetric Efficiency vs Pump Speed – Test 2

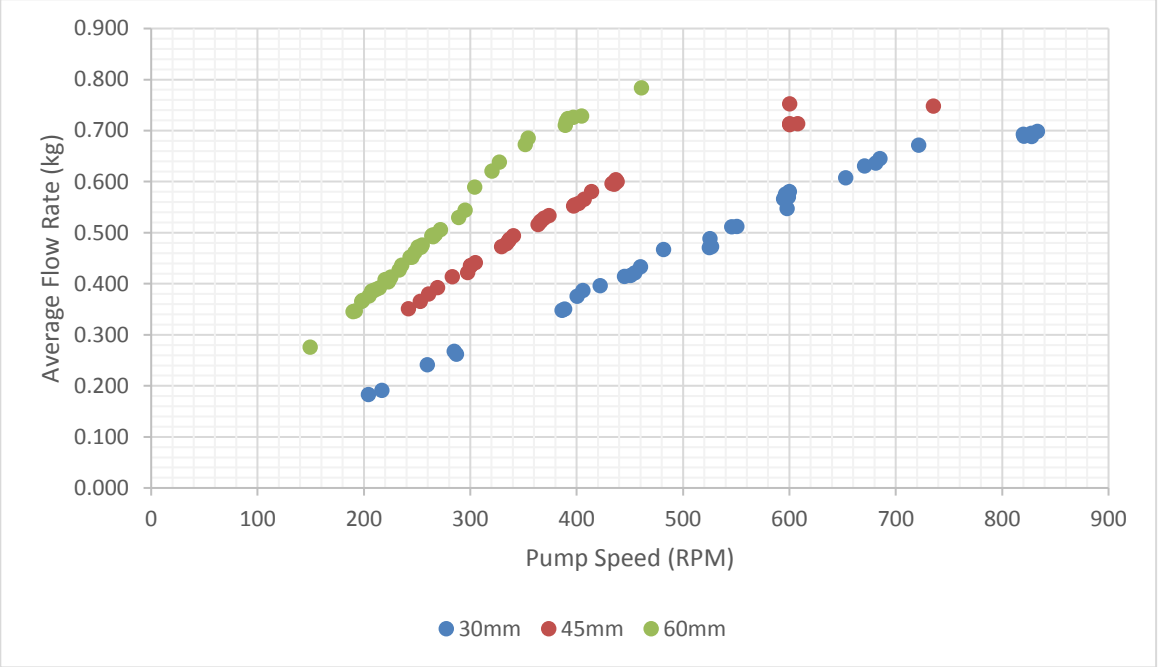

Figure 4-28: Average Flow Rate vs Pump Speed - Test 2

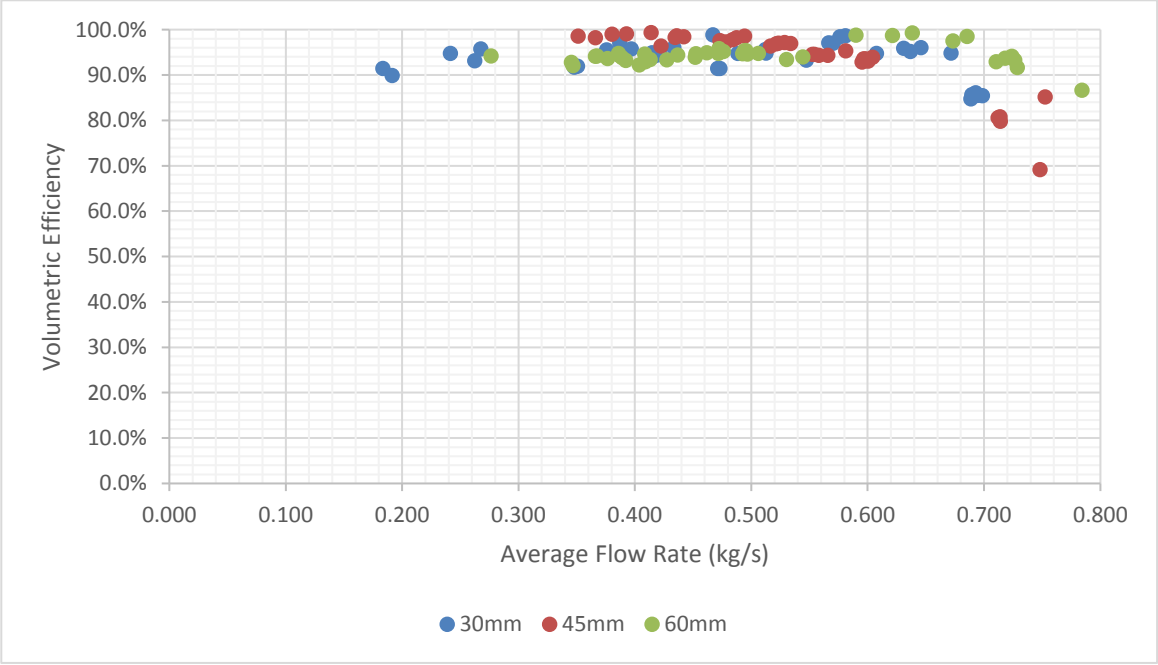

Figure 4-29: Volumetric Efficiency vs Flow Rate – Test 2

Volumetric efficiencies and flow rates vs pump speed were compared in Figure 4-27 and Figure 4-28 respectively. The new piston design has improved the n_v which now lies in the range from 90% to 100% for most of the cases. Volumetric efficiency only declined below 90% for the high pump speeds. Furthermore, Figure 4-27 shows that shorter stroke lengths have a higher threshold at which the pump performance starts declining. This suggests that the pump performance is affected by the flow rate or velocity of the piston.

As previously described, poor valve design caused high-pressure drops across the valves which led to the poor performance. To test this hypothesis, a volumetric efficiency vs flow rate graph was plotted in Figure 4-29. The graph indicates that volumetric efficiency is similar for all stroke

configurations, up to 0.675kg/s then it sharply declines. This decline suggests that at higher flow rates cavitation is more severe and hence increases the losses.

The graph in Figure 4-28 of the new piston shows that the flow rate increases with the pump speed. The previous data from the old piston design was inconsistent, especially when the speed exceeded 600RPM (Figure 4-22). This discrepancy in the data of the old piston was caused by the increased levels of cavitation at higher speeds which diminished the efficiency. Furthermore, the data in Figure 4-28 shows that s=30mm has the smallest gradient, thus the pump must run at a higher speed to achieve the same flow rates as in the other two configurations.

The evidence strongly supports that for high-speed piston pumps, a short stroke length is more desirable, as it offers higher volumetric efficiencies and lower vibration intensity (caused by pulsation). However, in some cases longer stroke lengths might be necessary to achieve the desired flow rates, thus the optimum balance between pump speed, stroke length and vibration levels must be found.

During the test, it was noted that the metal to metal contact between the petal and base of the valve did not provide an adequate seal to prime the system effectively, therefore the pump had to be primed prior to the start. As the propellant tanks are typically installed above the pump system in a launch vehicle, gravity will keep the pump primed. As expected, these valves performed very poorly under static conditions, such as when the pump is not turned on. To keep the pump primed, the inlet port was plugged after each test to prevent leakage.

After running a few tests, it was noted that the leakage rate increased under static conditions. After further inspection, it was found that the petals of the valves were slightly deformed, causing sealing issues (Figure 4-30). It was determined that high flow rates required the petals to sustain loads above the material's yield strength leading to plastic deformation. While this made it more difficult to prime the pump, it did not cause any problems while running the pump. When the pump was operating, it created a back-flow pressure on the valves, which kept the petals shut, hence eliminating sealing problems. These reeds have been successfully tested for a total of over 30min, but did not show any signs of fatigue failure and the magnitude of deflection remained constant.

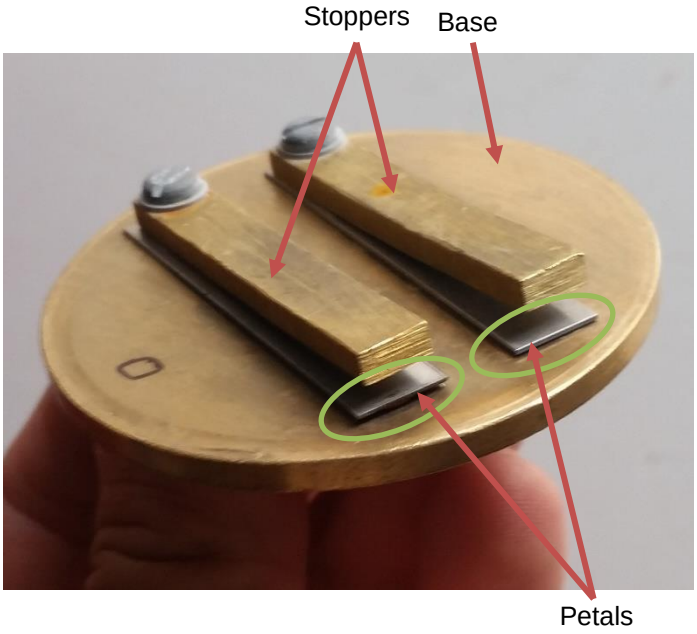

Figure 4-30: Deformed Petals of Outlet Valve

4.3.8 Reed Valve Improvements

The initial tests confirmed that the valves can work at the almost double the target speed and deliver flow rates just below the required values. As a reminder, the launch vehicle LOX triplex pump will have to deliver 21.4kg/s or 7.1kg/s per cylinder. Target average flow rates were calculated using Equation 4-10, and recorded in Table 4-3, by assuming that the same volumetric efficiencies of the full-scale rocket piston pump can be achieved for the scaled down version. Due to the valve limitations described previously, it was not possible to test the pump at ≈1,000RPM, therefore the valves had to be redesigned to allow higher flow rates.

$$\dot{m} = V_{piston} \times n \times \eta_v \times \rho \times \frac{1}{6 \times 10^{10}} \quad (4\text{-}10)$$

Where $\dot{m}$ – mass flow rate (kg/s), V_{piston}– Piston Velocity (m/s) n – speed of the pump (RPM), η_v – volumetric efficiency and ρ – density of media.

Table 4-3: Target Average Flow rates at 1,000RPM, D=50mm and η_v=0.9

Stroke Length	Flow Rate
30mm	0.88kg/s
45mm	1.32kg/s
60mm	1.76kg/s

The CFD results in section **4.3.4 Valve Selection & Concept Design** show that restricted flow passages resulted in high flow velocity, consequently leading to a higher pressure drop. Furthermore, poor design led to flow direction changes which further contributed to the pressure drop. To overcome these issues, and to minimise the interaction between the fluid and the valve the following changes were made:

- A third flow passageway was added to provide a greater area for the flow to go through.

- The valve base was angled, as shown in Figure 4-31 to minimise the momentum change of the propellant. Also see Figure 4-15 and Figure 4-25 for comparison.

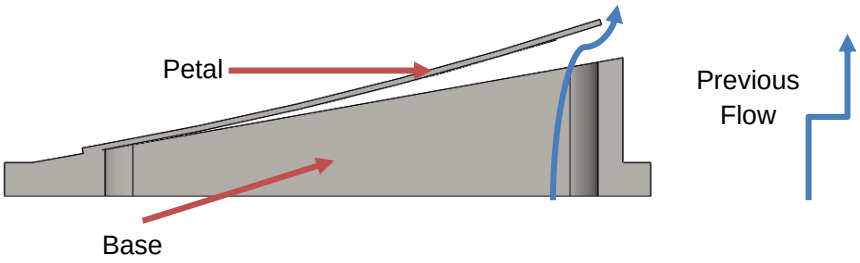

Figure 4-31: Angled Valve

These changes were implemented to reduce the interaction between valve and liquid. Manufacturing is an expensive and time-consuming process, therefore CFD analyses were conducted with the same boundary conditions to investigate how these changes would affect the flow velocity. As shown in Figure 4-34, the additional passage has increased the flow area, despite its width being narrower by 2mm (the original width being 7mm). The width reduction was essential to balance the distance between petal gaps and petals. The third passage reduced, the maximum flow velocity from $\approx$11.6m/s to $\approx$8.8m/s. A smaller velocity value is more desirable as the acceleration of the fluid is lower, hence reduces the chance of cavitation. For more details about the CFD setup, refer to **Appendix H: CFD Setup of Angled Valves** (pg.171).

To determine the effects of an angled valve, the CFD results were obtained for comparison when the base was angled at 10°, 20°, 30° and 40°. A higher angle than 40° was not considered at this stage of the project because 40° as it is sufficient to evaluate the effects of angle. As shown in Figure 4-34, at a larger angle, the stopper interferes with the sealing face and this issue can only be mitigated by adding a recessed face, as shown in Figure 4-33. This adds extra manufacturing complexities when manufacturing with a manual lathe and mill, therefore this option was not considered. The openings in the valve also must be shifted towards the front of the valve, which results in a reduction in the equivalent length of the flow passage ways. The maximum pressure drops and maximum velocities for angled bases are shown in Table 4-4. The CFD results for 10°, 20° and 30° are shown in Figure H-7 - Figure H-9 in **Appendices**. As expected, the CFD results showed that by increasing the angled of the valve, the maximum velocity is gradually reduced, resulting in lower pressure drops. At steeper angles, the base surface becomes elliptical, hence longer reeds can be installed. This allowed a larger deflection to form which increased the affected area, thus resulting in a lower velocity. The flow trajectories, shown in Figure 4-35, confirm that when the base is angled at 40°, more fluid is pumped than in the valves with a flat base (Figure 4-34).

Based on the CFD results, the benefits of the 40°angled valve are evident. As such it was decided to manufacture this design and test it for further evaluation.

Table 4-4: Properties for Various Angled Bases

	Max Velocity	Max Change of Pressure
10°	≈7.4m/s	≈29kPa
20°	≈6.7m/s	≈27kPa
30°	≈5.9m/s	≈20kPa
40°	≈4.3m/s	≈10kPa

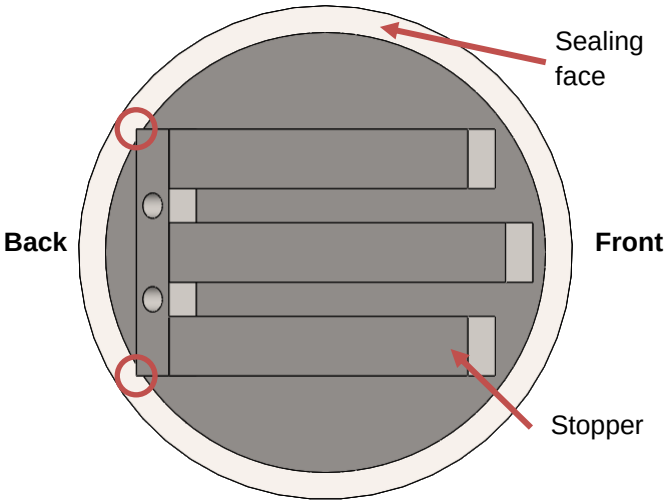

Figure 4-32: Angled Reed Valve

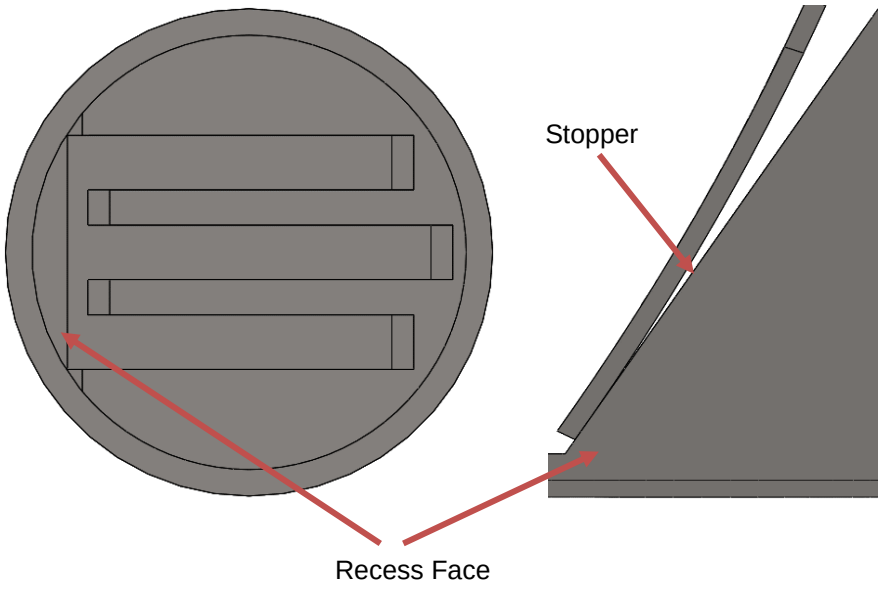

Figure 4-33: Reed Valve with a Recess Face

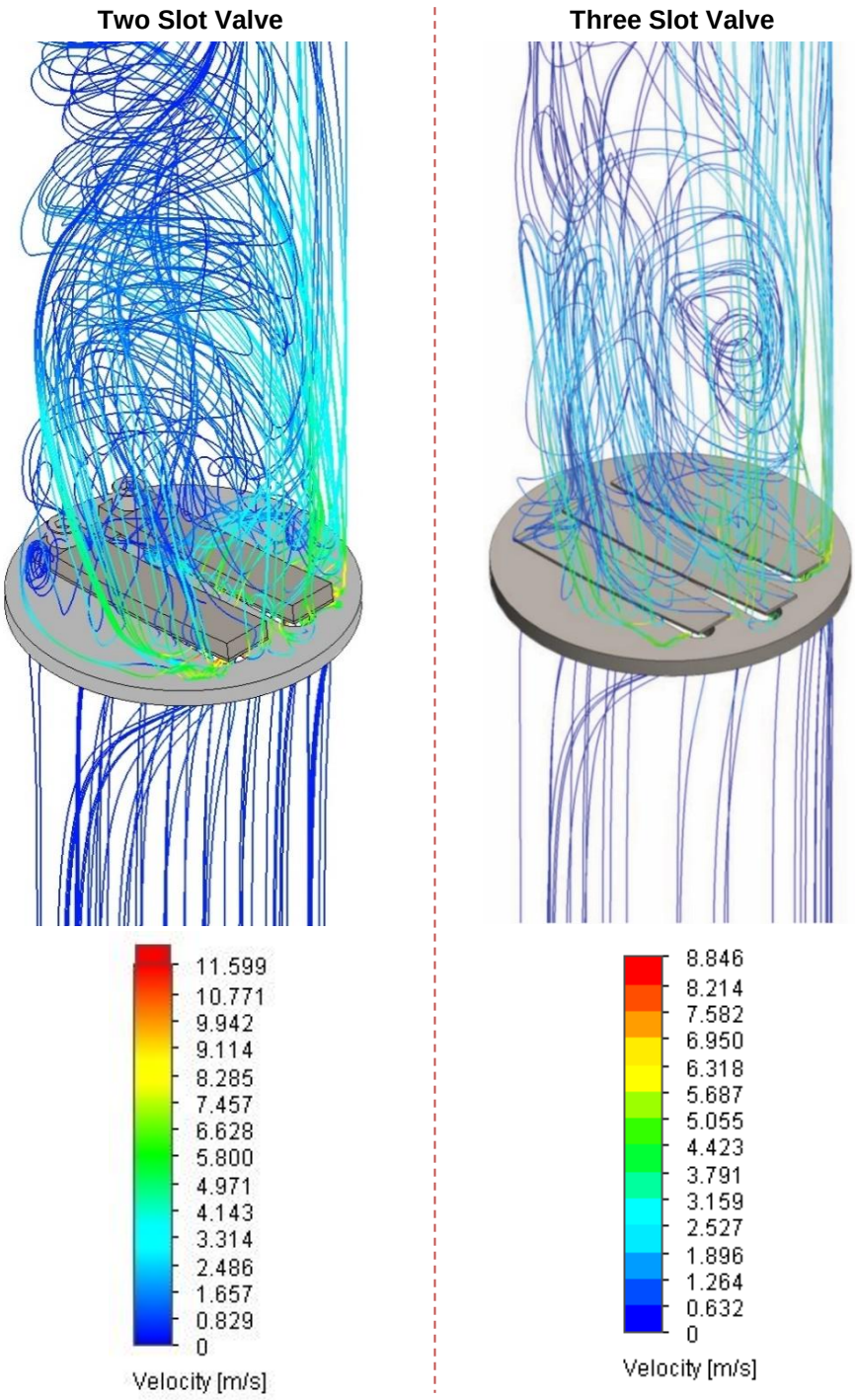

Figure 4-34: Two and Three Slot Valve Designs – Velocity Graphs

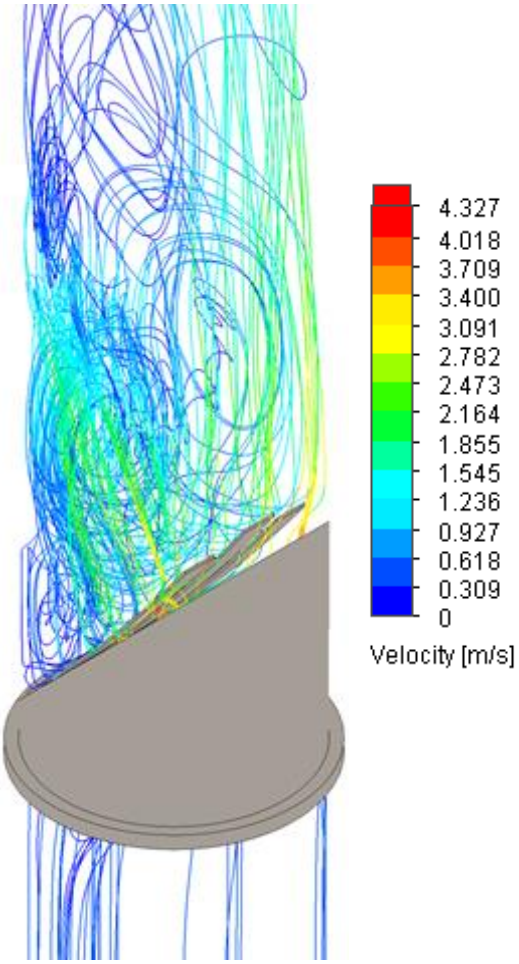

Figure 4-35: 40° Angled Valve – Velocity Graph

4.3.9 Test Setup 3

4.3.9.1 Overview & Methodology

The same methodology as in the previous tests was adopted for measuring the pump performance, with some changes to the hardware. Firstly, gears with a ratio of 60:26 were installed to deliver greater torque to the flywheel, which allowed smoother piston acceleration. This ratio was selected based on the availability of gears. Secondly, the new valve base was angled at 40° (Figure 4-36). During the test, it was noted that these valves offered very poor sealing performance under static conditions, therefore the decision was made to replace the intake valve with new angled valve while retaining the original outlet valve. This helped to maintain the system primed prior to the tests. As previously described cavitation occurs at the inlet (due to low pressure), thus the most efficient valve design was installed in this location. The new pump setup is shown in Figure 4-37. In addition, the running time of some tests was increased to determine the effects on the volumetric efficiency. Furthermore, the optimum operating speed was found and compared at various stroke lengths.

Figure 4-36: Reed Valves Angled at 40°

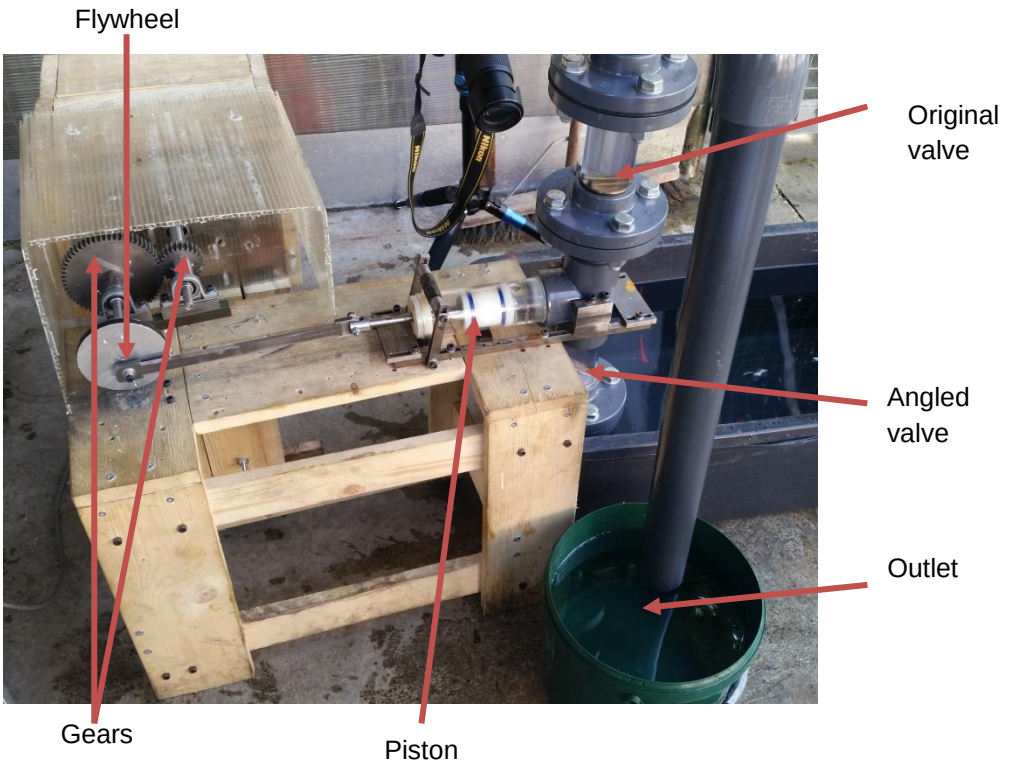

Figure 4-37: Reed Valves Angled at 40°

4.3.9.2 Experimental Data and Analysis

After proving the concept of the angled valves through experiments, both valves were replaced with the new concept design. As expected, by replacing the original inlet valve with the angled valve, volumetric efficiency has considerably increased (Figure 4-38). However, it was unexpected to see it rise above 100%. To verify that it was not caused by any kind of error, the calculations were checked multiple times and the experiment was repeated. Furthermore, the scales for measuring water content were loaded with a known amount of mass to test the calibration, but no fault with the equipment was found.

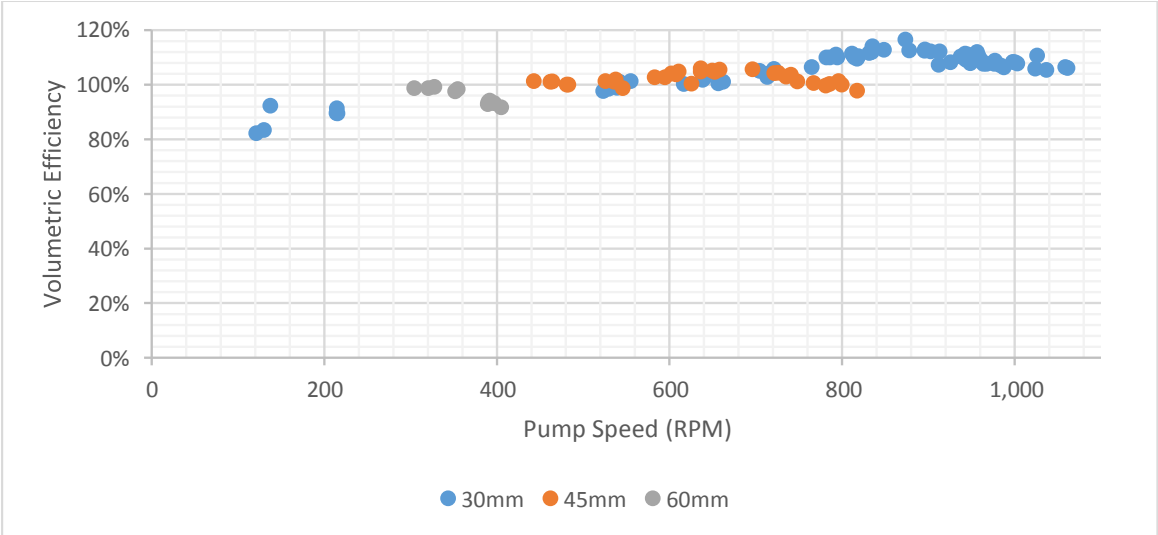

Figure 4-38: Volumetric Efficiency vs Pump Speed – Test 3, Setup with Original Outlet Valve

The diagrams in Figure 4-39 were drawn to illustrate the effects on the fluid's momentum at various stroke lengths. At shorter strokes, such as $s = 30$mm, the momentum is least altered, hence more energy is available to overcome restrictions posed by the outlet valve. At longer stroke lengths, more fluid is redirected to the pumping chamber, resulting in changes of the momentum vector from vertical to horizontal before switching back to the vertical. These changes cause the energy losses which are responsible for increased vibration levels during the experiments.

After careful investigation, the conclusion was drawn that the momentum of the water most likely caused the volumetric efficiency to exceed 100%. There are two scenarios that could have caused this. As previously mentioned, due to the inertia of the water, the piston and water do not accelerate at the same rate. Therefore, when the suction stroke reaches half of the stroke length, the piston starts decelerating, while the water maintains its velocity. As the water is incompressible, this extra volume is expelled through the outlet valve. Similarly, at full discharge stroke, the velocity of the piston is zero, but water continued travelling due to its momentum. These effects were not observed with the original (flat base) valves due to inefficient design. It should be noted that to exceed a volumetric efficiency of 100% may not be possible with actuated valves as the valves would only remain open at set intervals and fluid's momentum would be transferred to the valve instead. These valves have a pre-set cycle interval, similar to that used in a car, thus once it is shut all flow is instantaneously stopped. Any momentum remaining in the liquid, would be transferred to the valves and this can lead to a higher vibration intensity. Of course, these valves can be optimised to shut when the liquid carries the least momentum, but this would require dozens of experiments to find the optimum interval.

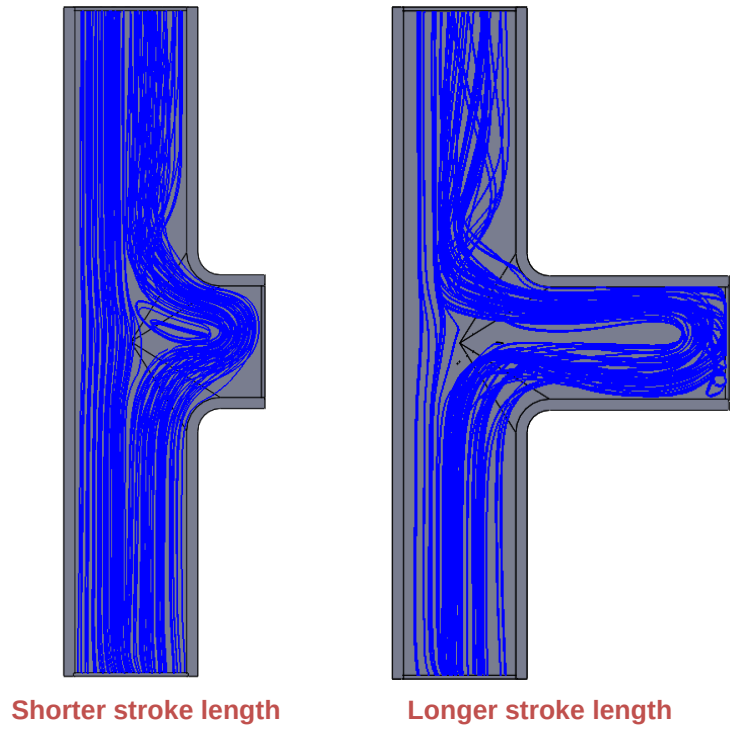

Figure 4-39: Changes of Momentum

As seen in Figure 4-10, the simplex pump outputs zero pressure during the suction cycle, but for the triplex pump, the lowest output pressure drops to ≈22bar (Figure 4-12). This increases the back pressure on the outlet valve, which can diminish the overall volumetric efficiency. To test the effects

of the higher back pressure, the triplex prototype must be built, but this is beyond the scope of this project.

Based on the data shown in Figure 4-38, each stroke length has an optimum running speed. Corresponding to the maximum volumetric efficiency, the optimum speed for the s=30mm is ≈850RPM, whereas for $s = 45$mm it is ≈650RPM. However, the motor could not produce enough torque to allow sufficient data to be gathered in order to determine the optimum speed for $s =$ 60mm. In addition, high vibration levels were observed which further influenced the decision to terminate the tests early. The high vibration intensity was caused by water pulsation and the low natural frequency of the system. Nonetheless, sufficient data was collected to notice that at 355RPM or greater, the pump efficiency rapidly began to decline. This inefficiency was likely caused by the fast acceleration of the piston in the suction cycle. As stated earlier, the piston and fluid do not accelerate at the same rate due to inertia limitations. On the suction side, the piston travels faster than the fluid. This creates a small area of low pressure between piston and fluid. As the piston acceleration increases, the area gets bigger and a large pressure drop ensues. If the acceleration is sufficient, the pressure will drop to below the water vapour pressure and this area would be filled with the compressible vapour. The density of water vapour can be as much as ≈780 times smaller than in liquid form, thus this resulted in a lower mass flow.

However, piston acceleration is not the only factor that contributes to the decline in efficiency at higher rates. The theoretical acceleration of the piston was plotted for all stroke length configurations at their optimum speeds in Figure 4-40. These values show that $s = 60$mm has the slowest acceleration and $s = 30$ the highest. Despite this difference, the $s = 60$mm system exhibits the lowest volumetric efficiency, followed by $s = 45$mm and $s = 30$mm. As the piston moves back, a low-pressure area is produced between the piston and the fluid as mentioned above. This sucks the 1st layer of the liquid towards the piston followed by the 2nd, 3rd layers and so on (refer to Figure 4-41). At the longer stroke lengths, there are more of the fluid layers and thus the inertia of the fluid increases. Due to lack of time at higher operating speeds, only a small amount of the momentum is transferred to the last layers of the fluid cells. Consequently, this leads to a greater distance between piston and liquid, and as a result, the low-pressure area is formed. If the speed is fast enough, the pressure can drop below the water vapour pressure. Hence, to increase the pump efficiency, further study is needed to optimise the stroke length to diameter ratio of the piston cylinder according to the flow rate requirements.

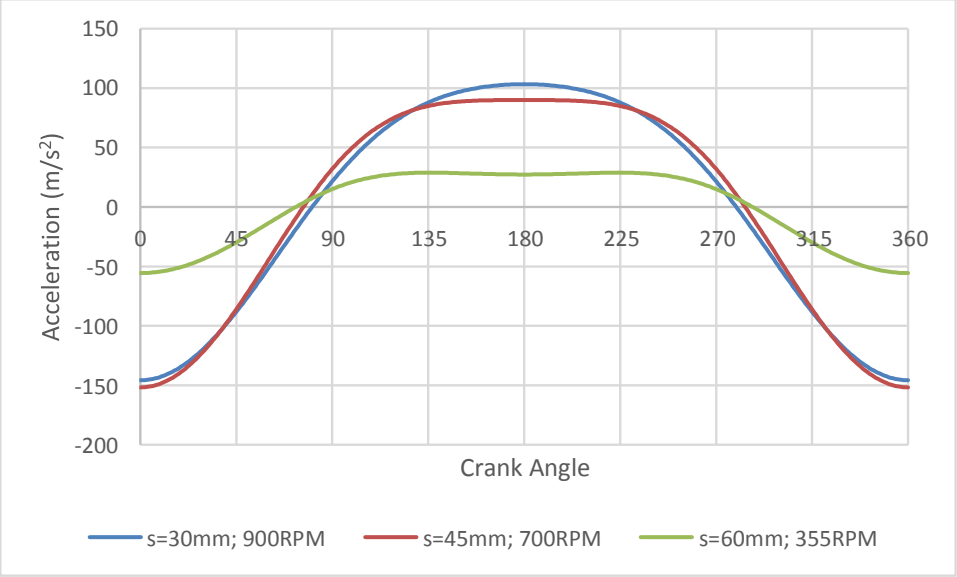

Figure 4-40: Piston Acceleration of r = 15mm; 900RPM r = 22.5mm;700RPM and r = 30mm; 355RPM

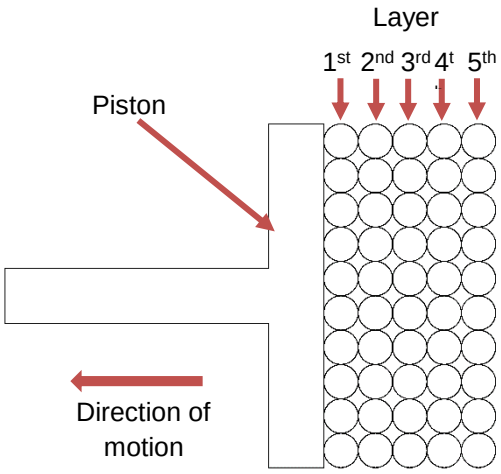

Figure 4-41: Piston Energy Transfer

The results in Figure 4-42 indicate that the pump configuration with the shortest stroke length is the most efficient design, despite the need to run at a higher speed to achieve the same flow rate. In most of cases, the volumetric efficiency of the s = 30mm configuration was higher by more than 5% than for s = 45mm. Despite this, higher flow rates were achieved for s = 45mm because of the following reasons:

- The highest tested speed was ≈1,060RPM. To match the flow rates of the s = 45mm setup, the pump speed had to be increased in order to displace the same volume in a given time but at a shorter stroke length.
- As shown in Figure 4-43, the volumetric displacement at s = 45mm outweighs the benefit of a greater volumetric efficiency at s = 30mm.

A typical total mass flow ranged from 7.9kg to 9.5kg. There were eight additional experiments conducted with the total mass ranging from 21kg to 37kg at s = 30mm but no changes in volumetric efficiency were seen.

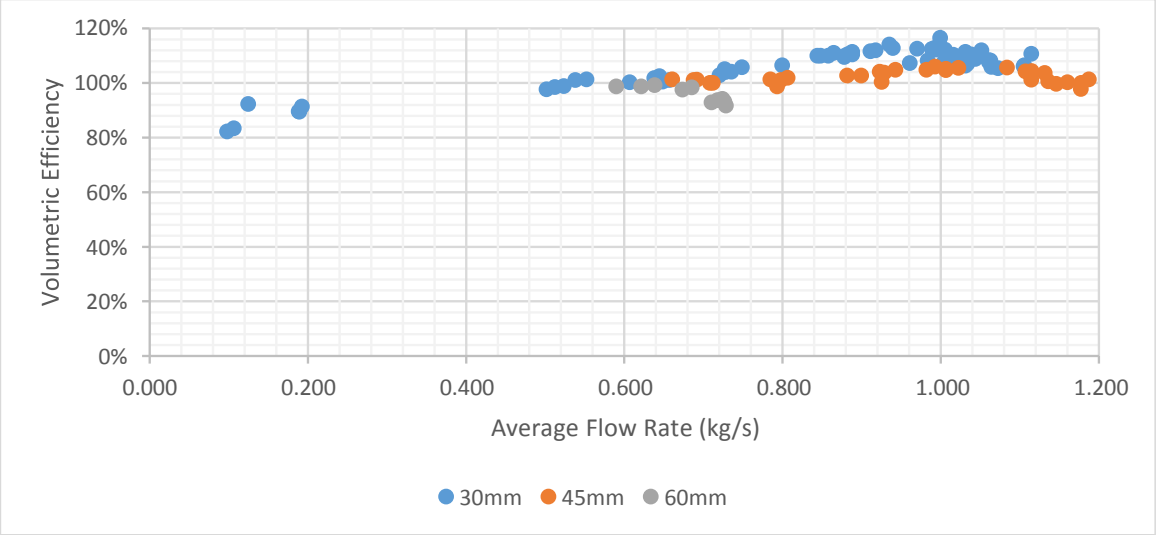

Figure 4-42: Volumetric Efficiency vs Average Flow Rate – Test 3, Setup with Original Outlet Valve

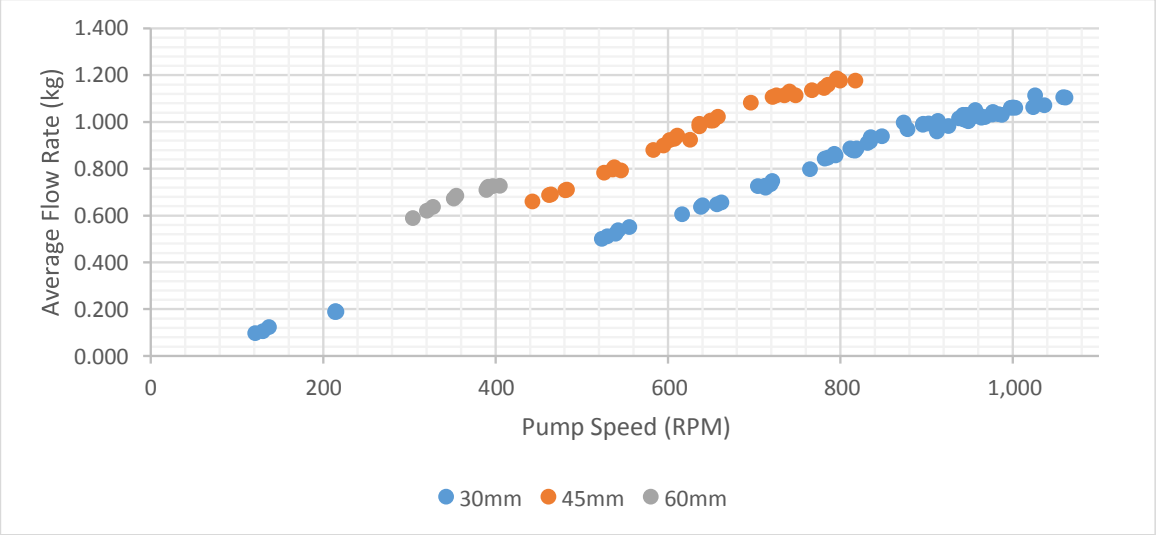

Figure 4-43: Average Flow Rate vs Pump Speed – Test 3, Setup with Original Outlet Valve

The concept of the angled reed valve design was experimentally verified with water and the efficiency benefits were clearly noted. Regardless of pump priming issues, both original valves were replaced with the angled design to evaluate the full potential. The previous tests showed that the highest volumetric efficiencies and the highest speeds were achieved at a stroke length of 30mm. Taking into consideration the PhD time constraints, further tests were carried out at $s =$ 30mm.

As shown in Figure 4-44 by using both angled reed valves, it resulted in further volumetric efficiency gains which in some cases surpassed 145%. It should be noted that the prototype did not have a tachometer to control the pump speed, therefore these values ranged from 925RPM to 1,050RPM. The pump speed was adjusted by altering the output voltage on the Variac.

The experimental data in Figure 4-44 show no correlation between volumetric efficiency and speed of the pump. At a higher voltage output, it was expected that the pump speed would go up. The pump speed ranged from 925RPM to 1,050RPM, and the higher voltage led to a higher volumetric flow rate.

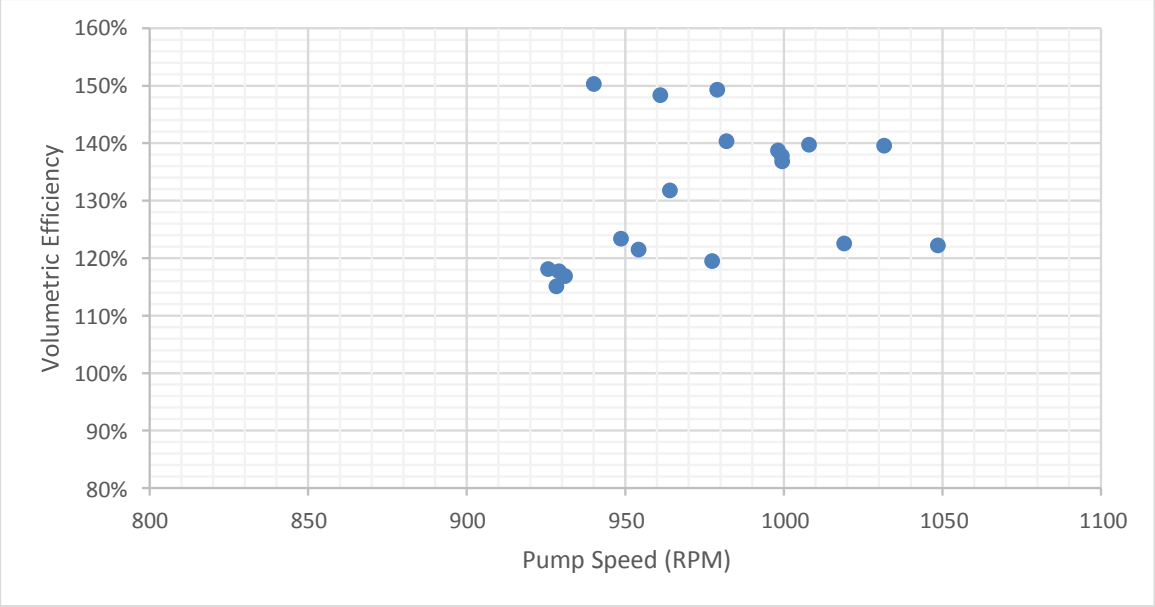

Figure 4-44: Volumetric Efficiency vs Pump Speed – Test 3, s=30mm

4.4 Summary

To draw out the requirements of the piston pump, an analysis and sizing study was carried out which indicated that a triplex pump configuration offers the most effective solution when factors such as acceleration head, system size, flow rate and inlet pressure were taken into consideration. A dynamics study was conducted, which further supported the selection of the triplex configuration. The study showed that to obtain the target average pressure of 30bar, the pump must deliver a maximum pressure of 33bar. This set the system requirements for the Mark II demonstrator.

Several valve concepts were analysed and a CFD study was conducted to calculate the potential pressure losses, and to analyse the flow trajectories through the valves. The Mark I concept was then designed and manufactured to investigate values of the volumetric efficiency, flow rates and operating speed. In the process of testing valves, areas of improvement of the pump were identified and changes were made.

Due to leakage issues and poor predicted performance, reed valve concept 2 was rejected and therefore all experiments were carried out based on concept 1. After carrying out several tests, it was noted that the petal of the concept 1 design plastically deformed and caused leakage under static conditions, but it was manageable. The deformation stayed at a relatively level value throughout the experiments and did not cause any further concerns or show any fatigue failure. In addition, reed valves were found experimentally to offer the maximum operating frequency of ≈1930RPM, almost double the target.

After testing various stroke lengths, the shortest stroke (30mm) was found to offer the most desirable results – lowest vibration levels, lowest starting power requirements and highest volumetric efficiencies. Due to lower power requirements, it was possible to carry out the tests at over 1,000RPM.

After validating the reed valve concept, the valve base was angled by 40° which provided an increase in volumetric flow efficiency exceeding 100% in almost all cases. To ensure consistent results are achieved in all cases, valve operation durations were varied from 8s to 40s for speeds of 800RPM and greater.

In **Chapter 5**, further feasibility studies were carried out to determine the suitability of the piston pump at cryogenic temperatures and to monitor the pressure profile. The current material selection is not compatible for such tests, therefore the Mark II had to be developed. The study in the next chapter included: an investigation of material suitability for cryogenic temperatures and a detailed evaluation of dynamic seals. The concept design of the Mark II was modelled on SolidWorks and FEA analyses were carried out to ensure the components are able to withstand the required operating pressures. Detailed descriptions of the fabrication processes and components were provided, which were then used to assess the complexity of the piston pump.

Once the Mark II was manufactured, it was decided to carry out the tests in three phases. In phase one, water tests were carried out, to ensure the results are consistent with the Mark I. in phase two, pressure sensors were added and the pressure profile was monitored. And in the final stage, the compatibility with LN_2 and LOX were tested. These results are presented in the next chapter.

Chapter 5

Piston Pump – Mark II Demonstrator

5.1 Overview

After verifying the concept design of the Mark I, another demonstrator was built to evaluate a wider range of parameters. The primary focus of this demonstrator was to test the compatibility with cryogenic and oxidising liquids, pressure variation, flow rates and validate component reliability. Secondary goals included: evaluation of manufacturing techniques, costs and to identify areas for improvement.

5.2 Design & Manufacture of Mark II

5.2.1 Material Evaluation

The Mark I prototype was mostly made from PVC and acrylic tubing. The yield strength (YS) and ultimate tensile strength (UTS) of these materials often range below 100MPa, whereas aluminium alloy of a similar density can offer a UTS of around 400MPa [76-78]. Also, the small difference between the YS and UTS makes these materials very brittle. The PVC and acrylic are very soft when compared with metal alloys, which can pose sealing difficulties for dynamic conditions at high pressures, due to high surface wear. In addition, these materials pose a fire hazard when working with LOX. Based on this data, the PVC and acrylic were deemed to be unsuitable for Mark II. Therefore, the materials of the technology demonstrator must meet the following criteria:

- Must be compatible with oxidising liquids.
- Must retain ductility to prevent catastrophic failure.
- They must offer limited reduction in strength or toughness at cryogenic temperatures
- Low-cost.
- Ease of machining.

Based on the cryogenic compatibility requirements as above, the following metals were shortlisted for further evaluation [79]:

- Aluminium alloys
- Stainless steel alloys
- Titanium alloys

Other metals, such as platinum, lead or brass were also reportedly compatible with cryogenic liquids but due to high density, high price or low strength these materials were not considered.

Aluminium alloys are suitable for structural parts at temperatures of -270°C [80]. Most aluminium alloys show very little change in properties between room temperature and -270°C; ultimate tensile strength can increase from 30 to 40%, yield strength from 5 to 10% and elongation between 60 to 100% between room temperature and -195°C [80]. 5083-O is the most widely used alloy for cryogenic temperatures, as it exhibits a 40% increase in UTS and 10% in YS [80]. Other alloys often used for such applications are 1100, 2014, 2024, 2219, 3003, 5083, 5456, 6061, 7005, 7039, 7075 and 7475 [80]. The properties of several aluminium alloys were recorded in Table 2-1. 5083-O is a non-heat treatable alloy and as such has low mechanical properties when compared with the aerospace grade 6061-T6 and 7475-T61 alloys.

304 and 304L are the most widely used stainless steel alloys, while other types 316, 316L, 321 and 347 are also used, depending on the application [81]. Similarly to aluminium alloys, YS and UTS of the stainless steel increases at lower temperatures and UTS triples in some cases (refer to Table 2-1 for more details). There is also a large margin between YS and UTS which makes it more ductile than aluminium, even at -195°C. However, stainless steel is hard metal which makes it difficult to machine, but good for piston cylinder due to a lower surface wear than Aluminium alloys. Stainless steels also have a poorer specific strength.

The titanium alloys are divided into three types: alpha, near-alpha and alpha-beta. Alpha alloys have low to medium strength and possess excellent mechanical properties at cryogenic temperatures [82]. Ti-5Al-2.5Sn is a commercially available alloy and its properties are recorded in Table 2-1. The YS and UTS for titanium alloys increase at cryogenic temperatures, but the data for Ti-5Al-2.5Sn at -195°C could not be found [82]. It should be further added that titanium alloys are very expensive relative to aluminium and stainless steel.

The following material properties were evaluated in Table 5-2 at -195°C:

- $UTS - YS$: to define the material ductility – the higher the number, the more ductile the material is.
- UTS/ρ: specific strength – were used to assess the strength-to-weight ratio of the material. It is often used in the aerospace industry in order to keep the weight of the material at a minimum, while retaining adequate strength.
- YS/ρ: was used to assess the material at which point deformation occurs with respect to density.
- E/ρ: specific modulus – was used to assess the stiffness-to-weight ratio of the material. This can be used to determine which alloy offers the minimum structural weight.
- σ_T: thermal stress (Equation 5-1) – thermal stresses were calculated from Equation 2-9, assuming the temperature difference is -220°C [83, 84].

$$\sigma_T = E \times CTE \times \Delta T \quad (5\text{-}1)$$

Where σ_T – Thermal stress (MPa), CTE – Linear Coefficient of Thermal Expansion (m/(m°C)) and ΔT – Change in temperature (°C).

Table 5-1: Properties of Alloys [78, 85-91]

Alloy	YS (≈20°C)	YS (-195°C)	UTS (≈20°C)	UTS (-195°C)	ρ	CTE	E
5083-O	145MPa	165MPa	290MPa	405MPa	2.66g/ cm^3	22.3 µm/(m°C)	70.3GPa
6061-T6	276MPa	324MPa	310MPa	414MPa	2.70g/ cm^3	23.6 µm/(m°C)	68.9GPa
7475-T61	490MPa	600MPa	565MPa	683MPa	2.81g/ cm^3	21.6 µm/(m°C)	70.3GPa
304	215MPa	269MPa	505MPa	1524MPa	8.00g/ cm^3	17.3 µm/(m°C)	193GPa
316	290MPa	517MPa	580MPa	1276MPa	8.00g/ cm^3	16.0 µm/(m°C)	193GPa
347	275MPa	284MPa	655MPa	1282MPa	8.00g/ cm^3	17.3 µm/(m°C)	195GPa
Ti-5Al-2.5Sn	827MPa	>827MPa	861MPa	>861MPa	4.48g/ cm^3	9.40 µm/(m°C)	110-125GPa

Table 5-2: Alloy Comparison Table at -195°C

Alloy	UTS-YS (MPa)	UTS/ρ (MPa/(g/ cm^3))	YS/ρ (MPa/(g/ cm^3))	E/ρ (MPa/(g/ cm^3))	σ_T (MPa)
5083-O	240	152.3	62.0	26.4	-345
6061-T6	90	153.3	120.0	25.5	-338
7475-T61	83	243.1	213.5	25.0	-345
304	1255	19 0.5	33.6	24.1	-947
316	759	159.5	64.6	24.1	-947
347	998	160.3	35.5	24.4	-957
Ti-5Al-2.5Sn	>34	>192.2	>184.6	27.9	-540 - (-613)

*ΔT=220°C; YS and UTS values are taken at -195°C.

As a reminder, values of the YS and UTS of titanium were used at room temperature due to insufficient data at cryogenic temperatures. The negative value in the σ_T column indicates that the stresses are created due to shrinkage.

Values in this table show that the aluminium alloy 7475-T61 has the highest specific strength, followed by the titanium, stainless steel and the rest of aluminium alloys. However, this aluminium alloy is expensive. 6061-T6 alloy cost $1,000-$5,000 per metric ton but the 7475-T61 can cost as much as $8,000 [92]. In addition, most of the aluminium alloys are much easier to machine when compared with a stainless steel or titanium, but it has the highest CTE value, meaning its shrinkage the most. Material CTE must be taken into a consideration when two materials with a different CTE are used in order to retain adequate tolerances.

The titanium alloy Ti-5Al-2.5Sn could potentially offer a higher strength-to-density ratio than 7475-T61 alloy but this could not be verified due to insufficient data. Both these alloys have a small difference between the YS and UTS values, therefore little elongation would be observed before fracturing.

Stainless steel alloys have the highest Modulus of Elasticity (E) which is twice that of the aluminium alloys. Therefore, this alloy is much stiffer but a large difference between the YS and UTS makes it ductile. Furthermore, the YS values are very similar to aluminium alloy but the stainless steel alloy is much denser.

Based on the data in the tables, it was concluded that stainless steel can potentially offer a safer option due to the large difference between the YS and UTS. This means that the material will exhibit some elastic deformation before fracturing occurs, which is desirable in a pressurised application. In addition, these alloys are considerably cheaper than titanium or aerospace grade aluminium alloys. Therefore, stainless steel alloys are a good option for making a prototype to verify the technology feasibility, but due to the high density, they are unlikely to offer a flight ready solution. Flight readiness will have to be evaluated in future prototype pumps.

Aluminium alloys are another good option for prototyping, due to the relatively low-cost aluminium 6061 at least and it is much easier to machine than stainless steel. The relatively low density also makes them suitable for a flight ready model. In contrast, titanium is not considered to offer a practical option for manufacturing the prototype due to the high cost and difficulty in machining with standard tooling. Therefore, aluminium and stainless steel alloys were selected for Mark II manufacture.

5.2.2 Dynamic Reciprocating Seals

Dynamic reciprocating seals are used to separate the high piston cylinder pressure from atmospheric pressure and they typically exist in two configurations: bore mounted and piston mounted, as shown in Figure 2-3. Bore mounted seals come in two designs, as shown in Figure 5-2. The difference between these two seals is that the seal on the right has a flange which is clamped to the bore, as shown in Figure 5-3. The flanged seals are typically used for rotating applications to keep the seal stationary, but it can also be in with reciprocating applications.

According to the seal specification sheet, the performance parameters are identical for both bore and piston mounted seals [93]. This experimental rig is likely to require several modifications to optimise the design, and piston mounted seals offer higher flexibility for these changes. To accommodate new seal requirements in a bore mounted system, a new cylinder would have to be machined which is more complex than making a new piston. To keep the manufacturing process as simple as possible, the decision was made to mount seals on the piston.

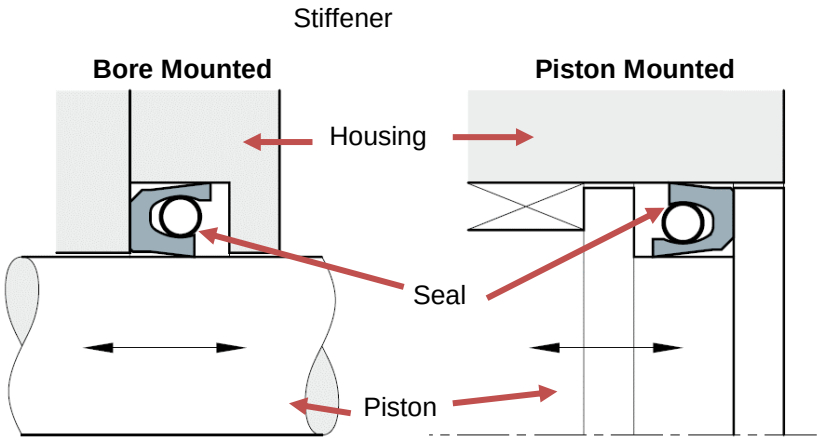

Figure 5-1: Seal Mount Configuration [93]

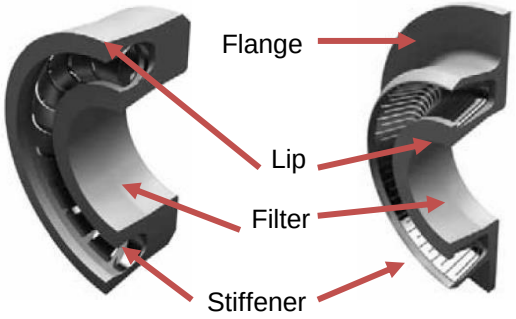

Figure 5-2: Bore Mounted Seals [93]

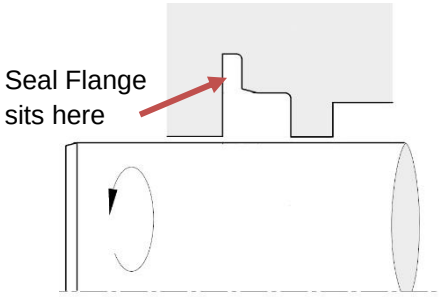

Figure 5-3: Lip Seat [93]

As seen in Figure 5-2, the width of the seals gradually increases, forming the lip and the stiffener is fitted. To minimise the friction forces, the lip is the only sealing part that is in contact with a dynamic face and as it wears, the stiffener is used to ensure the contact between seal, piston cylinder and piston is maintained at all times. Typically, two seals are used on each side of the piston to maximise the sealing performance. The area between the two seals creates a buffer pressure zone between the high internal pressures and atmosphere. Furthermore, to ensure the leakage is kept to a minimum, the gap between the piston and piston bore must be kept as small as possible.

At cryogenic temperatures, lubricants that are liquid at room temperature will freeze on contact. Furthermore, oil based lubricants, assuming sufficiently low viscosity, could ignite with LOX. It should be noted that lubrication cannot be used at cryogenic temperatures, therefore to reduce wear and tear and to increase the life expectancy of the seals, rubbing faces made of low coefficient of friction materials are used, mostly based on Polytetrafluoroethylene (PTFE). PTFE is

non-oxidising and has a very low static coefficient of friction of 0.04, but the CTE ranges from 112 to 135 µm/(m-K), which is 7 times greater than that of the stainless steel alloys [94]. This means that while cooling, virgin PTFE seals would shrink more than metals, leading to leakage between bore and piston. To ensure adequate sealing is maintained at cryogenic temperatures, stiffeners are added, as seen in Figure 5-2, to reduce the shrinkage. The spring stiffener is critical to ensure good sealing between piston and bore. The spring stiffeners come in four types: helical, cantilever, cantilever heavy-duty and canted coil, as shown in Figure 5-4.

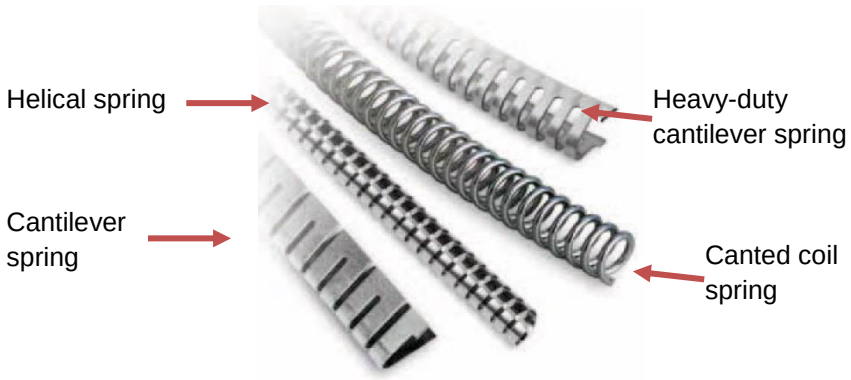

Figure 5-4: Types of Stiffeners [93]

The helical spring offers high-loading versus small-deflection as shown in Figure 5-5 [93]. This stiffener is typically used under static conditions, for reciprocating and cryogenic applications or where the pressure is too low to energise the spring [93]. However, due to a relatively small deflection range, high tolerances must be maintained (i.e. the narrow precise gap between the items to be sealed).

The cantilever spring allows a wider tolerance than the helical spring and it experiences high-deflection for small loads, as seen in Figure 5-5. It is also typically used to seal reciprocating pumps [93].

The heavy-duty cantilever spring design is very similar to a cantilever spring and it results in high-loading versus high-deflection, as seen in Figure 5-5. This stiffener is often used for cryogenic applications under static or slow dynamic loading [93].

The canted coil springs load versus deflection is plotted in Figure 5-5. This design is similar to the helical spring and it is intended to be used for reciprocating applications and at cryogenic temperatures.

It is proposed that the coil spring could be the most suited stiffener for the cryogenic applications, high-pressure and reciprocating pistons, followed by helical, cantilever heavy duty and finally the cantilever springs.

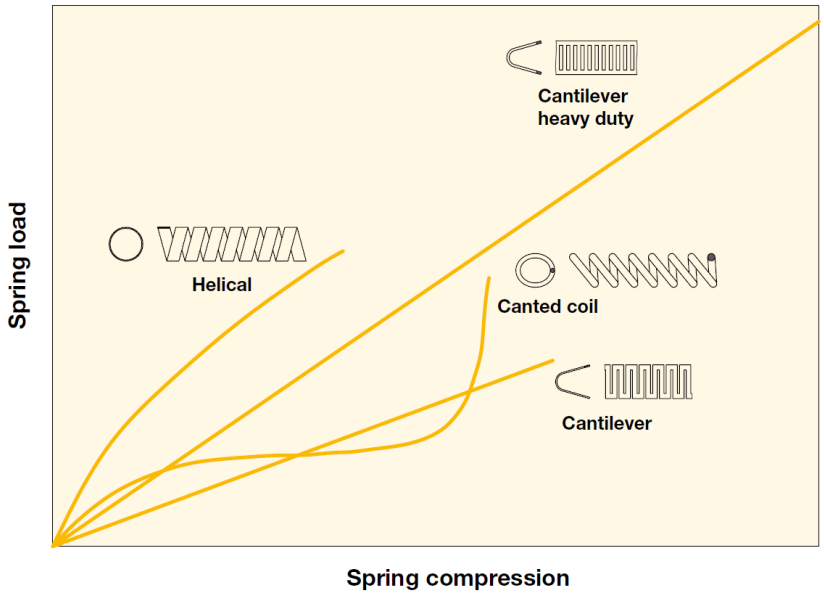

Figure 5-5: Load-deflection Curves of the Spring [93]

The Parker PTFE seal design guide was further used to evaluate the pressure and surface speed limitations. Seals with a similar design as seen in Figure 5-2 (on the left) with loaded helical spring are certified for use at pressures of ≤ 55MPa (550bar), surface speeds of ≤ 15m/s and temperatures as low as -260°C [93]. The same seal design but with a cantilever spring are also suitable for cryogenic temperatures but operating pressures and surface speeds are ≤20MPa and ≤5m/s respectively [93].

For tests on the cryogenic compatibility of the Mark II, the seals were stiffened by the cantilever and canted coil springs. The canted coil springs were the preferred option but were expensive at a price tag of £568.02 for 5 seals and a lead time of over 6 weeks. The cantilever seals offered a much cheaper option at a price of £64.03 for 2 seals with a lead time of 2-3weeks. Due to significant cost difference and the shorter lead time, the cheaper option was explored first. The sealing filter material was 25% carbon and 75% PTFE.

5.2.3 Reed Valves

The mark I pump successfully demonstrated that reed valves can operate at high speed and can produce the required flow rates. The Mark II was then used to verify valve feasibility under full operating conditions which include: cryogenic and oxidising liquids, high pressures, high flow rates and high speeds. To keep the manufacturing process as simple as possible valves were made from aluminium alloy 6082-T6, whose properties are similar to 6061-T6 (Table 2-1) but it is more widely available. 0.5mm thick stainless steel 316L shims were in stock and to minimise the manufacturing cost, petals were made from them. Stainless steel is also more ductile than aluminium alloys.

It was previously estimated that to produce an average pressure of 30bar in a triplex configuration, the pump must deliver a maximum pressure of 33bar. To ensure the valve design could withstand these pressures, FEA analyses were carried out. As shown in Figure 5-6 and Figure 5-7, two separate FEA studies were carried out for both base and petal. For more details of how loads were applied, refer to **Appendix I: Mark II – FEA Analysis** (pg.176). It should be noted that these

simulations were carried out for closed valves. As seen in these figures, the reed valve base has a minimum Factor of Safety (FOS) of 2.61, whereas the petal's minimum FOS is 1.09. In order to minimise pressure losses, the decision was made to retain the passage ways as large as possible, which resulted in a low value of FOS of the petal. A thicker petal could have been used to increase the FOS, but this would have compromised the petal deflection size. Previously, the Mark I demonstrated that some petal plastic deformation is unlikely to affect the performance of the valve, supporting the decision for a low FOS. Furthermore, the petals can be easily modified or replaced if the need arises, whereas valve base modifications are slower and more costly. It should be noted that the properties of the metals were taken at room temperature and at cryogenic temperatures the YS and UTS would increase, which would further increase the FOS. This further supports the acceptance of the lower FOS of the petals, to ensure that any critical failure occurs at the petals, not the base.

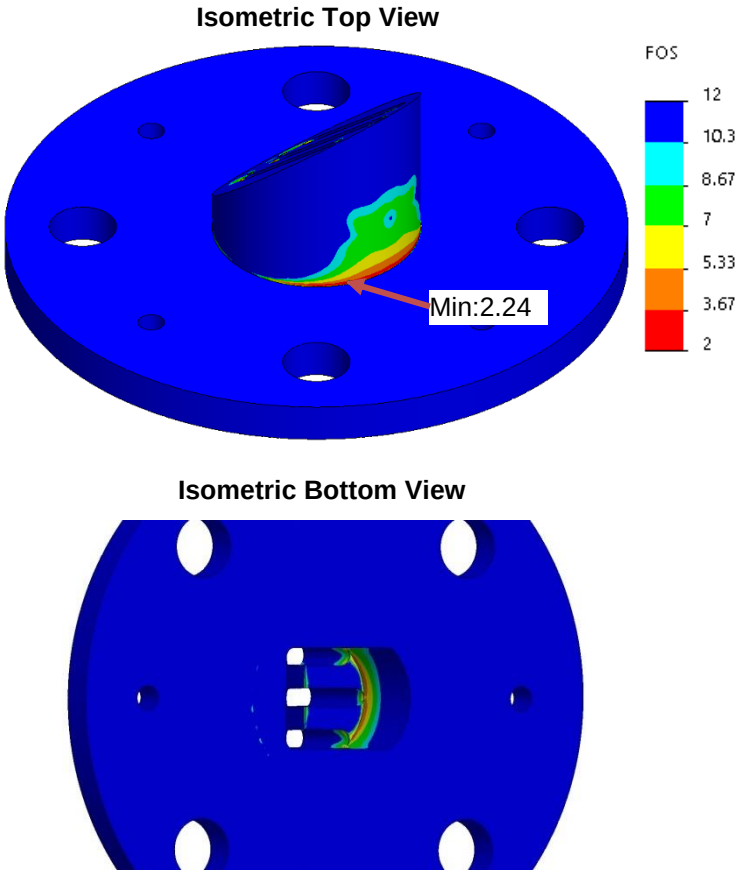

Figure 5-6: FEA Analysis of Valve Base

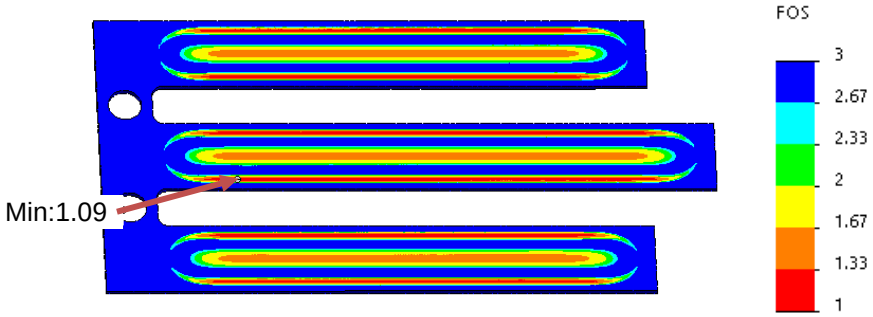

Figure 5-7: FEA Analysis of Valve Petals

5.2.4 Mark II Concept Design & Manufacture

The CAD model of the Mark II with its major components is shown in Figure 5-9 - Figure 5-11. The main pump assembly is made of a piston cylinder, and a piston guide and the remaining sections are constructed from welded flanges and piping. To construct the pump assembly, two methods were considered: 1) machine the desired parts from a block of metal such as aluminium or 2) use prefabricated flanges and pipes to weld to the desired sizes. The first option would require substantially more time to machine the parts, and due to limited workshop availability, it was not possible to complete within the given PhD time constraints, therefore prefabricated parts were bought. To match the CTE of the aluminium valves, it was considered to use flanges and pipes made from aluminium, but these aluminium components are not readily available, whereas SS316L alloy parts are widely used in the food industry. The difference of the CTE between aluminium and stainless steel is approximately 7.6µm/(m °C). Given that the flange thickness is 10mm at -200°C aluminium will shrink 0.175µm more than stainless steel. Provided that suitable face seals are used this shrinkage will not cause any significant issues, therefore the main pump body was constructed from SS316 while the valves were made from aluminium. The CAD drawings of the Mark II pump can be found in **Appendix J: Mark II – Drawings** (pg.180).

To ensure the system is leakproof, grooves for the static PTFE seals in the flanges and the sensor adapters were machined. As shown in Figure 5-11, the inlet and outlet valves were orientated by 180° to streamline the flow. A 5mm milling cutter was used to machine the slots which had a maximum depth of approximately 40mm.

To reduce the risk of critical failure, a further FEA was carried out to ensure that the pump can withstand the operating pressures. The tee section (Figure 5-11, circled in blue) is the weakest point of the structure due to its geometry, therefore the SolidWorks FEA was performed on this section. This section has a minimum FOS of 2 (at room temperature), as shown in Figure 5-8. For more details how loads were applied, refer to **Appendix I: Mark II – FEA Analysis**, **c Tee Section**.

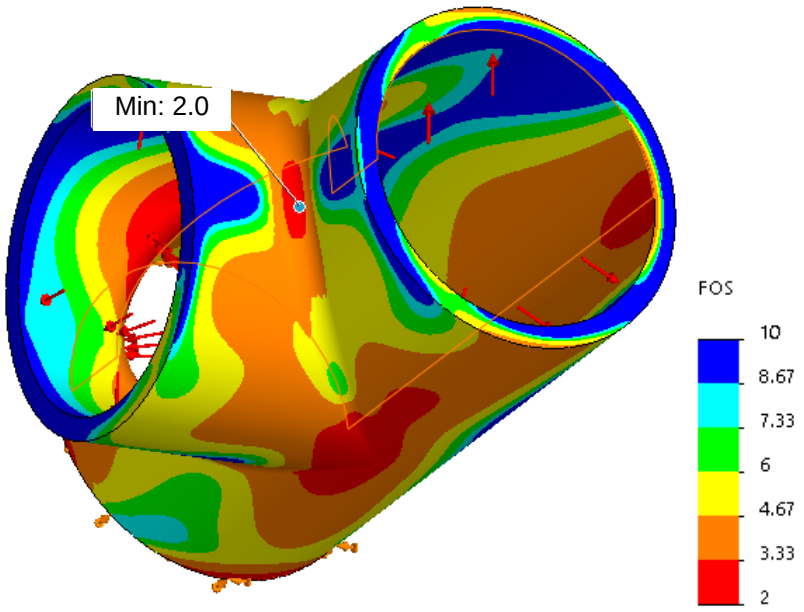

Figure 5-8: FOS of Tee Section

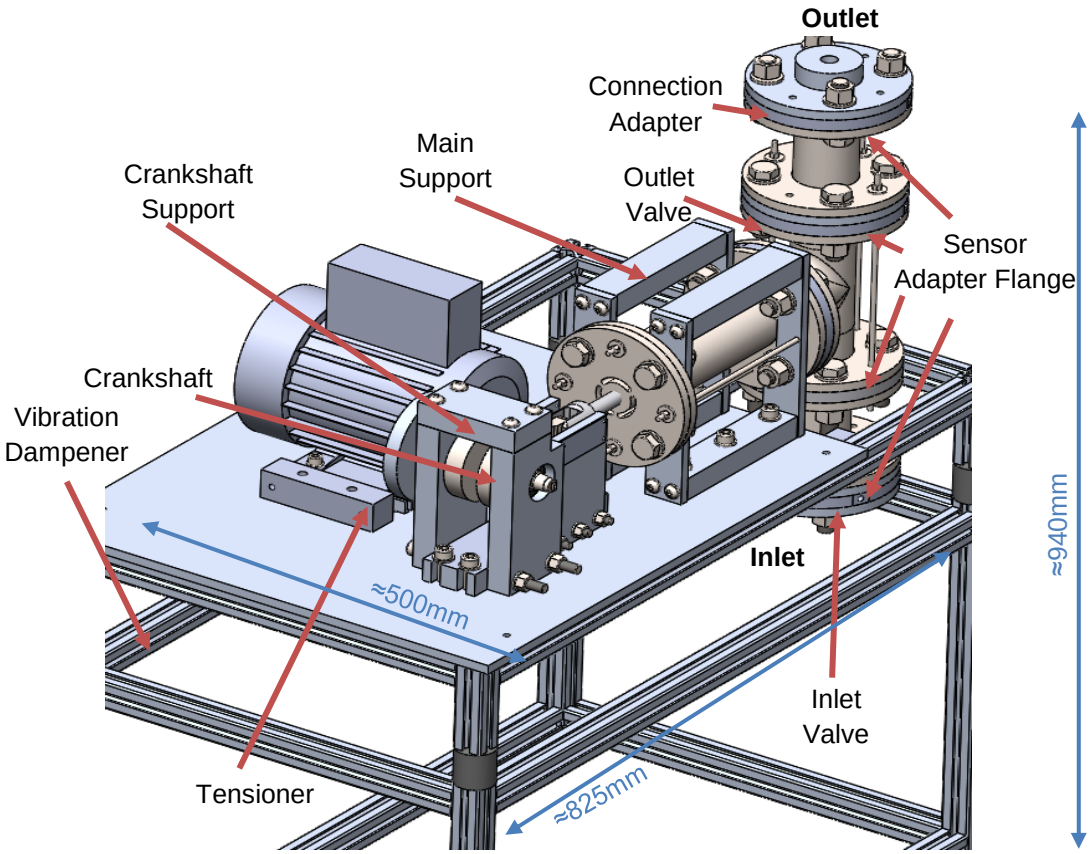

Figure 5-9: Mark II CAD Model – Isometric View

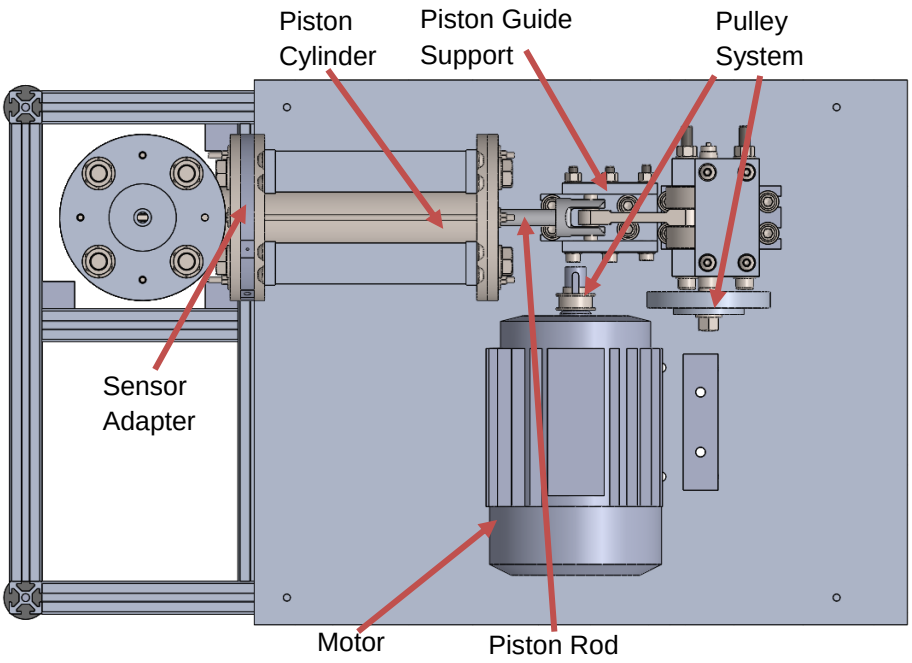

Figure 5-10: Mark II CAD Model – Top View

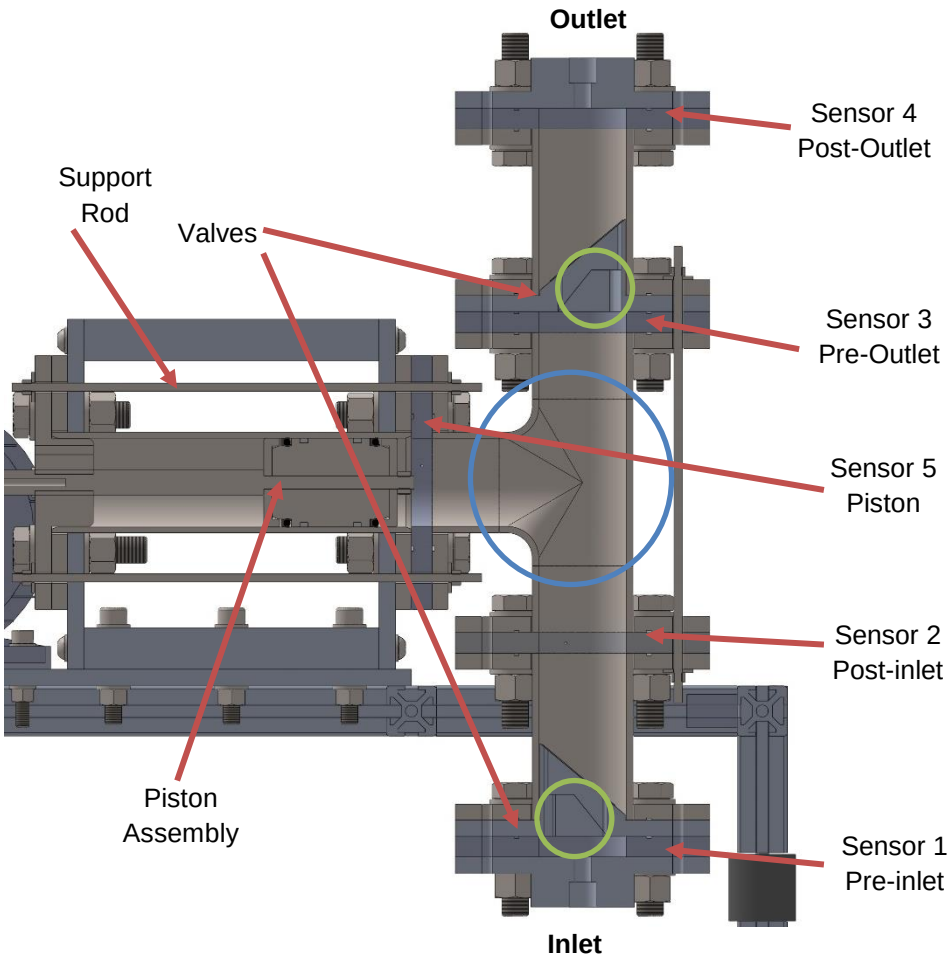

Figure 5-11: Mark II CAD Model – Section View

To determine the variation of the pressure fluctuation across various sections of the pump, five To determine the variation of the pressure fluctuation across various sections of the pump, five sensor flanges were installed: pre-inlet valve, post-inlet valve, pre-outlet valve, post-outlet valve and at the piston cylinder as shown in Figure 5-11. Data from the pressure sensor at the pre-inlet valve can be used to determine the minimum inlet pressure requirements and combined with the sensor at the post-inlet, the pressure drop across the valve can be calculated. Similarly, the pressure sensor at the post-outlet valve can be used to determine the output pressure and the pressure drop. While conducting experiments with the Mark I pump, cavitation was observed near the piston, as indicated by sensor 5 in Figure 5-11. To determine the pressure loss due to the reciprocating motion of the piston, the sensor flange was added to the bore. The flanges were also modified to house thermocouples which were used to monitor the temperature in the pump. The connecting adapters were then installed to allow the cryogenic tank to be connected via the hose and to control the outlet flow direction.

To minimise leakage and to reduce wear and tear of the reciprocating seals, the piston cylinder was honed with a fine polish stone. Using this process the surface finish (Roughness Average (RA)) of 0.1µm or better can be achieved which is required by a seal requirement. After honing, the internal diameter of the bore was verified using the CMM and other parameters, such as roundness and roughness, using Cylindricity Measuring Instrument and Mitutoyo SurftestSJ-400 surface finish tool. The following measurements were obtained these instruments:

- Bore Diameter: 53.36mm
- Maximum Roundness error: 48.762µm
- Surface Finish Ra: 0.04µm

The metrology data is attached in **Appendix K: Mark II – CMM, Roundness & Surface Finish > a: Piston Bore with no Flanges**. To give confidence in the results, several readings were taken. The maximum roundness error was much more significant than initially expected, but the initial water tests did not indicate any issues with leakage.

As seen in Figure 5-11 or shown in drawing Figure J-9 (pg.188),

To allow the seals and a guide ring to be fitted, the piston was divided into several segments as shown in Figure 5-12. The orientation was installed as shown in this figure, which was based on the illustration provided by the SKF [95].

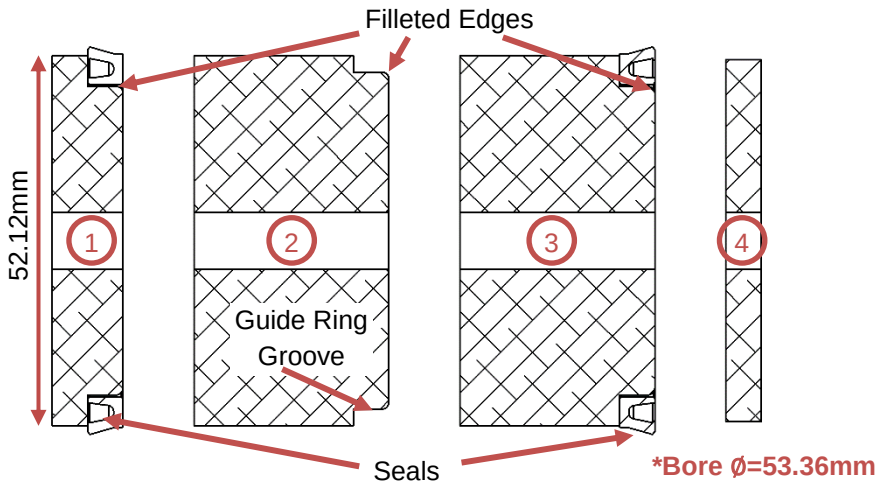

Figure 5-12: Section View of Aluminium Piston

The Mark I experiments showed that the highest volumetric efficiencies were achieved at the shortest stroke length, therefore a crankshaft with a stroke of 30mm was sought. Unfortunately, it was not possible to find an off-the-shelf crankshaft with the desired stroke, but the KTM 65 SX crankshaft offered the next closest match at a stroke length of 40.8mm [96]. To manufacture a custom-made crankshaft can lead to a cost of over £500 with at least 4 weeks lead time. Mark I tests at 45mm did not indicate any significant decrease in efficiency or issues with sealing, therefore the KTM 65 SX crankshaft was used to reduce the costs and manufacturing time.

For the initial test, a 1hp Clarke Motor was installed to validate the cryogenic compatibility. At this stage of the project, it was not possible to calculate the operating power requirements as it was unclear how much resistance the seals would cause. To control the operational speed of the pump, the motor and crankshaft were connected via the gears and belt system.

5.3 Initial Trials

The setup of the initial trials is shown in Figure 5-13. The system was equipped with a single Swagelok 0-100bar pressure transducer on the outlet side and to measure the change in current a WinDaq DI-1100 Data Acquisition Unit (DAU) was used. Other components such as inlet and outlet containers, a DC power supply and a computer which ran WinDaq software to record the pressure output were also incorporated into the Mark II. The DAU system is capable of sampling the data at 20kHz when all 4 channels are enabled, meaning that up to 1,200 points can be obtained in one cycle at 1,000 RPM. For the details of how the transducer was set up and calibrated, refer to **Appendix L: WinDaq & Thermocouple Sensor Setup** (pg.210).

The reciprocating piston seals for the Mark I were sourced through SEALCO which proved to be very successful. Hence, the same company was used to make the custom seals, as shown in Figure 5-14. The full drawing of these seals can be found in **Appendix M: Mark II – Seals,** Figure M-1 (pg.216). The Jacket was made from 25% carbon, 75% PTFE, and the stiffener from Stainless Steel 316. The diameters at point A and B measured 52.73mm and 54.3mm respectively. The piston bore diameter was 53.36mm therefore the fitted seals were compressed which loaded the stiffener.

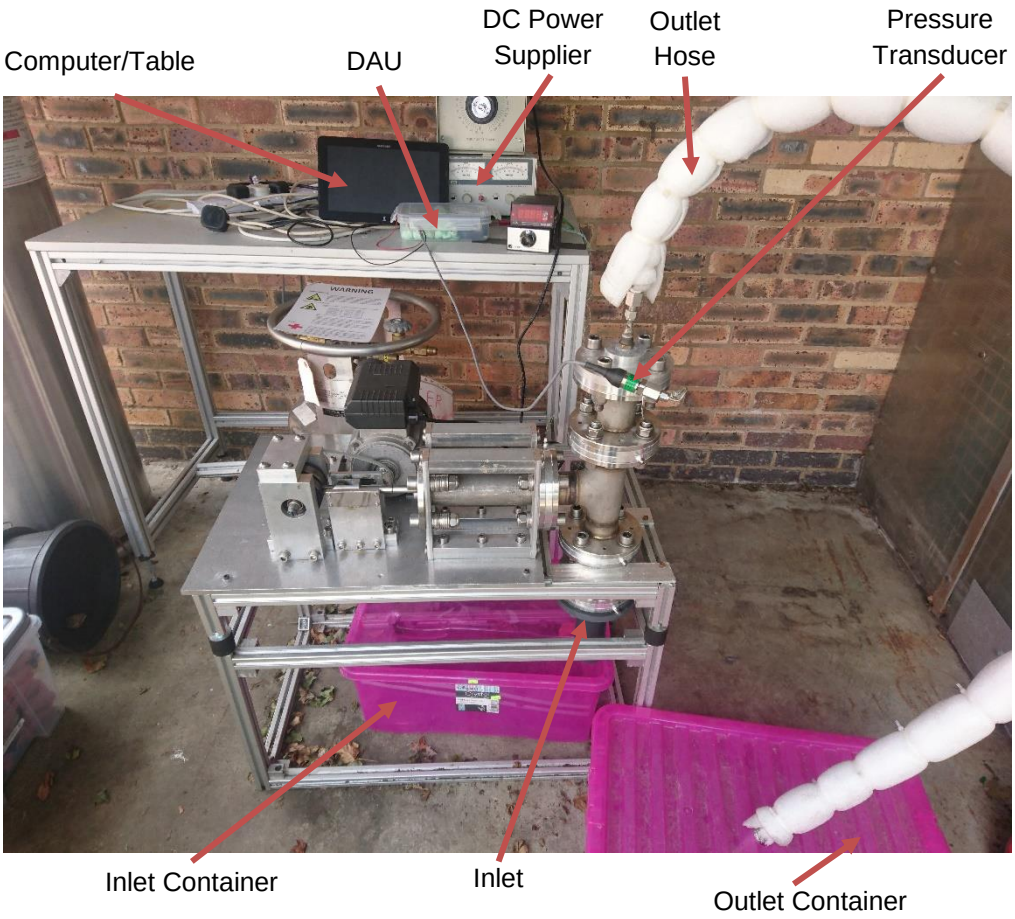

Figure 5-13: Mark II Pressure Testing with Water

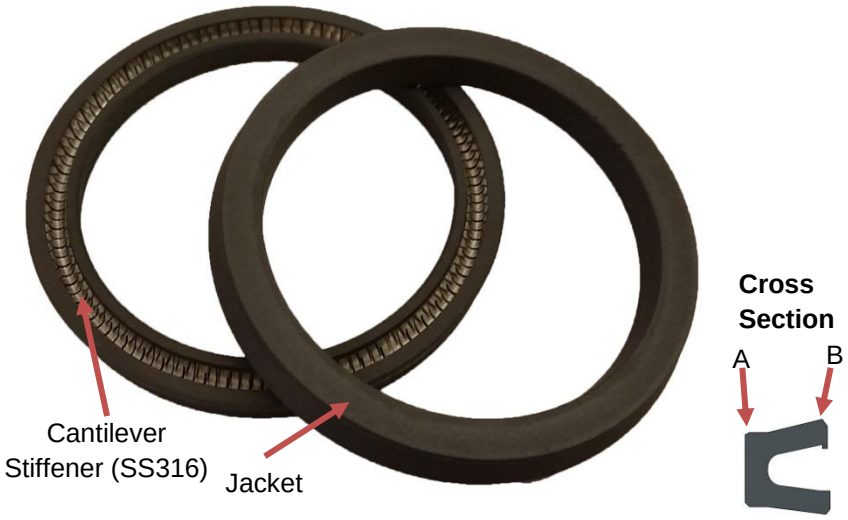

Figure 5-14: Reciprocating Seals – Cantilever Stiffener 25% Carbon & 75% PTFE

For the initial trials water was used as the working fluid to ensure the test results are consistent with the Mark I. For consistency, the same techniques and equipment were used in calculating the average flow rate and duration. It should be noted that the tests were carried out at an average speed of ≈370RPM. The outlet diameter of the outlet hose was reduced from ≈53mm to ≈10mm to increase the system pressure. To increase the result accuracy, the water temperature was recorded to account for density changes. The pump operating speeds varied from 360RPM to 395RPM. As shown in Figure 5-15, the pump efficiency fluctuated from 125% to 135% for most of

the tests, but in some cases it was as low as 120% and as high as 143%. As explained in the previous chapter, the volumetric efficiency exceeds 100% due to the momentum of the fluid. The pulsating motion in the outlet hose detached the pipe on several occasions, which consequently led to a lower pump volumetric efficiency, hence there were some inaccuracies when measuring weight.

Nonetheless, the Mark II prototype produced similar volumetric efficiencies as the Mark I, even at much lower speeds. Assuming the minimum volumetric efficiency of 120% is maintained at 1,000RPM, the pump would deliver 1.81kg/s of water. Furthermore, supposing the volume displaced by the piston of a full-scale pump can be scaled down with a linear correlation, this would set a target of ≈1.4kg/s for the Mark II at 1,000RPM. Given the current results, this should be possible to achieve, but a further test must be carried out to verify if the same results can be achieved at an outlet pressure of 30bar.

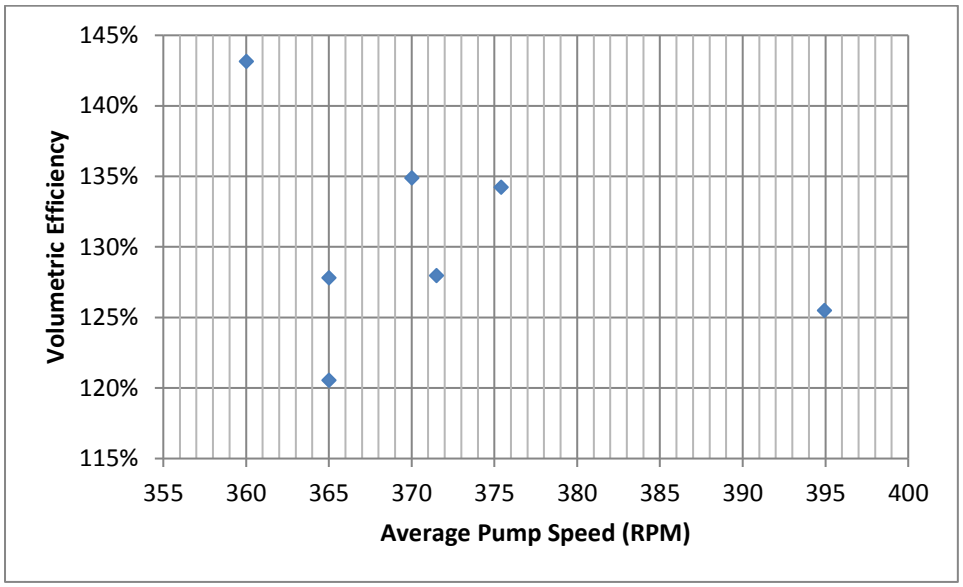

Figure 5-15: Volumetric Efficiency vs Average Pump Speed

In the next test, the instantaneous pressure was measured, and the key parameters were summarised in Table 5-3. The sampling rate was set by the user, while the remaining parameters were obtained from the output data. Data from WinDaq, were saved as an Excel file (.xlsx) in order to calculate the average pressure and to illustrate the results on the graph, as shown in Figure 5-16.

Table 5-3: Summary Table of Water Pressure Test 1

Sampling rate	100Hz
Test Duration	≈6.66s
Max Pressure	8.23bar
Average Pressure (P_{av})	1.85bar
Average Operation Speed	≈300RPM

It was expected to see pressure peaks of a similar magnitude, but they varied from around 5bar to just over 8bar. This does not include the first peak, as the lower value could have resulted by the piston being accelerated to the operating speed, and therefore this is a transient value. Furthermore, the graph did not follow a sinusoidal pattern as theoretically approximated in **Chapter**

4, section **4.3.3 Dynamics**. After the test, the tooth on the timing belt wore away which resulted in a variation of the maximum pressure. The worn tooth prevented an adequate grip, causing the belt to slip, hence resulting in lower peak values. After approximately 6.66s into test, the belt completely failed.

The current evidence shows that pressure changes are more sudden than they were theoretically approximated. This led to the average pressure being 5.67 times lower than the peak pressure value. In the spreadsheet for calculating the pump dynamics, outlined in **Appendix D: Dynamics – Graphs**, known parameters, such as operating speed and maximum pressure were substituted to estimate theoretical average pressure (Figure 5-17).The average theoretical pressure was estimated to be 2.6bar, but taking into consideration irregularities in the pressure due to the worn timing belt, lower average pressures were expected.

The data in Figure 5-16, can also be used to evaluate the sealing performance of the petal valves. As the graph shows, some minima points drop below zero (below atmospheric pressure), indicating that some leakage occurs during the suction cycle, which again was expected due to poor valve sealing performance. It can also support the hypothesis that at delivery both valves are opened momentarily which could explain the >100% volumetric efficiency.

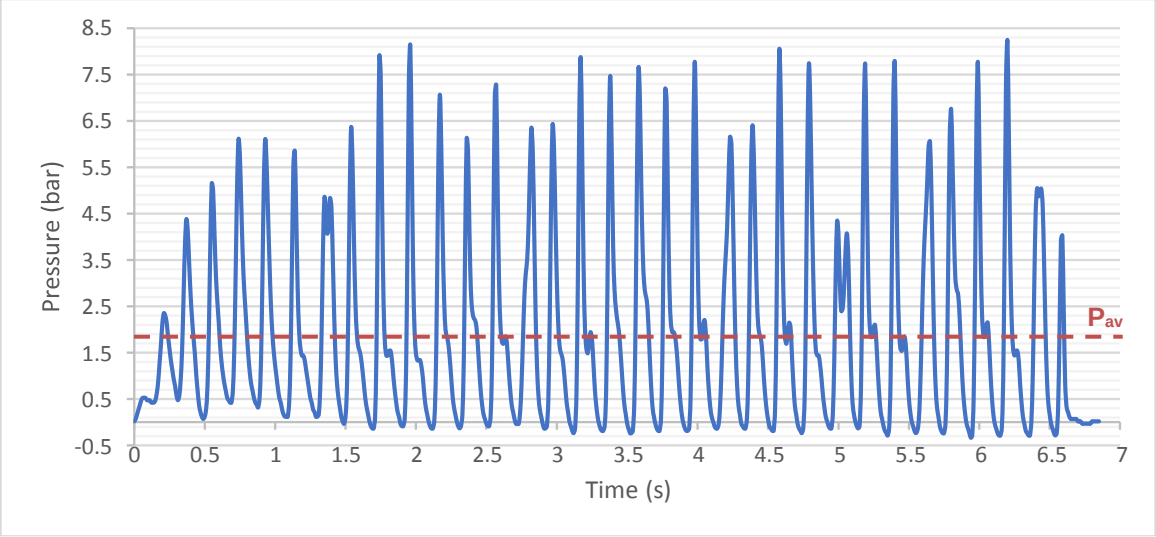

Figure 5-16: Water Pressure Test 1

l	0.088	m	v_max	0.478	m/s
r	0.015	m	v_min	-0.478	m/s
RPM_pist	300		A_max	279	deg
ω_piston	31.41593	rad/s	A_min	81	deg
m_piston	0.5	kg	P	8.23	bar
D_pisotn	0.03	m	P/v_max	17.21657	
A_piston	0.000707	m^2			
			P_av/cycle	2.6	bar

Figure 5-17: Average Theoretical Pressure for Data from Table 5-3 for the Simplex Pump

Previously it was identified that to achieved desired flow rates and to keep the pulsation at the minimum, triplex pump configuration will have to be used. The data in Figure 5-16 were used to calculate theoretical pressure fluctuation for triplex pump and plotted in Figure 5-19. As shown in Figure 5-18 two identical plots (as seen in Figure 5-16) were added on the same diagram and offset by 120° and 240° respectively. These graphs were then combined to give theoretical flow variation of triplex pump (Figure 5-19). In these estimates the worst case was assumed, meaning flow cannot be delivered unless pressure in the cylinder is equal or greater than outlet pressure. As all cylinders discharge in the same chamber, pressure of each cylinder was calculated at a given time and the largest value was selected as outlet pressure. However, as stated in Chapter 2, displacement pumps do not have a shut-off head, thus flow rate of incompressible would be produced fluid regardless of the outlet pressure. Based on Bernoulli Equation 2-5, a higher flow rate would consequently lead to a greater outlet pressure. To better understand how pressure head could be affected, a triplex pump will have to be built and tested.

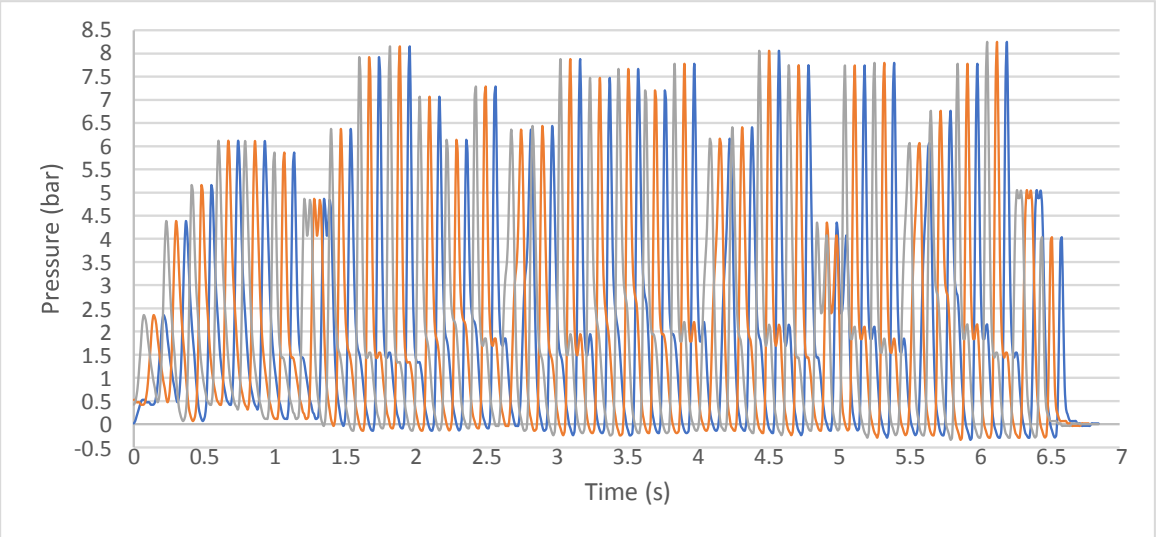

Figure 5-18: Water Pressure Test 1 – Offset Values

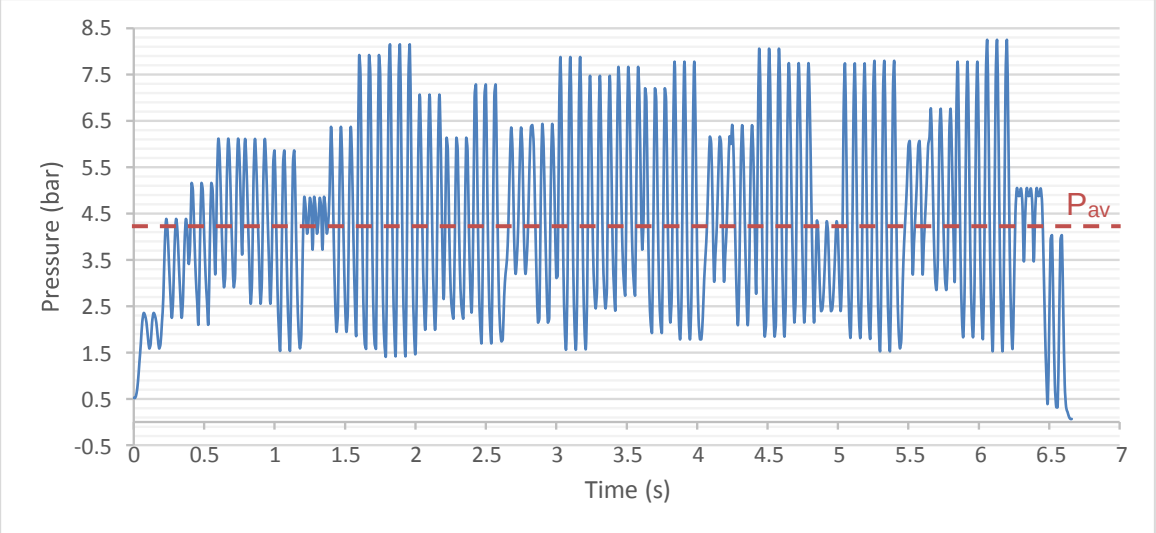

Figure 5-19: Water Pressure Test 1 – Estimated Triplex Values

Due to excessive wear of the timing belt, the system would have to be replaced with a geared system. But before implementing these changes, the cryogenic compatibility was assessed. As

shown in Figure 5-20, insulation was not used, as the aim was to identify the immediate issues during the chilling process. The only difference in the setup was that the water tank was replaced with Liquid Nitrogen (LN_2) dewar. LN_2 was used to cool the pump, as unlike LOX, it does not pose a fire risk. Initial trials identified issues with the piston cylinder seals as shown in Figure 5-20. The leakages were fixed by shortening the main supports (refer to Figure 5-9) by 1mm to allow a tighter connection.

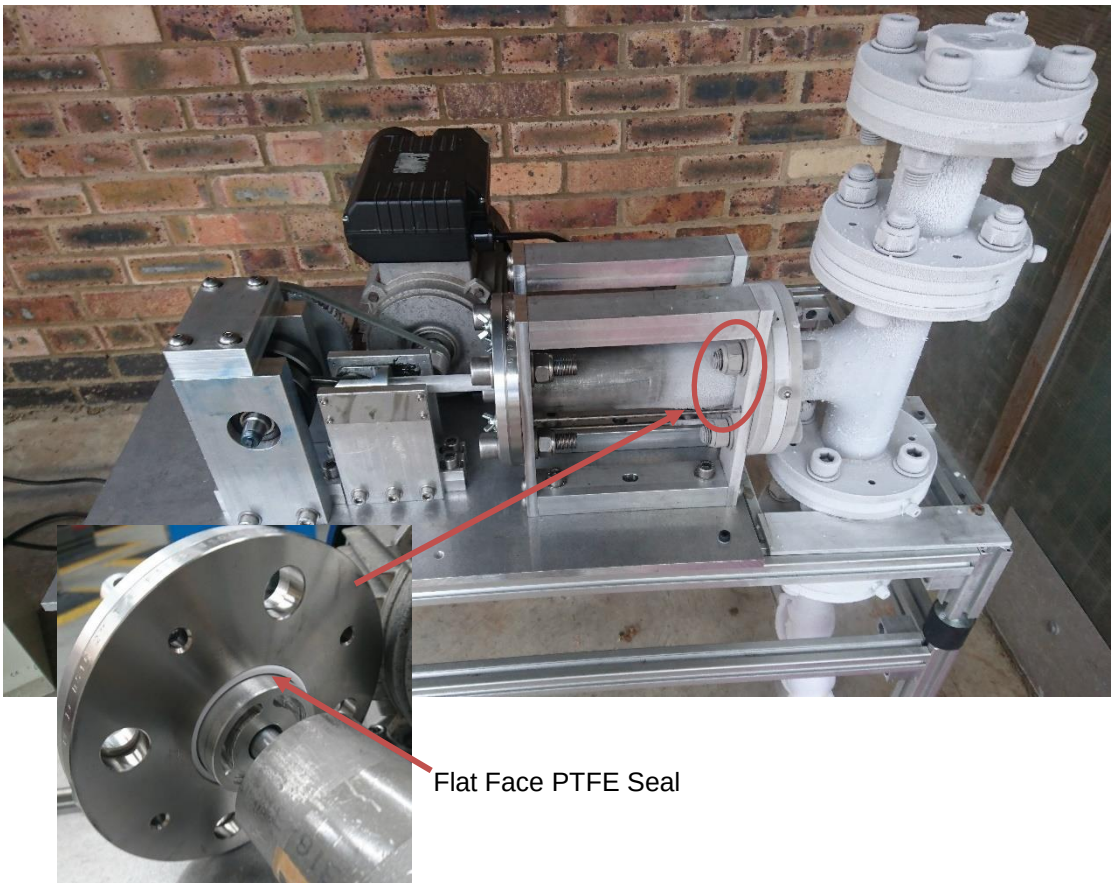

Figure 5-20: Mark II Initial Cryogenic Test

5.4 LN_2 Trials with Cantilever Stiffened Seals

To reduce heat absorption from the atmosphere, the pump was insulated and K-type thermocouples were fitted to all sensor flanges (refer to Figure 5-11) to monitor the temperature change at various parts of the pump. The new setup is shown in Figure 5-21. It should be noted that the thermocouple was inserted 4.5mm from the inside wall (i.e. 4.5mm of metal separating the thermocouple from the flow). Prior to commencing with the tests the components were kept in an oven at 60°C for over 8 hours to remove any water vapour. To prevent freezing during the trials, the pump was switched on for a short interval.

For further reference, LN_2 in the dewar was pressurised to approximately 1.3 bar with a maximum capacity 25l. The LN_2 tank was connected to the pump via the inlet hose. While cooling down, the flow rates were controlled using the outlet valve to maximise heat absorption by nitrogen.

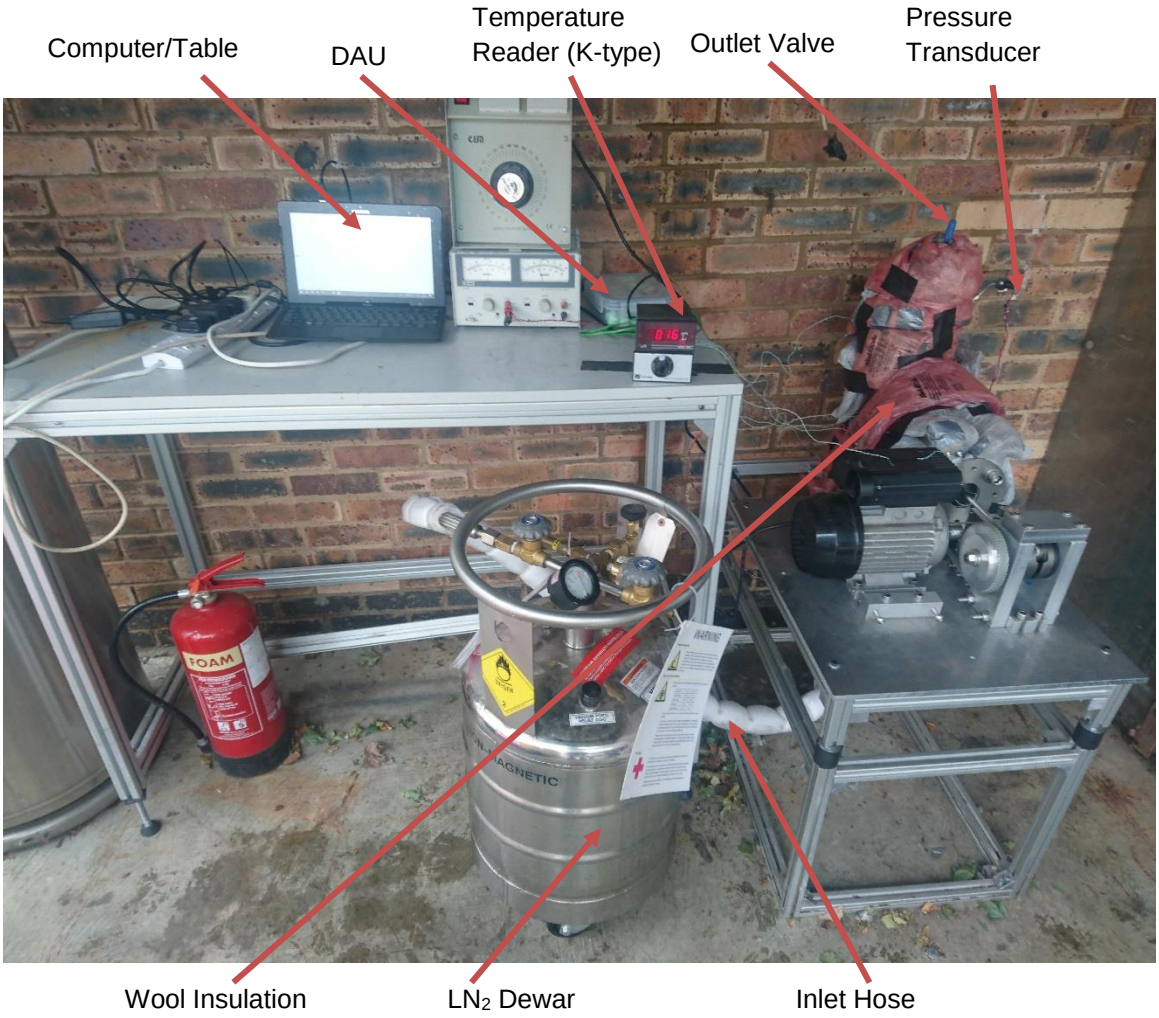

Figure 5-21: Fully Insulated Mark II with DAU System

The aim of these tests was conduct further compatibility trials with cryogenic liquids. The experiments showed that poor flow circulation in the piston cylinder led this section to cool very slowly. It was further observed that thermocouple sensors did not record temperatures lower than -154°C (the target was -196°C) and there could be several factors that might have influenced the lower readings. 1) While K-type thermocouples can in theory measure as low as -270°C, the reader itself may have had a temperature range limitation [97]. Nonetheless, the thermocouples may not

have been sensitive below -154°C. 2) As previously described, the hole for installing a thermocouple was drilled 4.5mm away from the inner wall. There would be some heat transfer between LN_2 and the wall, hence the thermocouple could never record directly the temperature of LN_2 due to a thermal gradient. In addition, the distance between the thermocouple and the wall might have varied slightly, which could further have reduced the accuracy of the result. It was noted that the components which were cooled down to contain LN_2 recorded temperature ranges between -150°C. and -154°C which were quite consistent.

Cantilever stiffened Carbon PTFE seals performed adequately with water, however they were unable to retain a tight seal at cryogenic temperatures, as shown in Figure 5-22. At this point, sensors 1, 2, 3, 4 and 5, measured temperatures of -151°C, -151°C, -133°C, -79°C and -50°C respectively (refer to Figure 5-11, pg.97 for sensor locations). Other factors as listed below could have contributed to the leakage and were investigated further:

- Ice formation on the sealing face of the cylinder
- Seal wear and tear
- Piston design
- Material of the piston

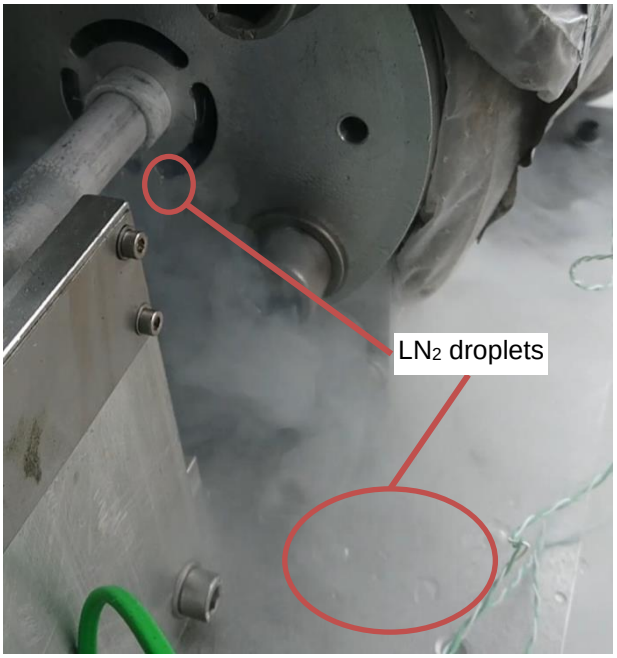

Figure 5-22: LN_2 Leakage – Test 1

Before it can be concluded that these seals were not compatible with cryogenic fluids, some modifications to the rig were made to eliminate other causes that could have contributed to the leakage. Firstly, a plastic liner, as shown in Figure 5-23 was installed, to minimise contact with the airborne water vapour in atmosphere, thus reducing icing on the piston cylinder. To match the CTE of the piston cylinder, the piston was made from SS316L alloy. The piston diameter was also increased from 52.12mm to 52.6mm to reduce the gap between the piston and piston cylinder which consequently minimised the contact area between LN_2 and the seals. In the next tests, the seal groove diameter was increased from 42.5mm to 43.2mm and groove width reduced from 5.5mm to 5mm to preload the cantilever stiffener. Moreover, to acquire a more accurate

temperature reading of the piston temperature, a piston thermocouple was added, as shown in Figure 5-24. For the last option new seals with the maximum outer diameter of 55.53mm were installed. At ΔT = 220°C the seal should theoretically not shrink to a diameter less than ≈53.81mm. This contracted diameter was larger by ≈0.73mm than the contracted piston cylinder diameter.

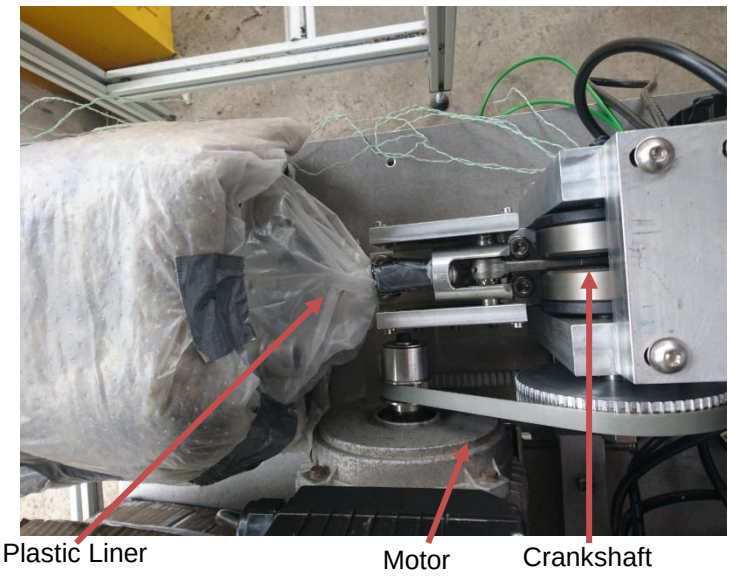

Figure 5-23: Piston Cylinder Isolated with a Plastic Liner

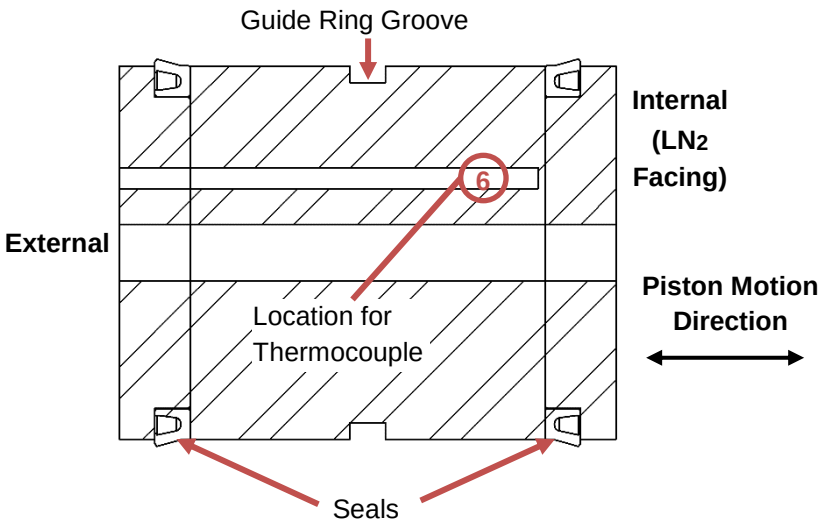

Figure 5-24: Section View of Stainless Steel Piston with a Thermocouple – Sensor 6

None of these changes mitigated issues with the shrinkage, thus it was concluded that the piston design or ice formation was not the primary cause of the leakage. The temperatures at which leakage appeared for each test are shown in Table 5-4. Some evidence, as shown in Figure 5-25 suggests that wear and tear of the seals could have contributed to the seal failure. While this had some influence on the leakage, evidence in Table 5-5 suggests that the primary reason of failure is due to the seals shrinking at a higher rate than the piston cylinder. For this experiment, the piston remained stationary most of the time to minimise wear on the seals. It is evident that the power requirements to move the piston declined as the temperature decreased. Furthermore, the

indication of chamber pressure drop at - 199°C suggests that seals had already failed as the pressure in the system had dropped.

Table 5-4: Temperature Summary Table for Tests 2-4

	Lowest Temperature of Thermocouple before leak (°C)					
	1	**2**	**3**	**4**	**5**	**6**
Test 2	-154	-154	-92	-68	-48	N/A
Test 3	-152	-151	-145	-90	-65	-119
Test 4	-151	-153	-127	-97	-69	-127

Refer to Figure 5-11 for sensor 1-5 positions & for sensor 6 position to Figure 5-24

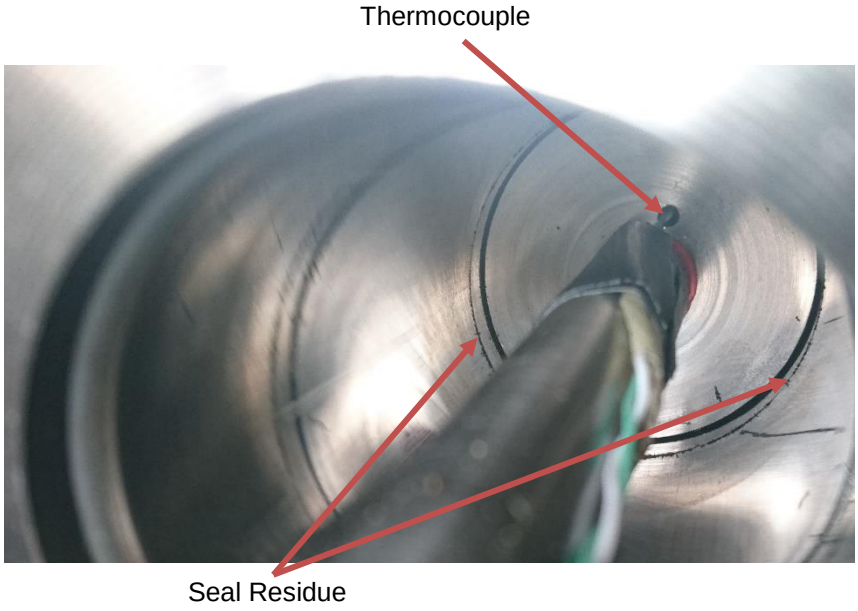

Figure 5-25: Seal Residue – Test 3

Table 5-5: Piston Power requirements – Test 3

Power	Chamber Pressure	Piston Temperature
560W	0.83 bar	13°C
280W	0.83 bar	-98°C
140W	0.57 bar	-119°C

5.5 Cryogenic Tests – Coil Energised Stiffener Seals

5.5.1 Changes to The Setup

To mitigate issues with the shrinkage of the seals, professional help was sought from a cryogenic seal specialist – Saint-Gobain. This company has a proven track record for designing and manufacturing seals for rocket turbopumps and other space applications. A new set of seals was designed based on the following criteria:

- Max 50bar pressure – the maximum pressure Saint-Gobain can design for.
- Maximum Piston Velocity 2.2m/s – calculated from Equations 4-5 to 4-8.
- Bore Surface Hardness 79HRB (Rockwell B Hardness) – SS316L hardness.
- Life expectancy 30min – expected total test life.
- Operating temperature -196°C – Temperature of LN_2.

The Saint-Gobain seals are illustrated in Figure 5-26 and a full drawing can be found in **Appendices**, Figure M-3 (pg.218). The sealing jacket is made from Fluoroloy® A12 and coil stiffener from cobalt nickel alloy. Nickel alloy has a lower CTE than SS316L which further influenced the success of this seal [98]. Fluoroloy® A12 material was developed by Saint-Gobain which is made from a polymer filled with the PTFE and designed for operating temperatures as low as -210°C [99]. This material has a low friction coefficient (0.09) and excellent wear resistance, therefore it is excellent for dry running applications against soft surfaces, such as untreated SS316L [99]. It is also described as excellent for reciprocating applications [99].

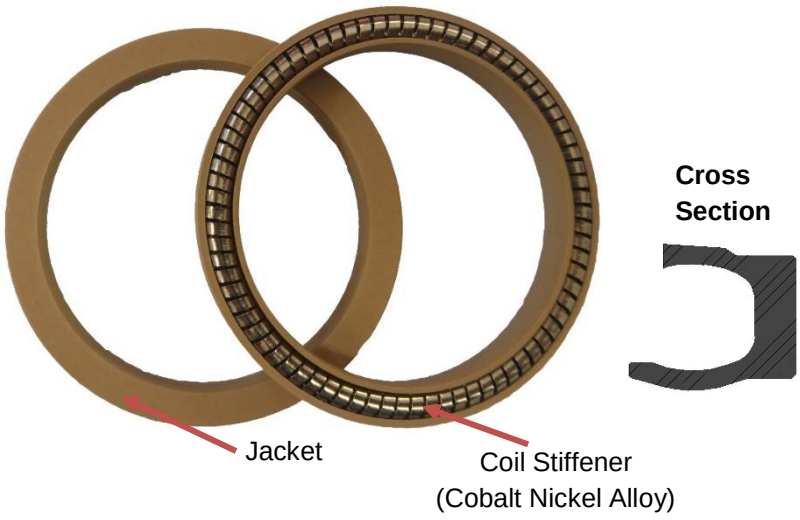

Figure 5-26: Saint-Gobain with a Coil Energised Stiffener

To comply with the new seal configuration and guidelines, a new piston was designed and built, as shown in Figure 5-27. Furthermore, to minimise the contact area between the LN_2 and the seals a <0.05mm gap between the piston and piston cylinder was maintained.

To mitigate the roundness inaccuracies of the piston cylinder, a new cylinder was made. Flanges were welded on the cylinder to allow it to be clamped during the honing process. This reduced

stress created on the actual piston cylinder and contributed to a greater roundness accuracy. Surface roughness and diameter were again measured to ensure tolerances were maintained. The following tolerances were achieved:

- Bore Diameter: 5.371mm
- Maximum Roundness error: 4.284µm
- Surface Finish Ra: 0.05µm

The CMM, surface roughness and cylindricity measurement results can be found in **Appendix K: Mark II – CMM, Roundness & Surface Finish > b: Piston Bore with Flanges**.

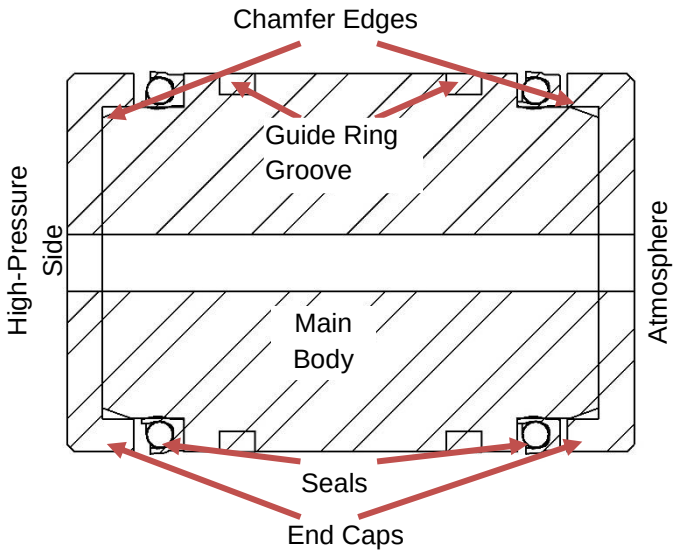

Figure 5-27: Section View of Stainless Steel Piston for Saint-Gobain Seals

To ensure the piston itself met the sealing requirements, the dimensions of the piston body and end caps were verified using a micrometre gauge, and then the same CMM techniques as previously were applied to obtain more accurate readings. These results are shown in **Appendix K: Mark II – CMM, Roundness & Surface Finish > c: Piston Body & Piston End Caps**

During the cooling process, it was noted that the PTFE static seals, installed on the piston cylinder flanges, did not work as effectively as before. Unlike rubber seals, whenever these seals were used, they plastically deform and after re-assembly of the pump, the PTFE (Figure 5-28) no longer adjusted to the new profile, resulting in a poor sealing performance. To rectify this issue, these seals were replaced with nitrile rubber, as shown in Figure 5-29. The nitrile rubber is ductile at room temperature, therefore it will deform to fit each individual face. It is fully understood that rubber becomes brittle at low temperatures, but a failure at cryogenic temperatures was not expected as they were used under static conditions.

Figure 5-28: PTFE Seals (non-reusable)

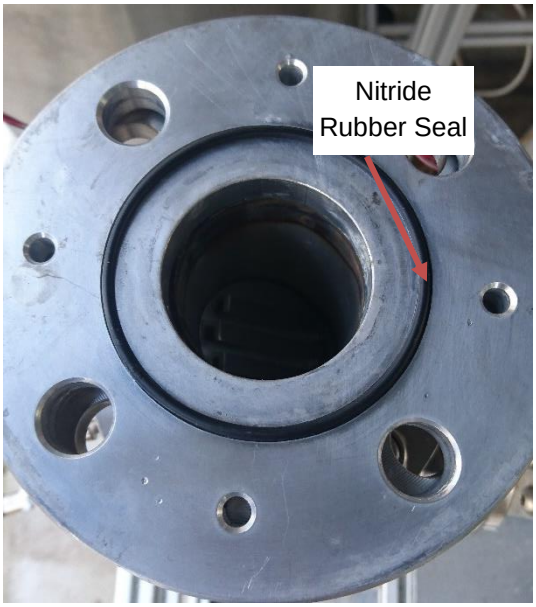

Figure 5-29: Nitrile Rubber Seals

It was further noted that to move the piston required ≈43Nm of torque (a cantilever stiffener required ≈10Nm), but this force varied depending on the piston position. These seals are also based on PTFE, thus it was expected for them to shrink a fraction more than the piston chamber, reducing torque requirements.

To measure the torque, a wrench was attached to the crankshaft and the scales were used to calculate the force required to move the piston. The radius was measured between centres of the crankshaft and scales (see Figure 5-30). This provided sufficient information to calculate the torque using Equation 5-2.

$$\tau = r \times F \tag{5-2}$$

Where: τ – torque (Nm), r – radius and F – force (N)

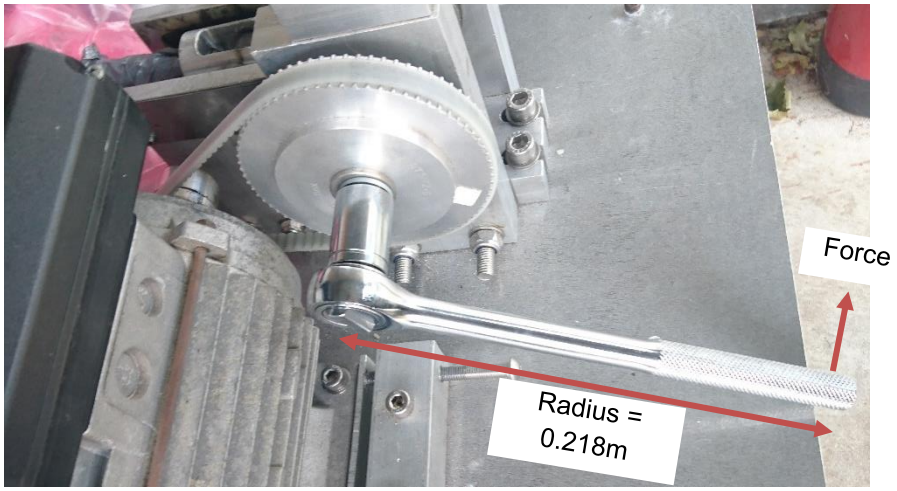

Figure 5-30: Measuring Torque

In further tests, the position of thermocouple 5 was moved from sensor flange 5 and placed directly on the piston cylinder, as shown in Figure 5-31. Thermocouple 6 also was attached to the back of the cylinder (the uncooled side). Attaching both sensors on the piston provided a more accurate approach for determining the temperature difference between the two sides of the piston.

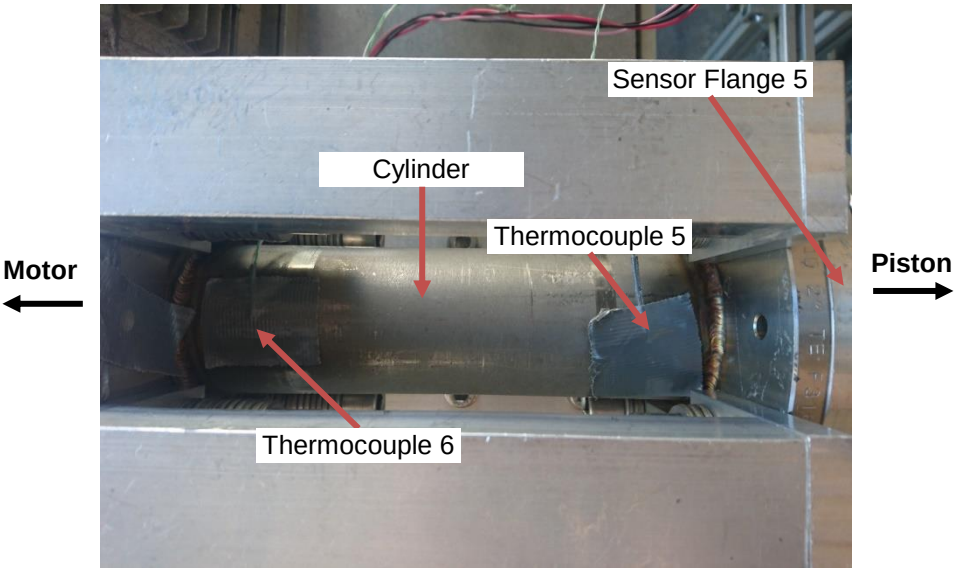

Figure 5-31: Thermocouple Locations – Sensor 5 & 6

Further changes were made to the pump insulation. The piston cylinder was connected to the main aluminium structure and aluminium has a high thermal conductivity, bringing heat to the pump. To minimise the heat absorption, the piston pump was suspended on PTFE blocks as shown in Figure 5-32. The thermal conductivity of the PTFE is 0.25W/(mK), where the thermal conductivity of the aluminium is 205W/(mK), thus this material was chosen [100].

If that failed alternative methods for cooling down the pump were considered, which includes reducing the thermal mass or increasing the LN_2 flow rate. A higher LN_2 flow rate would require fitting the Dewar with a larger diameter hose. It must be said, that if high flow rates, such as those produced in a launch vehicle, are delivered to the pump, cooling down the pump would not be an issue. This is probably why the XCOR pump seemed to have very little insulation when installed in the vehicle (Figure 4-4 pg.52). In addition, the XCOR pump seems to be made from aluminium with a reduced thermal mass. However, none of these changes were necessary.

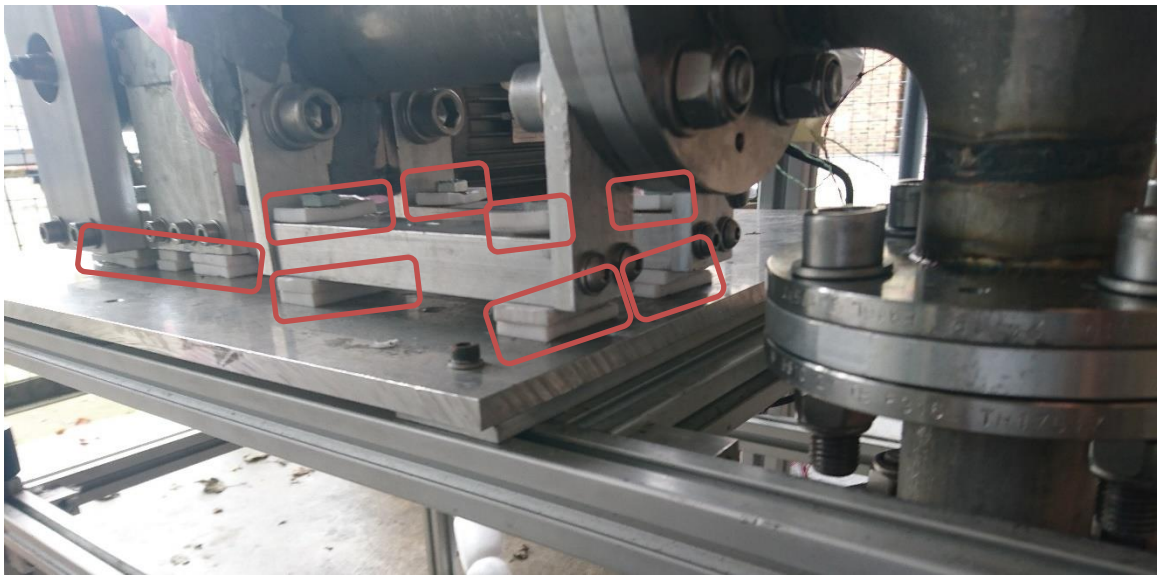

Figure 5-32: Insulated Main Support

5.5.2 Cryogenic Compatibility Tests

The initial test revealed that keeping the gap between the piston and piston cylinder less than 0.05mm, which was recommended by the seal manufacturer, resulted in rubbing at cryogenic temperatures, and was due to partly matched thermal expansion between the parts. As the system grew colder, the stroke distance gradually declined to a point where the piston could no longer be moved. To rectify the issue, the piston diameter was reduced from ≈53.30mm to ≈53.06mm to allow 0.07mm for SS316 contraction and the remaining 0.18mm for misalignment when mounted on the piston. This provided sufficient clearance at cryogenic temperatures and torque requirements to move the piston reduced from 43Nm to 6Nm. Moreover, the increased gap size did not lead to any leakage.

Furthermore, the static nitrile rubber gasket seals sealed much more efficiently than initially was anticipated. In fact, they outperformed the static PTFE seals as no leakage was seen. More efficient seals have contributed to the full LN_2 tank lasting for approximately 10min longer.

Two batches of 25l of LN_2 were used to cool down the piston pump as one full Dewar was not sufficient. The LN_2 refilling station was based on a different campus, consequently this led to a minimum 1-hour delay between cooling cycles. The temperature of the pump was recorded every two minutes and illustrated on the graphs in Figure 5-33 - Figure 5-38. Unlike the previous seal design which failed at a temperature range between -50 and -60°C at Sensor 5 location, the minimum temperatures of -112°C and -140°C on the first and second tests were recorded without any sign of leakage. It can be further noted that the cooling rates of both these tests were much slower as PTFE insulation was not fitted. Moreover, it would have been expected to see a linear correlation between temperature and time, but the flow of LN_2 varied and the pump was switched on and off, which led to a non-linear decline of the temperature. This was particularly noticeable in Figure 5-35 for Sensor 5, when the pump was switched on to check for leaks under dynamic conditions, but no visible leakage was observed.

The temperature data in Figure 5-37 and Figure 5-38 shows that the improvements to the insulation significantly improved the efficiency of the system cooling. In the previous tests, the temperature never went below -140° when cooled for over 120min, however this time the temperatures below - 148°C were reached in just under 65min. It was not expected for Sensor 6 to fall to cryogenic temperatures as it did not interact with LN_2. To confirm that the system was fully primed, the flow rates of LN_2 were increased to a point where a stream of LN_2 was seen leaving the outlet.

For further comparison, temperatures of the second and third tests were recorded to highlight effects of PFTE insulation. It is evident that this insulation has significantly reduced the heat channels, thus the pump cooled down more efficiently.

Table 5-6: Temperature Summary Table for Test 6 & Test 7 – 1st Cooling Cycle

	Thermocouple											
	1		**2**		**3**		**4**		**5**		**6**	
	T	**t**	**T**	**t**	**T**	**t**	**T**	**t**	**T**	**t**	**T**	**t**
Test 2	-151	23	-151	33	-151	62	-128	85	-130	56	-32	78

Test 3	-151	14	-151	20	-150	38	-152	46	-147	46	-147	-56

*T = Temperature (°C); t = time (min)

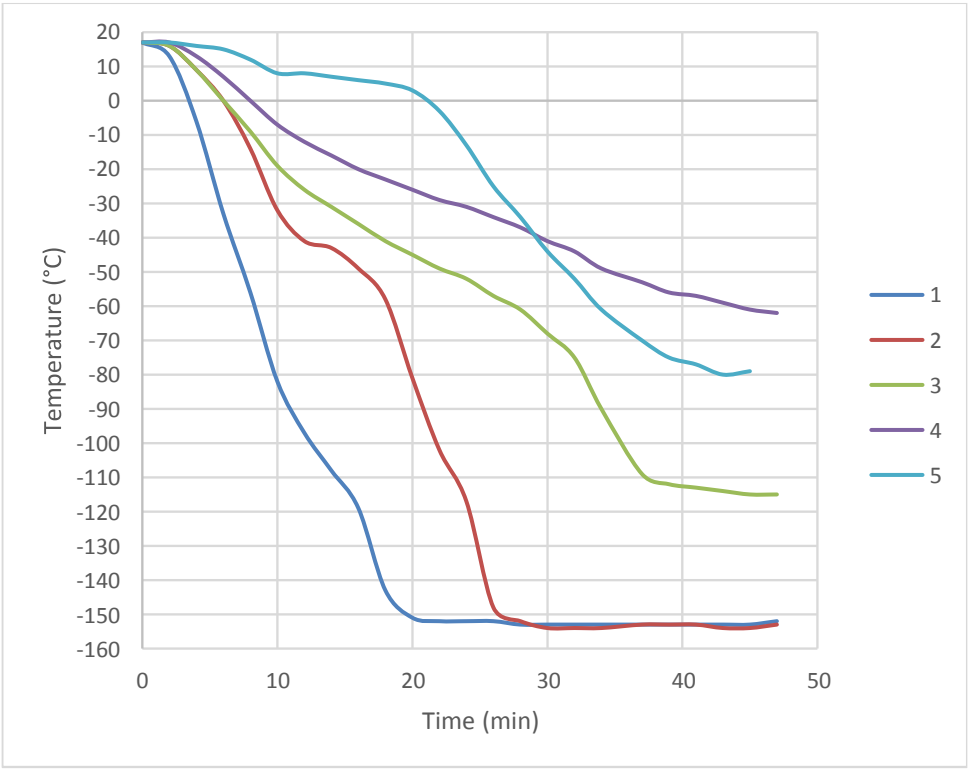

Figure 5-33: 1st Cooling Stage of the Test 1: Finished at 11:00

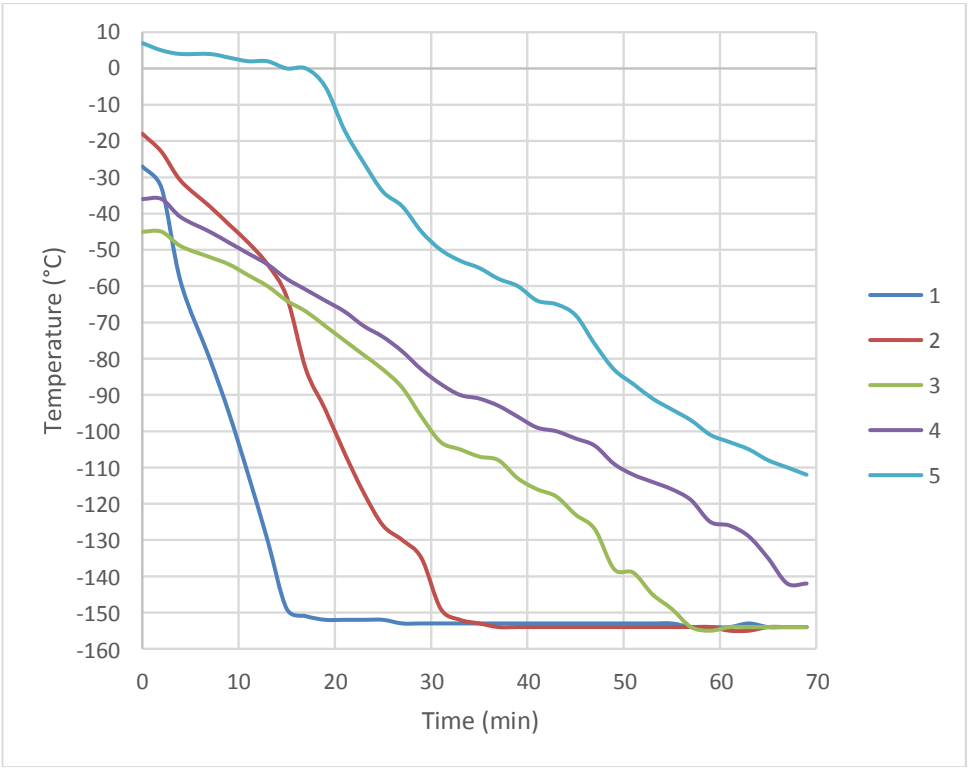

Figure 5-34: 2nd Cooling Stage of the Test 1: Started at 13:47

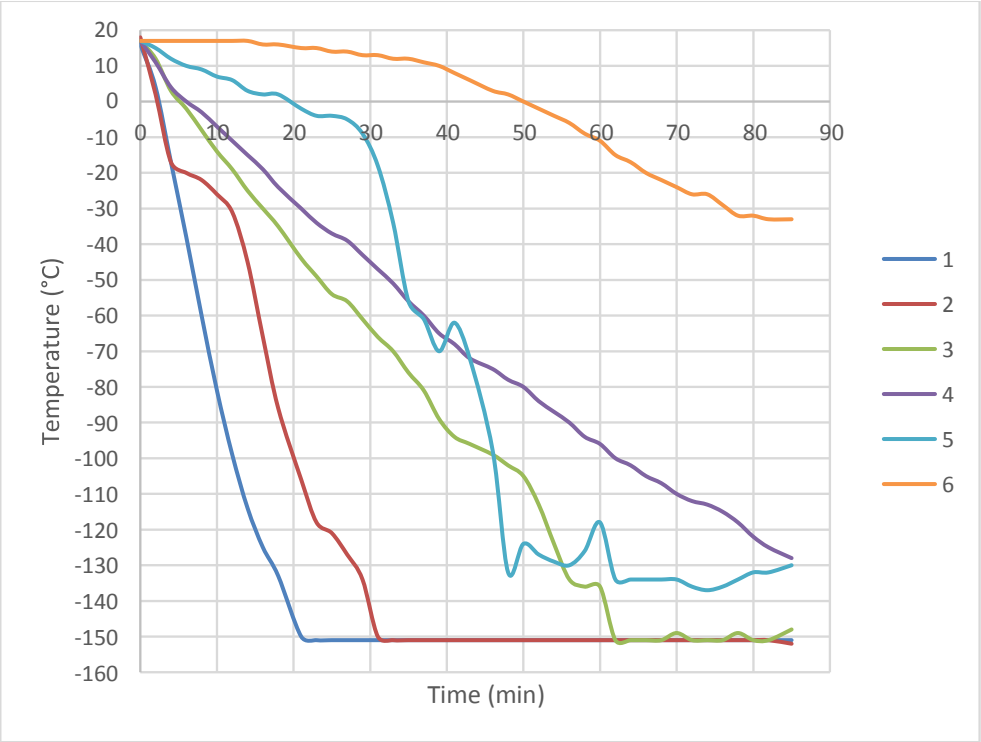

Figure 5-35: 1st Cooling Stage of Test 2: Finished at 14:15

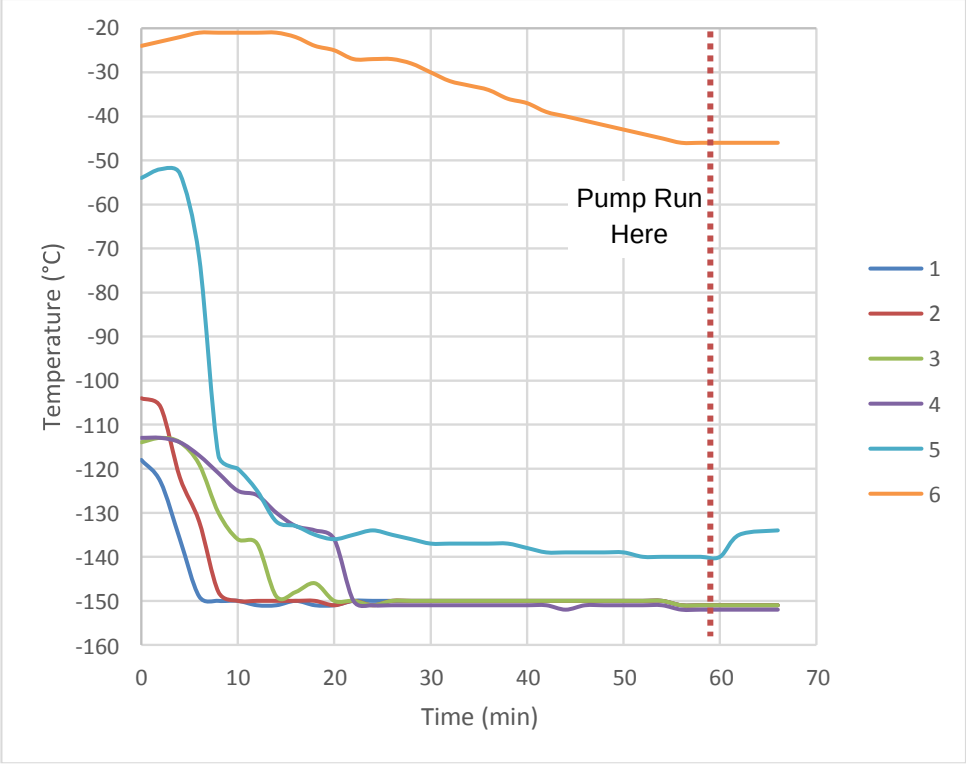

Figure 5-36: 2nd Cooling Stage of the Test 2: Started at 15:14

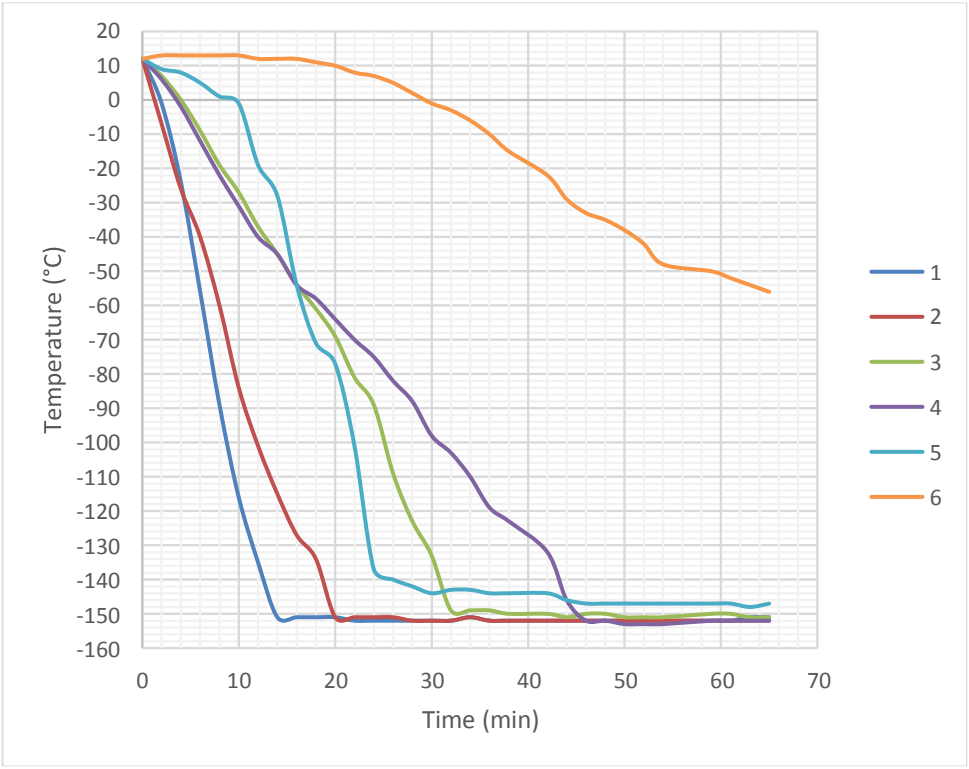

Figure 5-37: 1st Cooling Stage of Test 3: Finished at 13:08

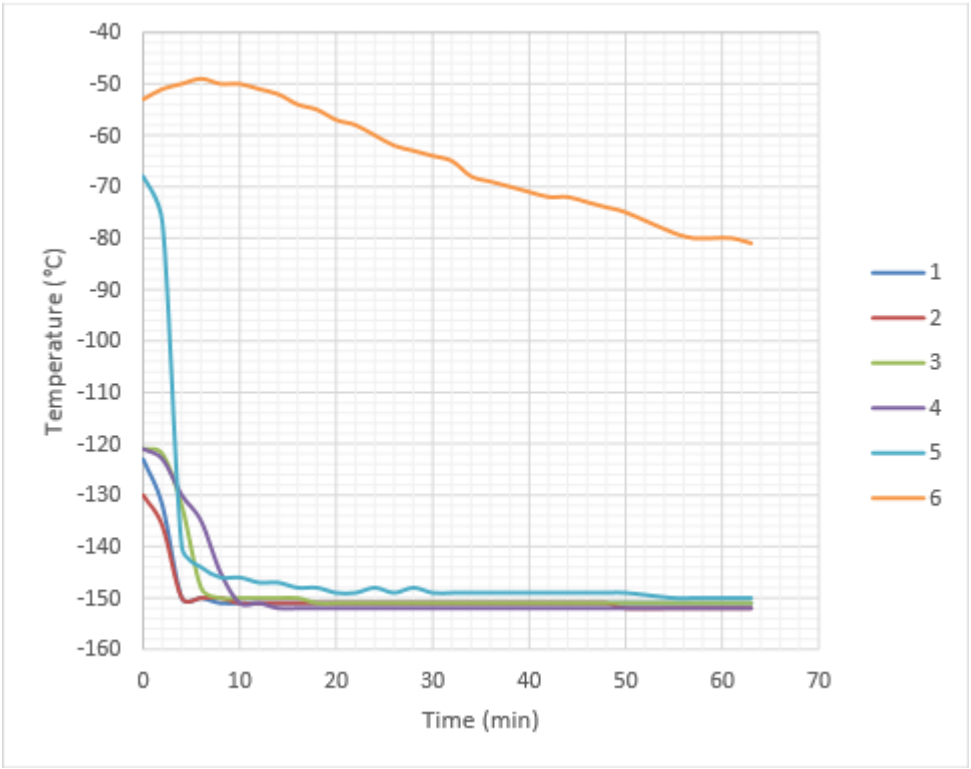

Figure 5-38: 2nd Cooling Stage of Test 3: Started at 14:18

5.5.3 LOX Compatibility & Pressure Tests

It was previously identified that the belt driven mechanism would have to be replaced with a geared system to allow operation at greater pressures, thus the changes were implemented as shown in Figure 5-39. In addition, another Swagelok 0-20bar pressure transducer was installed at the pre-inlet location, for more details refer to Figure 5-11 (pg. 97).

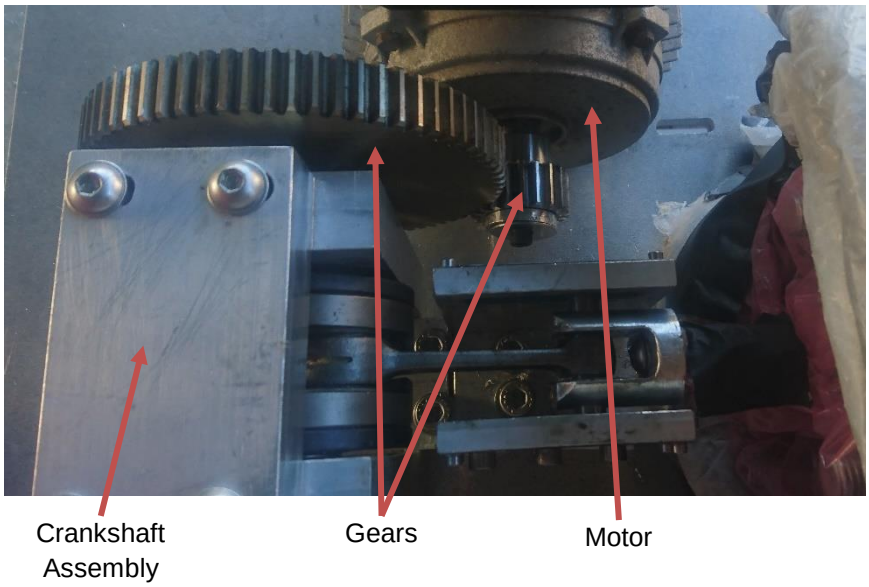

Figure 5-39: Gear System

While these changes were being implemented, several tests were run with the belt driven system. To cool down the system, 25l of LN_2 was used to precool the pump, as shown in Figure 5-4, which was sufficient to reach LOX operating temperature. During the LOX test, the temperatures were no longer continuously monitored as the output pressure values were a more important parameter and recording both readings was not possible. However, an exception was made and temperature readings were noted 65 minutes into the test, as shown in Table 5-7. It should be noted, operating temperature of LOX are higher, thus there was an increase in the temperature.

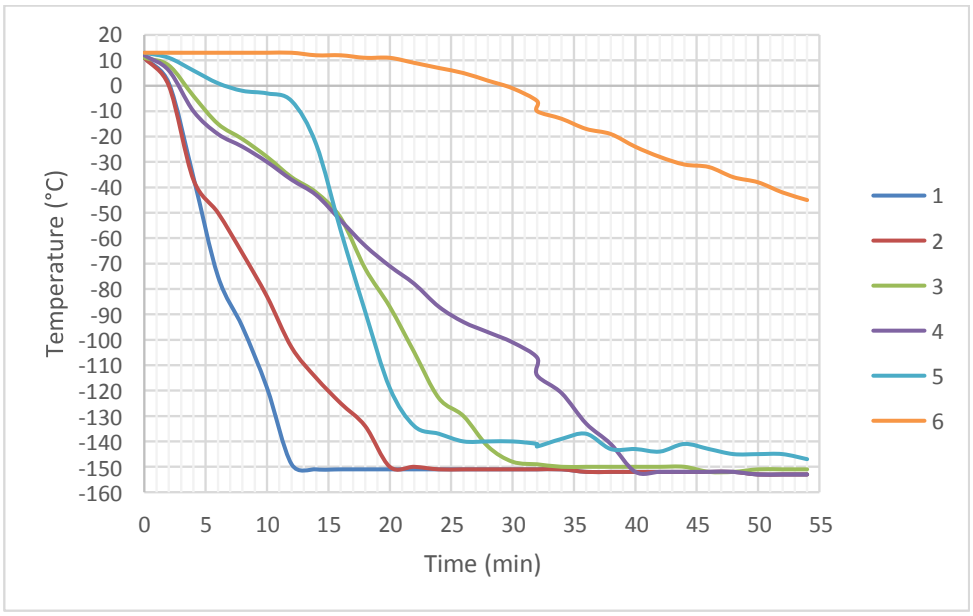

Figure 5-40: Cooling Temperatures

Table 5-7: LOX Operating Temperatures – 65min into the Test

Thermocouple					
1	**2**	**3**	**4**	**5**	**6**
-140	-145	-146	-140	-137	-67

During the test, the pressures of the system were recorded a number of times, including during the LN_2 cooling process. The results with LN_2 did not produce any novel data, which did not indicate any pressure increase. This was due to insufficient LN_2 flow rates, it was not possible to prime the pump. LOX is supplied at higher pressures which were sufficient to prime the pump for a short duration. It should be noted that to prime the system the outlet valve had to be partially opened to ensure sufficient inlet flow rates were achieved. Once the pressure in the system stabilised, and a constant stream of LOX has seen leaving the chamber, it was assumed that the system was fully primed. The pressure tests were carried out several times, but only two sets of readings were recorded, as shown in Figure 5-41 and Figure 5-42. For the majority of the first test, peak pressures of 20bar and above were achieved, over a run duration of approximately 2s. In the second graph, a maximum pressure of just over 29bar was achieved, but the test lasted for less than 1s before the timing belt. Similarly to the previous trials, higher pressures introduced higher torque requirements which led to the belt failure. Furthermore, after stopping the test around 2 to 5 seconds elapsed before the pressures returned to their initial readings. This was likely caused by LOX evaporation in the cylinder.

During these tests, a maximum pressure of 29.2 bar was achieved at an inlet pressure of 5.1bar. This corresponds to a pressure difference or delta P of 24.1bar which is 8.9 bar lower than the target pressure of 33bar. Taking into consideration the data collected, it was concluded that target pressures of 33bar or above would be possible to achieve, but this requires further tests to verify. It should be noted, that flow rates could only be measured using water by a volumetric, as cryogenic propellants evaporated on contact with the atmosphere and a dedicated flow meter for such applications was not available.

Furthermore, due to high inlet pressures, the data did not follow the pressure profile predicted in section **4.3.3.2 Instantaneous Pressure**. For example, there were no regions with a zero-positive pressure, but instead, the minimum pressure is ≈3bar above the inlet pressure. Higher outlet pressures could have been due to LOX momentum or during inlet vaporisation expansion as it warmed up. This resulted in average pressures for the 1st and 2nd tests of 13.7 and 17.0 bar respectively within given intervals as shown in these figures. The average pressures were once again calculated from an Excel file. It was further observed that the peak pressure was lower every other cycle and this required further investigation. This was especially noticeable in Figure 5-41.

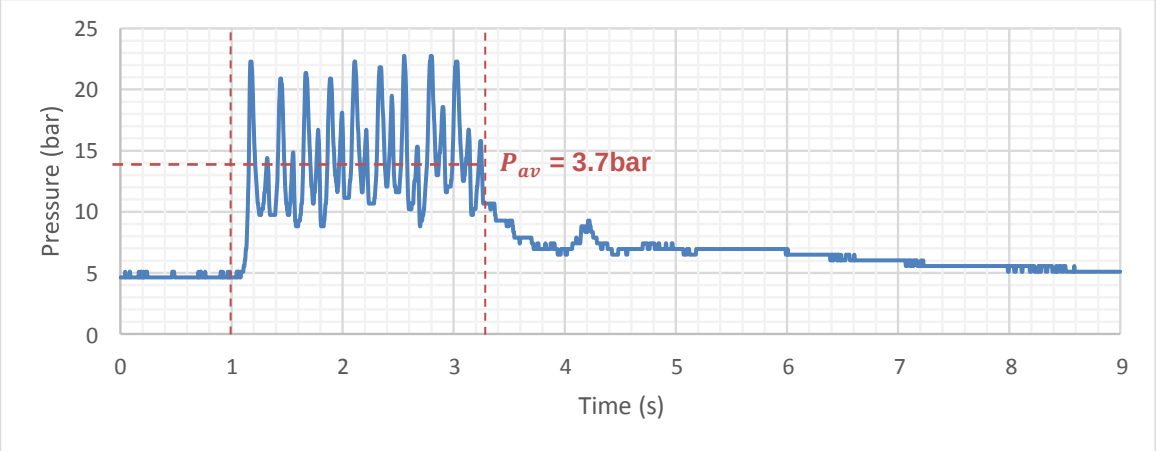

Figure 5-41: Pressure Results of the 1st LOX Test

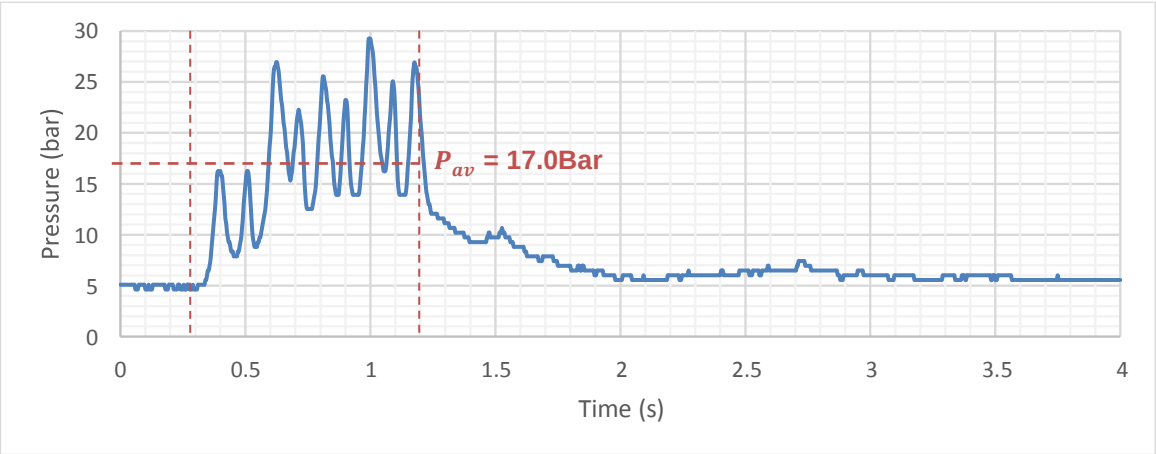

Figure 5-42: Pressure Results of the 2nd LOX Test

After making alterations to the driving mechanism and installing an inlet pressure sensor, trials were resumed and recorded in Figure 5-44 – Figure 5-48. The first graph of each figure illustrates the pressure readings at the inlet and outlet, while in the second graph, the instantaneous pressure difference between inlet and outlet is shown. For more pressure data refer to **Appendix N: LOX Pressure Tests** (pg.219).

The data in these figures clearly show that the Mark II pump can raise the pressure of LOX, but the ΔP design requirements of 33bar was not achieved, which was most likely due to a combination of factors:

- More volume was displaced by the piston than the inlet could supply, and as a result, the peak pressures declined every other cycle (i.e. Figure 5-44) or the peak pressure gradually decreased as time passed (i.e. Figure 5-48).
- The motor was not powerful enough to produce the desired pressures at the desired speed. When the outlet volume was restricted to a smaller size, the motor struggled to keep the crankshaft turning and, in some cases, ceased.

It should be noted, that in most cases the tests were carried out for less than 10s and the non-steady state of the pressure graphs indicates that the readings were at a transient stage. Nonetheless, despite irregularities in the flow pressures, the Mark II pump demonstrated that it can be used to pressurise LOX and the pump is compatible with cryogenic and oxidising liquids. The

demonstrator was kept at cryogenic temperatures for over an hour without any signs of leakage. In addition, the graphs evidently show that there is a pressure difference between the inlet and the outlet of the pump, which further validates the concept of the reed valves. However, it can be noted that the inlet pressure varies slightly due to poor sealing performance between the petals and the valve base, and this issue should be addressed in future work. Furthermore, this test rig showed that the experimental repeatability can be achieved and more evidence of this can be found in **Appendix N: LOX Pressure Tests,** as stated previously. However, the pressure profile depended on how well the system was primed, the temperature of the system and the size of the outlet opening as well as the inlet pressure.

As previously stated, irregular patterns also could have meant that the piston displaces more volume than the inlet can supply. As a result, an accurate pressure profile could not be achieved and therefore tests were carried out for short durations only. Furthermore, data in Figure N-3, Figure N-4 and Figure N-6 in **Appendices** (pg.219), shows that the pressures decreased over a test, further suggesting that the inlet flow rates was insufficient to prime the system fully, i.e. maintain it full of liquid.

Two cycle variability, as seen in Figure 5-44, is a further indication that the inlet flow rates are insufficient to keep the system primed and was most likely caused by oxygen vapour in the system. As shown in Figure 5-43 (a), the cycle begins with a fully primed system at full stroke length. After discharge, the piston returns to the full stroke length (b) but this time the system contains a mixture of LOX and oxygen vapour, due to an insufficient flow rate at the inlet. At the discharge cycle (c), the piston compresses gas and expels it from the outlet, at a lower overall pressure. When the piston returns to the full stroke, the system contains more LOX which is incompressible, hence it results in a higher-pressure peak. This cycle is repeated throughout the duration of the test.

A factor that these anomalies could have also been influenced by the motor not being able to deliver the required torque to keep the crankshaft turning cannot be eliminated. This was especially true when delivering high pressures, thus further investigation was carried out with water. In summary, the final LOX tests showed that proof of concept was achieved.

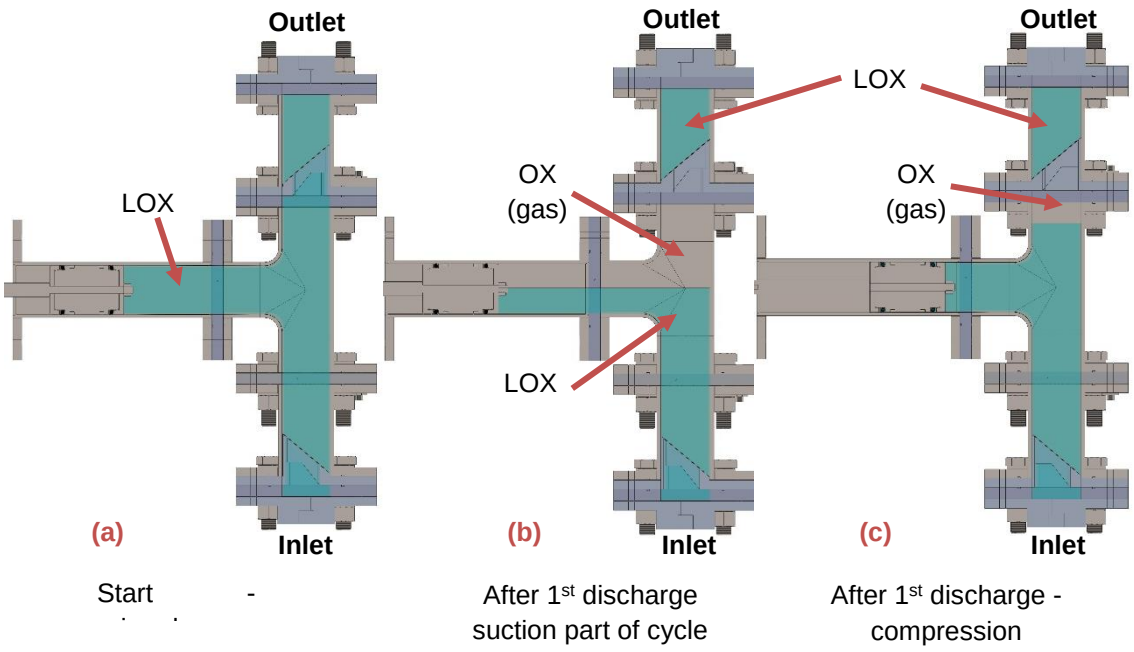

Figure 5-43: Two Cycle Variability

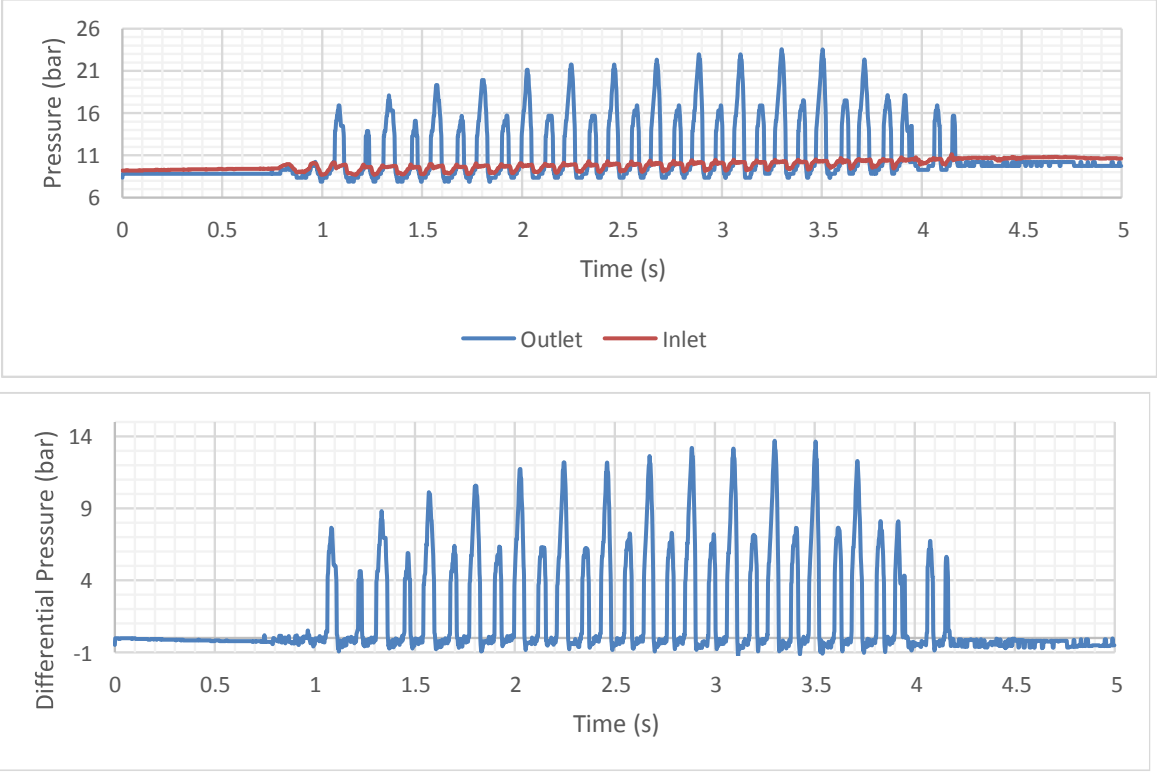

Figure 5-44: Pressure Results 4 – Test 1

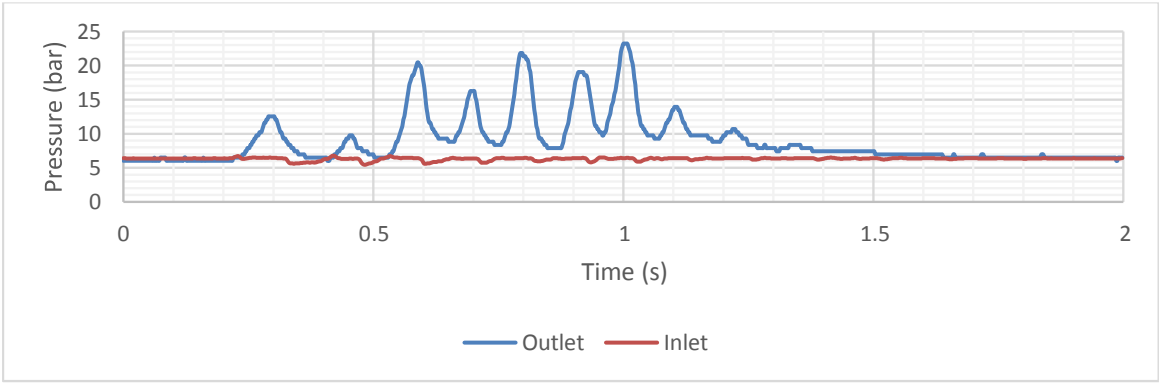

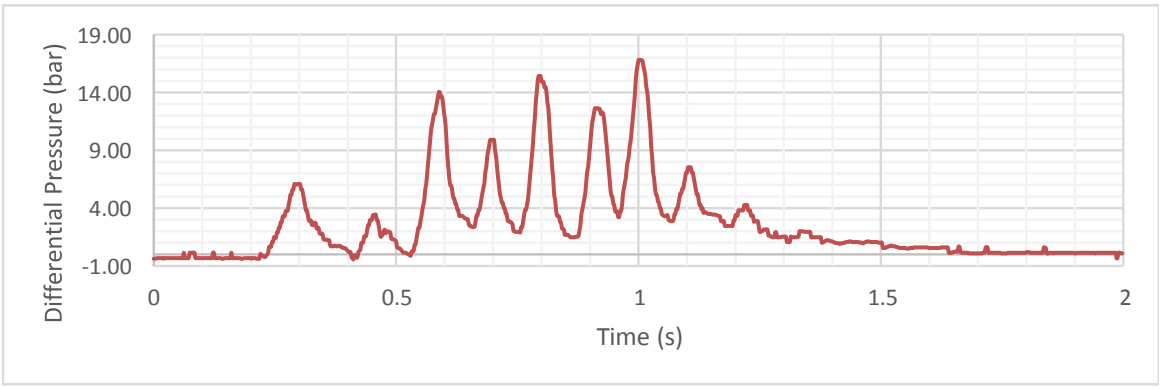

Figure 5-45: Pressure Results 1 – Test 2

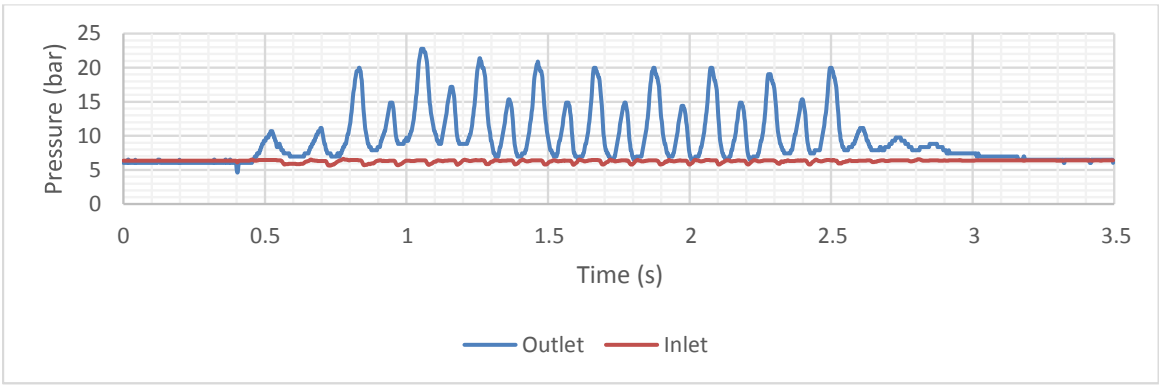

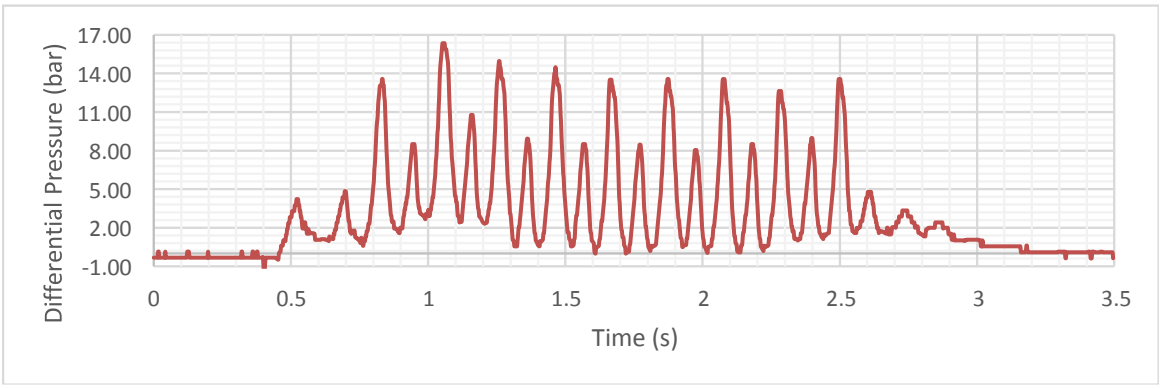

Figure 5-46: Pressure Results 2 – Test 2

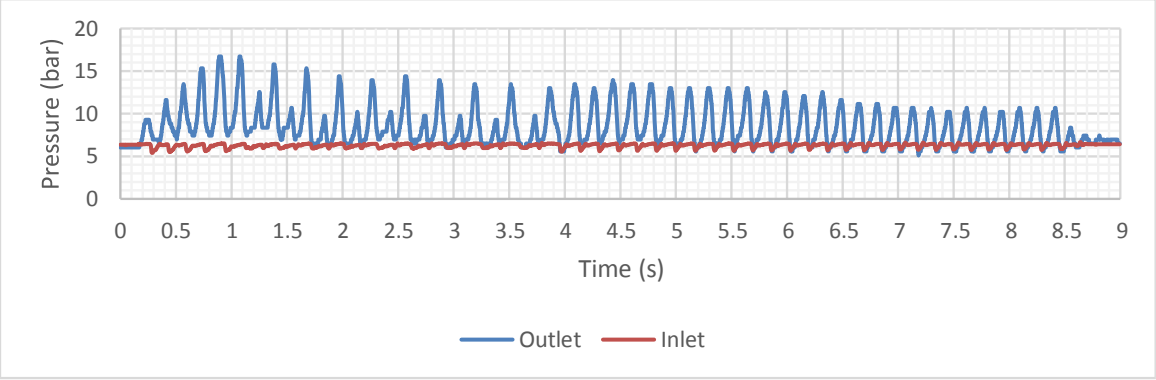

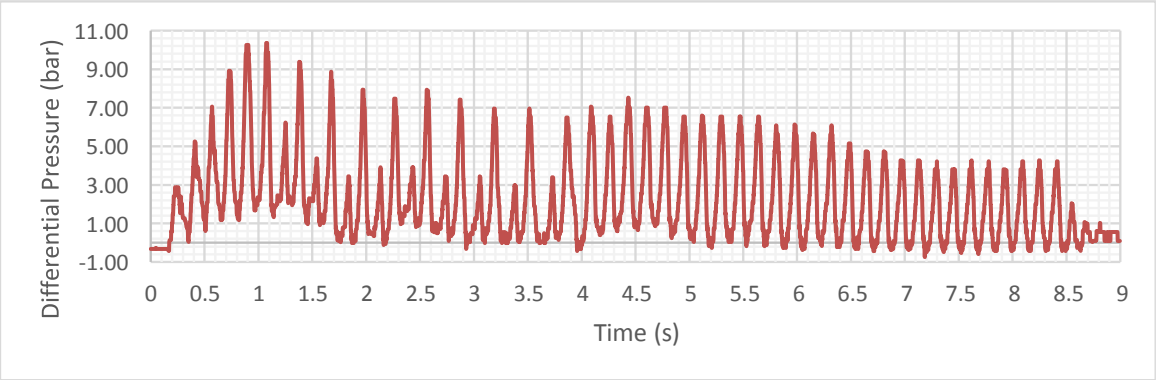

Figure 5-47: Pressure Results 3 – Test 2

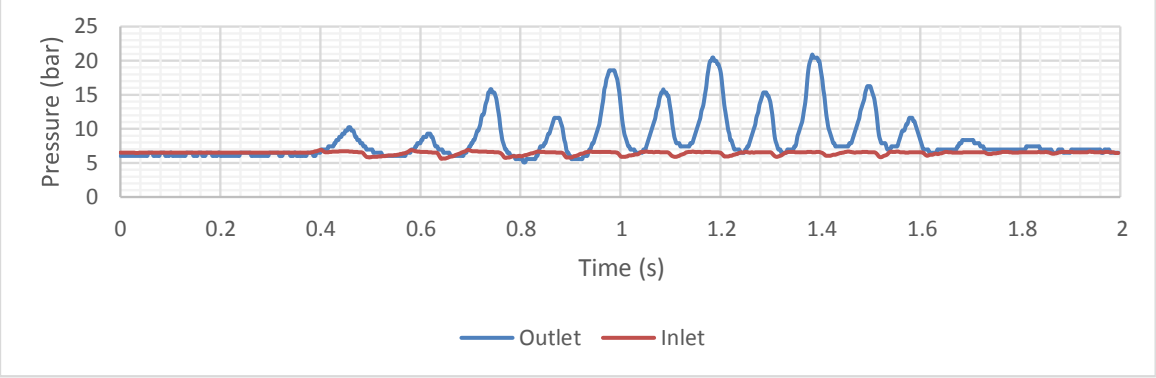

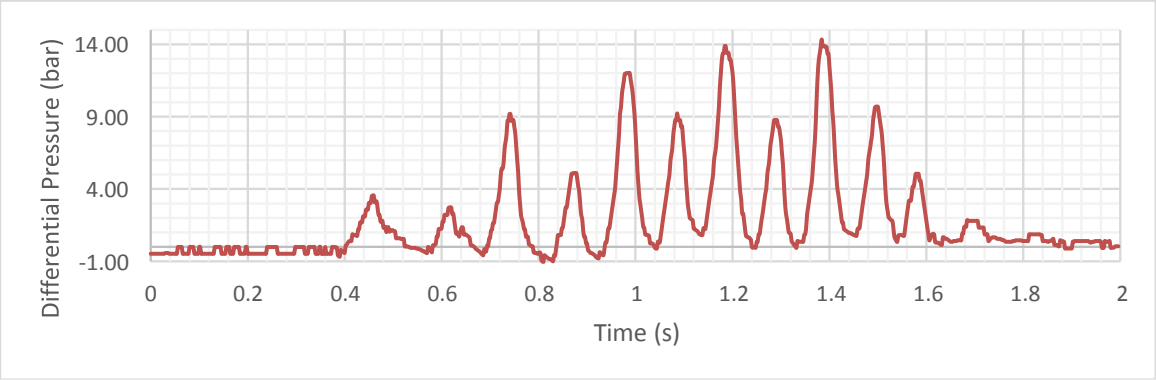

Figure 5-48: Pressure Results 4 – Test 2

5.5.4 Final Water Pressure Tests

Evidence suggested that adequate flow rates could not be supplied to maintain the system primed, therefore the tests were switched to water which aimed to monitor the pressure profile over a longer duration. In total 15 experiments were carried out with two outlet size constraints; 7mm and

12mm to evaluate the effects of an underpowered motor. These sizes were selected based on pipe availability. For each test the duration, average flow rate and volumetric efficiency were recorded in Table 5-8. The pressure data of these tests is shown in Figure 5-49, Figure 5-50 and further test data can be found in **Appendix O: Water Pressure Tests**. The top graph shows the pressure variation of the whole experiment, while the bottom part only the partial section to enhance the cycle details.

The data in the table shows that volumetric efficiencies exceeded 100% but this varied depending on the outlet diameter. The data further indicate that the flow rates and volumetric efficiencies were consistent for each outlet size, but the values were lower for the 7mm diameter orifice. These results were expected as higher back pressure restricted the outlet flow. However, based on the Mark I results, the volumetric efficiencies can be further increased by running the pump at a higher speed which would increase the momentum of the fluid.

Table 5-8: Final Water Test Data

Outlet size (mm)	duration (s)	$\dot{m}$ (kg/s)	$\eta_{volumetric}$	RPM_{av}	
12	24	0.676	124%	360	
12	28	0.682	125%	360	High $\eta_{volumetric}$ average
12	24	0.701	128%	362	
12	19	0.710	130%	360	
12	26	0.693	127%	360	
6	37	0.477	110%	285	
6	29	0.487	115%	279	
6	22	0.507	116%	289	
6	30	0.517	115%	296	
6	36	0.514	116%	293	Lower $\eta_{volumetric}$ average
6	21	0.488	107%	300	
6	21	0.486	107%	300	
6	23	0.488	110%	293	
6	27	0.540	118%	300	
6	23	0.490	110%	293	

By examining the pressure profile graphs, seen in Figure 5-49 and Figure 5-50, for two different outlet constraints, it is evident that using a smaller diameter leads to a two-peak profile, similar to that seen when tested with LOX. It was further visually observed that the motor speed varied with respect to a crank angle which lowered the average operating speed, as seen in the RPM_{av} column. After evaluating the video footage of the experiments, it was noted that a two-peak variability has occurred in a single cycle due to variable motor speed. The motor used for these experiments was not specified but happened to be available. At this stage of the project, the focus was to validate the concept of the piston pump at the lowest cost possible and this motor made it possible to achieve this objective. It was determined too late in the project that the motor was underpowered, hence it could not support high pressures at high flow rates, therefore when the peak motor power was reached, it was no longer able to accelerate the fluid further which led to a

decline in the motor speed. Once the pressures in the system declined to a sufficient level, the motor accelerated once again, which caused the second pressure spike. A variable pump speed could also have contributed to the decline in the volumetric efficiency, as it was found in with the Mark I that the volumetric efficiency declines at low speeds. A high volumetric efficiency may be linked to momentum of liquid passing through the pump, and low efficiency to gas being entrained in the flow. However, it was not possible to verify this as the project budget could not cover a liquid flow rate meter, therefore this must be address in future work.

For the outlet constraint of 12mm, the power required to deliver peak pressures was below the limit of the motor, therefore the required pressure profile, similar as in the previous chapter was achieved.

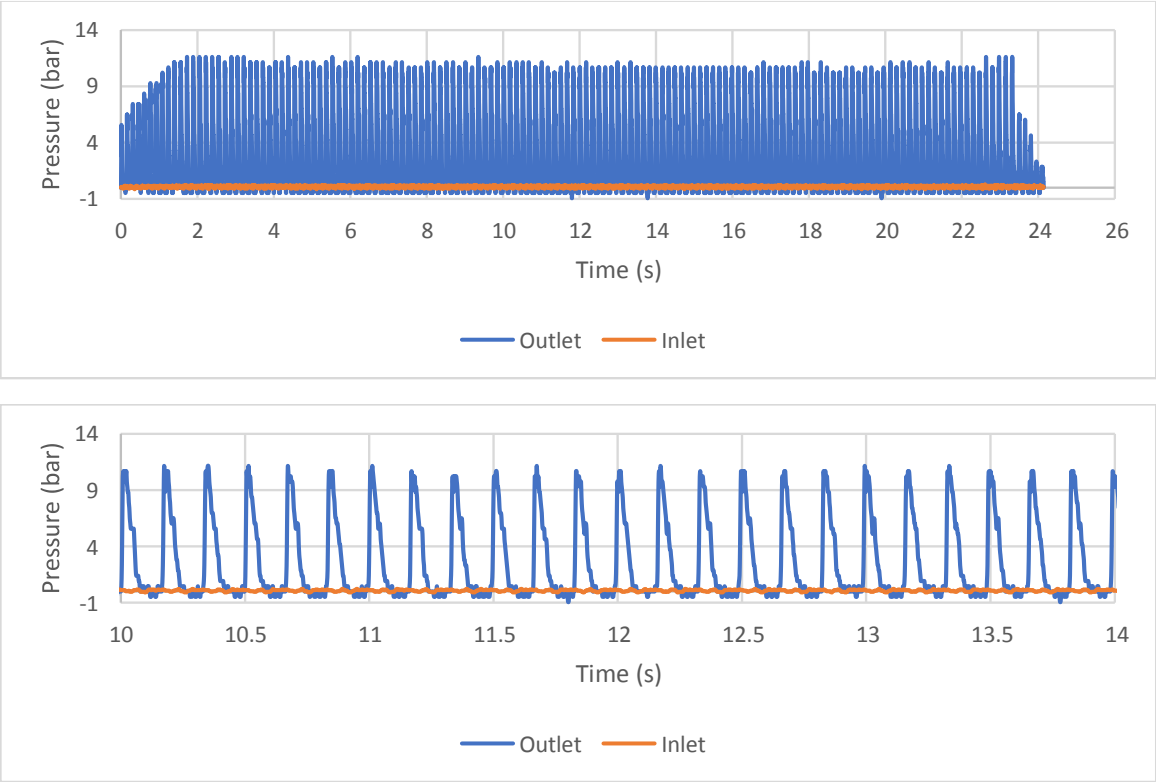

Figure 5-49: Water Pressure Test 1 – Outlet Diameter 12.6mm

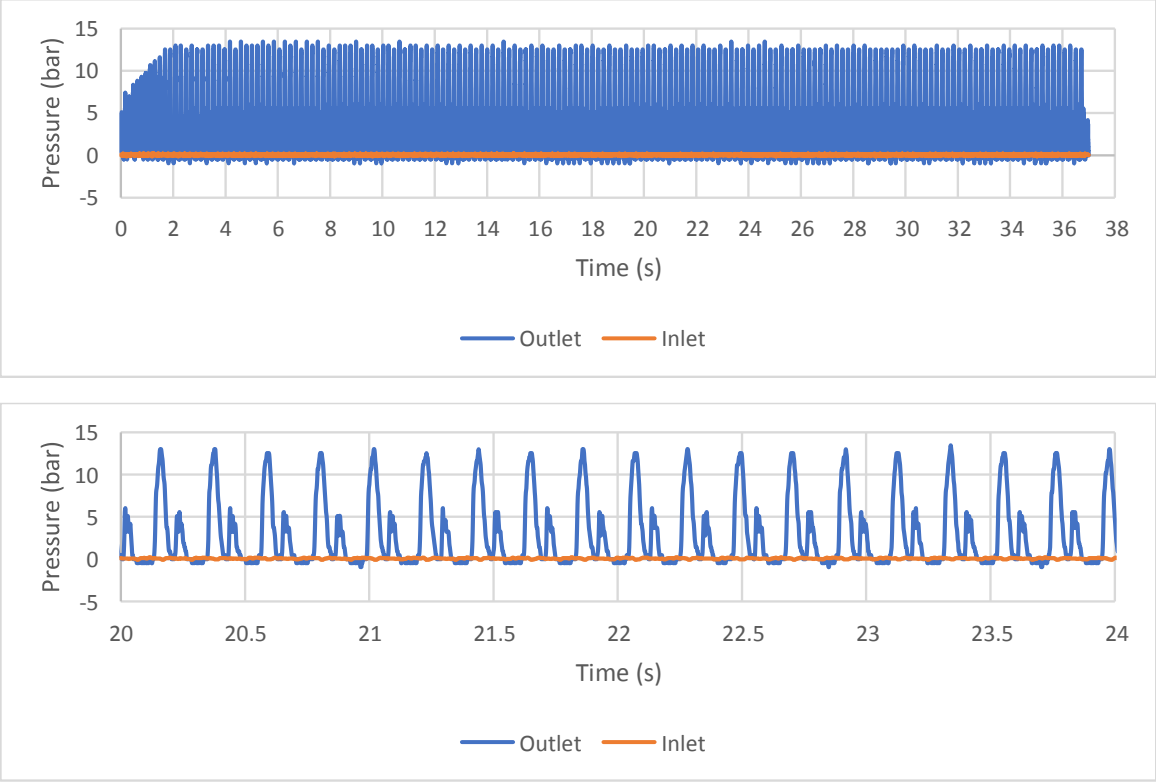

Figure 5-50: Water Pressure Test 6 – Outlet Diameter 7mm

To support the theory that the two-peak anomaly at high pressures resulted from to the variable motor speed, the motion of the crank rod was recorded using a GoPro Hero 3 camera at 240fps. Unfortunately, due to the low resolution of the camera, it was not possible to determine the instantaneous stroke length (position) of the piston. But the footage showed that the motor speed fluctuated during the experiment. To show this, some key frames were removed and illustrated in in Figure 5-51. At the start of the experiment (T = 0s) and at T = 0.133s, the gear of the motor is blurred, which indicates that the motor is moving (circled in green), but at T = 0.075s the teeth of the gears are visible in much finer detail and this is only possible if the motor runs at lower speed. In Figure 5-52, the pressure data of this cycle was extracted for comparison. The data shows that the pressure peaked at 14bar at ≈0.03s and then it dropped to zero at 0.075s and remained this value for 0.01s. When this was compared with the time-lapse footage, the pressure profile corresponds directly with the velocity of the motor. For a motor able to sustain a constant velocity, the peak pressures should have occurred close to a crank angle of ≈90°.

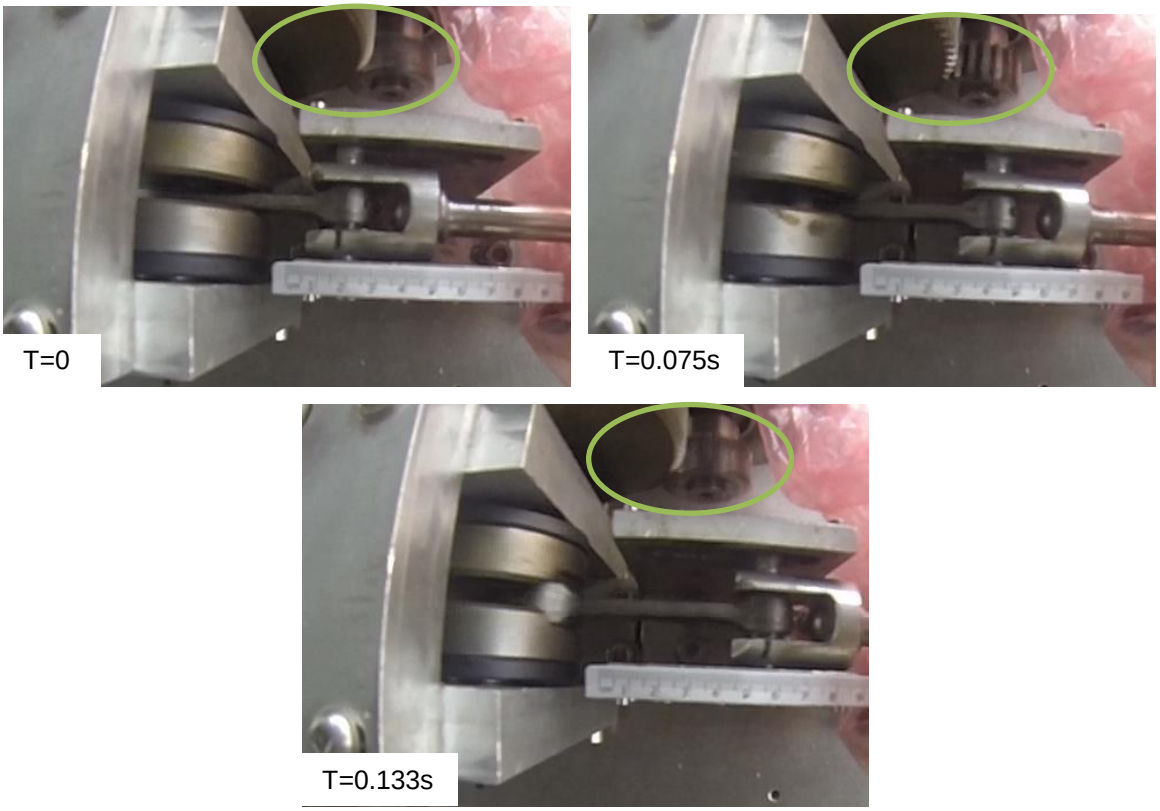

Figure 5-51: Test 10 Water Test Cycle Timelapse

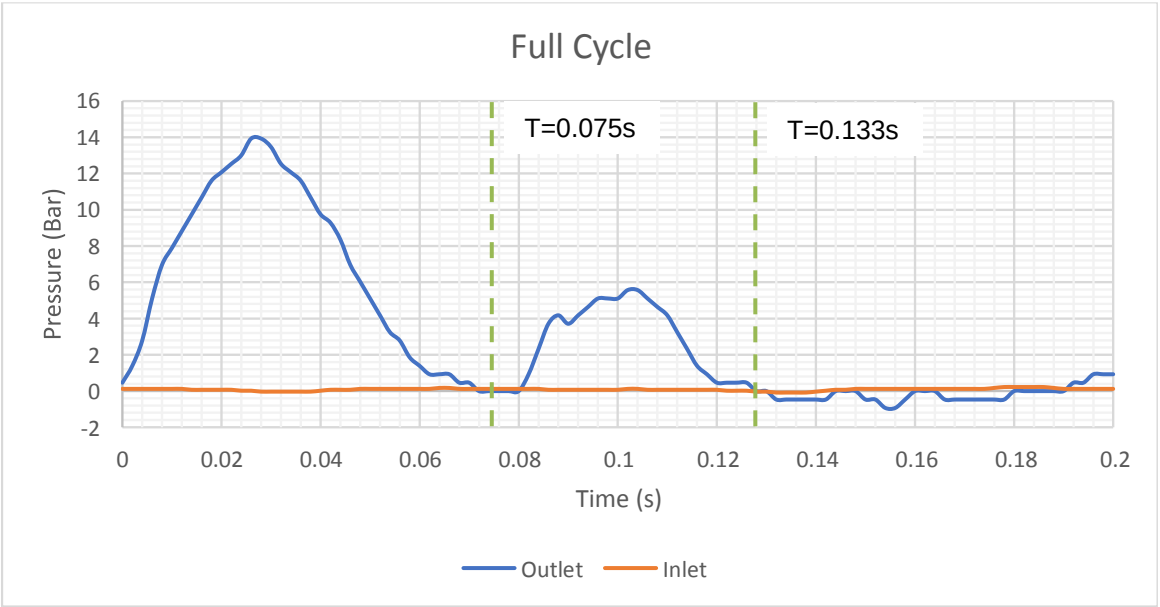

Figure 5-52: Test 10 Water Test Full Cycle – Outlet Diamter 7mm

Based on the evidence obtained from the water tests, the data from the experiments with LOX were re-evaluated to determine if the underpowered motor could have contributed to two cycle variability at high pressures as well. The operating speed in pressure results 4, test 9 (Figure 5-44) was determined by taking a part of the pressure data, as shown Figure 5-53, and then determining the number of highest peaks over a given time. From this, the average operating speed was calculated to be ≈283RPM, but video footage was not available to confirm this. Prior to the tests, it was determined that the unloaded crankshaft operates at ≈365RPM, and if the smaller peaks were counted, it would result in an average speed of ≈565RPM. The loaded crankshaft speed cannot be larger than for the unloaded therefore the pump could not be working at ≈565RPM. The same

process was applied for calculating the speed for the test shown in Figure 5-46, Figure 5-47, Figure O-4 and Figure O-8 which again showed that the operating speed was lower than expected.

It should be noted that not all experiments exhibited the two cycle variability profile, this phenomenon mostly occurred when the pressures exceeded 14bar, which closely corresponded with the results obtained using water. However, a theory that insufficient inlet flow rates were delivered to the system cannot be ruled out, as this phenomenon did not occur for all tests. It is evident that for the test in Figure 5-47, after 4s the pressure profile indicates that the motor completes the cycle without a significant reduction in speed. This can only be explained if the pump was not fully filled as less fluid would have resulted in lower power requirements and development of lower pressures. Other test results shown in **Appendices** in Figure N-4, Figure N-6, Figure N-7and Figure N-8 support this as a gradual decline in the peak pressure can only be explained if the inlet flow was reduced.

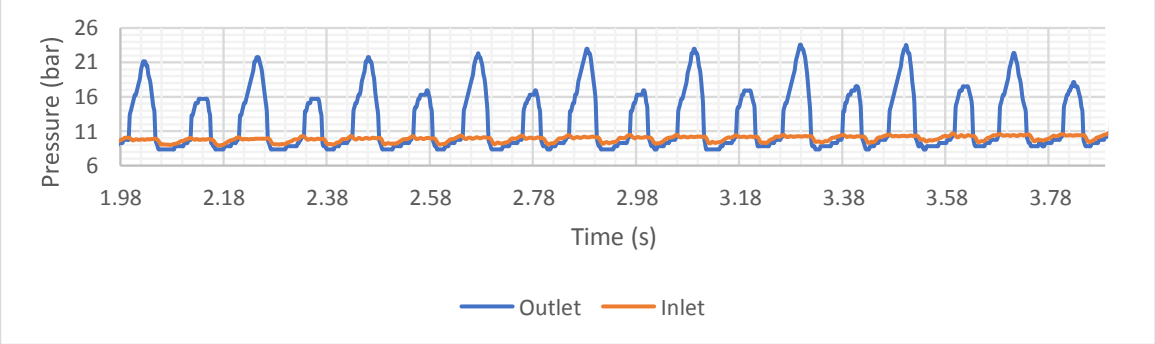

Figure 5-53: Pressure Results 4 – Test 9 – Part of Data

In addition, the data from the water tests allows one to further refine the theoretical pressure profile of the triplex pump. A similar study was already carried out in section **5.5.3**, but due to the reasons given above, a consistent pressure profile was not achieved. Therefore, the data from Water Pressure Test 1 (Figure 5-49) was used to approximate the pressure profile for the triplex configuration. In Figure 5-54, the ΔP pressure profile was extracted from the data and shown in the simplex view. For estimating the pressure profile for the triplex configuration, it was assumed that each piston will produce an identical pressure profile to the simplex pump. Similarly, as before these results were offset by 60° and laid over as shown in the triplex view. As predicted, this eliminates the pressures with zero flow rate and the duration between maxima and minima were reduced. However, as seen in Figure 4-12, the theoretical pressure values follow a smooth sinusoidal curve, while the pressure profile obtained experimentally, exhibits a sudden spike and decline in the pressure. Based on the evidence that the volumetric efficiency exceeds 100% because of the momentum of the fluid, this could also have contributed to the spike seen in the experimental data. However, for the triplex configuration, the momentum is likely to be dissipated to the upstream propellant which would lower volumetric efficiency and reduce the pressure spike seen in the tests. The reason volumetric efficiency exceeds 100% is because fluid is pumped from high pressure chamber to atmosphere. Because air is less dense and lower pressure, fluid does not transfer much of its energy to air. In the triplex pump, each piston will dispense fluid into a “common” chamber where fluid from all piston meets. This will mean that fluid interacting with

denser and higher pressure medium and thus momentum will be transferred and volumetric efficiency would drop.

Moreover, the data seen in Figure 5-54 suggests that the triplex pump would produce an average pressure of 7.2bar for a maximum pressure of ≈10.1bar. The theoretical pressure profile in Figure 4-12 predicts that the maximum pressure should be ≈8% greater than the average pressure, but the experiments suggest that this likely to be ≈40%. As stated previously, this discrepancy is expected to be lower as the momentum of the fluid would be dissipated in the triplex pump, especially when operating at pressures close to 30bar.

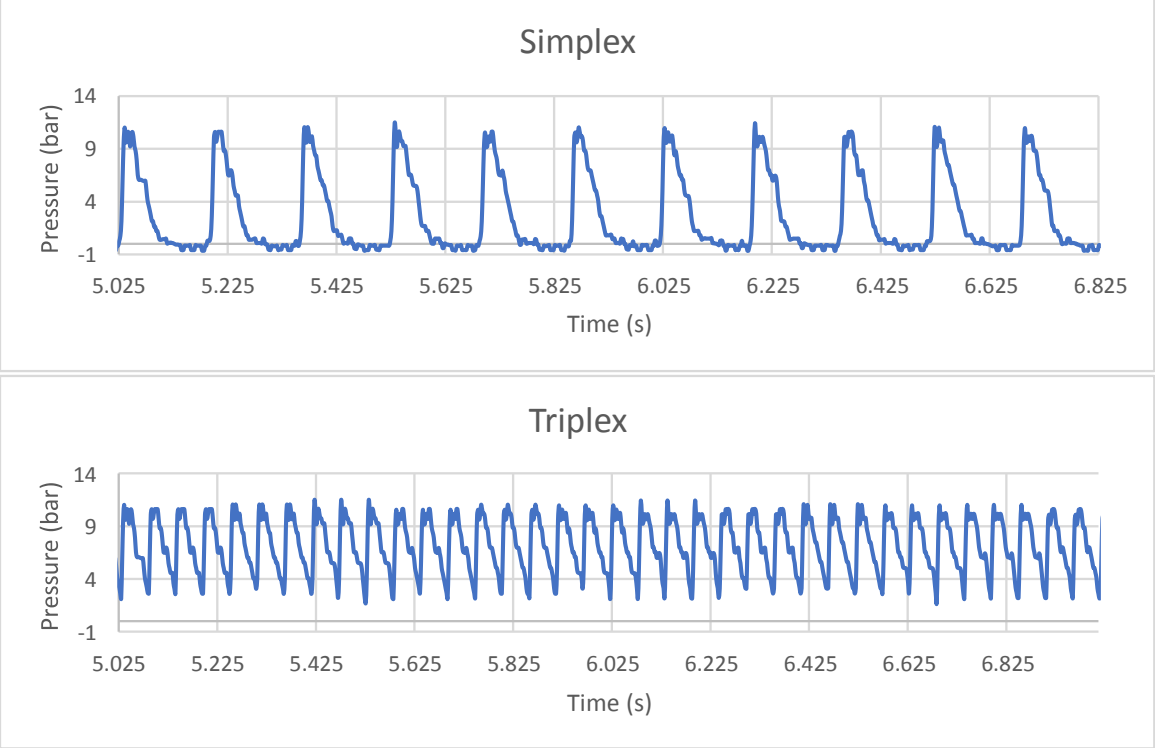

Figure 5-54: Pressure Results 4 – Water Pressure Test 1 Simplex Vs Triplex

5.6 Chapter Summary

In this chapter, it was established that dynamic seals are one of the most critical parts of the pump; they must operate at high-pressures, high-velocity and at cryogenic temperatures. The PTFE/carbon based seals with a cantilever stiffener and PTFE seals with a coil stiffener were tested for such applications. At cryogenic temperatures, oil based lubrication cannot be used on the sliding face to reduce wear and tear on the seals. As the PTFE has a very low coefficient of friction this makes it an excellent choice for cryogenic applications. However, the linear thermal expansion of the PTFE is several magnitudes greater than of the aluminium or stainless-steel, therefore a correct stiffener must be used to ensure the tolerances are maintained.

Throughout the tests, it was found that the PTFE/carbon with the cantilever stiffener seals did not work at cryogenic temperatures. The factors that contributed to the failure are:

- The PTFE/carbon seal showed excessive wear and tear, which led to worse sealing tolerances.
- A cantilever stiffener did not provide sufficient stiffness to counteract the filter shrinkage.

On the other hand, Fluoroloy® A12 based seal with a coil stiffener proven to be a very effective seal at cryogenic temperatures and further tests were carried out using this design of seal.

The first few tests were carried out to test the flow rates of the pump, which matched those values obtained with the Mark I. In addition, the pressure fluctuation was tested using water and with LOX. The pump proved that the prototype can raise the pressure of LOX and repeatability of results were demonstrated. However, the desired pressure difference of 33bar was not achieved – the maximum pressure difference that this prototype delivered at was ≈24.1bar. Based on the data obtained from the Mark II, it can be concluded that the peak pressure of 33bar can be achieved if the inlet flow rates are increased and a more powerful motor is installed.

While the Mark II pump demonstrator proved that it can raise the pressure of the LOX, the data was collected over a very short period as the inlet could not produce sufficient flow rate to prime the system adequately (i.e. to ensure the internal cavities stayed filled with LOX). The flow rates could have been increased by increasing the inlet pressure or by installing a hose with a larger diameter. The simplest option is to increase the inlet pressure, but this would lead to a higher inlet flow velocity and consequently a higher propellant tank pressure resulting in a heavier tank mass. As a result, this will produce a fast, and narrow flow of the LOX, as illustrated in Figure 5-55, which would reduce priming effectiveness. Of course, the interaction with valves would alter the stream velocity. Alternatively, by replacing the original hose with a wider diameter hose, the flow velocity can be decreased without reducing mass flow rate.

Further water tests were carried out to obtain the pressure profile for longer durations. These tests also indicated that a more powerful motor is needed in order to test at the desired flow rates and pressures. It is also should be noted that the Mark I demonstrator already proved that the pump can repeatedly operate at durations of over 30s. The pump requirement was to run for 150s, however the outlet container was limited to approximately 25l, thus most of the tests were carried out for less than 30s. It should be noted that the total accumulated time for the tests exceeded 5min.

In addition, the tests showed that thermal conductivity pathways, such as the support structures, must be taken into consideration and where possible thermal mass must be reduced. But if this becomes an issue, alternative materials, such as carbon fibre can be considered but would be more expensive to manufacture. Furthermore, the piston cylinder will have to be equipped with a thin layer of stainless steel or other hard metal to ensure the surface smoothness is maintained in order to provide adequate seal and minimise wear and tear on the seals.

Moreover, a pump design was outlined which showed how to achieve the target flow rates, raise the pressure and to achieve cryogenic compatibility. In the process of doing this, manufacturing techniques were explored and evaluated. While some parts of the piston pump, such as the piston cylinder, required a high degree of precision, most of the other components can be manufactured

by using readily available CNC processes. The finishing process for the production of the piston cylinder was also found to be cost effective.

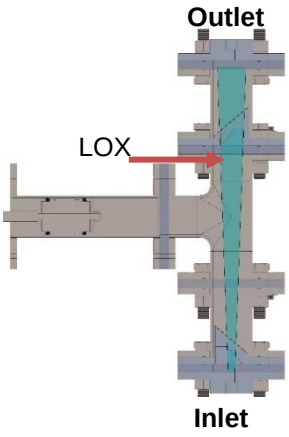

Figure 5-55: LOX Stream At High Inlet Pressures

Chapter 6

Conclusion & Further Work

6.1 Summary of Conclusions

6.1.1 Literature Review

In the literature review, the importance of the pressurisation system for rocket propulsion was explained. Various types of pumps and other pressurisation methods, such as pistonless pump and gas pressure-fed systems were compared against the state-of-the-art rocket turbopump in the content of a small satellite launch vehicle with a payload under 500kg to LEO. A detailed analysis of how these systems work was evaluated and pros with cons were identified. It was determined that most of other pump designs cannot meet the mission requirements or did not offer any potential benefits over the turbopump for a small-low cost launcher due to cryogenic non viscous fluid compatibility, size, bulkiness, complexity and other reasons. Based on the data obtained, four potential pressurisation options – the turbopump, piston pump, gas pressure-fed system and pistonless pump, were shortlisted for further evaluation. These evaluations were carried out in the **Mass Model** section.

6.1.2 Mass Model

Due to time and budget constraints, it was not possible to evaluate the shortlisted technologies experimentally. To choose the system with the most potential, a mass model was developed which was used to estimate the GLOM (Gross Lift of Mass) of hypothetical small satellite launcher with the turbopump, gas pressure-fed and pistonless pump propulsion pressurisation. Due to a lack of data, this study could not be carried out for the piston pump, therefore a decision had to be based purely on the information obtained from the **Literature Review**.

The mass model has shown that a launcher gas pressure-fed propulsion is very sensitive to the payload mass – a slight payload mass increase would lead to a significant GLOM rise. Because the pistonless pump is based on the pressure-fed design, it is also sensitive to these changes, but not to the same degree. As expected, the launcher with the turbopump showed the lowest GLOM and is the least sensitive to the payload mass. This supports the use of turbopumps as the state-of-the-art technology for launcher propulsion.

While the turbopump offers a higher power to weight ratio compared to the pressure-fed or pistonless systems, the cost of the turbopump is likely to be an order of magnitude more expensive than both of these systems, dues to the complexities associated, such as delivering flow at high-pressure and high-flow rate from the low-pressure inlet, manufacturing process and cavitation. However, according to XCOR Aerospace in the USA, the cost of the pump can be significantly reduced for lower thrust rocket engines. As a small launcher with low launch mass around 20

tonnes requires smaller engines to accelerate it, the piston pump might be an attractive low-cost solution for these vehicles, which are also of the interest to the UK. Based on the XCOR Aerospace claims that the piston pump can achieve the same performance as a turbopump, the pressure-fed system offers low research potential and the pistonless pump is too novel and requires a whole vehicle to validate, the piston pump was selected to investigate XCOR Aerospace's claims.

6.1.3 Piston Pump – Mark I Demonstrator

To test the concept of the piston pump for rocket applications, a preliminary concept design was produced, this matched XCOR Aerospace findings that a triplex (3 cylinder) configuration offers the best compromise between weight, flow rates and acceleration head. Sizing of a full-size pump was carried out to estimate the dimensions. Further parameters, such as operating speed and maximum pressure calculated as part of the design process.

A valve design was then selected based on the pressure, flow rate and operating speed requirements. Reed valves proved to be best suited for this application as other valves could not meet all three requirements simultaneously. A concept valve design was tested and with the help of CFD, an optimisation took place. The new valve was angled at 40° to its base plate to reduce the interference with fluid flow and thus reduce momentum loss from change in flow direction which affected the volumetric efficiency. A third passageway was also added to reduce the flow resistance and pressure drop through the valves.

To verify the valve functionality, the Mark I demonstrator was built. It confirmed that reed valves were able to operate at speeds of up to ≈1,930 cycles per minute and support flow rates exceeding 1.2kg/s at speeds of ≈980 cycles per minute.

Due to the properties of the materials, the Mark I was not designed to operate with cryogenic liquids or at high pressures, and its transparent parts allowed observation of the flow patterns in various sections of the pump. It was also used to assess manufacturing techniques for the development of the Mark II demonstrator.

6.1.4 Piston Pump – Mark II Demonstrator

The Mark I validated that the target flow rates could be achieved while operating at ≈1,000RPM. However, further tests had to be carried out to validate compatibility with cryogenic liquids, identify manufacturing and other challenges, and to determine the flow output flow characteristics. The Mark II prototype was built principally from off-the-shelf stainless steel 316L components to reduce the manufacturing costs and time. To minimise the wear and tear on the seals and reduce leakage especially at cryogenic temperatures, honing – a process to increase the quality of a metal surface was used on the piston cylinder. This precision finishing technique is essential for the piston pump but was fortunately available at a relatively low cost for low volume production components.

The dynamic seals mounted on the piston cylinder were found to be one of the most critical parts of the system – especially when cryogenic liquids are tested, therefore an investigation was carried out to determine the type of seals suitable for operating at pressures above 30bar, speeds of over 1,000RPM and compatible with cryogenic liquids. The material of the seal and the type of stiffener were two key parameters which dictated the compatibility under these specified conditions. The

evaluation showed that PTFE based seals must be used as they have a low coefficient of friction which minimises wear and tear. Low-cost carbon-PTFE seals with a cantilever stiffener were tested and showed a high degree of wear but sealed with water. However, at -50 – -60°C the material experienced a high degree of shrinkage and no longer offered an adequate seal. These seals were replaced with Saint-Gobain Fluoroloy® A12 seals which had a coil stiffener. These seals were cooled down to LN_2 temperatures and did not show any signs of leakage, giving repeatable results.

The Mark II demonstrated that the pump could achieve a maximum pressure difference of ≈24.1bar between inlet and outlet. Furthermore, the pump has validated the concept of using reed valves with LOX, but further work is required to reduce backflow. Unfortunately, the target pressure values were not possible to achieve because sufficiently high inlet flowrates could not be delivered from the inlet pipe setup and the motor used was not powerful enough sufficiently powerful to give a large pressure head and flow rate simultaneously.

6.2 Novelty and Research Achievements

Within the course of this work, the following novel contributions have been made towards the state-of-the-art in low-cost pressurisation systems for small launch vehicles:

- Various pressurisation options were critically evaluated and it was concluded that the reciprocating pump could meet the pressurisation requirements for a sub 20,000kg vehicle at lower cost than a turbopump. This option has never been explored for orbital launch vehicles at this given GLOM, but NASA and XCOR Aerospace have investigated the piston pump for other applications.
- Two piston pump demonstrators were designed, built and tested in order to investigate potential challenges, and solutions and identify the feasibility of this type of pressurisation approach.
- While XOCR Aerospace has claimed that they have developed a piston pump for rocket applications there is no detailed information of how this system works. This project has showed what type of materials, components and valves must be used for such applications.
- A valve design was adapted and tested which is compact, able to operate at high-cycle speeds, is suitable for high pressures and high flow rates and is compatible with cryogenic liquids.
- The Mark II demonstrator produced high-flow rates, raise the pressure of liquid oxygen and is compatible with cryogenic liquids.

6.3 Further Work

This thesis opens the opportunity for others to expand on the work that has been carried out, in particular the following areas of research are recommended:

- Reed valve validation: while valve performed under high flow rates, pressures and cycle speed, were individually verified, further study needs to be carried out when subjected to a combination of these demanding conditions.

- Increasing the inlet hose size should allow higher inlet flow rates to confirm the ability to deliver a higher pressure head. A pressure test with LOX but for longer durations of 30s-1:30min is further recommended.
- Improve reed valve sealing performance: after several tests, the petals plastically deformed, and did not seal well under static conditions. Irregularities between the surface of the petal and the valve body also caused some leakage. Polishing the contact faces between the petal and valve can eliminate defects, in turn leading to a greater sealing performance. To ensure the petals do not plastically deform, springs as shown in Figure 6-1, could be installed to return the petals to their original position. Also, thicker petals can then be considered for higher pressures. It should be noted that stoppers must be installed (not shown in this figure) to ensure petals do not open too far, this may however reduce valve response time, which is important at high cycle rates.

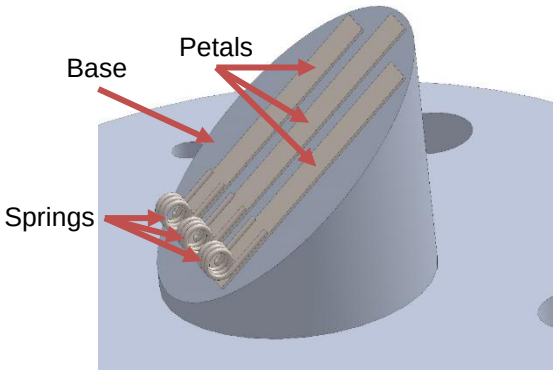

Figure 6-1: Mark II CAD Model – Section View

- Further verification at cryogenic temperatures: a light weight Mark III prototype with reduced thermal mass and/or use the existing Mark II prototype to verify the flow rates, pressures and cycle speeds under cryogenic temperatures are recommended. It should be noted that for the Mark II a new cryogenic container must be considered, which would allow it delivery of at least 1kg/s of LN_2 or LOX.
- After implementing all the changes as above, development of a triplex pump to compare flow rates, pressures and volumetric efficiency against a single acting pump is the next step. The manufacturing challenges of a triplex pump and an accurate cost estimation are needed.
- Operational issues with a piston pump, such as vibration and flow pulsation need to be evaluated for example, how these factors are affected by the pump parameters, such as the stroke length, operating speeds and cylinder diameter. An investigation into how these issues can be mitigated or minimised is required.
- Further experiments should vary the pump parameters as outlined above to find the optimum setup, offering a balanced solution between the performance and cost.
- Pressure sensors must be installed in all key locations to determine the pressure variations across the system.
- Alternative materials, such as carbon fibre for manufacture of the piston pump should be explored.

- Power sources: investigate potential novel power sources that could drive the pump. Electric power sources could be compared against existing gas driven turbines. The complexities of both systems must be assessed, pros and cons identified and compared against the costs and the impact in the launch mass of the vehicle.
- Finally, the last step in the roadmap would be to develop and build a flight-ready triplex Mark IV pump to evaluate its performance. This should provide a thorough comparison against the turbopump.

References

[1] SpaceX, "FALCON 9," http://www.spacex.com/falcon9 [cited 20.08.2017

[2] Rocket Lab, "Our Mission," https://rocketlabusa.com/our-mission/ [cited 08.05.2016 2016].

[3] Rocket Lab, "Rocket Lab Reveals First Battery-Powered Rocket for Commercial Launches to Space," https://www.rocketlabusa.com/latest/rocket-lab-reveals-first-battery-powered-rocket-for-commercial-launches-to-space/ [cited 22.06.2017

*[4] NIST, "Isothermal Properties for Water," http://webbook.nist.gov/cgi/fluid.cgi?T=20&PLow=1&PHigh=50&PInc=50&Applet=on&Digits=5&ID=C7732185&Action=Load&Type=IsoTherm&TUnit=C&PUnit=bar&DUnit=kg%2Fm3&HUnit=kJ%2Fkg&WUnit=m%2Fs&VisUnit=uPa*s&STUnit=N%2Fm&RefState=DEF [cited 22.03.2017*

[5] NIST, "Isobaric Properties for Oxygen," http://webbook.nist.gov/cgi/fluid.cgi?P=1&TLow=-250&THigh=-185&TInc=1&Applet=on&Digits=5&ID=C7782447&Action=Load&Type=IsoBar&TUnit=C&PUnit=bar&DUnit=mol%2Fl&HUnit=kJ%2Fmol&WUnit=m%2Fs&VisUnit=cP&STUnit=N%2Fm&RefState=DEF [cited 10.07.2016

[6] NIST, "Isobaric Properties for Propane," http://webbook.nist.gov/cgi/fluid.cgi?P=1&TLow=-150&THigh=-45&TInc=1&Applet=on&Digits=5&ID=C74986&Action=Load&Type=IsoBar&TUnit=C&PUnit=bar&DUnit=mol%2Fl&HUnit=kJ%2Fmol&WUnit=m%2Fs&VisUnit=cP&STUnit=N%2Fm&RefState=DEF [cited 10.07.2016

[7] Humble, R.W., Henry, G.N., and Larson, W.J., "Space Propulsion Analysis and Design," The McGraw-Hill Companies, Inc., United States of America, 1995,

[8] Hyperphysics, "Specific Heats of Gases," http://hyperphysics.phy-astr.gsu.edu/hbase/Kinetic/shegas.html [cited 14.09.2017

[9] Propulsion-Analysis, "Rocket Propulsion Analysis," http://www.propulsion-analysis.com/index.htm [cited 14.09.2017

[10] SpaceFlight101, "Soyuz 2-1v Specifications," http://spaceflight101.com/spacerockets/soyuz-2-1v/ [cited 10.05.2016

[11] Barske, U.M., "High Pressure Pumps For Rocket Motors," Royal Aircraft Establishment, Farnborough, 1950.

[12] Deltatsys, "Positive Displacement vs Centrifugal Pump," http://www.deltatsys.com/resources/pd-pump-centrifugal-pump [cited 30.05.2016

[13] The Engineering Toolbox, "Bernoulli Equation," http://www.engineeringtoolbox.com/bernouilli-equation-d_183.html [cited 31.08.2016

[14] Hayes Pump, "Positive Displacement Pump or Centrifugal – Which one do you need?" https://hayespump.com/positive-displacement-pump/ [cited 22.06.2017

[15] Karassik, I., J., Messina, J., P., Cooper, P., "Pump Handbook," McGraw-Hill, United States, 2008,

[16] Sutton, G.P., and Biblarz, O., "Rocket Propulsion Elements," John Wiley & Sons, Inc., New Jersey, 2010,

[17] The Engineering Toolbox, "NPSH - Net Positive Suction Head," http://www.engineeringtoolbox.com/npsh-net-positive-suction-head-d_634.html [cited 25.06.2017

[18] Emerson, "Fisher Cavitation-Control Technologies," http://www.documentation.emersonprocess.com/groups/public/documents/brochures/d351912x012.pdf [cited 31.07.2016

[19] Benjamin, T.B., and Ellis, A.T., "The Collapse of Cavitation Bubbles and the Pressures thereby Produced against Solid Boundaries," Vol. 260, No. 1110, 1966, pp. 31.07.2016.

[20] ESWT, [online database]http://eswt.net/wp-content/uploads/2011/10/cavitation.gif [cited 30.07.2016

[21] Anonymous "Cavitation Propeller Damage," https://commons.wikimedia.org/wiki/File:Cavitation_Propeller_Damage.JPG [cited 07.08.2016

[22] Christensen, D.L., "ROCKETDYNE MARK 3 TURBOPUMP," [online database]http://heroicrelics.org/info/h-1/mark-3-turbopump.html [cited 30.04.2017

[23] Douglass, H.W., Schmidt, H.W., Bailey, M.M., "TURBOPUMP SYSTEMS FOR LIQUID ROCKET ENGINES," NASA, Springfield, Virginia, 1974.

[24] Hill, C.N., "A Vertical Empire," Imperial College Press, London, 2012,

[25] Campen, B., "XCOR Piston Pumps – the Holy Grail," http://mail.xcor.com/blog/pumpsandgrails/ [cited 03.08.2016

[26] XCOR Aerospace, "XCOR PISTON PUMPS- THE HOLY GRAIL," http://www.xcor.com/news/xcor-piston-pumps-the-holy-grail/ [cited 21.08.2016

[27] Cannon, J.L., "Liquid Propulsion: Propellant Feed System Design," Encyclopedia of Aerospace Engineering, Volume 2, Wiley Publishers, 2010,

[28] Huzel, D.K., and Huang, D.H., "DESIGN OF LIQUID PROPELLANT ROCKET ENGINES," NASA, Washington, DC, 1967,

[29] Chaurette, J., "CENTRIFUGAL PUMP SPECIFIC SPEED PRIMER AND THE AFFINITY LAWS," http://www.pumpfundamentals.com/download-free/spec_speed_primer.pdf [cited 05.08.2016

[30] Huzel, D.K., and Huang, D.H., "Modern Engineering for Design of Liquid-Propellant Rocket Engines," Vol. 147, AIAA, Washington, DC, 1992,

[31] Knoll-mb, http://www.knoll-mb.de/fileadmin/knoll_mb/aktuelles/bilder/Pressemitteilungen/B03_Knoll_Energieeffizienz_KTS_3D_silber.jpg [cited 01.05.2017

[32] Pump School, "Comparing 4 Types Of PD Pumps," http://www.pumpschool.com/intro/selection.asp [cited 10.07.2016

[33] Viking Pumps, "External Gear Pump," http://www.vikingpump.com/sites/vikingpump.dev/files/styles/210px-210px/public/Tech_External_2.png?itok=zXgQ8XyS [cited 02.05.2017

[34] Viking Pumps, "Internal Gear Pump," http://www.vikingpump.com/sites/vikingpump.dev/files/styles/210px-210px/public/Tech_Internal_1.png?itok=JGtxoL9_ [cited 02.05.2017

[35] Viking Pumps, "Vane Pump," http://www.vikingpumpeurope.com/sites/vikingpump.dev/files/styles/750_wide_variable_height/public/Cut_Lobe.png?itok=CqVJPI1H [cited 02.05.2017

[36] Corken, "Sliding Vane Pumps Explained," http://www.corken.com/sliding_vane_technology [cited 18.07.2016

[37] PromoTec, "Wanner Hydra-Cell T-serie," https://www.promotec.nl/producten/verdringerpompen/niet-magneetgekoppeld/membraanpompen/wanner-hydra-cell-t-serie/ [cited 11.07.2017

[38] TS7 StudyZone, "Radial Piston Pump Working Animation With Detail Explanation," https://www.youtube.com/watch?v=2T-6jDm_ebI [cited 19.01.2019

[39] Wikipedia, "Axial piston pump," https://en.wikipedia.org/wiki/Axial_piston_pump [cited 19.01.2019

[40] ACD CRYO, "Reciprocating Pumps," http://www.acdcryo.com/reciprocating_pumps.asp [cited 23.07.2016

[41] ACD CRYO, "X9 Series," http://www.acdcryo.com/brochures/X9%20Series.pdf [cited 23.07.2016

[42] Campen, B., "LIQUID OXYGEN PISTON PUMP READY FOR REUSABLE SPACE FLIGHT," http://www.xcor.com/news/liquid-oxygen-piston-pump-ready-for-reusable-space-flight/ [cited 2017.01.04

[43] XCOR Aerospace, "Nitrogen-pump," http://www.xcor.com/media/5945/09-01-16_nitrogen-pump-1592.jpg [cited 06.09.2016

[44] Miller, J.M., "THE RECIPROCATING PUMP THEORY, DESIGN, AND USE," KRIEGER PUBLISHING COMPANY, Florida, 1995,

[45] Henshaw, T., "Acceleration Head," http://www.pumpsandsystems.com/topics/pumps/centrifugal-pumps/acceleration-head [cited 09.08.2016

[46] United States Plastic Corporation, "What does cracking pressure mean?" http://www.usplastic.com/knowledgebase/article.aspx?contentkey=870 [cited 25.08.2016

[47] Motor Car, "Engine Poppet valve," http://www.motor-car.co.uk/engine-components/item/14731-valve-poppet [cited 04.05.2016

[48] GlobalSpec, "Check Valves Information," https://www.globalspec.com/learnmore/flow_control_flow_transfer/valves/check_valves [cited 29.01.2019

[49] ChemValve, "Model 880 Lined Ball Check Valve," http://www.nilcor.com/check-valves.php [cited 03.05.2017

[50] Wikimedia, "Sleeve Valve Closeup," https://upload.wikimedia.org/wikipedia/commons/d/d8/Sleeve_Valve_Closeup.JPG [cited 03.05.2017

[51] Motorcross Action Magazine, "TEN THINGS YOU NEED TO KNOW ABOUT REED VALVES," http://motocrossactionmag.com/news/10-things-you-need-to-know-about-reed-valves [cited 03/12/2016

[52] Karting Magazine, "Tech Talk: Reeds," http://www.kartingmagazine.com/features/technical/tech-talk-reeds/ [cited 03.12.2016

[53] DeLong, D.L., Valant, M.E., and Greason, J.K., "High-speed check valve suitable for cryogens and high reverse pressure," 2012,

[54] Bikeman Performance, "V-Force 3 Reed Valves," https://bikemanperformance.ca/v-force-3-reed-valves.html [cited 04.05.2017

[55] Starling, R., "New study: compressed natural gas for automobile use," https://www.energyglobal.com/downstream/gas-processing/27052015/new-study-compressed-natural-gas-for-automobile-use-851/ [cited 04.12.2016

[56] Zahroof Valves Inc, "The Straight Flow Valve," http://zahroofvalves.com/products.html [cited 04.12.2016

[57] Cozzani, "CC: Thermoplastic Profile Ring Valve," http://www.cozzani.com/compressor-valves/cc-thermoplastic-profile-ring-valve/ [cited 04.05.2017

[58] Duk, "Pressure fed rocket cycle," https://commons.wikimedia.org/wiki/File:Pressure_fed_rocket_cycle.svg [cited 04.05.2017

[59] Harrington, S., "Launch Vehicle and Spacecraft System Design Using the Pistonless Pump," No. AIAA-RS2 2004-7004, 2004,

[60] Pacheco, N., "HELIUM," http://minerals.usgs.gov/minerals/pubs/commodity/helium/mcs-2009-heliu.pdf [cited 10.12.2016

[61] Flometrics, I., "How the pistonless pump operates," http://www.rocketfuelpump.com/technology/operation/ [cited 06.05.2017

[62] Hooser, K.V., Bailey, J., and Majumdar, A., "NUMERICAL PREDICTION OF TRANSIENT AXIAL THRUST AND INTERNAL FLOWS IN A ROCKET ENGINE TURBOPUMP," Vol. AIAA-99-2189, 1999, pp. 07.08.2016.

[63] Groth, C., and Zingg, D.W. eds., "Computation Fluid Dynamics 2004: Proceedings of the Third International Conference on Computational Fluid Dynamics," Springer, New York, 2004,

[64] GemmeCotti, "EM-P Atex Roatary Vane Pump," http://www.gemmecotti.com/en/atex-pumps/em-p.html [cited 19.07.2016

[65] McKeei, K., Street, M., Remillard, C., "Advancing ORS Technologies and Capabilities with a Space Tourist Suborbital Vehicle," Vol. AIAA 2009-6690, 2009, pp. 1.

[66] David, L.A., "Mass Estimation Relations," http://spacecraft.ssl.umd.edu/academics/483F09/483F09L13.mass_est/483F09L13.MER.pdf [cited 21.05.2017

[67] Yu, J., "Lecture 2: Atmospheric Thermodynamics," https://www.ess.uci.edu/~yu/class/ess55/lecture.2.thermodynamics.pdf [cited 01.06.2017

[68] The Engineering Toolbox, "Universal and Individual Gas Constants," http://www.engineeringtoolbox.com/individual-universal-gas-constant-d_588.html [cited 01.06.2017

[69] Porwal, G.P., "High Specific Speed in Circulating Water Pump Can Cause Cavitation, Noise and Vibration," Vol. 9, No. 12, 2015, pp. 2103-2115.

[70] McKee, K., Street, M., and Remillard, C., "Advancing ORS Technologies and Capabilities with a Space Tourist Suborbital Vehicle," No. AIAA 2009-6690, 2009, pp. 1-13.

[71] XCOR Aerospace, "Rocket Propulsion & Spacecraft," https://xcor.com/ [cited 08.08.2017

[72] Mhwirth, "Triplex Double-acting Piston Diaphragm Pumps," http://mhwirth.com/our-products/slurry-pumps/triplex-double-acting-piston-diaphragm-pumps/ [cited 09.08.2017

[73] NIST, "Thermophysical Properties of Fluid Systems," [online database]http://webbook.nist.gov/chemistry/fluid/ [cited 22.03.2017

[74] XCOR Aerospace, "Piston Pumps," https://xcor.com/propulsion/piston-pumps/ [cited 21.07.2017

[75] SKF, "Polyurethane U-cup rod seals," http://www.skf.com/uk/products/seals/industrial-seals/hydraulic-seals/rod-and-buffer-seals/rod-seals/polyurethane-u-cup-rod-seals/index.html [cited 15.06.2017

[76] MatWeb, "Overview of materials for Acrylic, Extruded," http://www.matweb.com/search/DataSheet.aspx?MatGUID=632572aeef2a4224b5ac8fbd4f1b6f77 [cited 15.08.2017

[77] MatWeb, "Overview of materials for PVC, Extruded," http://www.matweb.com/search/DataSheet.aspx?MatGUID=bb6e739c553d4a34b199f0185e92f6f7 [cited 15.08.2017

[78] MatWeb, "Aluminum 6061-T6; 6061-T651," http://www.matweb.com/search/DataSheet.aspx?MatGUID=b8d536e0b9b54bd7b69e4124d8f1d20a [cited 29.06.2017

[79] NIST, "Cryogenic Material Properties Index," https://www.nist.gov/mml/acmd/structural-materials-group/cryogenic-material-properties-index [cited 26.06.2017

[80] Total Materia, "Properties of Aluminum Alloys at Cryogenic and Elevated Temperatures," http://www.totalmateria.com/Article23.htm [cited 27.06.2017

[81] NiDL, "Materials for Cryogenic Service: Engineering Properties of Austenitic Stainless Steel," https://www.nickelinstitute.org/~/media/Files/TechnicalLiterature/MaterialsforCryogenicService_EngineeringPropertiesofAusteniticStainlessSteel_4368_.ashx [cited 30.06.2017

[82] Total Materia, "Titanium Alloys and Their Characteristics: Part One," http://www.totalmateria.com/page.aspx?ID=CheckArticle&site=ktn&NM=218 [cited 30.06.2017

[83] Virginia Polytechnic Institute and State University, "Structure And Form Analysis System (SAFAS)," http://www.setareh.arch.vt.edu/safas/007_fdmtl_29_stress_due_to_temperature_change.html [cited 21.08.2017

[84] Mathalino, "Thermal Stress," http://www.mathalino.com/reviewer/mechanics-and-strength-of-materials/thermal-stress [cited 21.08.2017

[85] MatWeb, "Aluminum 7475-T61," http://www.matweb.com/search/DataSheet.aspx?MatGUID=9301e602923c4bca973c5856a82249ca [cited 29.06.2017

[86] MatWeb, " Aluminum 5083-O," http://www.matweb.com/search/DataSheet.aspx?MatGUID=d105c2a24d6942cdad79259f770fb806 [cited 29.06.2017

[87] Penflex, "Austenitic Steels: Mechanical Properties at Cryogenic Temperatures," http://www.penflex.com/austenitic-steels-mechanical-properties-at-cryogenic-temperatures/ [cited 30.06.2017

[88] MatWeb, "304 Stainless Steel," http://www.matweb.com/search/DataSheet.aspx?MatGUID=abc4415b0f8b490387e3c922237098da&ckck=1 [cited 30.06.2017

[89] MatWeb, "316 Stainless Steel, annealed sheet," http://www.matweb.com/search/DataSheet.aspx?MatGUID=50f320bd1daf4fa7965448c30d3114ad [cited 30.06.2017

[90] MatWeb, "347 Stainless Steel, annealed, sheet," http://www.matweb.com/search/DataSheet.aspx?MatGUID=674116a5648146d2b1916a84599e4dd6 [cited 30.06.2017

[91] MatWeb, "Titanium Ti-5Al-2.5Sn (Grade 6)," http://www.matweb.com/search/DataSheet.aspx?MatGUID=e234a0ea74ea4680b116a1bccd59ca00 [cited 30.06.2017

[92] Triton Alloys Inc., "7475 Aluminum Plate," http://www.tritonalloysinc.com/aluminum/aluminum-plate-aluminum-plates/aluminum-plate-type-7475-plate/ [cited 01.07.2017

[93] Parker Hannifin GmbH, "PTFE Seals Guide," http://www.parker.com/literature/Praedifa/Catalogs/Catalog_PTFE-Seals_PTD3354-EN.pdf [cited 02.07.2017

[94] The Engineering Toolbox, "Friction and Friction Coefficients," http://www.engineeringtoolbox.com/friction-coefficients-d_778.html [cited 19.07.2017

[95] SKF, "Single-acting piston seals," http://www.skf.com/group/products/seals/industrial-seals/hydraulic-seals/piston-seals/single-acting-piston-seals/index.html [cited 22.08.2017

[96] Bikez, "KTM 65 SX 2008," http://www.bikez.com/motorcycles/ktm_65_sx_2008.php [cited 18.08.2017

[97] Thermocoupleinfo, "Type K Thermocouple," http://www.thermocoupleinfo.com/type-k-thermocouple.htm [cited 12.07.2017

[98] The Engineering Toolbox, "Coefficients of Linear Thermal Expansion," http://www.engineeringtoolbox.com/linear-expansion-coefficients-d_95.html [cited 02.07.2017

[99] Saint-Gobain, "Innovative Sealing & Polymer Solutions," https://www.seals.saint-gobain.com/sites/imdf.seals.com/files/saint-gobainseals_omniseal_handbook_eu.pdf [cited 26.07.2017

[100] The Engineering Toolbox, "Thermal Conductivity of common Materials and Gases," http://www.engineeringtoolbox.com/thermal-conductivity-d_429.html [cited 30.08.2017

Appendices

A. Mass Model

a. Turbopump

In Figure A-1, Table 1 The GLOM and L/D ratio of the vehicle are displayed. In Table 2, the assumed Delta-v and the split across each stage is recorded, followed by the target L/D ratio and payload mass. The assumptions in Table 3 were used for estimating the mass of the propellant and tanks and for estimating thrust chamber mass – it refers to Table 4. The 1st stage used a cluster of three 2nd stage engines, thus Table 5 was used to ensure that the engines on both stages deliver a similar amount of thrust.

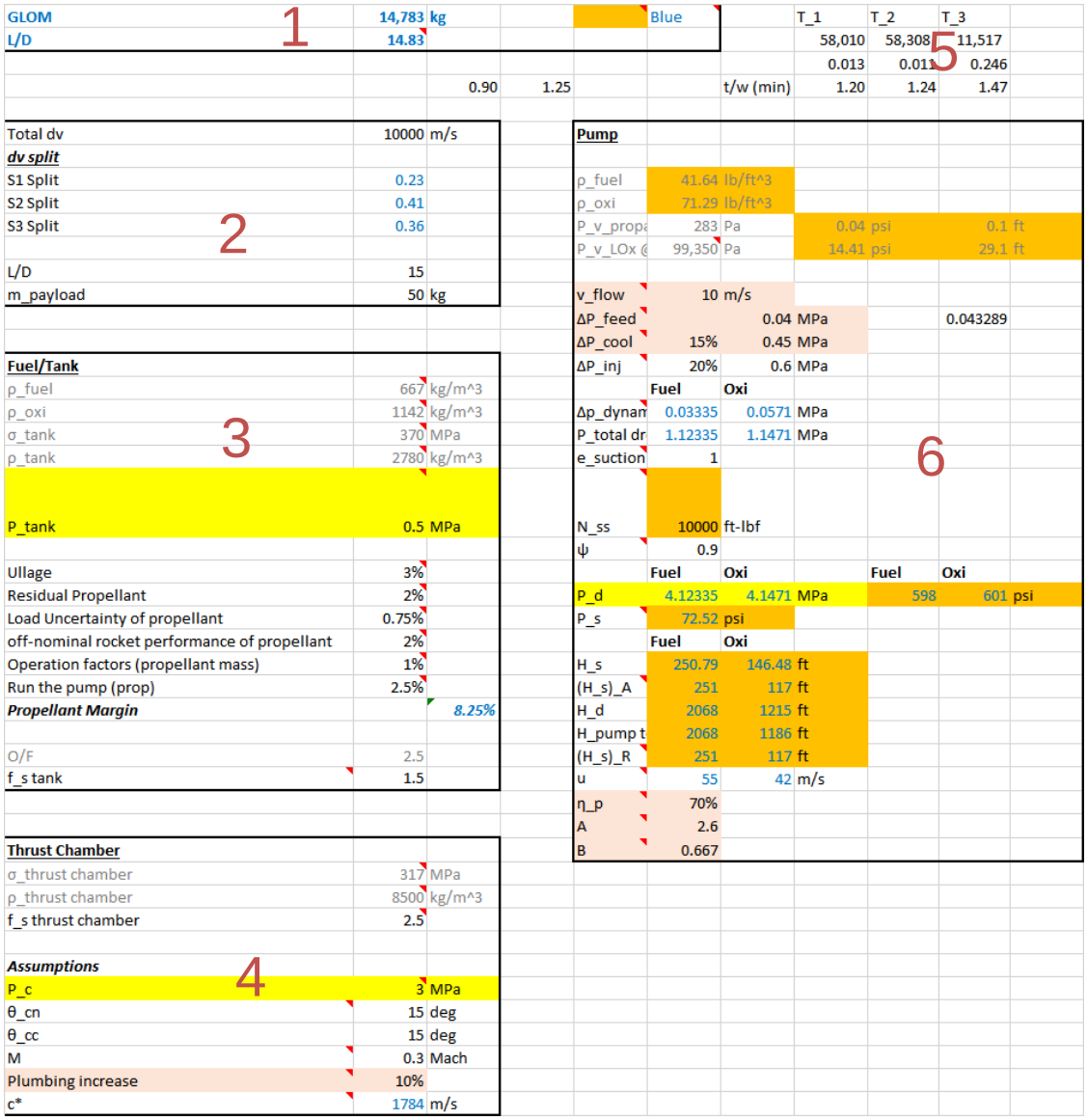

GLOM	14,783	kg			Blue		T_1	T_2	T_3	
L/D	14.83						58,010	58,308	11,517	
							0.013	0.011	0.246	
		0.90	1.25			t/w (min)	1.20	1.24	1.47	
Total dv	10000	m/s		**Pump**						
dv split										
S1 Split	0.23			ρ_fuel	41.64	lb/ft^3				
S2 Split	0.41			ρ_oxi	71.29	lb/ft^3				
S3 Split	0.36			P_v_propa	283	Pa	0.04	psi	0.1	ft
				P_v_LOx @	99,350	Pa	14.41	psi	29.1	ft
L/D	15									
m_payload	50	kg		v_flow	10	m/s				
				ΔP_feed		0.04	MPa		0.043289	
Fuel/Tank				ΔP_cool	15%	0.45	MPa			
ρ_fuel	667	kg/m^3		ΔP_inj	20%	0.6	MPa			
ρ_oxi	1142	kg/m^3			**Fuel**	**Oxi**				
σ_tank	370	MPa		Δp_dynam	0.03335	0.0571	MPa			
ρ_tank	2780	kg/m^3		P_total dr	1.12335	1.1471	MPa			
				e_suction	1					
P_tank	0.5	MPa		N_ss	10000	ft-lbf				
				ψ	0.9					
Ullage	3%				**Fuel**	**Oxi**		**Fuel**	**Oxi**	
Residual Propellant	2%			P_d	4.12335	4.1471	MPa	598	601	psi
Load Uncertainty of propellant	0.75%			P_s	72.52	psi				
off-nominal rocket performance of propellant	2%				**Fuel**	**Oxi**				
Operation factors (propellant mass)	1%			H_s	250.79	146.48	ft			
Run the pump (prop)	2.5%			(H_s)_A	251	117	ft			
Propellant Margin			***8.25%***	H_d	2068	1215	ft			
				H_pump t	2068	1186	ft			
O/F	2.5			(H_s)_R	251	117	ft			
f_s tank	1.5			u	55	42	m/s			
				η_p	70%					
Thrust Chamber				A	2.6					
σ_thrust chamber	317	MPa		B	0.667					
ρ_thrust chamber	8500	kg/m^3								
f_s thrust chamber	2.5									
Assumptions										
P_c	3	MPa								
θ_cn	15	deg								
θ_cc	15	deg								
M	0.3	Mach								
Plumbing increase	10%									
c*	1784	m/s								

Figure A-1: Turbopump Assumptions

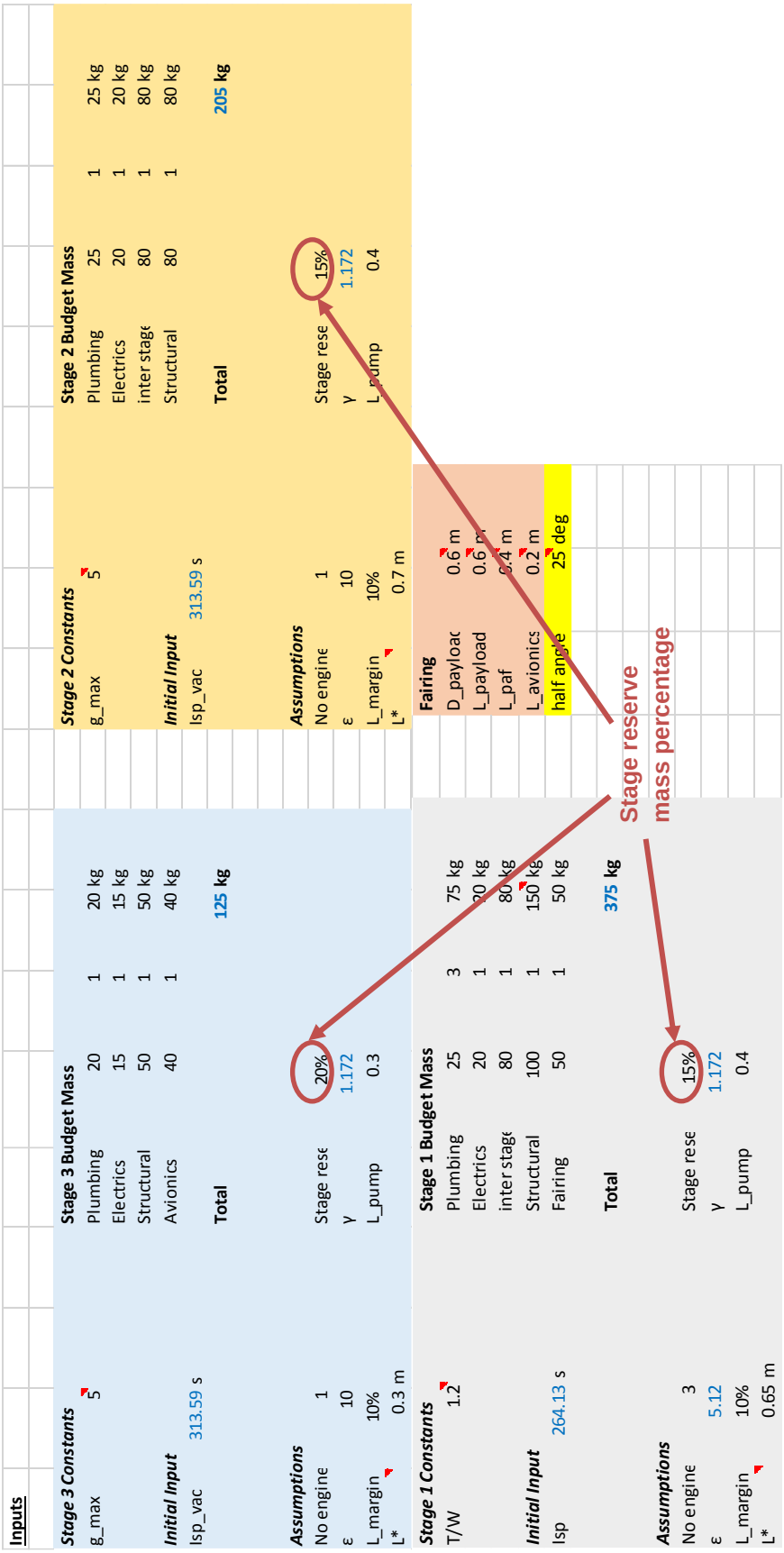

Figure A-2: Inert Mass & Size Assumptions of Turbopump

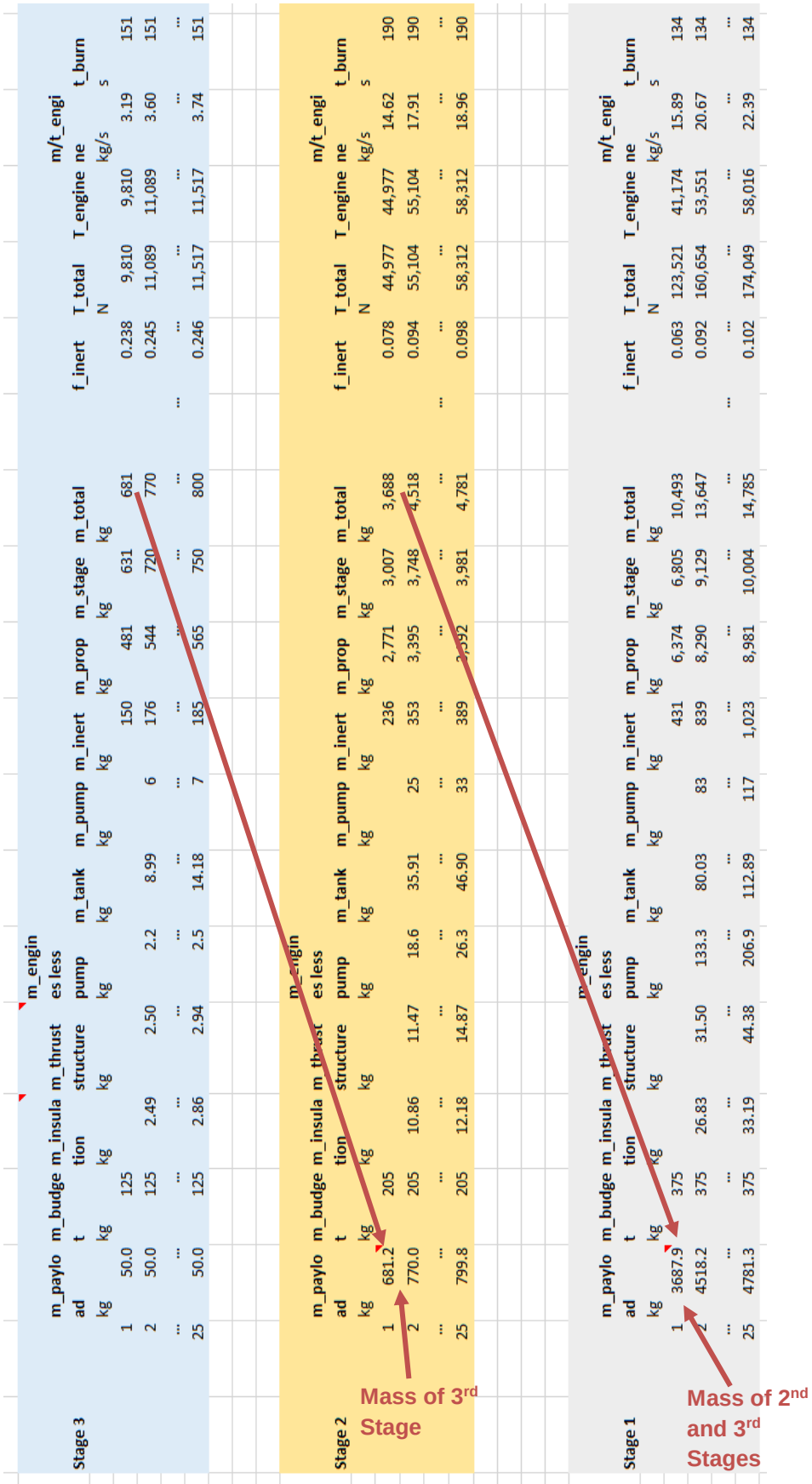

Figure A-3: System Mass Estmate for Turbopump

Thrust Chamber																
A_t	D_t	A_c	L_c	D_c	L_c/D_c	t_w	m_c	A_e	D_e	L_n	m_n	m_thrust chamber
m^2	m	m^2	m	m		m	kg	m^2	m	m	kg	kg
0.002	0.05	0.004	0.14	0.07	2.04	0.0010	0.34	0.019	0.155	0.20	0.54	2.20
0.002	0.05	0.004	0.14	0.08	1.92	0.0010	0.36	0.021	0.165	0.21	0.61	2.44
...	...	...	...	...	...	...	...	...	...	...	...	...
0.002	0.05	0.005	0.14	0.08	1.88	0.0010	0.37	0.022	0.168	0.21	0.64	2.52

Thrust Chamber																
A_t	D_t	A_c	L_c	D_c	L_c/D_c	t_w	m_c	A_e	D_e	L_n	m_n	m_thrust chamber
m^2	m	m^2	m	m		m	kg	m^2	m	m	kg	kg
0.009	0.11	0.018	0.34	0.15	2.22	0.0018	2.98	0.087	0.333	0.42	4.45	18.58
0.011	0.12	0.022	0.34	0.17	2.01	0.0020	3.72	0.106	0.368	0.47	6.04	24.40
...	...	...	...	...	...	...	...	...	...	...	...	...
0.011	0.12	0.023	0.34	0.17	1.95	0.0020	3.96	0.113	0.379	0.48	6.57	26.33

Thrust Chamber																
A_t	D_t	A_c	L_c	D_c	L_c/D_c	t_w	m_c	A_e	D_e	L_n	m_n	m_thrust chamber
m^2	m	m^2	m	m		m	kg	m^2	m	m	kg	kg
0.009	0.11	0.020	0.31	0.16	1.98	0.0019	3.07	0.048	0.248	0.26	2.31	40.40
0.012	0.13	0.026	0.31	0.18	1.73	0.0021	4.11	0.063	0.283	0.29	3.43	56.54
...	...	...	...	...	...	...	...	...	...	...	...	...
0.013	0.13	0.028	0.31	0.19	1.67	0.0022	4.49	0.068	0.295	0.31	3.87	62.69

Figure A-4: Thrust Chamber Mass Estimate

Propellant Tanks

D_stage	V_sphere	m_fuel	m_oxi	V_fuel	V_oxi	V_fuel tank	V_oxi tank	L_cyl fuel	L_cyl oxi	t_wall	m_spher e	m_cyl	m_bulkh ead	m_tank
m	m^3	kg	kg	m^3	m^3	m^3	m^3	m	m	m	kg	kg	kg	kg
0.80	0.268	137	344	0.21	0.30	0.21	0.31	0	0.08343	0.0010	5.6	0.6	2.8	8.99
0.85	0.322	155	389	0.23	0.34	0.24	0.35	0	0.050906	0.0010	6.3	0.4	3.2	9.87
...	...	...	...	...	...	...	...	...	...	...	...	...	...	...
0.90	0.382	161	404	0.24	0.35	0.25	0.36	0	0	0.0010	7.1	0.0	3.5	14.18

Propellant Tanks

D_stage	V_sphere	m_fuel	m_oxi	V_fuel	V_oxi	V_fuel tank	V_oxi tank	L_cyl fuel	L_cyl oxi	t_wall	m_spher e	m_cyl	m_bulkh ead	m_tank
m	m^3	kg	kg	m^3	m^3	m^3	m^3	m	m	m	kg	kg	kg	kg
1.10	0.697	792	1979	1.19	1.73	1.22	1.79	0.55	1.15	0.0011	11.8	18.2	5.9	35.91
1.15	0.796	970	2425	1.45	2.12	1.50	2.19	0.68	1.34	0.0012	13.5	23.6	6.7	43.84
...	...	...	...	...	...	...	...	...	...	...	...	...	...	...
1.25	1.023	1026	2566	1.54	2.25	1.59	2.31	0.46	1.05	0.0013	17.3	20.9	8.7	46.90

Propellant Tanks

D_stage	V_sphere	m_fuel	m_oxi	V_fuel	V_oxi	V_fuel tank	V_oxi tank	L_cyl fuel	L_cyl oxi	t_wall	m_spher e	m_cyl	m_bulkh ead	m_tank
m	m^3	kg	kg	m^3	m^3	m^3	m^3	m	m	m	kg	kg	kg	kg
1.10	0.697	1821	4553	2.73	3.99	2.81	4.11	2.23	3.59	0.0011	11.8	62.3	5.9	80.03
1.15	0.796	2368	5921	3.55	5.18	3.66	5.34	2.75	4.37	0.0012	13.5	83.5	6.7	103.78
...	...	...	...	...	...	...	...	...	...	...	...	...	...	...
1.25	1.023	2566	6415	3.85	5.62	3.96	5.79	2.40	3.88	0.0013	17.3	86.9	8.7	112.89

Figure A-5: Propellant Tank Mass Estimate

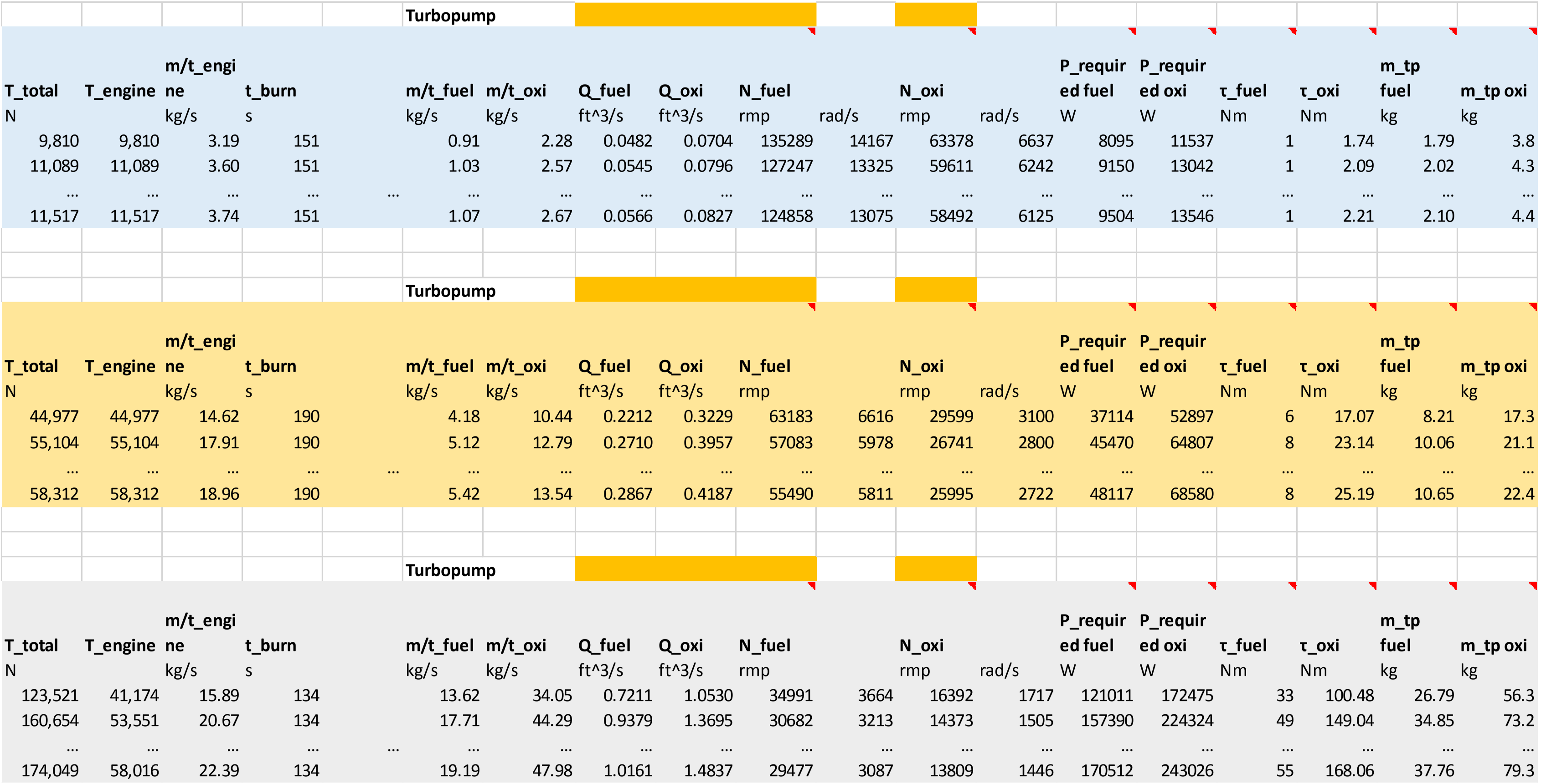

					Turbopump													
T_total	T_engine	m/t_engine	t_burn		m/t_fuel	m/t_oxi	Q_fuel	Q_oxi	N_fuel		N_oxi		P_required fuel	P_required oxi	τ_fuel	τ_oxi	m_tp fuel	m_tp oxi
N		kg/s	s		kg/s	kg/s	ft^3/s	ft^3/s	rmp	rad/s	rmp	rad/s	W	W	Nm	Nm	kg	kg
9,810	9,810	3.19	151		0.91	2.28	0.0482	0.0704	135289	14167	63378	6637	8095	11537	1	1.74	1.79	3.8
11,089	11,089	3.60	151		1.03	2.57	0.0545	0.0796	127247	13325	59611	6242	9150	13042	1	2.09	2.02	4.3
…	…	…	…	…	…	…	…	…	…	…	…	…	…	…	…	…	…	…
11,517	11,517	3.74	151		1.07	2.67	0.0566	0.0827	124858	13075	58492	6125	9504	13546	1	2.21	2.10	4.4

					Turbopump													
T_total	T_engine	m/t_engine	t_burn		m/t_fuel	m/t_oxi	Q_fuel	Q_oxi	N_fuel		N_oxi		P_required fuel	P_required oxi	τ_fuel	τ_oxi	m_tp fuel	m_tp oxi
N		kg/s	s		kg/s	kg/s	ft^3/s	ft^3/s	rmp		rmp	rad/s	W	W	Nm	Nm	kg	kg
44,977	44,977	14.62	190		4.18	10.44	0.2212	0.3229	63183	6616	29599	3100	37114	52897	6	17.07	8.21	17.3
55,104	55,104	17.91	190		5.12	12.79	0.2710	0.3957	57083	5978	26741	2800	45470	64807	8	23.14	10.06	21.1
…	…	…	…	…	…	…	…	…	…	…	…	…	…	…	…	…	…	…
58,312	58,312	18.96	190		5.42	13.54	0.2867	0.4187	55490	5811	25995	2722	48117	68580	8	25.19	10.65	22.4

					Turbopump													
T_total	T_engine	m/t_engine	t_burn		m/t_fuel	m/t_oxi	Q_fuel	Q_oxi	N_fuel		N_oxi		P_required fuel	P_required oxi	τ_fuel	τ_oxi	m_tp fuel	m_tp oxi
N		kg/s	s		kg/s	kg/s	ft^3/s	ft^3/s	rmp		rmp	rad/s	W	W	Nm	Nm	kg	kg
123,521	41,174	15.89	134		13.62	34.05	0.7211	1.0530	34991	3664	16392	1717	121011	172475	33	100.48	26.79	56.3
160,654	53,551	20.67	134		17.71	44.29	0.9379	1.3695	30682	3213	14373	1505	157390	224324	49	149.04	34.85	73.2
…	…	…	…	…	…	…	…	…	…	…	…	…	…	…	…	…	…	…
174,049	58,016	22.39	134		19.19	47.98	1.0161	1.4837	29477	3087	13809	1446	170512	243026	55	168.06	37.76	79.3

Figure A-6: Turbopump Mass Estimate

b. Pressure-fed

Figure A-7 shows the assumptions made in a pressure-fed system. This system does not require a pump so the table for estimating the mass of the pump, was replaced with a “Pressurant” table, which takes into an account the type of the pressurant used, the pressurant storing temperature ($T\_pressurant$; Figure A-7) and the pressurant temperature fed into propellant tanks (T_tank; Figure A-7).

m_total	**26,686**	**kg**			Blue			T_1	T_2	T_3
L/D	**15.99**							104,717	103,101	13,416
								0.143	0.133	0.210
	1.05	1.55					t/w (min)	1.2	1.227759	1.227759
Total dv	10000	m/s			**Other**					
dv split					v_flow	10	m/s			
S1 Split	0.18				ΔP_feed		0.04	MPa		
S2 Split	0.41				ΔP_cool	15%	0.15	MPa		
S3 Split	0.41				ΔP_inj	20%	0.2	MPa		
					Δp_dynam	0.0571	MPa			
L/D	16				P_total dr	0.4471	MPa			
m_payloa	50	kg								
					Pressurant					
					R_N2	297	J/(kg*K)			
Fuel/Tank					T_pressur	294	K			
ρ_fuel	667	kg/m^3			T_tank	294	K			
ρ_oxi	1142	kg/m^3								
σ_tank	370	MPa			He	2077	J/(kg*K)			
ρ_tank	2780	kg/m^3								
P_tank	1.447	MPa			**Thrust Chamber**					
					σ_thrust c	317	MPa			
Ullage	3%				ρ_thrust c	8500	kg/m^3			
Residual F	2%				f_s thrust	2.5				
Load Unce	0.75%									
off-nomin	2%				***Assumptions***					
Operation	1%				P_c	1	MPa			
Run press	1.0%				θ_cn	15	deg			
Propellant Margin		***6.75%***			θ_cc	15	deg			
					M	0.3	Mach			
O/F	2.5				Plumbing	10%				
f_s tank	1.5									
					c*	1745	m/s			

Figure A-7: Pressure-fed Assumptions

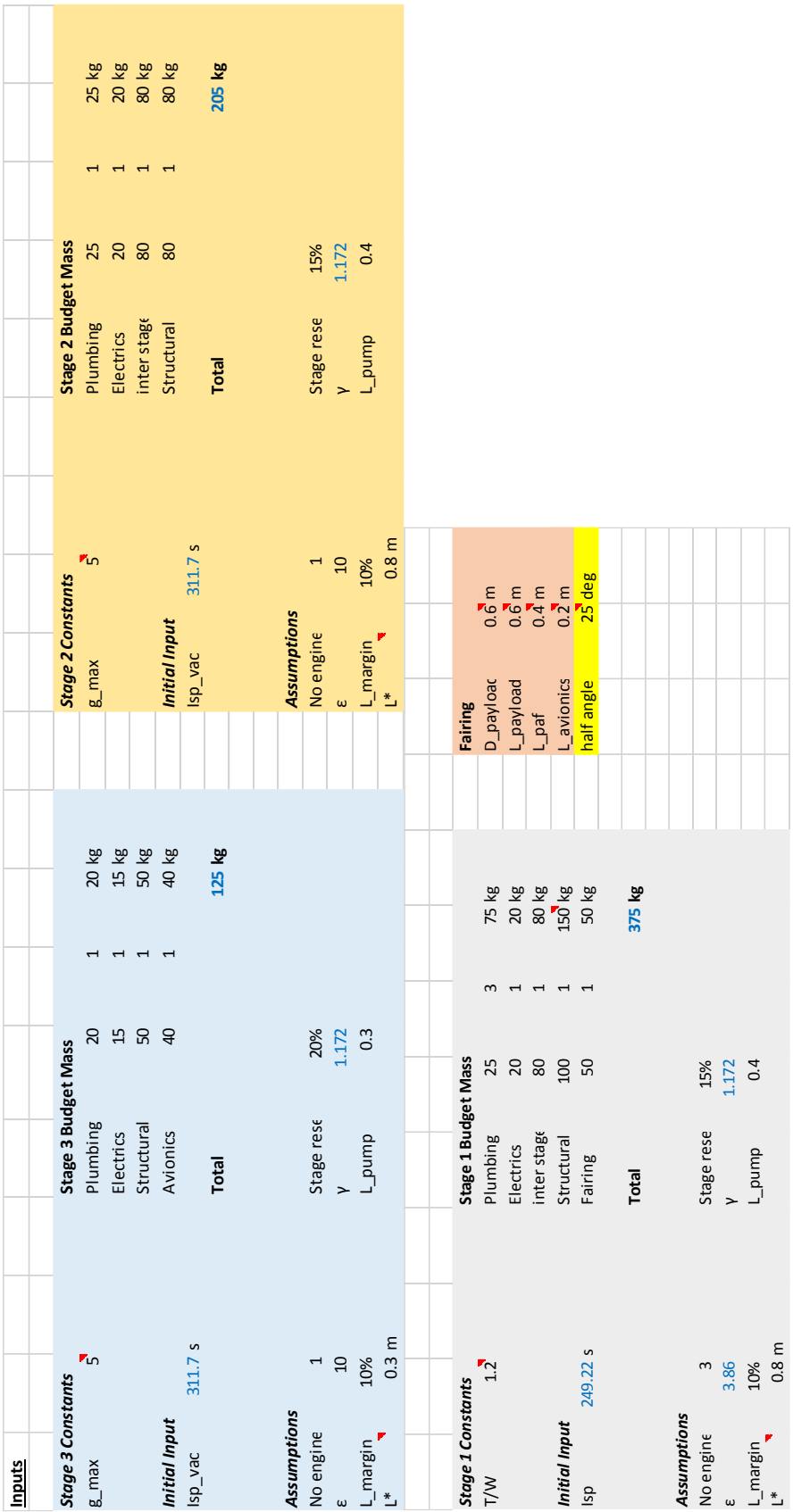

Figure A-8: Inert Mass & Size Assumptions of Pressure-fed

Pressurant tank				
P_pressure	V_s	R_sphere	t_tank	m_s tank
MPa	m^3	m	m	kg
30	0.032	0.20	0.01194	17.1
30	0.043	0.22	0.01318	22.9
...	...	...	...	...
30	0.046	0.22	0.01354	24.9
Pressurant tank				
P_pressure	V_s	R_sphere	t_tank	m_s tank
MPa	m^3	m	m	kg
30	0.167	0.34	0.02078	90
30	0.272	0.40	0.02443	146
...	...	...	...	...
30	0.355	0.44	0.02672	191
Pressurant tank				
P_pressure	V_s	R_sphere	t_tank	m_s tank
MPa	m^3	m	m	kg
30	0.340	0.43	0.02634	183
30	0.596	0.52	0.03175	321
...	...	...	...	...
30	0.855	0.59	0.03580	460

Figure A-9: Pressurant Tank Mass Estimate

Stage 3

	m_payload	m_budget	m_insulation	m_thrust structure	m_engines	m_tank	m_press urant	m_inert	m_prop	m_stage	m_total
	kg	t	kg	kg	kg	kg	kg	kg	kg	kg	kg
1	50.0	125						138	576	714	764
2	50.0	125	3.53	2.35	5.6	36.34	10.89	202	774	976	1026
...	...	...	...	...	...	...	...	...	...	...	...
25	50.0	125	3.89	3.42	7.8	47.21	15.88	224	840	1064	1114

Stage 2

	m_payload	m_budget	m_insulation	m_thrust structure	m_engines	m_tank	m_press urant	m_inert	m_prop	m_stage	m_total
	kg	t	kg	kg	kg	kg	kg	kg	kg	kg	kg
1	763.6	205						226	3039	3264	4028
2	1026.4	205	8.59	12.37	31.52	213.16	57.44	581	4938	5519	6546
...	...	...	...	...	...	...	...	...	...	...	...
25	1113.9	205	17.49	26.29	90.34	437.05	122.06	988	6458	7446	8560

Stage 1

	m_payload	m_budget	m_insulation	m_thrust structure	m_engines	m_tank	m_press urant	m_inert	m_prop	m_stage	m_total
	kg	t	kg	kg	kg	kg	kg	kg	kg	kg	kg
1	4028.0	375						413	6186	6598	10626
2	6545.7	375	19.24	31.90	167.0	415.00	116.91	1238	10842	12080	18625
...	...	...	...	...	...	...	...	...	...	...	...
25	8560.1	375	46.04	80.11	533.0	1028.29	293.61	2592	15535	18126	26686

Figure A-10: System Mass Estmate for Pressure-fed

c. Pistonless

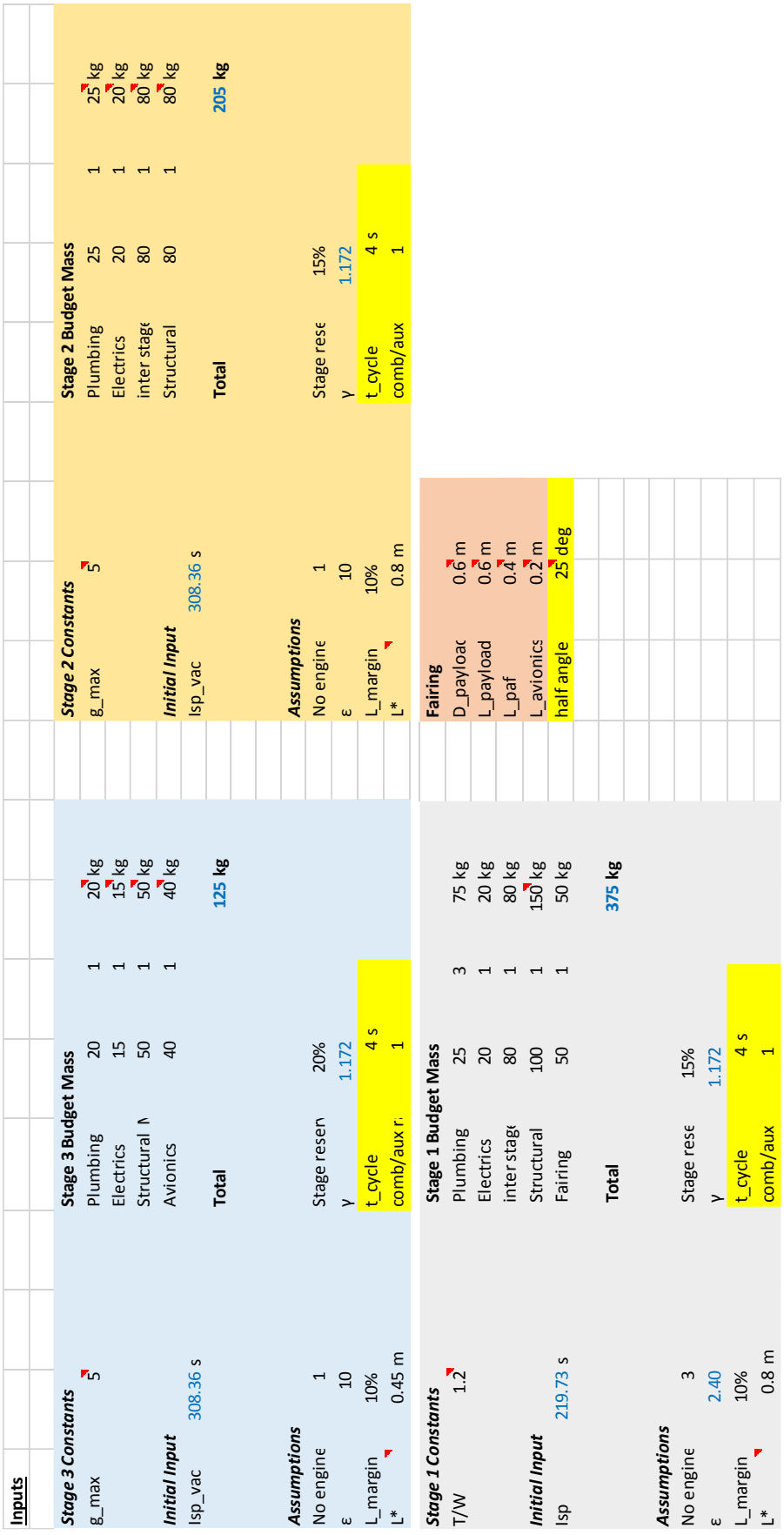

Figure A-11: Inert Mass & Size Assumptions of Pistonless

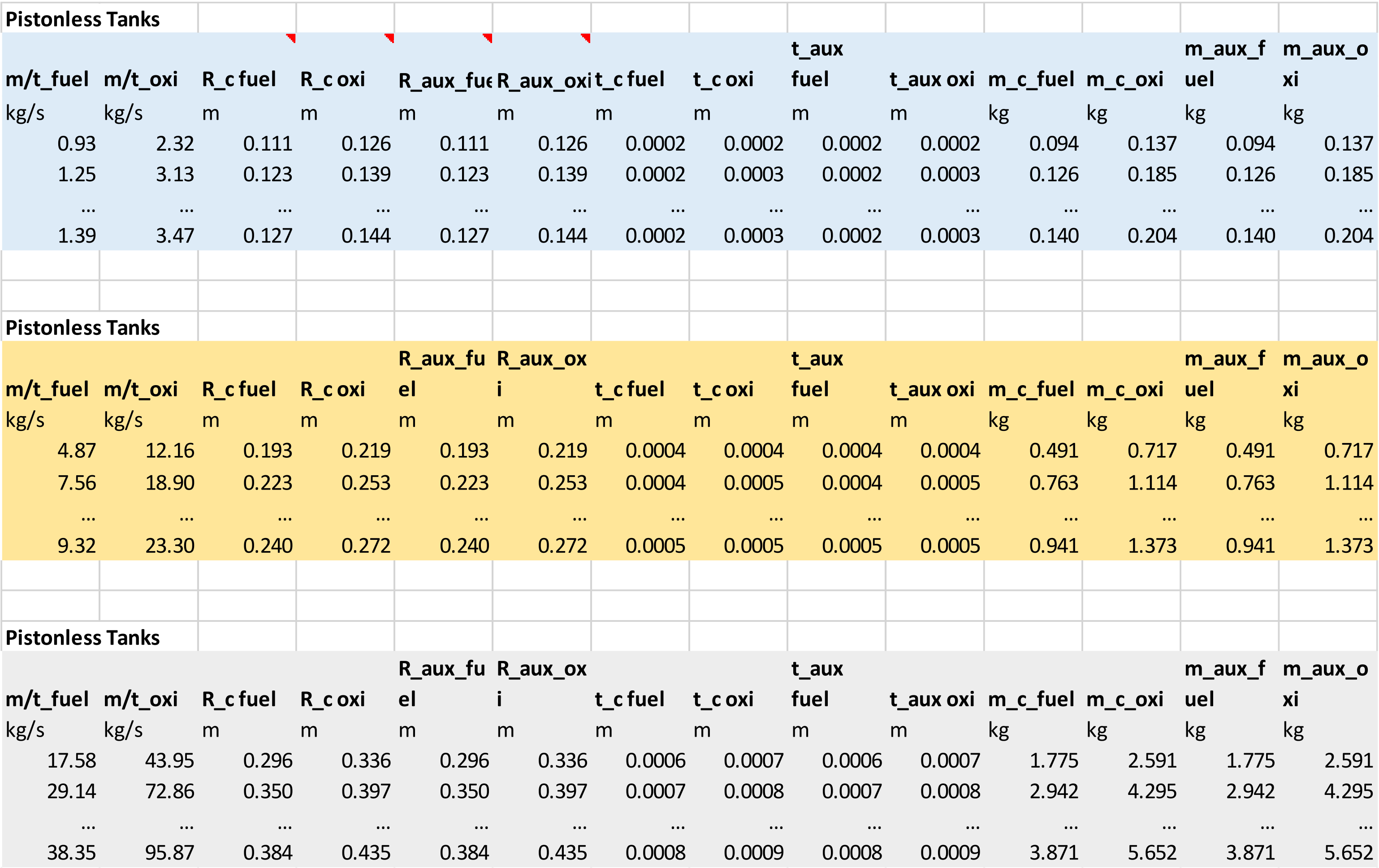

Pistonless Tanks

m/t_fuel	m/t_oxi	R_c fuel	R_c oxi	R_aux_fue	R_aux_oxi	t_c fuel	t_c oxi	t_aux fuel	t_aux oxi	m_c_fuel	m_c_oxi	m_aux_fuel	m_aux_oxi
kg/s	kg/s	m	m	m	m	m	m	m	m	kg	kg	kg	kg
0.93	2.32	0.111	0.126	0.111	0.126	0.0002	0.0002	0.0002	0.0002	0.094	0.137	0.094	0.137
1.25	3.13	0.123	0.139	0.123	0.139	0.0002	0.0003	0.0002	0.0003	0.126	0.185	0.126	0.185
…	…	…	…	…	…	…	…	…	…	…	…	…	…
1.39	3.47	0.127	0.144	0.127	0.144	0.0002	0.0003	0.0002	0.0003	0.140	0.204	0.140	0.204

Pistonless Tanks

m/t_fuel	m/t_oxi	R_c fuel	R_c oxi	R_aux_fuel	R_aux_oxi	t_c fuel	t_c oxi	t_aux fuel	t_aux oxi	m_c_fuel	m_c_oxi	m_aux_fuel	m_aux_oxi
kg/s	kg/s	m	m	m	m	m	m	m	m	kg	kg	kg	kg
4.87	12.16	0.193	0.219	0.193	0.219	0.0004	0.0004	0.0004	0.0004	0.491	0.717	0.491	0.717
7.56	18.90	0.223	0.253	0.223	0.253	0.0004	0.0005	0.0004	0.0005	0.763	1.114	0.763	1.114
…	…	…	…	…	…	…	…	…	…	…	…	…	…
9.32	23.30	0.240	0.272	0.240	0.272	0.0005	0.0005	0.0005	0.0005	0.941	1.373	0.941	1.373

Pistonless Tanks

m/t_fuel	m/t_oxi	R_c fuel	R_c oxi	R_aux_fuel	R_aux_oxi	t_c fuel	t_c oxi	t_aux fuel	t_aux oxi	m_c_fuel	m_c_oxi	m_aux_fuel	m_aux_oxi
kg/s	kg/s	m	m	m	m	m	m	m	m	kg	kg	kg	kg
17.58	43.95	0.296	0.336	0.296	0.336	0.0006	0.0007	0.0006	0.0007	1.775	2.591	1.775	2.591
29.14	72.86	0.350	0.397	0.350	0.397	0.0007	0.0008	0.0007	0.0008	2.942	4.295	2.942	4.295
…	…	…	…	…	…	…	…	…	…	…	…	…	…
38.35	95.87	0.384	0.435	0.384	0.435	0.0008	0.0009	0.0008	0.0009	3.871	5.652	3.871	5.652

Figure A-12: Auxiliary/Combustion Tank Estimate

B. Sizing and Acceleration Head Model

Fixed input values such as mass flow rate (m/t), O/F ratio, liquid compressibility constant (k), volumetric efficiency (η_v) and the number of pistons were recorded as shown in Figure B-1. The flow rates were determined in **Chapter 4**, section **4.3.2 Piston Pump Sizing & Analysis**. Compressibility, the constant (k) of water is 1.5 and this value was used because in **Chapter 4** it was shown that LOX and liquid propane share a similar volume reduction when compressed by 50bar [44]. A volumetric efficiency of 0.9 was assumed in this case. And finally, the number of pistons was specified to calculate the volume of each piston and intensity of the acceleration head.

m/t	30	kg/s
O/F	2.5	
k	1.5	
η_v	0.9	
m	1	

Figure B-1: Sizing and Acceleration Head Model - Fixed Values for Simplex Pump

The size of the pump for the propane and LOX were calculated separately, as shown in Figure B-2. Each table was further divided into two sections to estimate the size for the single-acting and double-acting configurations.

To determine the size of the cylinder, firstly the volumetric flow rates (Q) were calculated based on the propellant flow rate (m/t) and the density (ρ). This provided with the total volume which piston pump must displace in one second. To achieve this value, the volume of the bore was calculated (V) by defining the bore diameter ($D\_cylinder$) and stroke length (s). Then, the pump speed (n) required to deliver this volumetric flow rate was calculated using Equation B-1. As explained in **Chapter 4**, the bore dimension size was manually changed until the pump speed of approximately 1,000RPM were achieved.

$$n = \frac{6 \times 10^{10} Q}{Ams\eta_v} \tag{B-1}$$

Where n – speed of the pump (RPM), Q – volumetric flow rate (m^3/s), A – cross-sectional area of bore (mm), m – number of cylinders, s – stroke length (mm) and η_v – volumetric efficiency.

The acceleration head was calculated using Equation 2-10 to determine the inlet pressure requirements of the pump. The pump constant (c) was obtained from Table 2-2. It was assumed that propane is located above the LOX tank and the inlet pipe runs through the centre of the LOX tank. Further assumptions were made that the inlet pipe diameter (d_pipe) is 100mm and length (L) 4m and 1m for liquid propane and LOX respectively. Finally, the average flow velocity (v) was determined using Equation B-2. The acceleration head in terms of metres and bars were recorded in H_ac and P_ac respectively. To convert the acceleration to bar, Equation B-3 was used.

$$v = \frac{Q}{\left(\frac{d_{pipe}}{2} \times 10^{-3}\right)^2} \tag{B-2}$$

$$P_{ac} = \frac{g_0 \rho}{10^5} \quad \text{(B-3)}$$

To calculate the volume displaced in one second, the displacement had to be calculated first from Equation 4-2. This equation deduces the piston rod area (a). The same process for calculating the bore piston and acceleration head was used and this process was shown in Figure B-3 – Figure B-5.

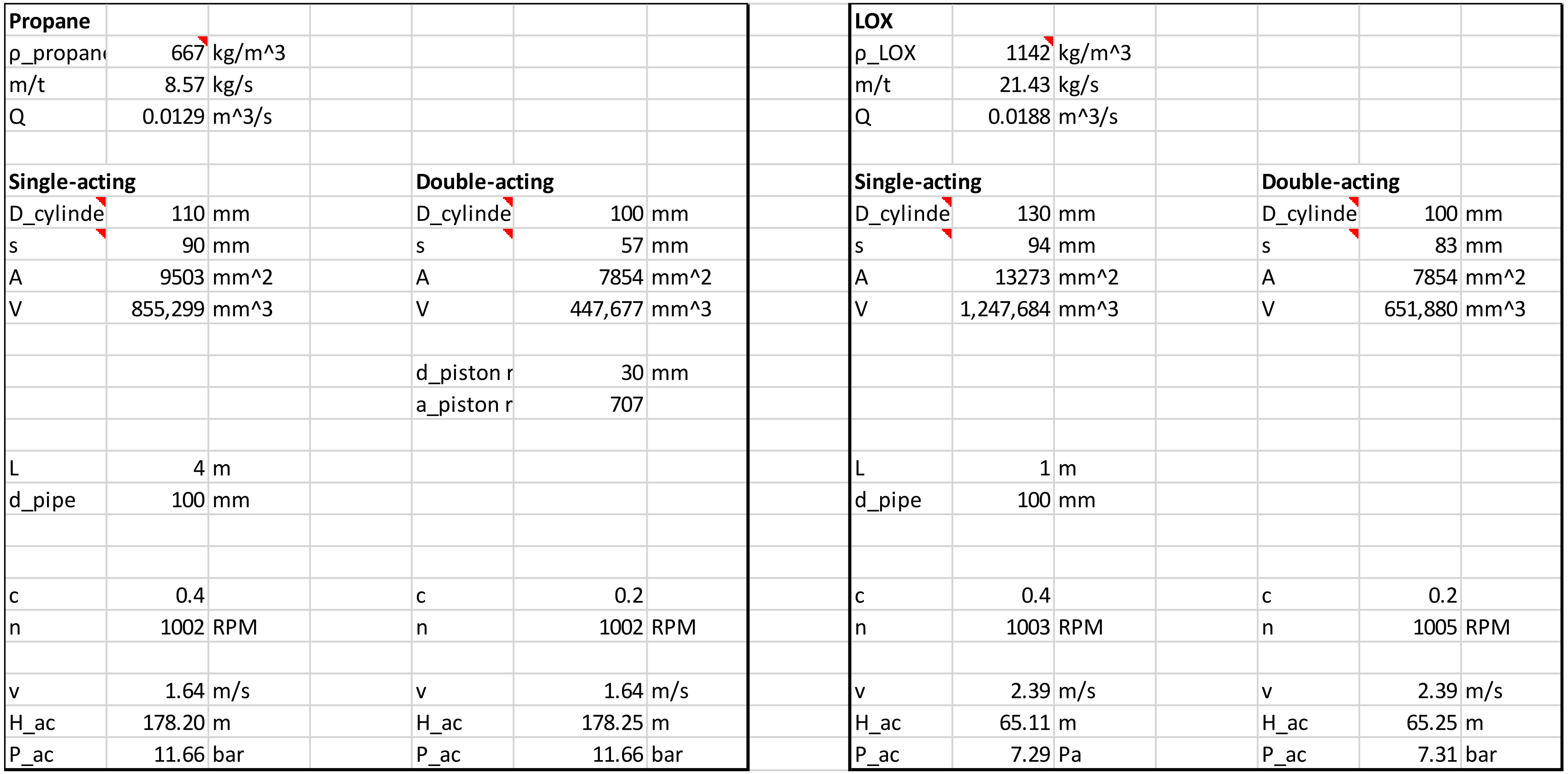

Propane						
ρ_propan	667	kg/m^3				
m/t	8.57	kg/s				
Q	0.0129	m^3/s				
Single-acting				**Double-acting**		
D_cylinde	110	mm		D_cylinde	100	mm
s	90	mm		s	57	mm
A	9503	mm^2		A	7854	mm^2
V	855,299	mm^3		V	447,677	mm^3
				d_piston r	30	mm
				a_piston r	707	
L	4	m				
d_pipe	100	mm				
c	0.4			c	0.2	
n	1002	RPM		n	1002	RPM
v	1.64	m/s		v	1.64	m/s
H_ac	178.20	m		H_ac	178.25	m
P_ac	11.66	bar		P_ac	11.66	bar

LOX						
ρ_LOX	1142	kg/m^3				
m/t	21.43	kg/s				
Q	0.0188	m^3/s				
Single-acting				**Double-acting**		
D_cylinde	130	mm		D_cylinde	100	mm
s	94	mm		s	83	mm
A	13273	mm^2		A	7854	mm^2
V	1,247,684	mm^3		V	651,880	mm^3
L	1	m				
d_pipe	100	mm				
c	0.4			c	0.2	
n	1003	RPM		n	1005	RPM
v	2.39	m/s		v	2.39	m/s
H_ac	65.11	m		H_ac	65.25	m
P_ac	7.29	Pa		P_ac	7.31	bar

Figure B-2: Sizing and Acceleration Head Model for Simplex Pump

m/t	30	kg/s
O/F	2.5	
k	1.5	
η_v	0.9	
m	2	

Propane		
ρ_propan	667	kg/m^3
m/t	8.57	kg/s
Q	0.0129	m^3/s
Single-acting		
D_cylinde	95	mm
s	60	mm
A	7088	mm^2
V	425,293	mm^3
L	4	m
d_pipe	100	mm
c	0.2	
n	1007	RPM
v	1.64	m/s
H_ac	89.60	m
P_ac	5.86	bar

Double-acting		
D_cylinde	75	mm
s	52	mm
A	4418	mm^2
V	229,729	mm^3
d_piston r	30	mm
a_piston r	707	
c	0.115	
n	1013	RPM
v	1.64	m/s
H_ac	90.14	m
P_ac	5.90	bar

LOX		
ρ_LOX	1142	kg/m^3
m/t	21.43	kg/s
Q	0.0188	m^3/s
Single-acting		
D_cylinde	115	mm
s	60	mm
A	10387	mm^2
V	623,213	mm^3
L	1	m
d_pipe	100	mm
c	0.2	
n	1004	RPM
v	2.39	m/s
H_ac	32.59	m
P_ac	3.65	bar

Double-acting		
D_cylinde	90	mm
s	52	mm
A	6362	mm^2
V	330,810	mm^3
c	0.115	
n	1001	RPM
v	2.389116	m/s
H_ac	32.50	m
P_ac	3.64	bar

Figure B-3: Sizing and Acceleration Head Model for Duplex Pump

m/t	30	kg/s
O/F	2.5	
k	1.5	
η_v	0.9	
m	3	

Propane		
ρ_propane	667	kg/m^3
m/t	8.57	kg/s
Q	0.0129	m^3/s
Single-acting		
D_cylinde	81	mm
s	55	mm
A	5,153	mm^2
V	283,415	mm^3
L	4	m
d_pipe	100	mm
c	0.066	
n	1008	RPM
v	1.64	m/s
H_ac	29.58	m
P_ac	1.94	bar

Double-acting		
D_cylinde	70	mm
s	40	mm
A	3,848	mm^2
V	153,938	mm^3
d_piston r	30	mm
a_piston r	707	
v	1.64	m/s
H_ac	29.98	m
P_ac	1.96	bar

LOX		
ρ_LOX	1142	kg/m^3
m/t	21.43	kg/s
Q	0.0188	m^3/s
Single-acting		
D_cylinde	90	mm
s	65	mm
A	6,362	mm^2
V	413,512	mm^3
L	1	m
d_pipe	100	mm
n	1008	RPM
v	2.39	m/s
H_ac	10.81	m
P_ac	1.21	Pa

Double-acting		
D_cylinde	80	mm
s	44	mm
A	5,027	mm^2
V	221,168	mm^3
n	1014	RPM
v	2.389116	m/s
H_ac	10.87	m
P_ac	1.22	bar

Figure B-4: Sizing and Acceleration Head Model for Triplex Pump

m/t	30	kg/s
O/F	2.5	
k	1.5	
η_v	0.9	
m	7	

Propane		
ρ_propane	667	kg/m^3
m/t	8.57	kg/s
Q	0.0129	m^3/s
Single-acting		
D_cylinde	62	mm
s	40	mm
A	3019	mm^2
V	120,763	mm^3
L	4	m
d_pipe	100	mm
c	0.028	
n	1013	RPM
v	1.64	m/s
H_ac	12.62	m
P_ac	0.83	bar

Double-acting		
D_cylinde	49	mm
s	39	mm
A	1886	mm^2
V	73,544	mm^3
d_piston r	30	mm
a_piston r	707	
n	1024	RPM
v	1.64	m/s
H_ac	12.75	m
P_ac	0.83	bar

LOX		
ρ_LOX	1142	kg/m^3
m/t	21.43	kg/s
Q	0.0188	m^3/s
Single-acting		
D_cylinde	80	mm
s	35	mm
A	5027	mm^2
V	175,929	mm^3
L	1	m
d_pipe	100	mm
n	1016	RPM
v	2.39	m/s
H_ac	4.62	m
P_ac	0.52	Pa

Double-acting		
D_cylinde	60	mm
s	35	mm
A	2827	mm^2
V	98,960	mm^3
n	1032	RPM
v	2.389116	m/s
H_ac	4.69	m
P_ac	0.53	bar

Figure B-5: Sizing and Acceleration Head Model for Septuplex Pump

C. Dynamics

a. Instantaneous Piston Displacement

Piston Displacement with respect to crank angle (see Figure 4-6, pg.56 for more details).

$$l^2 = r^2 + x^2 - 2rx\cos\theta$$

$$x^2 - 2(r\cos\theta)x + (r^2 - l^2) = 0$$

Using the quadratic formula x can be found.

$$x = \frac{-b \pm \sqrt{b^2 - 4ac}}{2a}$$

$$where\ a = 1, b = -2(r\cos\theta)\ and\ c = (r^2 - l^2)$$

$$x = \frac{2(r\cos\theta) \pm \sqrt{4(r\cos\theta)^2 - 4(r^2 - l^2)}}{2}$$

$$x = r\cos\theta \pm \sqrt{(r\cos\theta)^2 - (r^2 - l^2)} \rightarrow \therefore x = r\cos\theta \pm \sqrt{r^2\cos^2\theta - r^2 + l^2}$$

$$cos^2\,\theta = 1 - \sin^2\theta$$

$$x = r\cos\theta \pm \sqrt{r^2(1 - \sin^2\theta) - r^2 + l^2} \rightarrow \therefore\ x = r\cos\theta \pm \sqrt{l^2 - r^2\sin^2\theta}$$

Figure 4-6, x cannot be lower than zero, hence the negative value for x is ignored.

$$x = r\cos\theta + \sqrt{l^2 - r^2\sin^2\theta}$$

Piston Displacement with respect to time.

Assuming angular velocity (ω) is constant then it can be expressed in Equation C-1.

$$\omega = \frac{\theta}{t} \qquad \text{(C-1)}$$

Where t is time (s).

$$\therefore \boldsymbol{x = r\cos(\omega t) + \sqrt{l^2 - r^2\sin^2(\omega t)}}$$

b. Instantaneous Velocity

Instantaneous velocity with respect to time

$$x = r\cos(\omega t) + (l^2 - r^2\sin^2(\omega t))^{\frac{1}{2}}$$

$$\frac{dx}{dt} = -r\omega\sin(\omega t) + \frac{d}{dt}\left((l^2 - r^2\sin^2(\omega t))^{\frac{1}{2}}\right)$$

Using the chain rule, let $A = (l^2 - r^2\sin^2(\omega t)) = l^2 - r^2(\sin(\omega t))^2$

$$\frac{dA}{dt} = -2r^2\omega\sin\omega t\cos\omega t$$

From double angle identity:

$$\sin(2\omega t) = 2\sin(\omega t)\cos(\omega t)$$

$$\frac{dA}{d\theta} = -r^2\omega\sin(2\omega t)$$

$$x = -r\cos(\omega t) + A^{\frac{1}{2}}$$

$$\frac{dx}{dA} = \frac{1}{2}A^{-\frac{1}{2}} = \frac{1}{2}(l^2 - r^2\sin^2(\omega t))^{-\frac{1}{2}} = \frac{1}{2\sqrt{l^2 - r^2\sin^2(\omega t)}}$$

$$\frac{dx}{d\theta} = \frac{dx}{dA} \times \frac{dA}{d\theta} = \frac{1}{2\sqrt{l^2 - r^2\sin^2(\omega t)}} \times (-r^2\omega\sin(2\omega t)) - r\omega\sin(\omega t)$$

$$\boldsymbol{v = \frac{dx}{dt} = -\frac{r^2\omega\sin(2\omega t)}{2\sqrt{l^2 - r^2\sin^2(\omega t)}} - r\omega\sin(\omega t)}$$

c. Instantaneous Acceleration

$$a = \frac{d^2x}{dt^2} = \frac{dv}{dt}$$

$$\frac{dv}{dt} = -r\omega^2\cos(\omega t) + \frac{dv}{dt}\left(-\frac{r^2\omega\sin(2\omega t)}{2\sqrt{l^2 - r^2\sin^2(\omega t)}}\right)$$

Using quotient rule:

$$let\ f(t) = -\frac{1}{2}r^2\omega\sin(2\omega t)$$

$$g(t) = \sqrt{l^2 - r^2\sin^2(\omega t)} = (l^2 - r^2\sin^2(\omega t))^{\frac{1}{2}}$$

$$d\left(\frac{f(t)}{g(t)}\right) = \frac{g(t)f'(t) - f(t)g'(t)}{\big(g(t)\big)^2}$$

$$f'(t) = -r^2\omega^2\cos(2\omega t)$$

$$g'(t) = -\frac{r^2\omega\sin(2\omega t)}{2\sqrt{l^2 - r^2\sin^2(\omega t)}}$$

$$\frac{dv}{dt} = \frac{-r^2\omega^2\cos(2\omega t)\ \times\sqrt{l^2 - r^2\sin^2(\omega t)} - \left(-\frac{1}{2}r^2\omega\sin(2\omega t)\right)\times\left(-\frac{r^2\omega\sin(2\omega t)}{2\sqrt{l^2 - r^2\sin^2(\omega t)}}\right)}{l^2 - r^2\sin^2\theta} - r\omega^2\cos(\omega t)$$

$$\frac{dv}{dt} = \frac{-r^2\omega^2\cos(2\omega t)\sqrt{l^2 - r^2\sin^2(\omega t)} - \frac{r^2\omega^2\sin^2(2\omega t)}{4\sqrt{l^2 - r^2\sin^2(\omega t)}}}{l^2 - r^2\sin^2(\omega t)} - r\omega^2\cos(\omega t)$$

$$\boldsymbol{a = \frac{dv}{dt} = -\frac{r^2\omega^2\cos(2\omega t)}{\sqrt{l^2 - r^2\sin^2(\omega t)}} - \frac{r^4\omega^2\sin^2(2\omega t)}{4(l^2 - r^2\sin^2(\omega t))^{\frac{3}{2}}} - r\omega^2\cos(\omega t)}$$

D. Dynamics – Graphs

Figure D-1 shows the process used to determine the instantaneous properties of the pump. The stroke length (l), crank radius (r) and pump speed (n) were recorded in Table 1. The piston angular velocity (ω_{piston}) was then calculated using Equation D-1. In Table 2, the maximum cycle duration with the step was defined and used to calculate the stroke length (s) velocity (v) and acceleration (a) with respect to time using Equations 4-6, 4-7 and 4-8 respectively. Before these properties in Table 3 can be calculated, the time step (t) was determined using Equation D-2, where θ is a crank angle. Once the spreadsheet was set up, the value of the crank radius modified reading was taken when $r = 15$mm $r = 22.5$mm and $r = 30$mm.

To calculate the instantaneous pressure, it was assumed that a maximum pressure (30bar) occurs when the velocity is at a maximum, and there is no pressure when the flow rate is zero. Equation D-3 was then used to find the instantaneous pressure. In Table 4 the maximum and minimum velocities and the angle at which maxima and minima occur were recorded. And finally, the last row $P\_av/cycle$ shows the average pressure of the cycle. At the suction cycle, this equation would indicate a negative pressure, but the outlet valve would prevent a backflow. Hence, all suction cycle was replaced with a zero pressure (indicating discharge pressure is zero).

$$\omega_{piston} = \frac{2\pi n}{60} \tag{D-1}$$

$$t = \frac{n\theta}{6} \tag{D-2}$$

$$P = \frac{P_{max}}{v_{max}} \times v \tag{D-3}$$

l	0.088	m
r	0.0225	m
n	1000	RPM
ω_piston	104.7198	rad/s

v_max	2.432182	m/s
v_min	-2.43218	m/s
θ_max	284	deg
θ_min	76	deg
P_max	30	bar
P_max/v_	12.3346	
P_av/cycle	9.225091	bar

max	360 deg
step	1 deg

θ (deg)	t (s)	ωt (rad)	s (mm)	v (m/s)	a (m/s/s)	P (bar)
0	0	0	0	0	-309.827	0
1	0.000167	0.017453	0.004303	-0.05163	-309.753	0
2	0.000333	0.034907	0.01721	-0.10324	-309.531	0
3	0.0005	0.05236	0.038714	-0.1548	-309.16	0
4	0.000667	0.069813	0.068807	-0.20629	-308.642	0
5	0.000833	0.087266	0.107472	-0.25767	-307.976	0
...	...	...	...	...	...	...
358	0.059667	6.248279	0.01721	0.103243	-309.531	1.273458
359	0.059833	6.265732	0.004303	0.051634	-309.753	0.636881
360	0.06	6.283185	0	3.35E-15	-309.827	4.14E-14

Figure D-1: Mark I Data for Calculating Instantaneous Stroke, Velocity and Acceleration

E. Pressure Graph

In Figure E-3 the process for calculating the pressure at various crank angles is shown. Tables 1, 2 and 4 remain unchanged, while Tables 5, 6 and 7 were added. Each piston in a duplex pump is out of phase by 180° and a triplex pump by 120°. This information was recorded in Table 5. The triplex pump consists of three pistons, hence two values (120° and 240°) were required. Once the graph step ($step\_g$) is defined, the starting crank angle was changed to -240° to increase the range, as shown in Figure E-1. The additional columns, θ-180, θ-120 and θ-240, were then added to offset values by the amount stated in Table 5. The results of these offsets are shown in Figure E-2.

The duplex configuration requires to combine values at $\theta = 0°$ and $\theta = 180°$ and this was done in Table 6 using a series of INDEX and MATCH functions (P-180 column). For example, at a crank angle of 90°, this function looks up the value in columns θ and θ-180 respectively. This gives the values of 0 and 29.1 which were then combined to calculate the total output value. The same process was repeated for the triplex configuration (P-120 column).

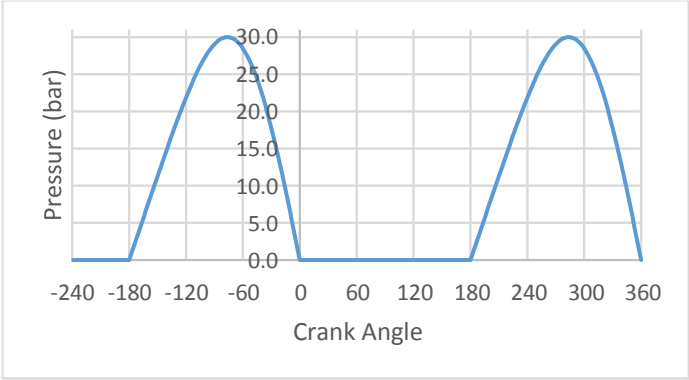

Figure E-1: Pressure vs Crank Angle for Range -240° - 360°

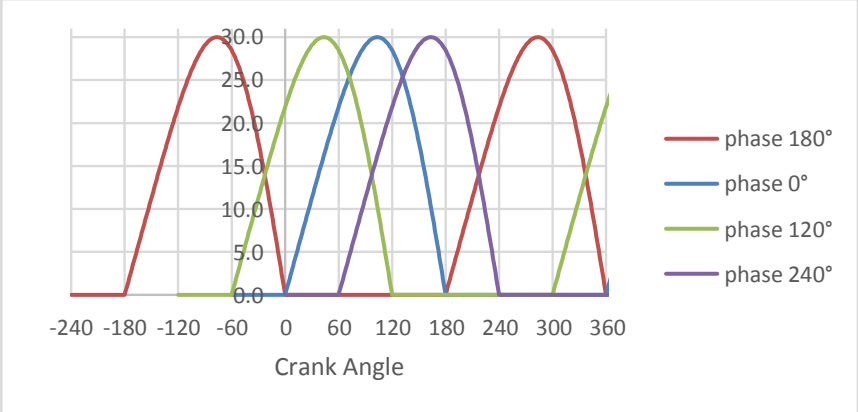

Figure E-2: Pressure vs Crank Angle at Various Phases

l	0.088	m
r	0.0225	m
n	1,000	RPM
ω_piston	104.7198	rad/s

1

max	360 deg
step	1 deg

2

Step_g	180 deg
Step_g	120 deg
Step_g	240 deg

5

v_max	2.432	m/s
v_min	-2.432	m/s
θ_max	-76	deg
θ_min	76	deg

4

P_max	30	bar
P_maxP/v	12.3346	
P_av/cycle	7.3	bar

P_max	30.0	30.0
P_min	0.0	21.9
P_av/cycle	18.5	27.75

7

θ (deg)	θ-180 (deg	θ-120 (deg	θ-240 (deg	t (s)	ωt (rad)	s (mm)	v (m/s)	a (m/s/s)	P (bar)
-240	-60	-120	0	-0.04	-4.189	35.9	-1.773	154.9	0.0
-239	-59	-119	1	-0.0398	-4.171	36.2	-1.747	156.6	0.0
-238	-58	-118	2	-0.0397	-4.154	36.5	-1.721	158.2	0.0
-237	-57	-117	3	-0.0395	-4.136	36.8	-1.694	159.7	0.0
...	...	...	...	...	...	...	...	...	...
356	536	476	596	0.0593	6.213	0.1	0.206	-308.6	2.5
357	537	477	597	0.0595	6.231	0.0	0.155	-309.2	1.9
358	538	478	598	0.0597	6.248	0.0	0.103	-309.5	1.3
359	539	479	599	0.0598	6.266	0.0	0.052	-309.8	0.6
360	540	480	600	0.0600	6.283	0.0	0.000	-309.8	0.0

3

6

θ (deg)	2 piston P-180 (bar	3 piston P-120 (bar
1	0.4	22.19
2	0.8	22.50
3	1.1	22.81
4	1.5	23.11
...	...	...
356	2.5	23.11
357	1.9	22.81
358	1.3	22.50
359	0.6	22.19
360	0.0	21.87

Figure E-3: Mark I Data for Calculating Instantaneous Pressure

F.CFD Setup of Concept Reed Valves

Step 1:

In the flow simulation setup, water as the flow medium was selected. The flow type *laminar and turbulent* was selected and cavitation was *enabled*.

The computation domain was defined – diameter 53mm, length above the outlet 300mm and below the inlet 200mm.

The global goal as average density was added.

Step 2:

The initial mesh in the Global Mesh Setting was set to the highest value of 7 and the Minimum Gap Size defined as 0.002m. Also, the localised mesh was added across the valves (Figure F-1) to refine the mesh. In the Localised Mesh Settings, the Level of Refining Fluid Cells was set to 3 and Level of the Refining Cells at Fluid/Solid Boundary set to 2. This selection was made to ensure the valve area is populated with enough cells. The mesh of the Reed Valve Concept 1 and Concept 2 are shown in Figure F-2 and Figure F-4 respectively. The total number of cells with a total number of iterations is shown in Figure F-3 and Figure F-5.

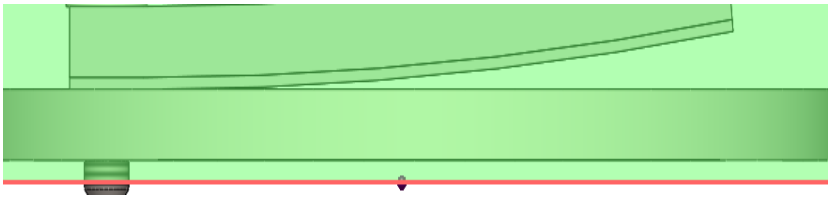

Figure F-1: Localised Mesh

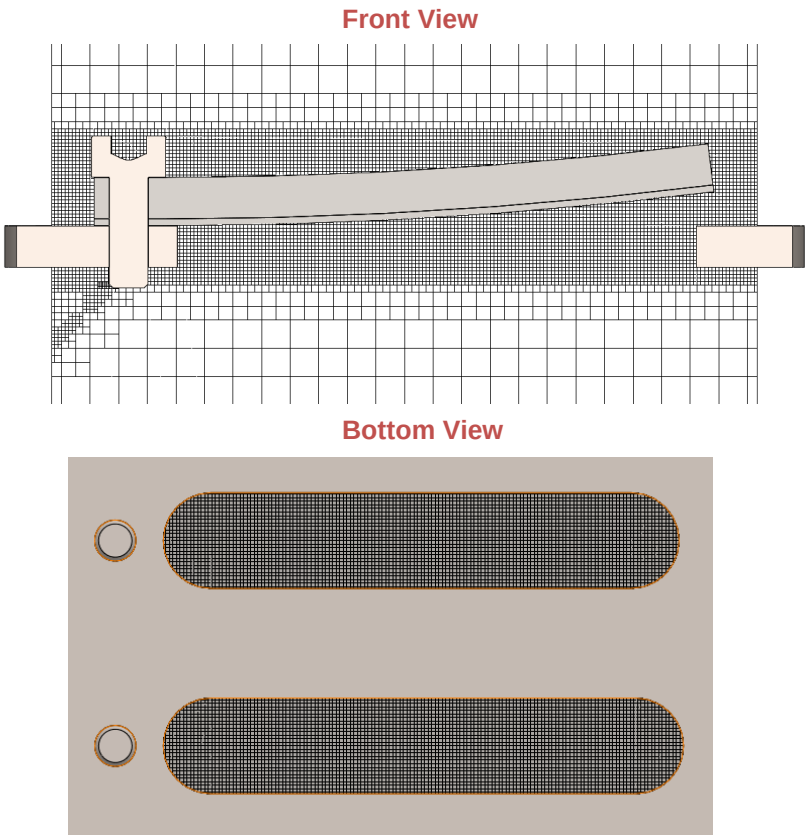

Figure F-2: Reed Valve Concept 1 Mesh

Parameter	Value
Status	Solver is finished.
Total cells	1,212,672
Fluid cells	1,212,672
Fluid cells contacting solids	154,057
Iterations	5,575
Last iteration finished	17:37:35
CPU time per last iteration	00:00:17

Figure F-3: Reed Valve Concept 1 Parameter Table

Front View

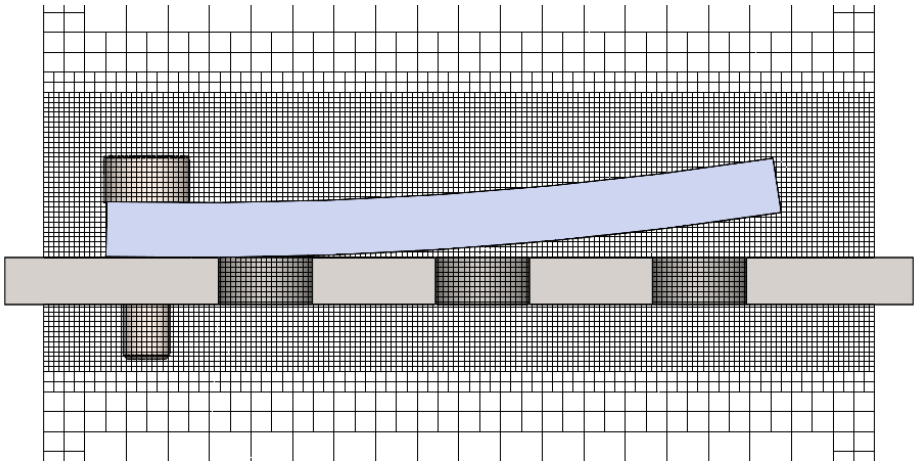

Bottom View

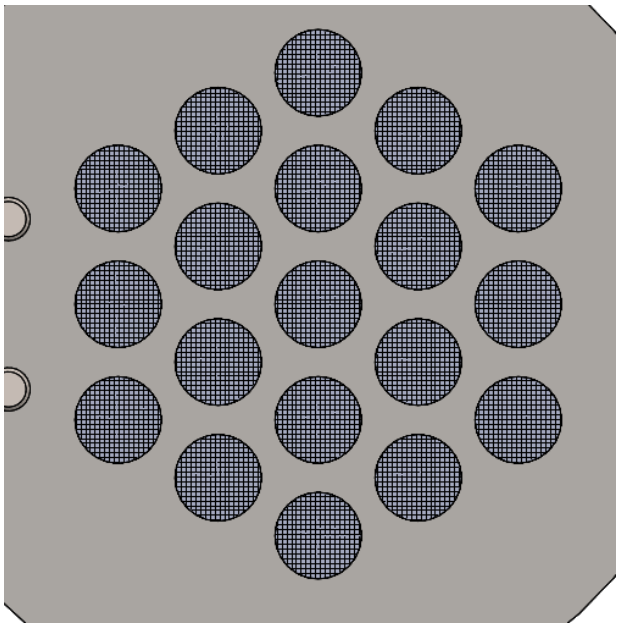

Figure F-4: Reed Valve Concept 2 – Mesh

Parameter	Value
Status	Solver is finished.
Total cells	1,067,935
Fluid cells	1,067,935
Fluid cells contacting solids	165,988
Iterations	5,260
Last iteration finished	20:30:36
CPU time per last iteration	00:00:11
Travels	
Iterations per 1 travel	5,265

Figure F-5: Reed Valve Concept 2 – Parameter Table

G. Piston Pump Mark I – Test Data

ρ_water (l	1000	kg/m^3							
	m_i (kg)	m_total (k	m_f (kg)	stroke (mi	Start (s)	Finish (s)	duration (	n_strokes	RPM_av
2016.04.06									
Test 1	0.365	5.59	5.225	45	8.98	38.60	29.62	61	124
…	…	…	…	…	…	…	…	…	…
Test 6	0.365	5.495	5.13	45	7.13	17.87	10.73	61.5	344
					0				
D_chambe	V_chambe	m_dot (kg	η_v	Inlet Reed	Outlet Re	V (V)	Piston gro	Gear Ratio	notes
50	88357	0.176	96.9%	2 v2	2 v2	130	40.5	1.00	
…	…	…	…	…	…	…	…	…	
50	88357	0.478	94.4%	2 v2	2 v2	180	40.5	1.00	

Figure G-1: Mark I Test Data Methodology

The Excel table in Figure A-12 shows how the acquired experimental data was used to calculate the necessary parameters to determine the pump performance. The values in grey indicate less critical columns and values in green – important parameters.

In these calculations, water density was assumed to be 1,000kg/m^3. In the m_i column, the mass of the container was measured which later was subtracted to determine the mass flow rate. In the m_total column, the total mass of liquid delivered, including the mass of the container was recorded. In the m_f column, the total mass of pumped water was calculated using Equation G-1. In the next column, the stroke length was recorded which was used to calculate the volume displaced by the piston pump. As previously explained, video footage was used to extract the precise duration of the experiment. The start and finish times of the test were recorded in the next two columns, and the duration was calculated using Equation G-2. The number of strokes was manually calculated and recorded in the n_stroke column. This provided sufficient data to calculate the average speed of the pump (RPM_av) using Equation G-3. After that, the bore cylinder diameter was recorded and volume displaced by the piston ($v\_chamber$) was determined using Equation G-4. Finally, the mass flow rate (m_dot) and the volumetric efficiency (η_v) were calculated using Equation G-5 and Equation G-6 respectively. In the last columns some additional information, such as valve type, piston groove diameter, pump to motor gear ratio and notes, were recorded for reference.

$$m_f = m_{total} - m_i \quad \text{(G-1)}$$

$$duration = finish - start \quad \text{(G-2)}$$

$$RPM_{av} = \frac{n_{strokes}}{duration} \quad \text{(G-3)}$$

$$V_{chamber} = \pi \left(\frac{D_{chamber}}{2}\right)^2 \times stroke \quad \text{(G-4)}$$

$$\dot{m} = \frac{m_f}{duration} \quad \text{(G-5)}$$

$$\eta_v = \frac{m_f}{V_{chamber} n_{strokes} \rho_{water} \times 10^{-9}} \quad \text{(G-6)}$$

H. CFD Setup of Angled Valves

For the setup, the same steps were used as described in **Step 1**, section **F CFD Setup of Concept Reed Valves**. A mesh with the parametric table is shown in Figure H-1 - Figure H-6 and the CFD results are displayed in Figure H-7 – Figure H-9. It should be noted, that the bottom view mesh (Figure H-1) is the same in all cases.

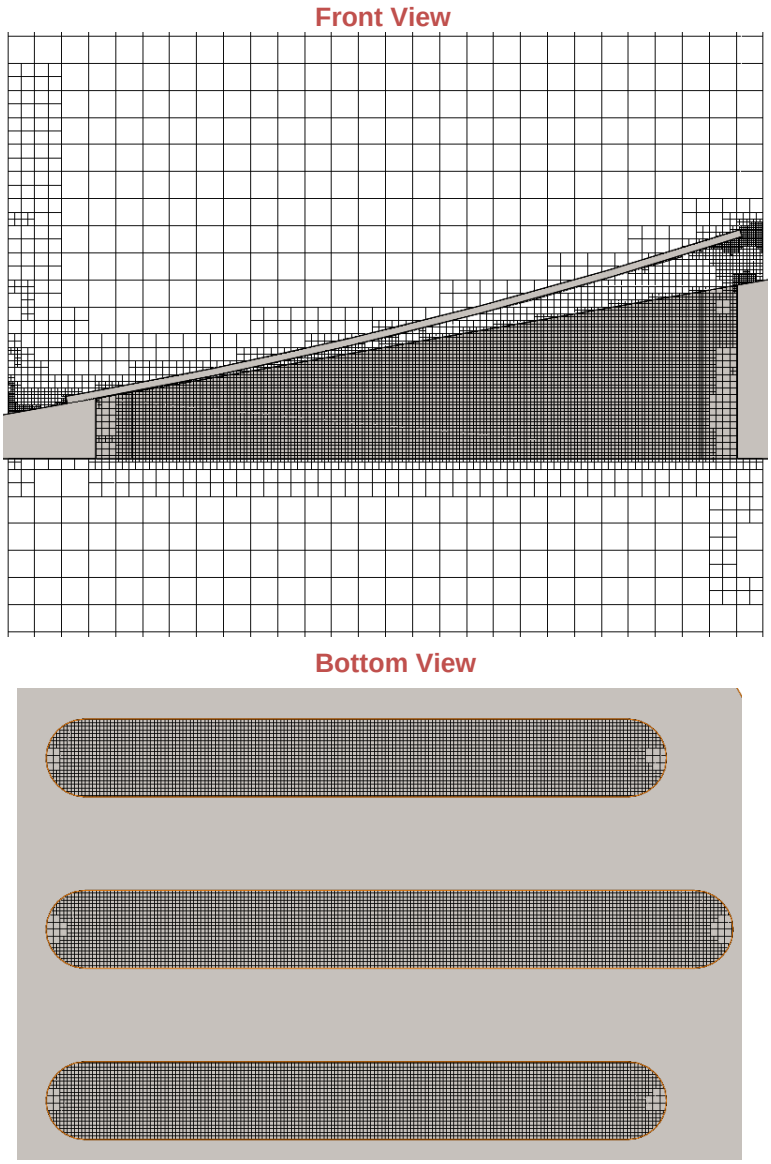

Figure H-1: 20° Angled Valve – Mesh

Parameter	Value
Status	Solver is finished.
Total cells	1,165,644
Fluid cells	1,165,644
Fluid cells contacting solids	224,434
Iterations	5,545
Last iteration finished	19:36:44
CPU time per last iteration	00:00:23

Figure H-2: 20° Angled Valve – Parameter Table

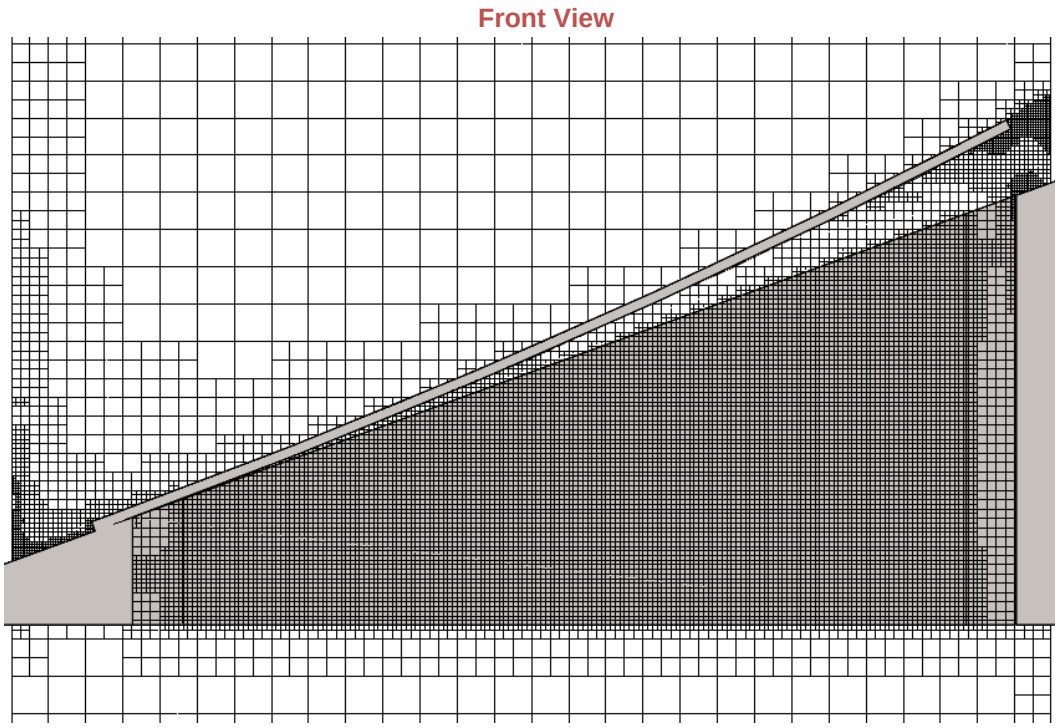

Figure H-3: 30° Angled Valve – Mesh

Parameter	Value
Status	Solver is finished.
Total cells	1,561,600
Fluid cells	1,561,600
Fluid cells contacting solids	291,152
Iterations	6,100
Last iteration finished	20:31:55
CPU time per last iteration	00:00:23

Figure H-4: 30° Angled Valve – Parameter Table

Front View

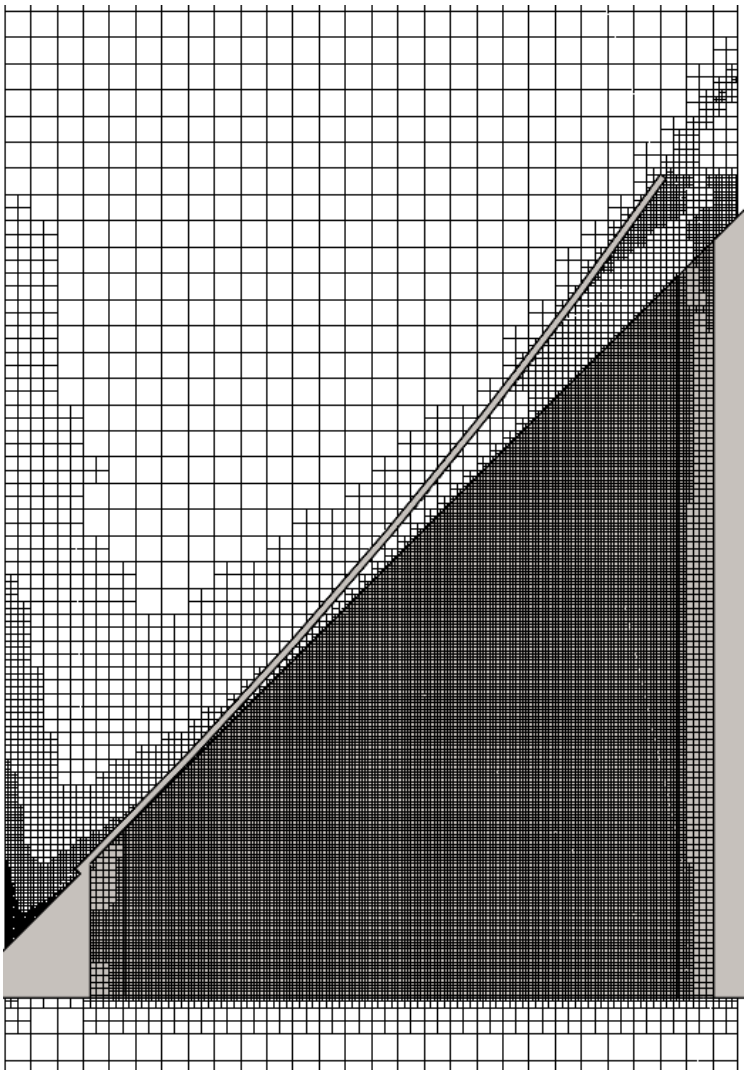

Figure H-5: 40° Angled Valve – Mesh

Parameter	Value
Status	Solver is finished.
Total cells	2,762,262
Fluid cells	2,762,262
Fluid cells contacting solids	447,953
Iterations	7,355
Last iteration finished	20:38:02
CPU time per last iteration	00:00:41

Figure H-6: 40° Angled Valve – Parameter Table

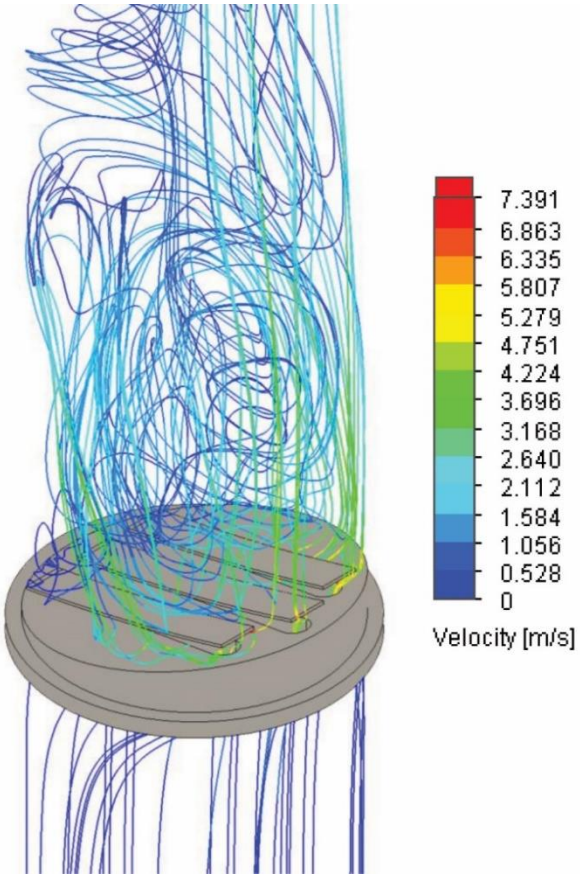

Figure H-7: 10° Angled Valve – Velocity Graph

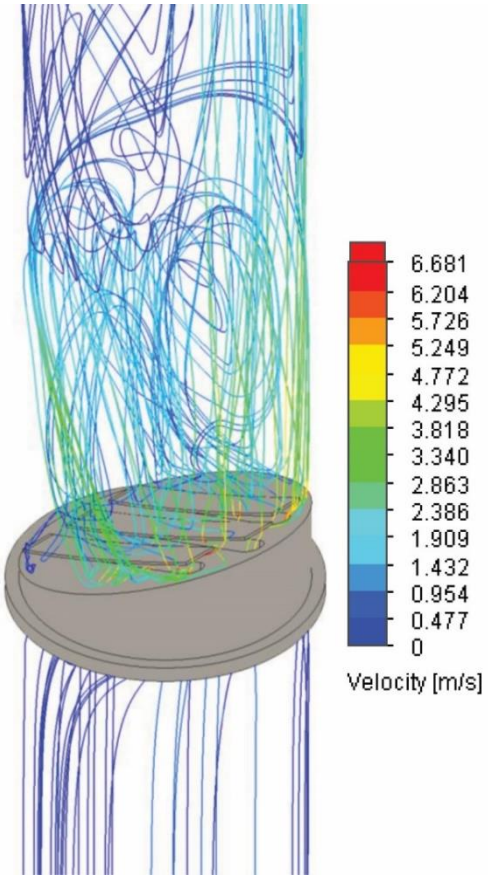

Figure H-8: 20° Angled Valve – Velocity Graph

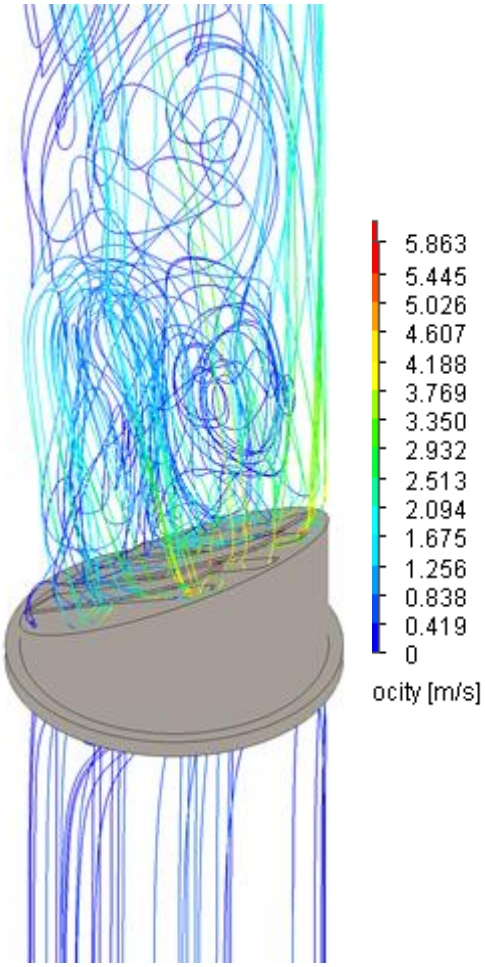

Figure H-9: 30° Angled Valve – Velocity Graph

I. Mark II – FEA Analysis

a. Valve Base

Step 1 – Fixtures and External Loads

The aluminium alloy 6082-T6 was added to the Solidworks database and selected as the valve base material. Flanges will be used to secure the valves in the system, therefore fixed geometry conditions were set, as indicated by the green arrows in Figure H-9. To calculate the force exerted by the petals, the total petal cross-section area was calculated in SolidWorks to be 1154.66mm^2. Using this area, the force applied by the petals was calculated to be 3810N at 33bar pressure using Equation I-1. This force was then applied perpendicularly to the sealing face at which the petals sit, as shown by the pink arrows. On the remaining sealing face, 3.3MPa pressure was applied, as shown by the red arrows.

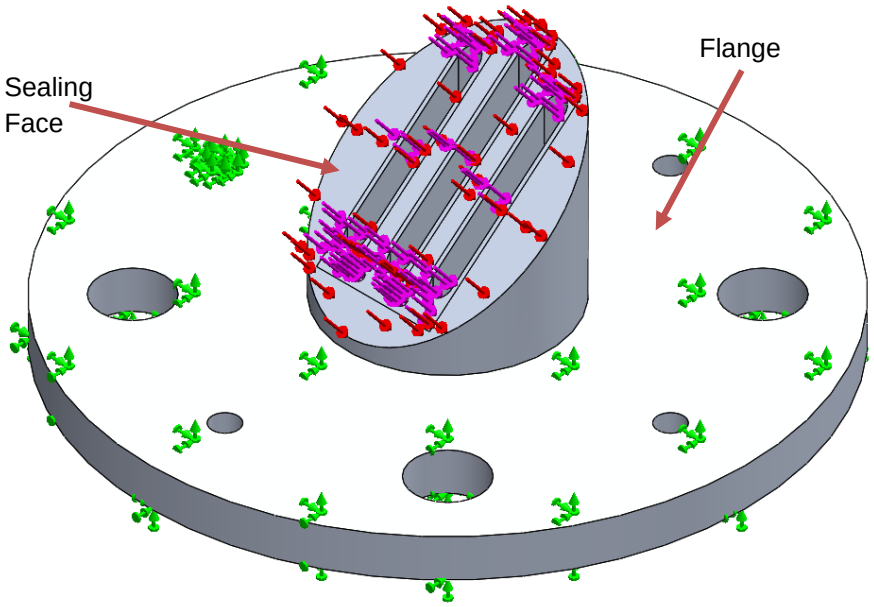

Figure I-1: Fixtures and External Loads Setup on the Valve Base

$$F = PA \quad \text{(I-1)}$$

Where F force applied (N), P pressure (Pa) and (A) cross-section area (m^2)

Step 2 – Meshing

Under the mesh setting global size and tolerances of 1mm and 0.05mm were set respectively. The full meshed model is shown in Figure I-2.

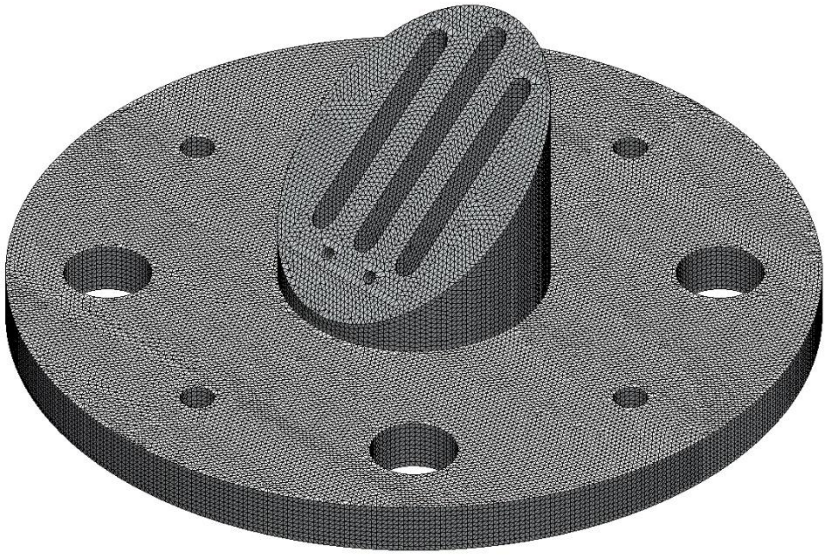

Figure I-2: Meshed Valve Base

b. Petal

Step 1 – Fixtures and External Loads

Stainless Steel 316L was selected as a petal material and fixed geometry conditions were set, as indicated by the green arrows in Figure I-3. The pressure loading of 3.3MPa was added on the opposing side, as indicated by the green arrows.

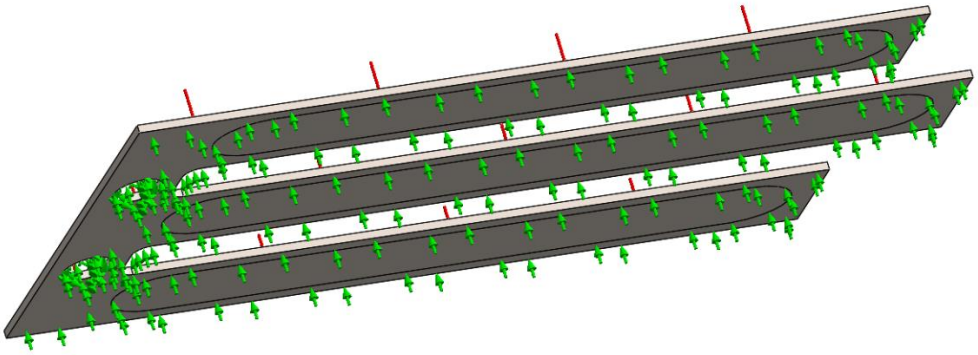

Figure I-3: Fixtures and External Loads Setup on the Petals

Step 2 – Meshing

Under mesh setting global size and tolerances of 0.25mm and 0.0125mm were set respectively. The full meshed model is shown in Figure I-4.

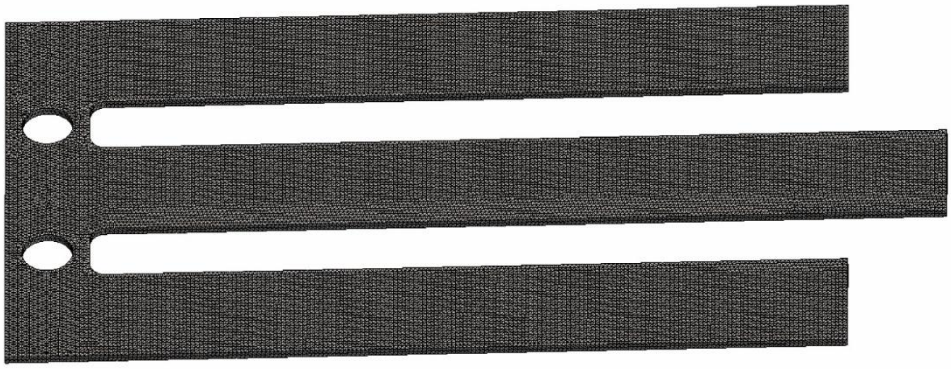

Figure I-4: Petal Mesh

c. Tee Section

Step 1 – Fixtures and External Loads

Stainless Steel 316L was selected for the tee section and fixed geometry conditions were set, as indicated by the green arrows in Figure I-5. The pressure loading of 3.3MPa was added on the internal faces, as indicated by the green arrows.

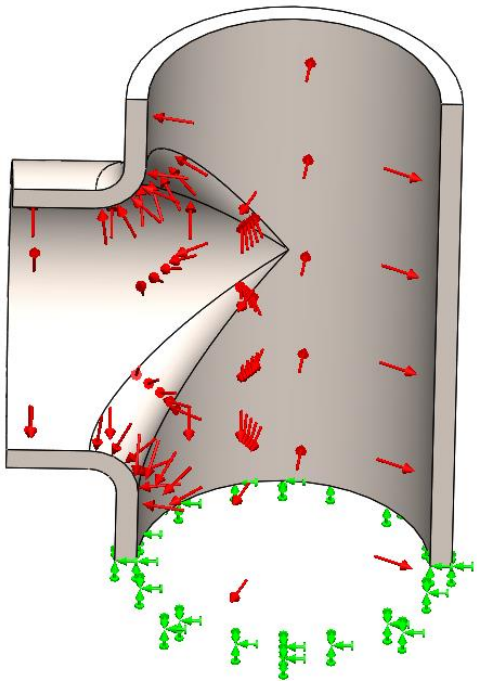

Figure I-5: Fixtures and External Loads Setup on the Tee Section

Step 2 – Meshing & Results

Under mesh setting global size and tolerances of 0.25mm and 0.0125mm were set respectively. The full meshed model is shown in Figure I-6.

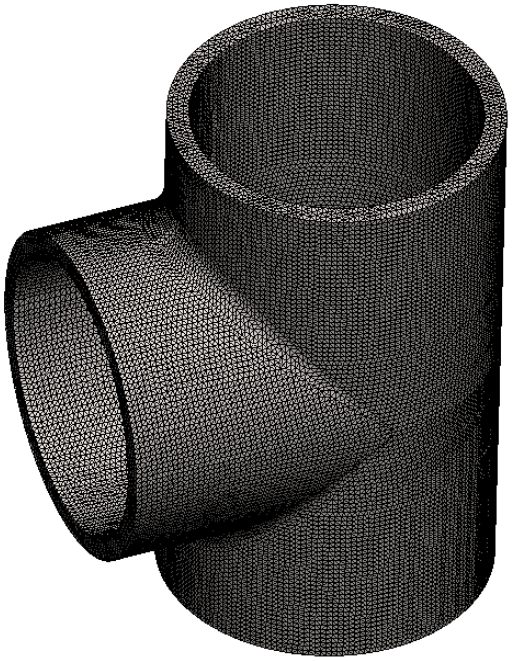

Figure I-6: Tee Section Mesh

J.Mark II – Drawings

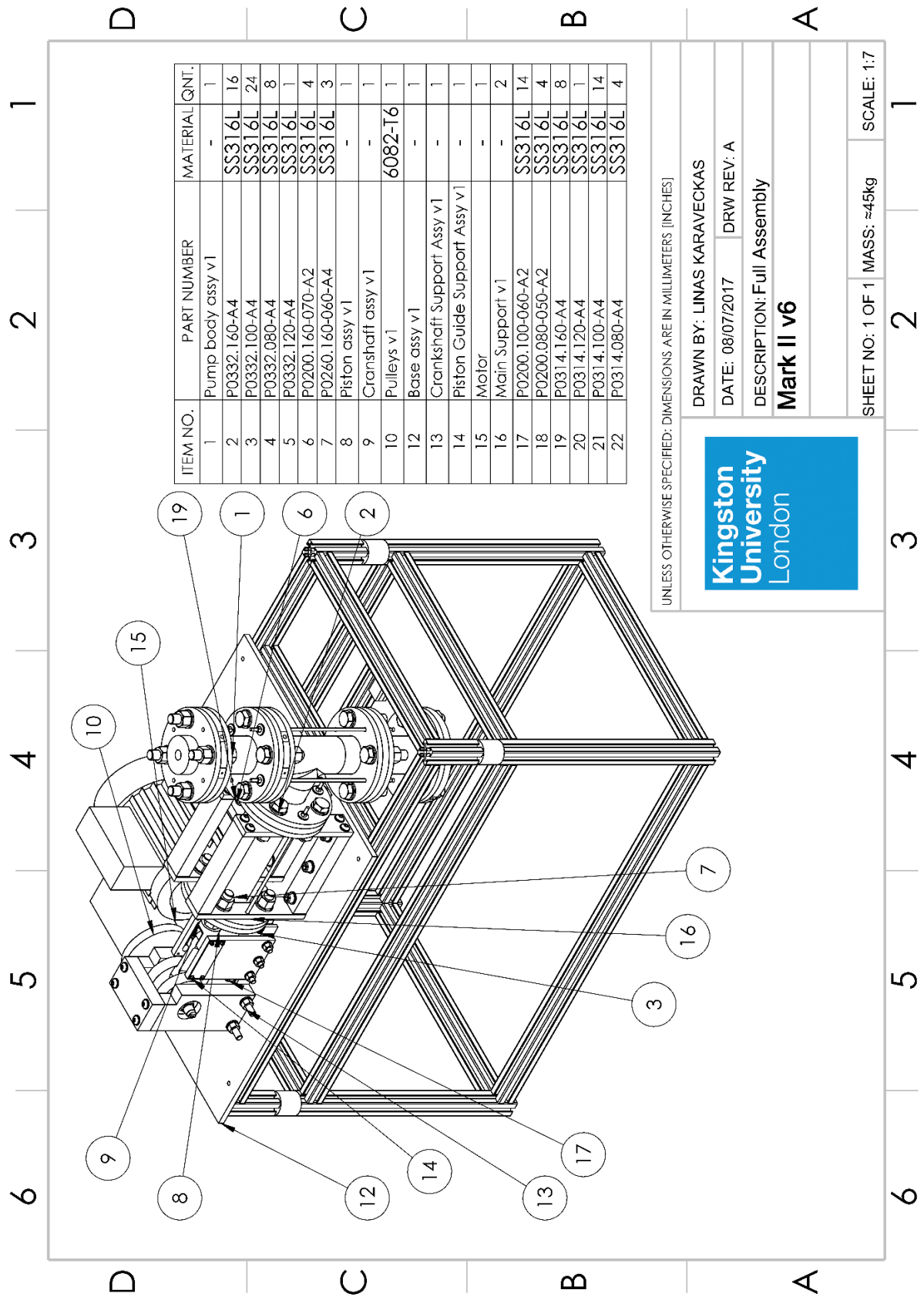

Figure J-1: Mark II Full Assembly Drawing

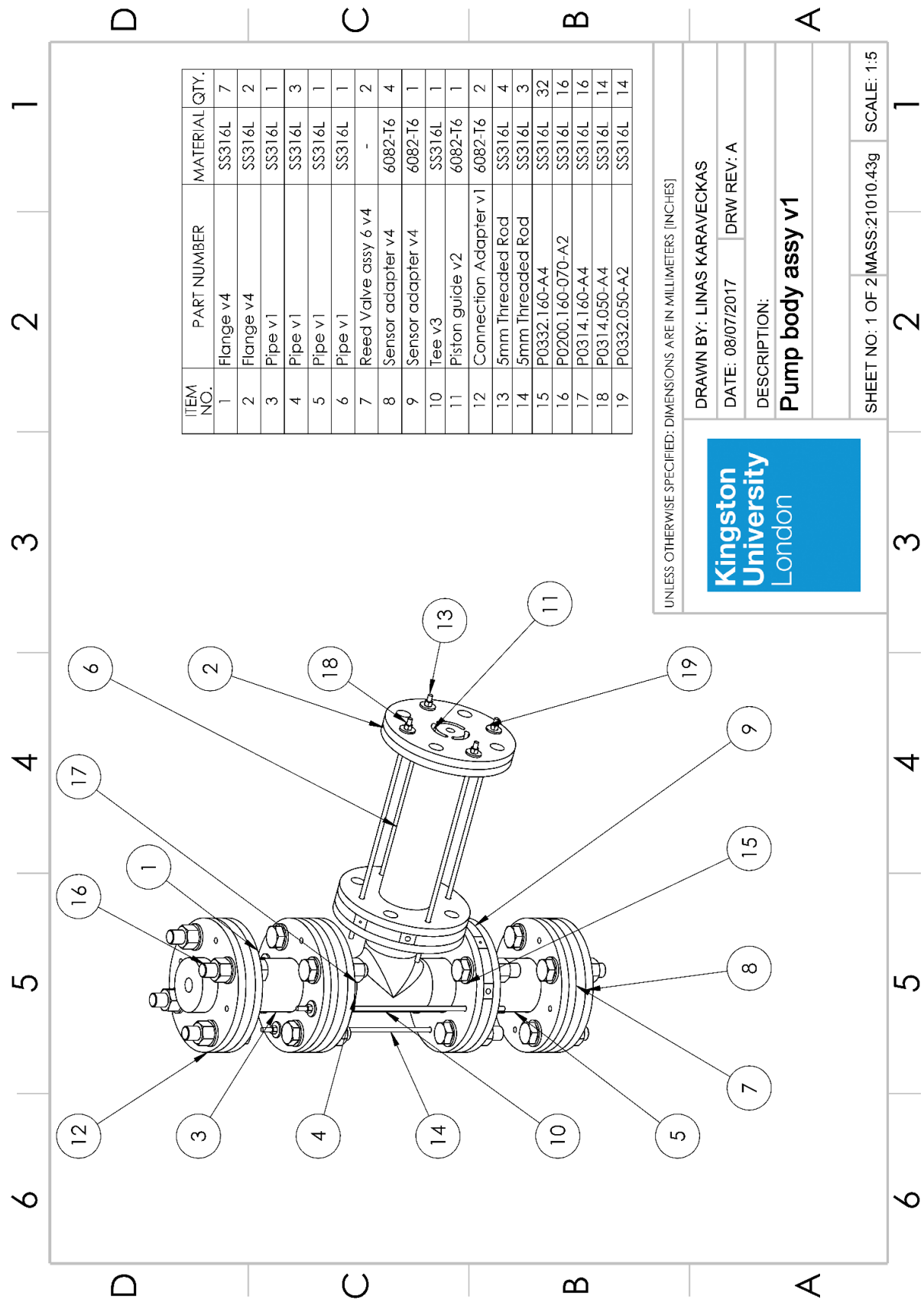

Figure J-2: Mark II Pump Main Body Drawing, Pg.1

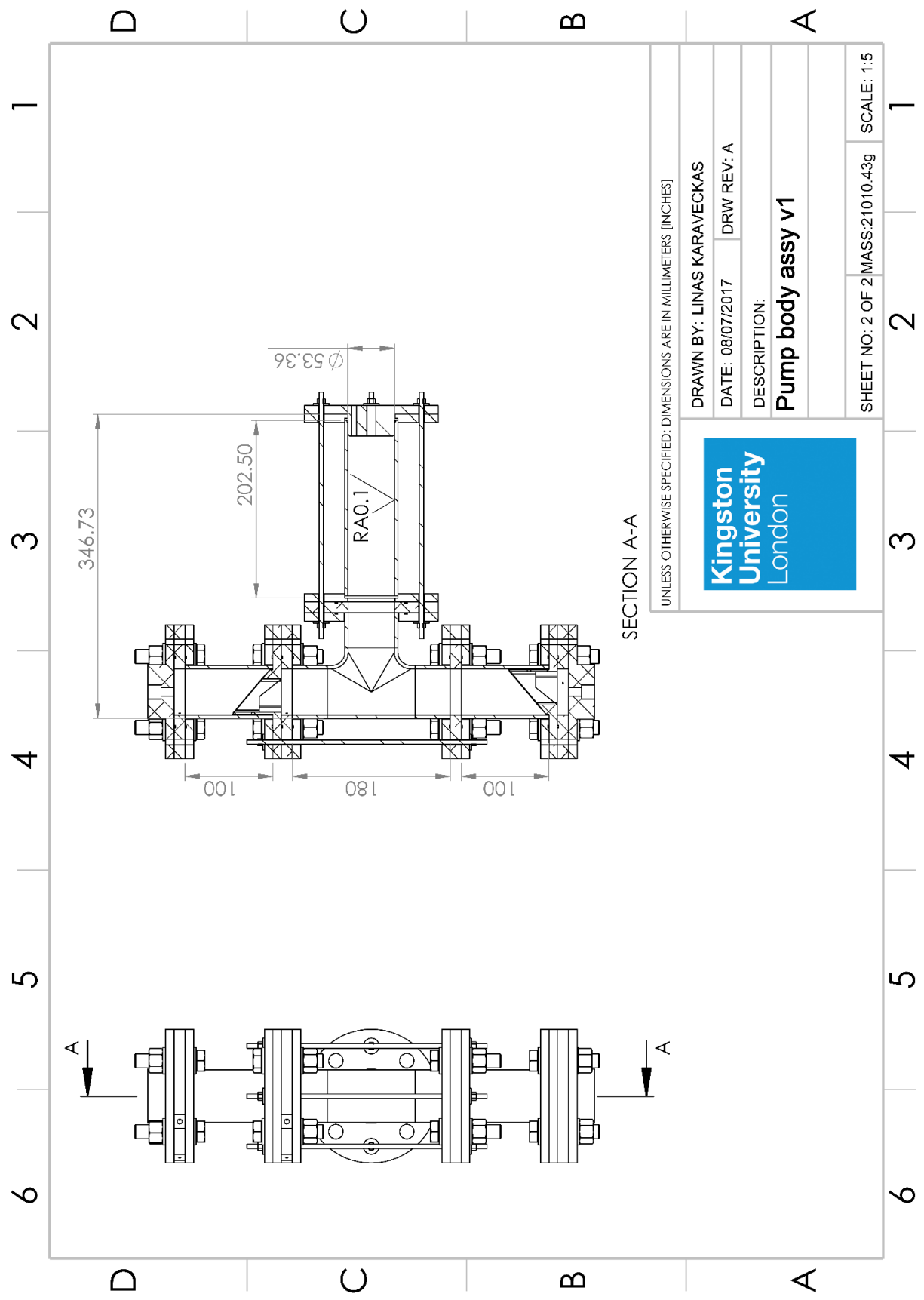

Figure J-3: Mark II Pump Main Body Drawing, Pg.2

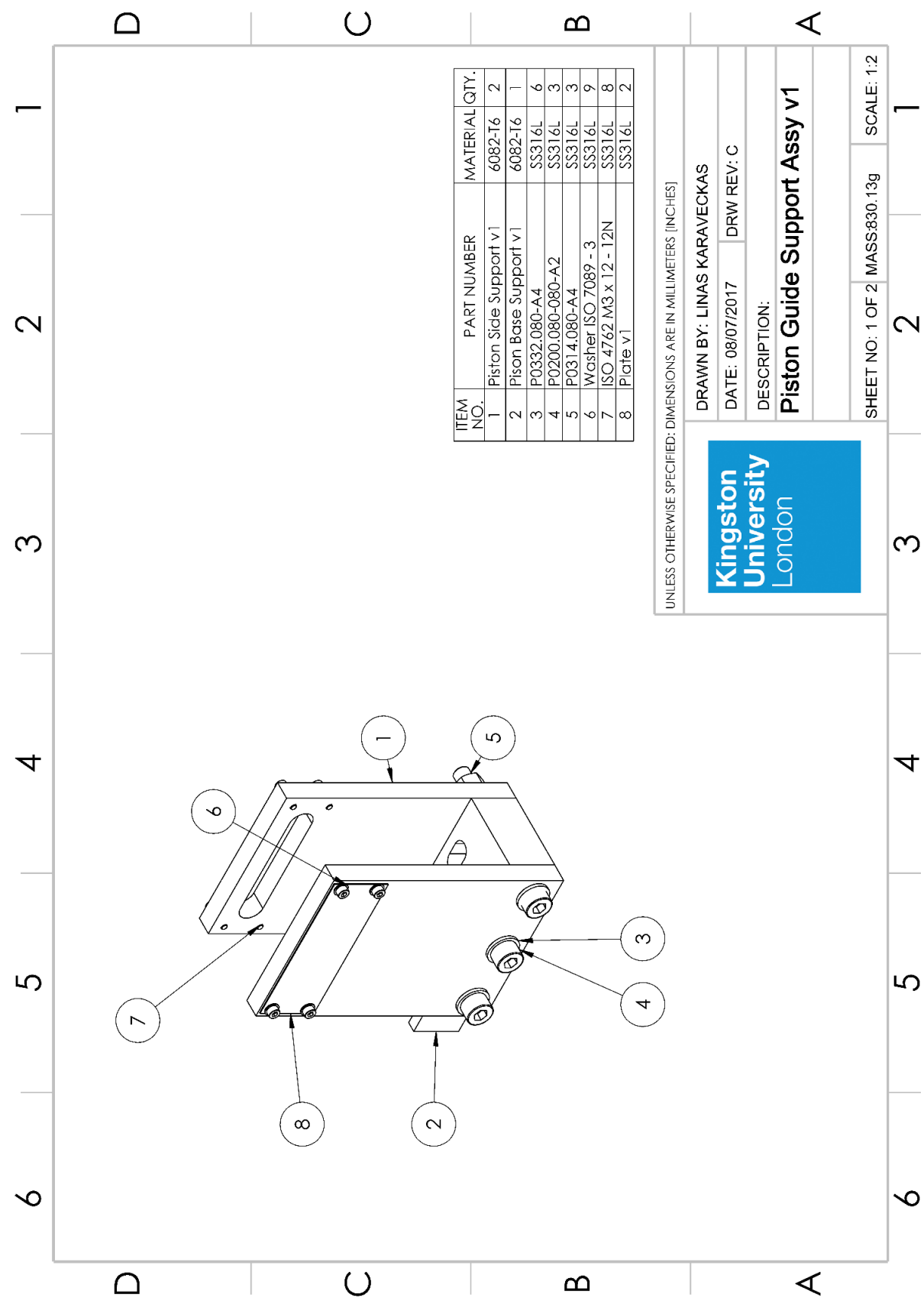

Figure J-4: Mark II Piston Guide Support Assembly Drawing, Pg.1

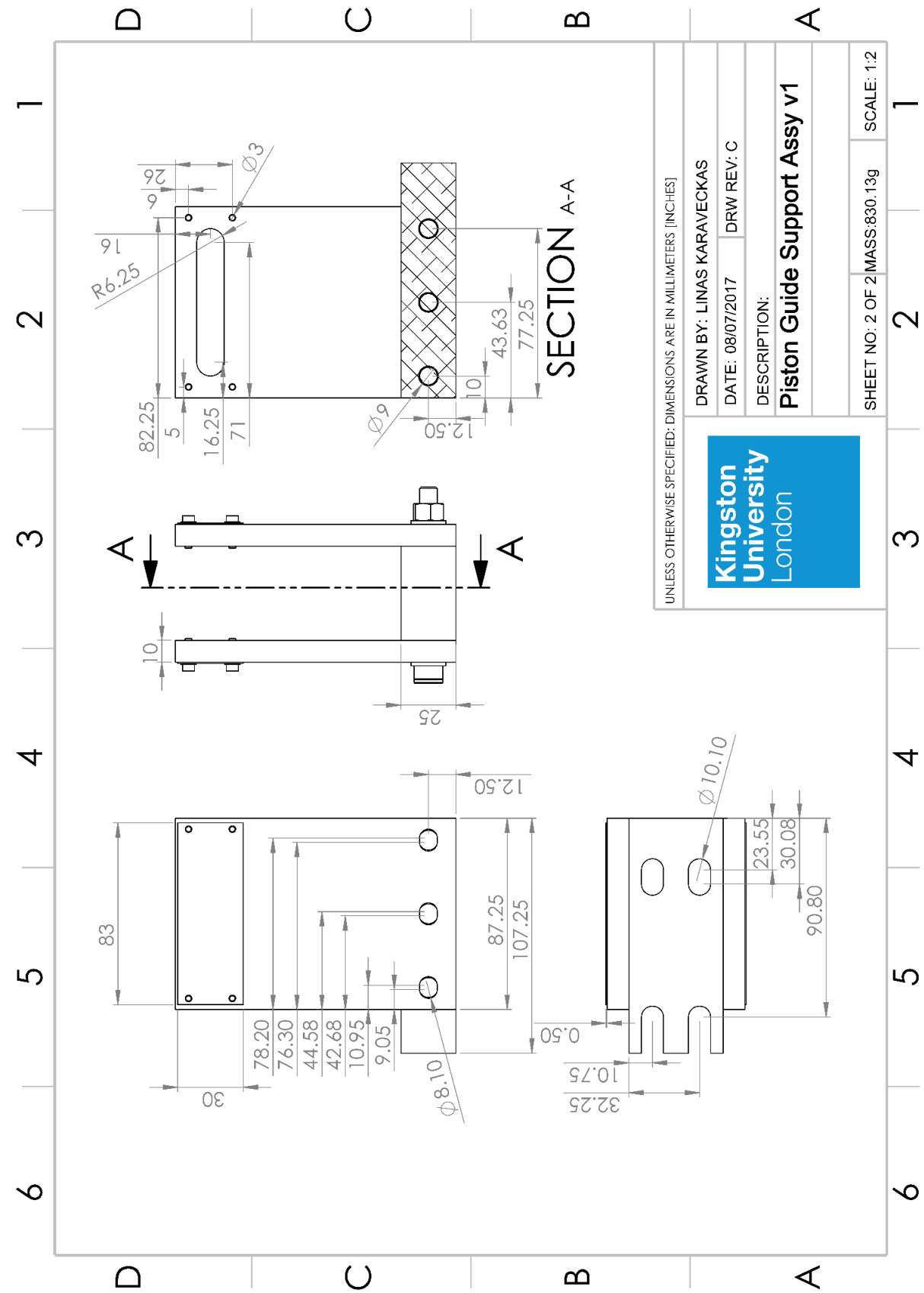

Figure J-5: Mark II Piston Guide Support Assembly Drawing, Pg.2

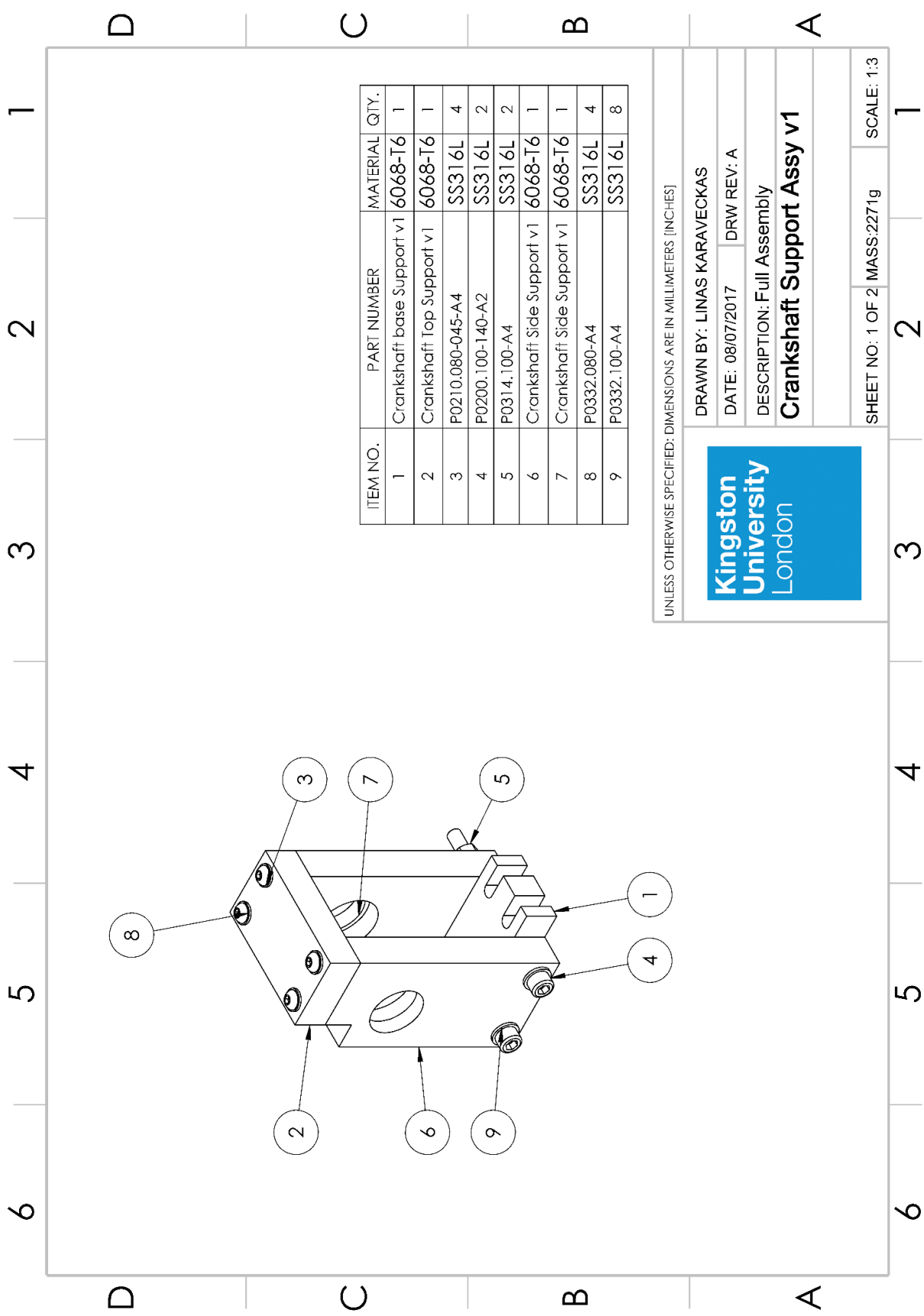

Figure J-6: Mark II Crankshaft Support Drawing, Pg.1

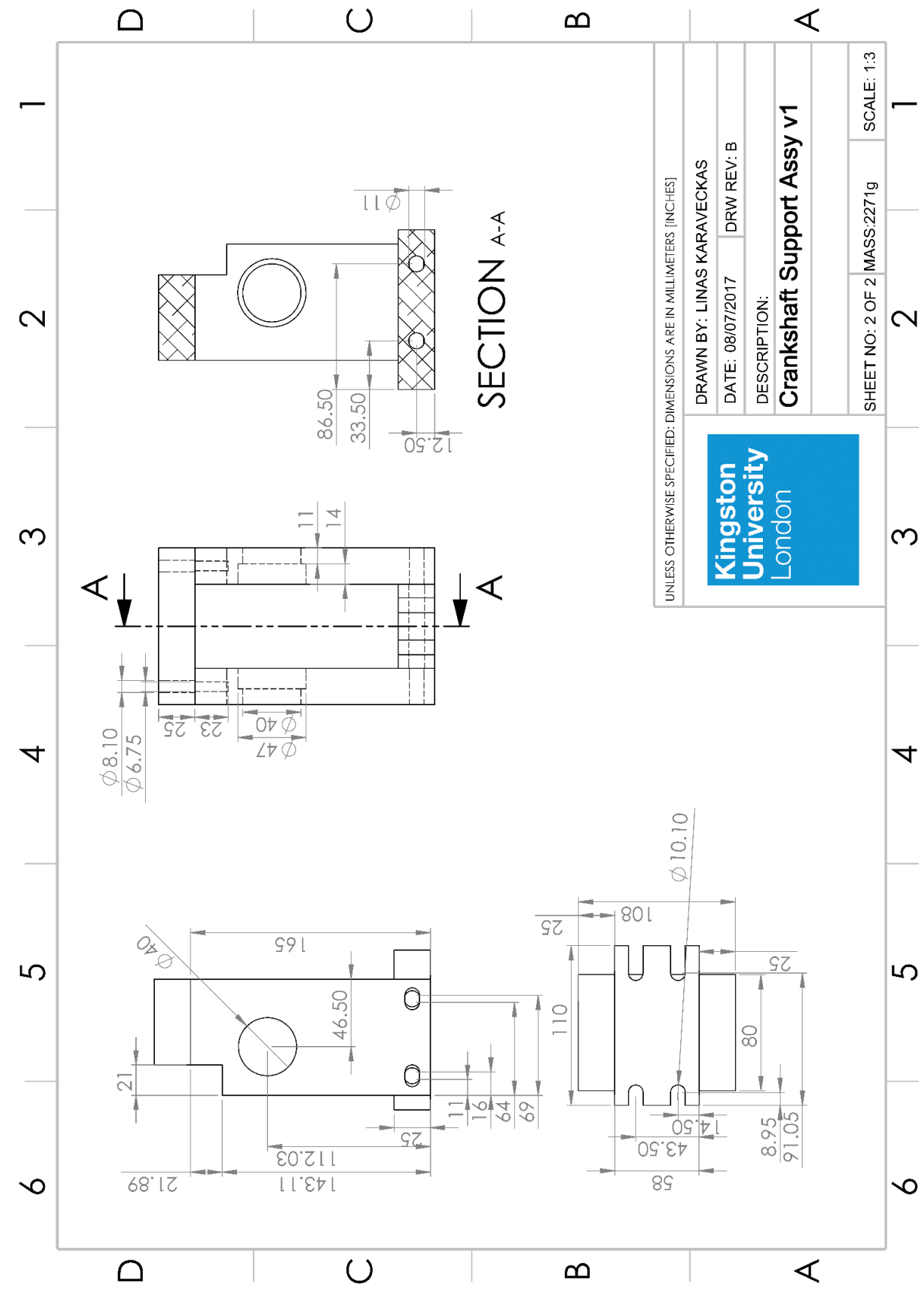

Figure J-7: Mark II Crankshaft Support Drawing, Pg.2

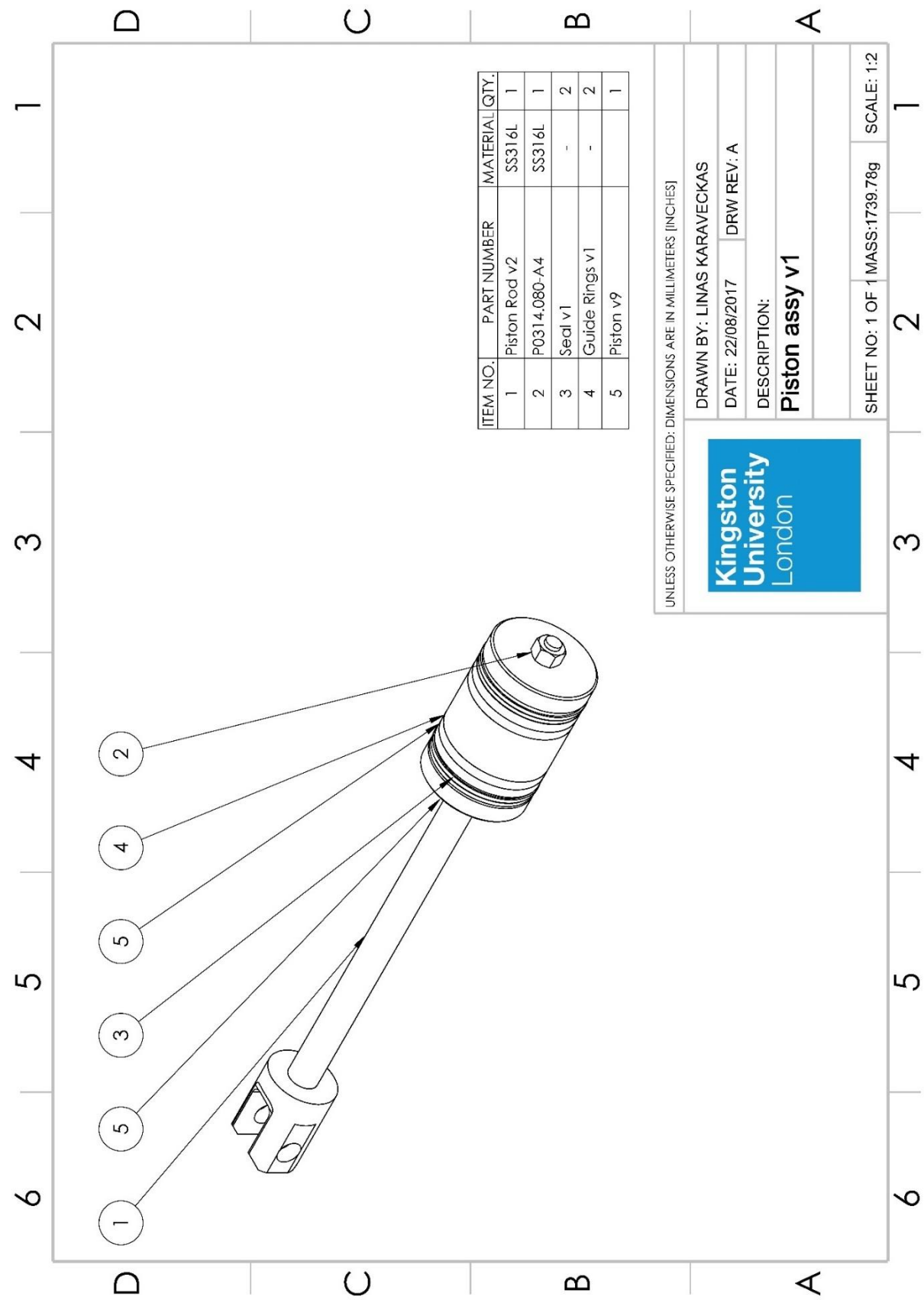

Figure J-8: Mark II Piston Assembly Drawing

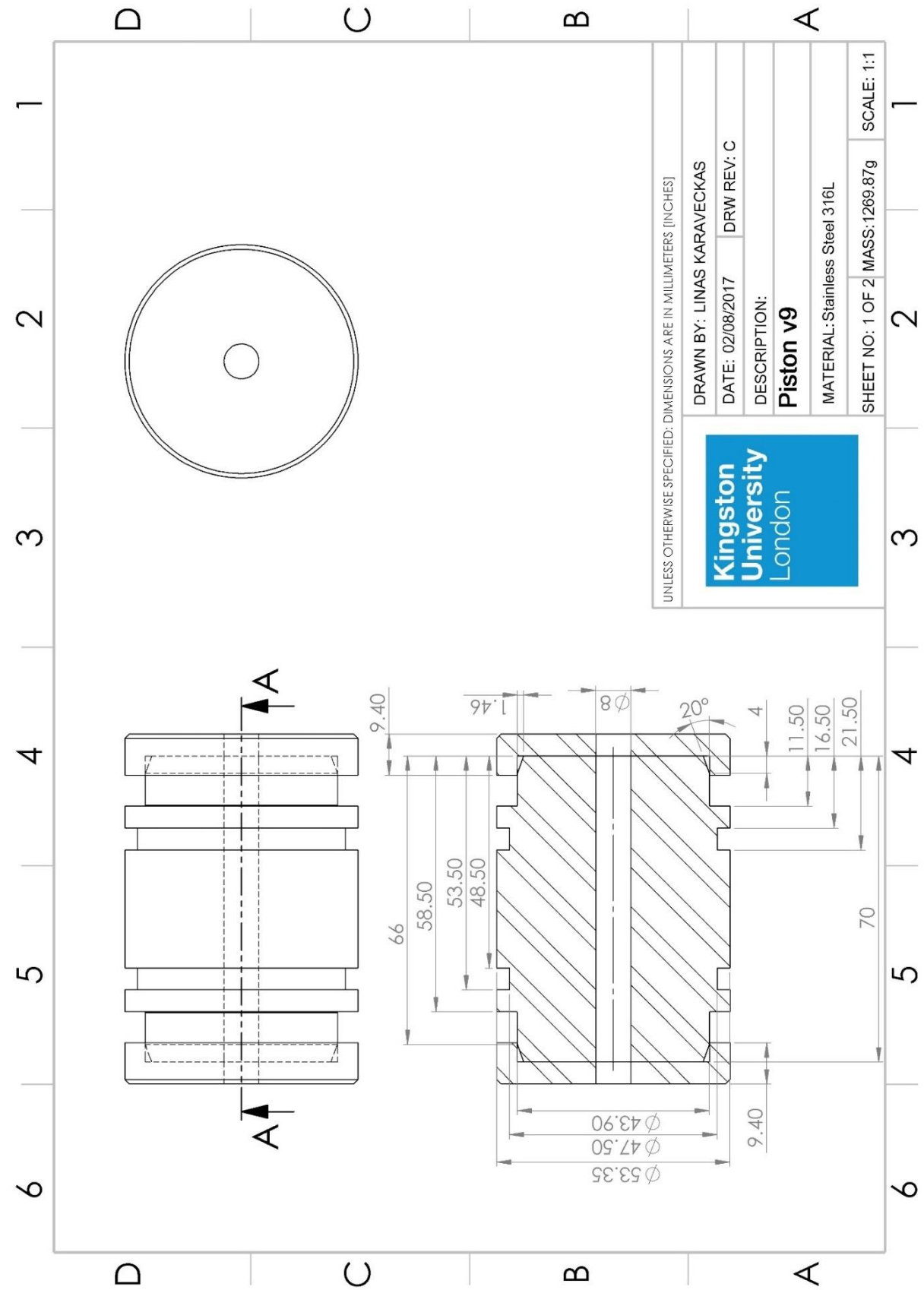

Figure J-9: Mark II Piston Drawing

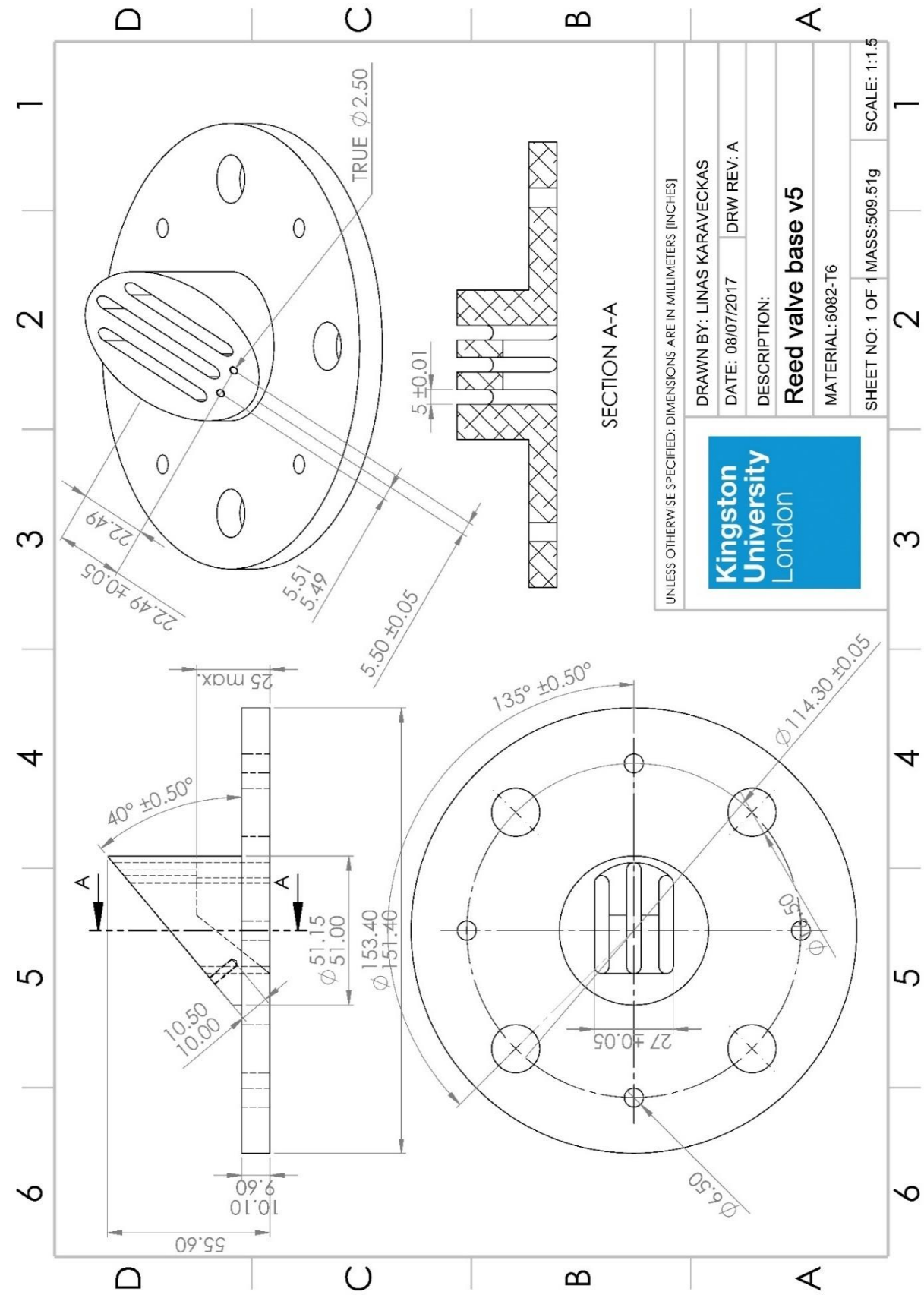

Figure J-10: Reed Valve Base Drawing

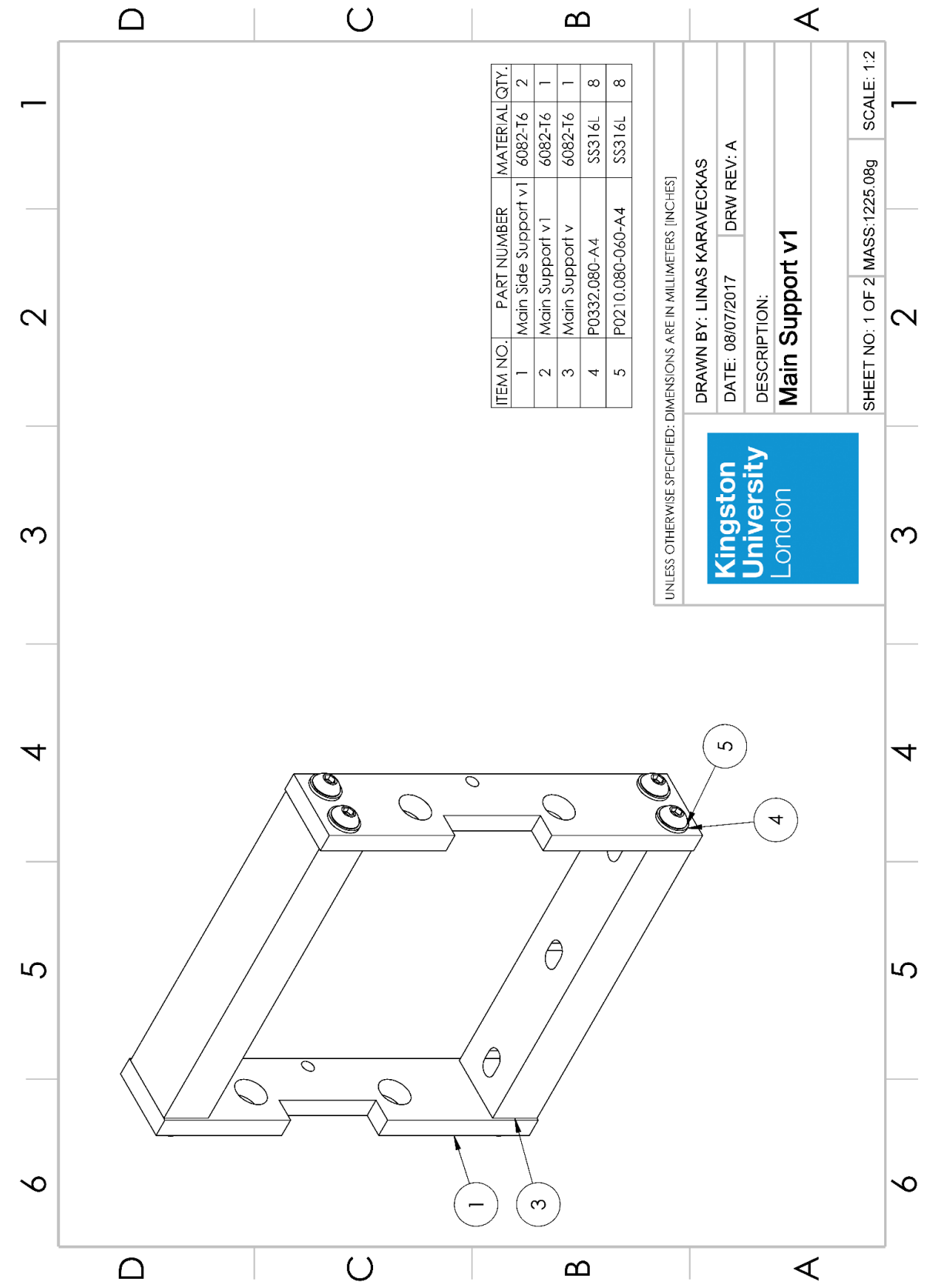

Figure J-11: Main Support Drawing, Pg.1

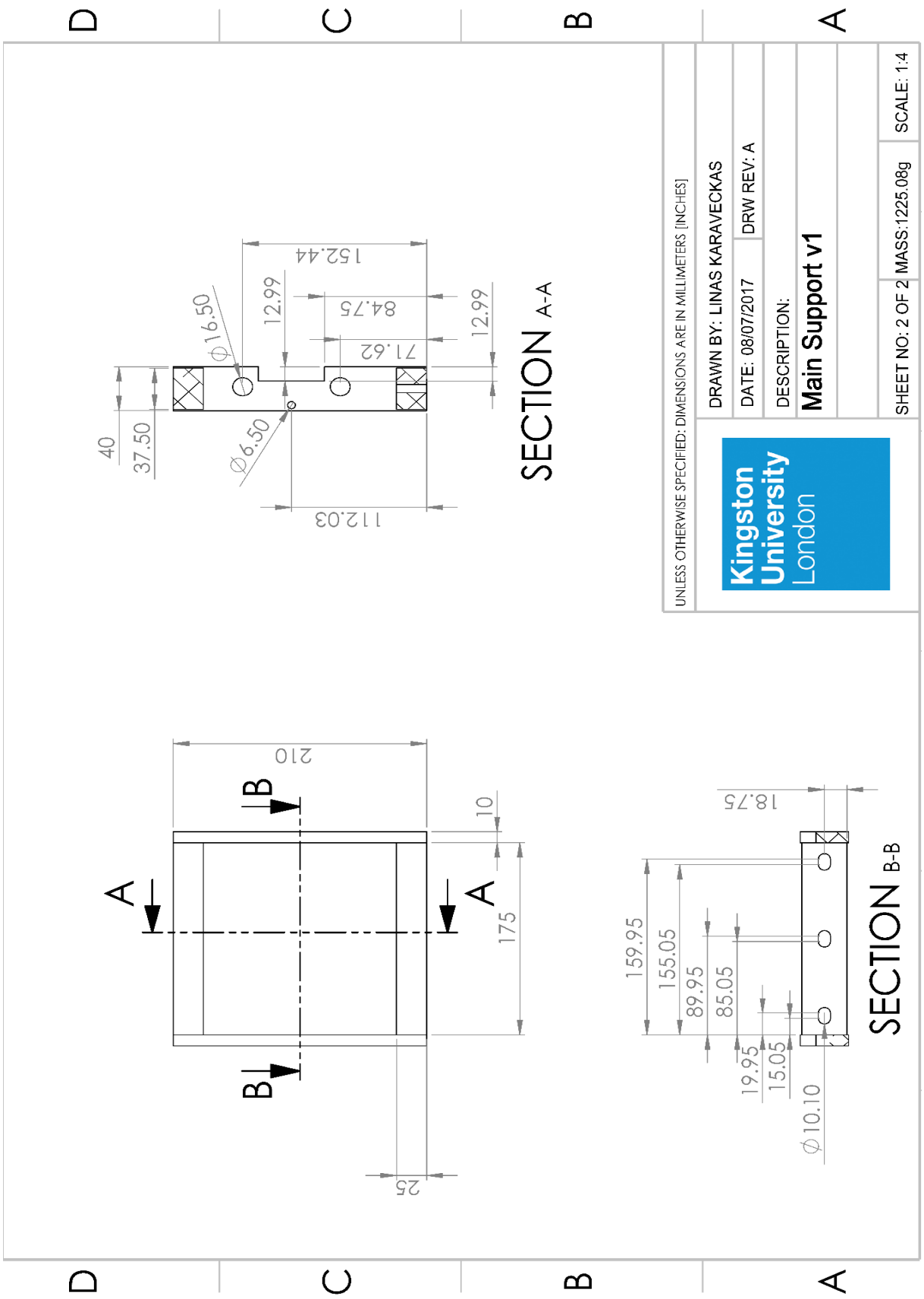

Figure J-12: Main Support Drawing, Pg.2

K. Mark II – CMM, Roundness & Surface Finish

a. Piston Bore with no Flanges

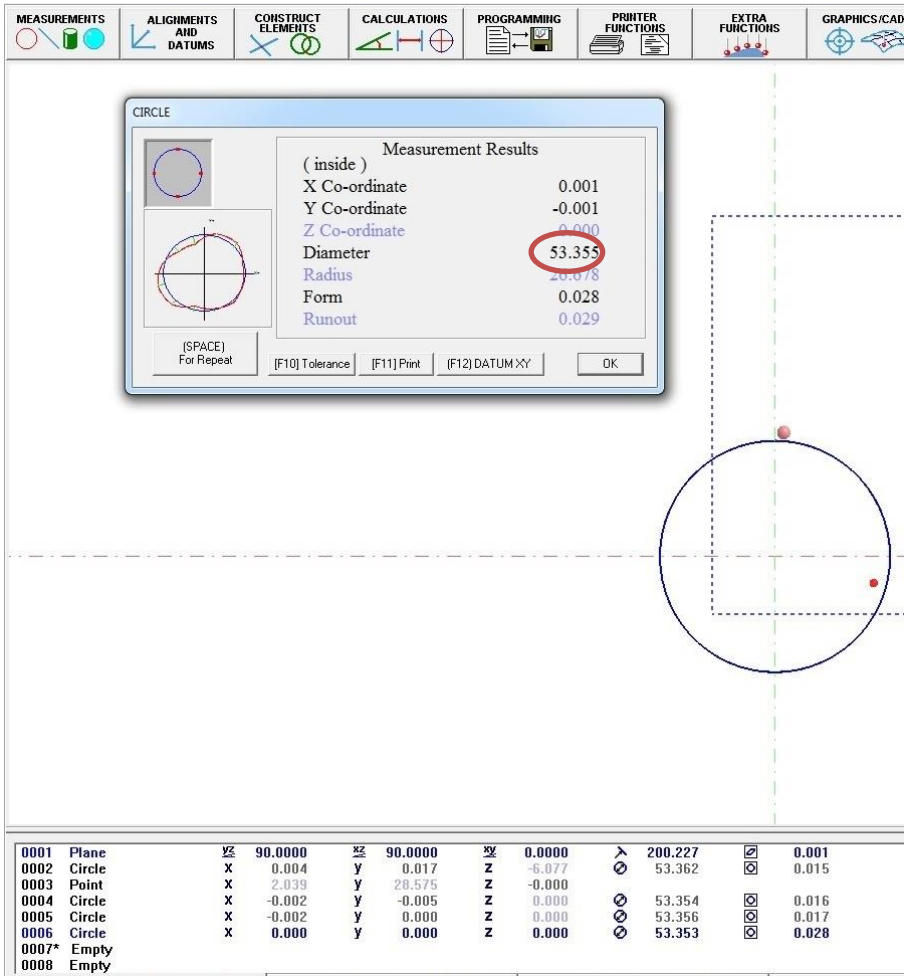

Figure K-1: CMM Results of Bore Diameter

Metrology Instrument Services CIRCOM 12:37:08 29/06/2017

Roundness

Measuring step: 0°21'

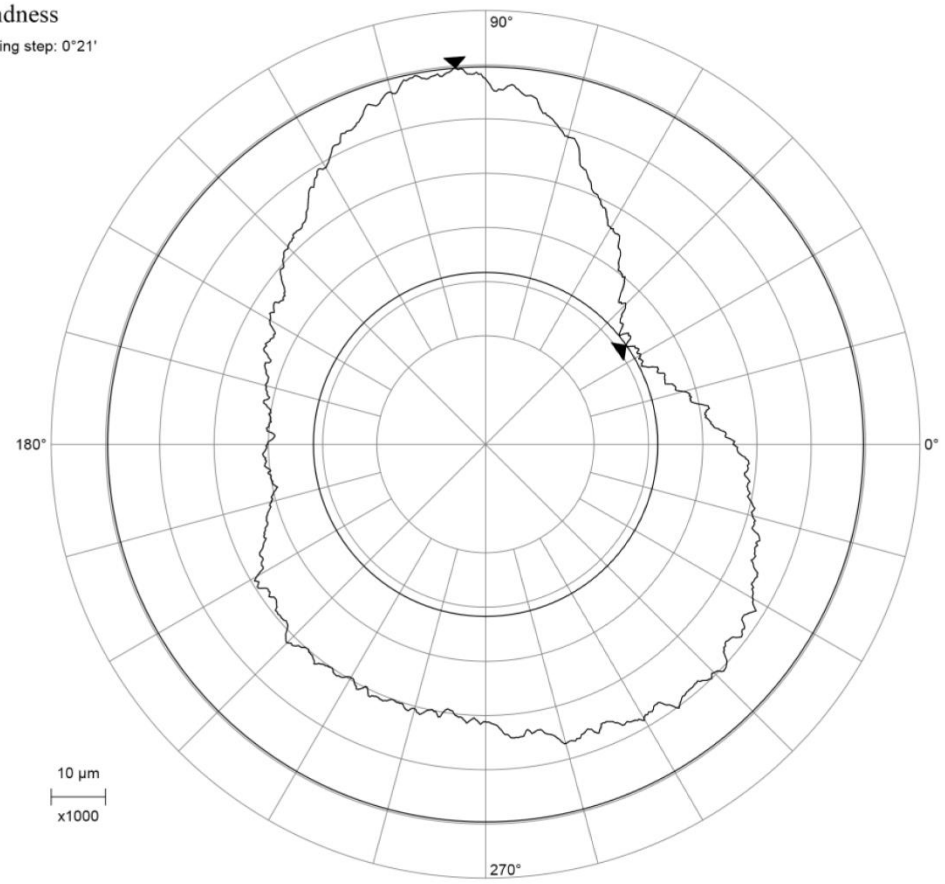

N	Position			Value		Tol	Met	Filter		Reference	Eccentr./ Misalign		Angle/ Slope
1	H	0.001 mm	Roundness error	37.860 µm	Ok	100.000	LSCI	2CR	1-50		E 48.762 µm	A	45.0°
1	H	0.001 mm	Internal roundness error	18.282 µm	Ok	100.000	LSCI	2CR	1-50		E 48.762 µm	A	45.0°
1	H	0.001 mm	External roundness error	19.577 µm	Ok	100.000	LSCI	2CR	1-50		E 48.762 µm	A	45.0°

Figure K-2: Roundness of Bore

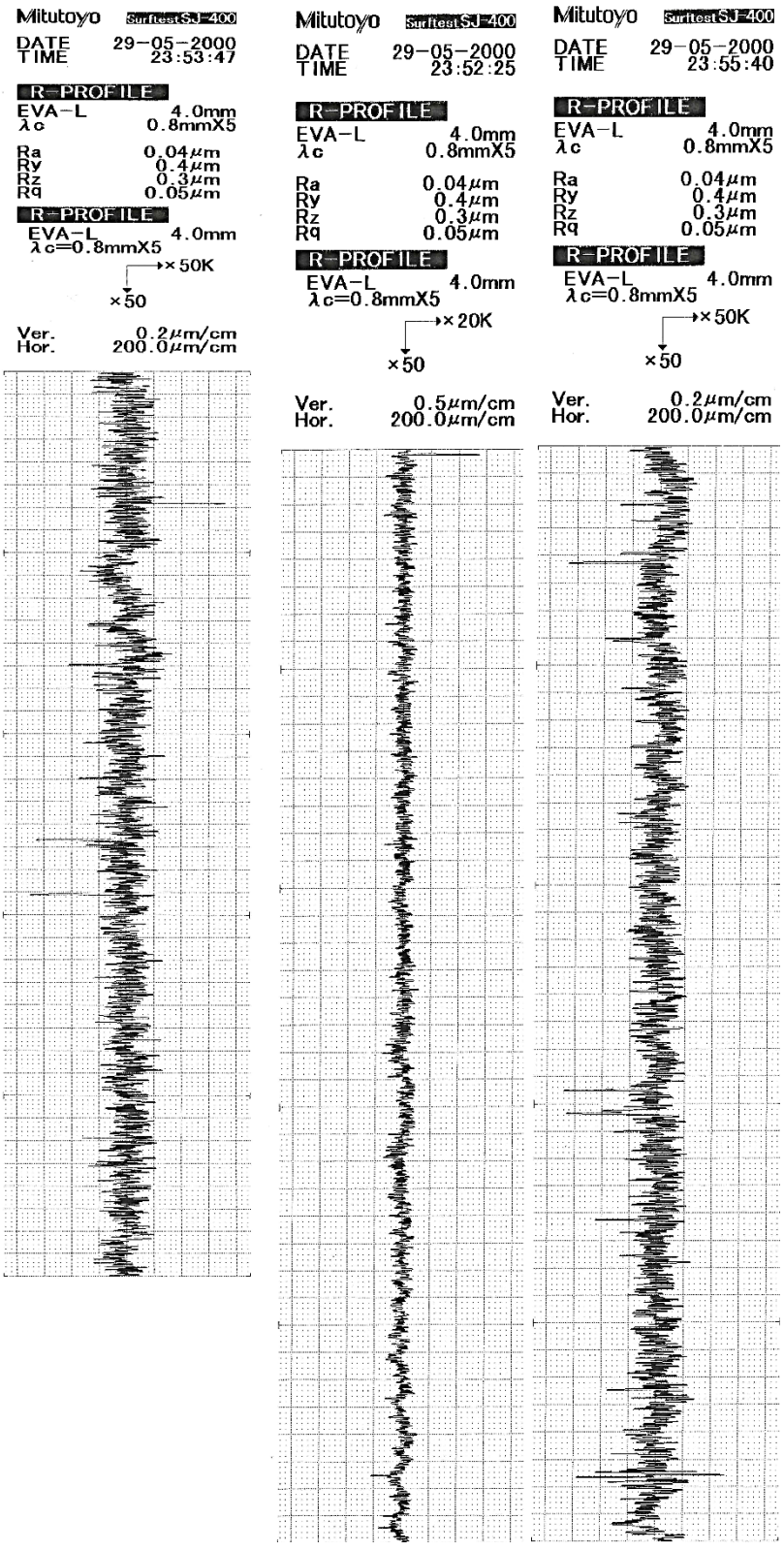

Figure K-3: Surface Finish of Bore

b. Piston Bore with Flanges

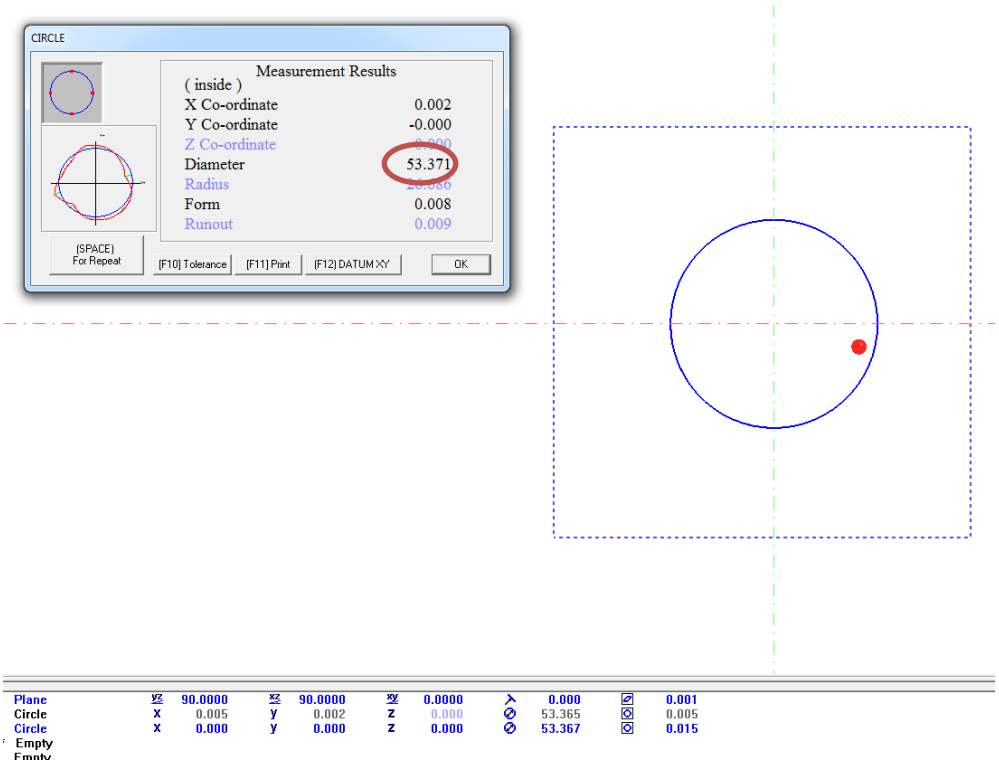

Figure K-4: CMM Results of Bore Diameter with Welded Flanges – 10mm Deep

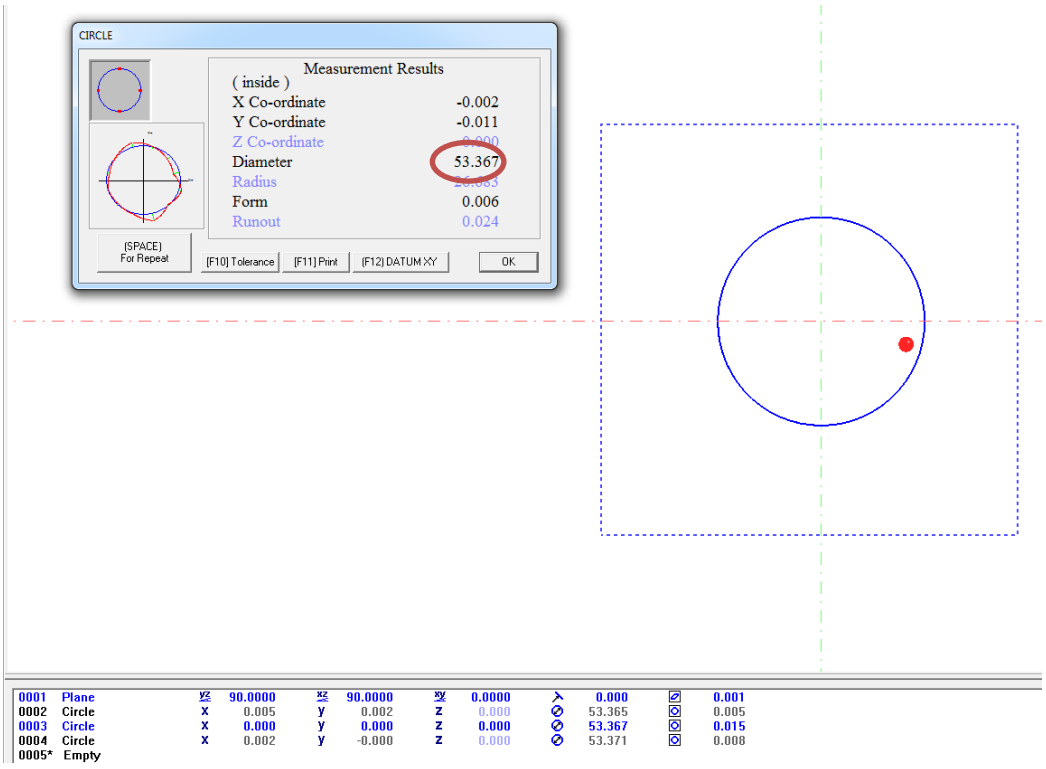

Figure K-5: CMM Results of Bore Diameter with Welded Flanges – 20mm Deep

Results

N	Position		Value		Tol	Met	Filter	Reference	Eccentr./ Misalign.		Angle/ Slope
1	H 0.001 mm	Roundness error	3.202 µm	OK	100.000	LSCI	2CR 1-50		E 28.036 µm	A	291.8°
1	H 0.001 mm	Internal roundness error	1.483 µm	OK	100.000	LSCI	2CR 1-50		E 28.036 µm	A	291.8°
1	H 0.001 mm	External roundness error	1.719 µm	OK	100.000	LSCI	2CR 1-50		E 28.036 µm	A	291.8°
2	H 0.001 mm	Roundness error	3.156 µm	OK	100.000	LSCI	2CR 1-50		E 28.165 µm	A	291.9°
2	H 0.001 mm	Internal roundness error	1.432 µm	OK	100.000	LSCI	2CR 1-50		E 28.165 µm	A	291.9°
2	H 0.001 mm	External roundness error	1.724 µm	OK	100.000	LSCI	2CR 1-50		E 28.165 µm	A	291.9°
		Roundness error	3.207 µm	OK	100.000						
		Internal roundness error	1.483 µm	OK	100.000						
		External roundness error	1.724 µm	OK	100.000						

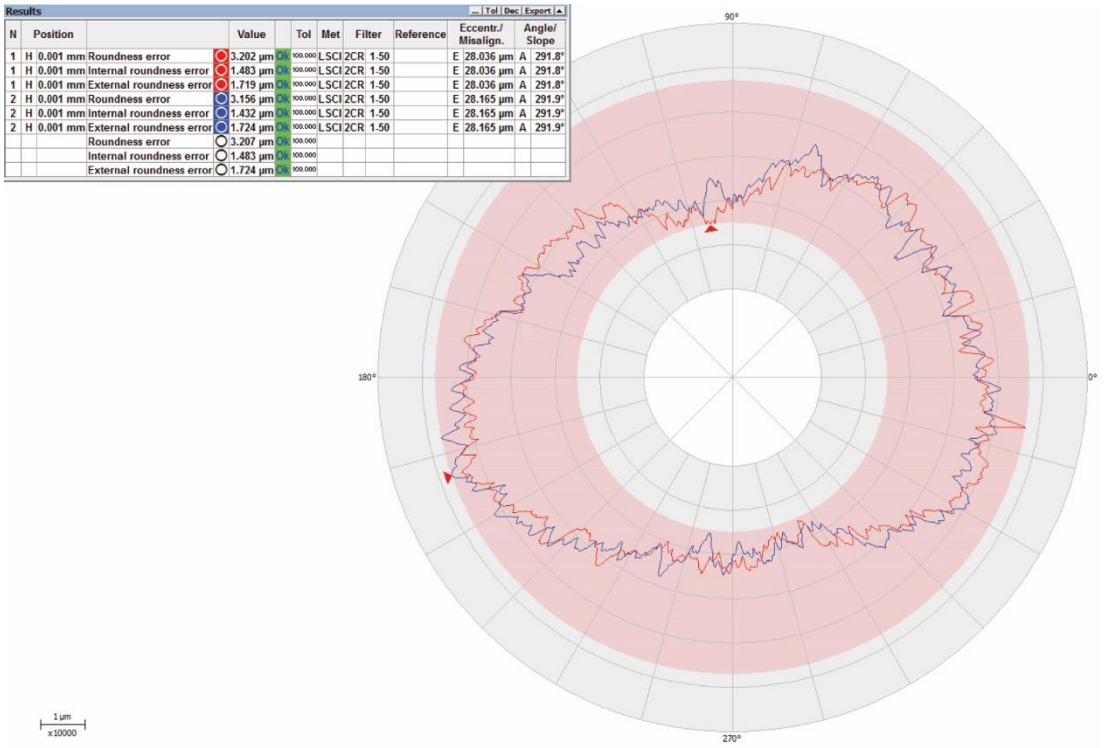

Figure K-6: Roundness of Bore with Welded Flanges – Measurement 1

N	Position		Value		Tol	Met	Filter	Reference	Eccentr./ Misalign.		Angle/ Slope
1	H 0.001 mm	Roundness error	4.284 µm	OK	100.000	LSCI	2CR 1-50		E 24.986 µm	A	288.8°
1	H 0.001 mm	Internal roundness error	1.984 µm	OK	100.000	LSCI	2CR 1-50		E 24.986 µm	A	288.8°
1	H 0.001 mm	External roundness error	2.299 µm	OK	100.000	LSCI	2CR 1-50		E 24.986 µm	A	288.8°
2	H 0.001 mm	Roundness error	4.680 µm	OK	100.000	LSCI	2CR 1-50		E 24.932 µm	A	289.5°
2	H 0.001 mm	Internal roundness error	2.342 µm	OK	100.000	LSCI	2CR 1-50		E 24.932 µm	A	289.5°
2	H 0.001 mm	External roundness error	2.338 µm	OK	100.000	LSCI	2CR 1-50		E 24.932 µm	A	289.5°
		Roundness error	4.680 µm	OK	100.000						
		Internal roundness error	2.342 µm	OK	100.000						
		External roundness error	2.338 µm	OK	100.000						

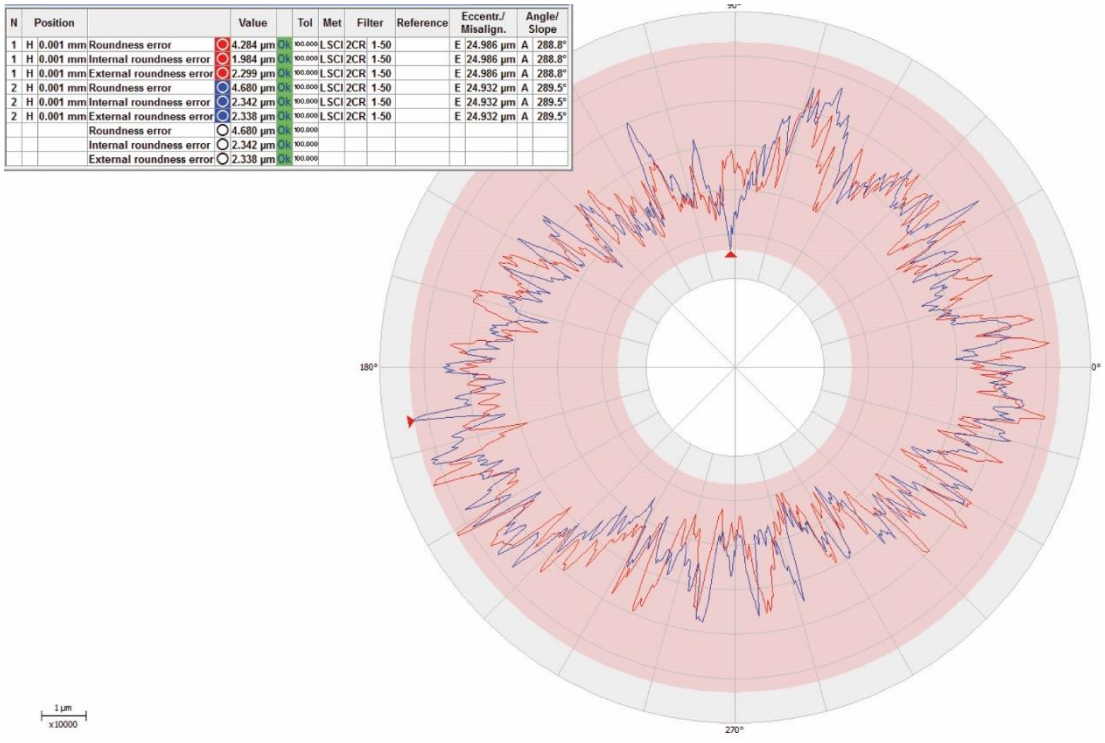

Figure K-7: Roundness of Bore with Welded Flanges – Measurement 2

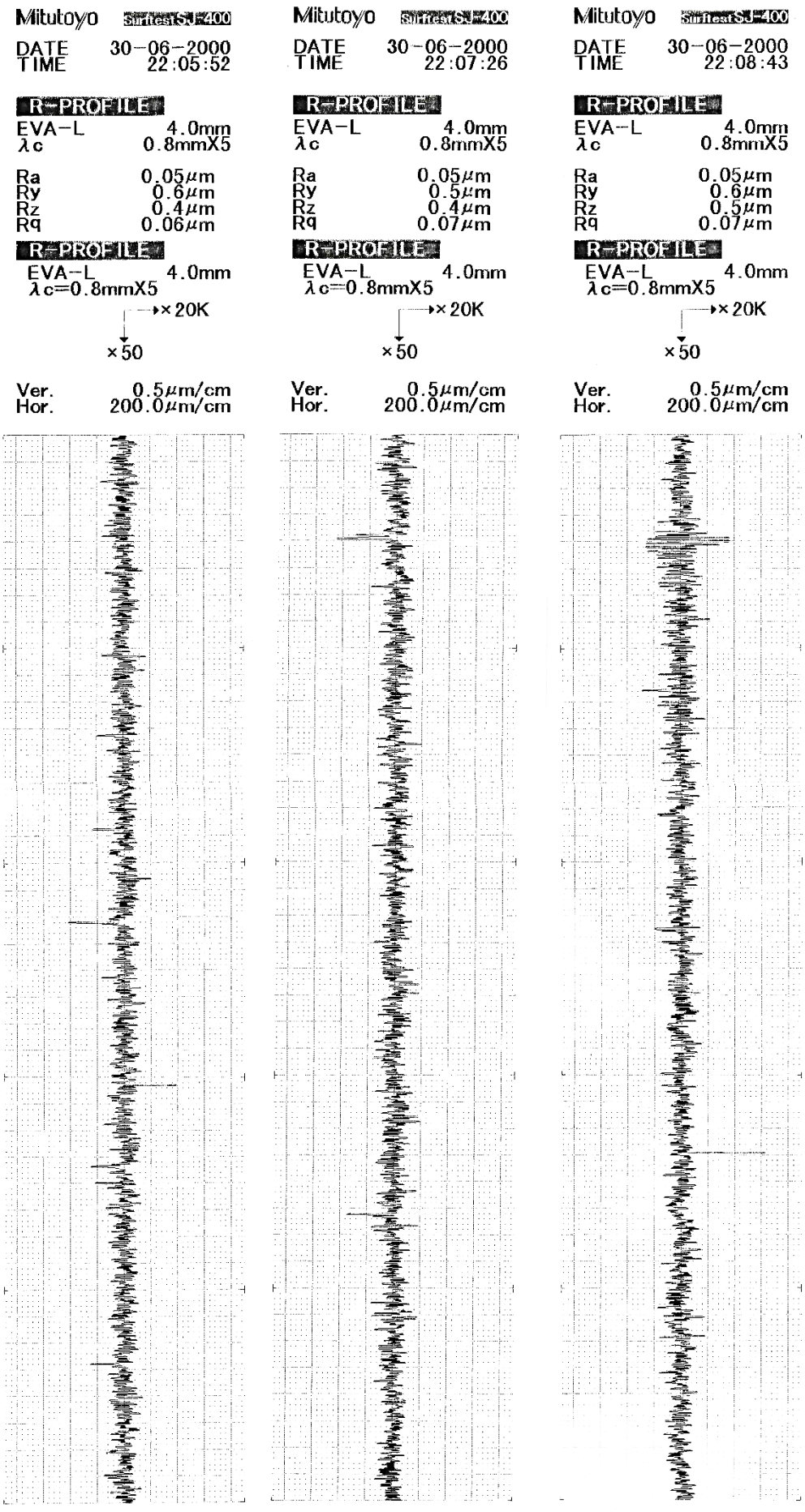

Figure K-8: Surface Finish of Bore with Welded Flanges

c. Piston Body & Piston End Caps

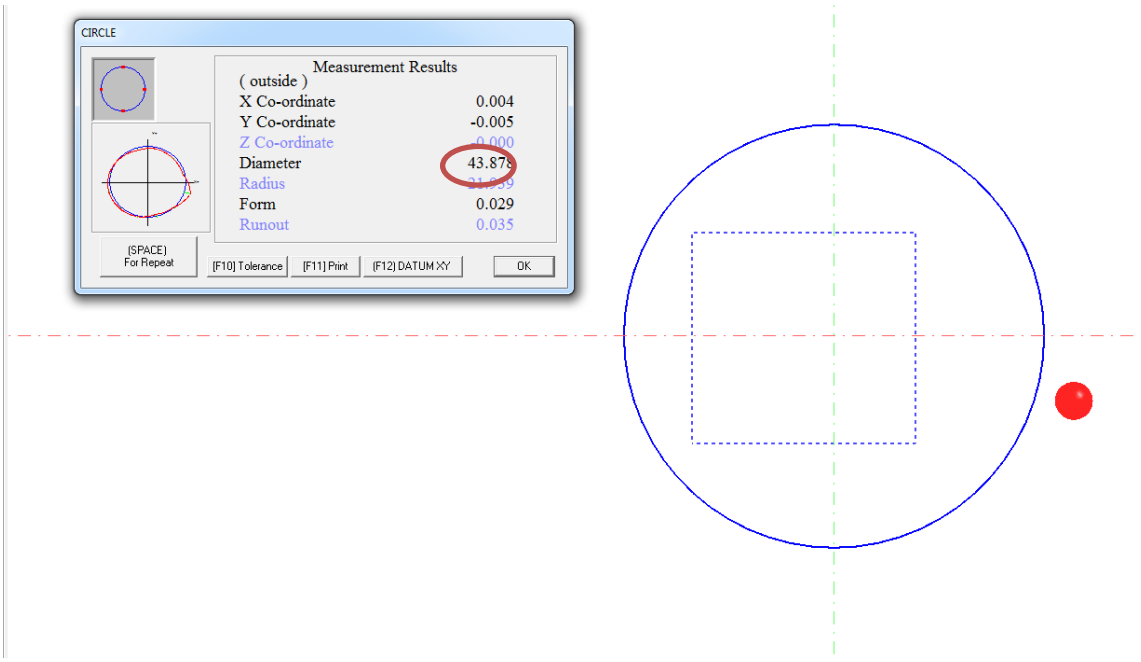

Figure K-9: CMM Results of Left-hand Side Seal Groove of the Piston

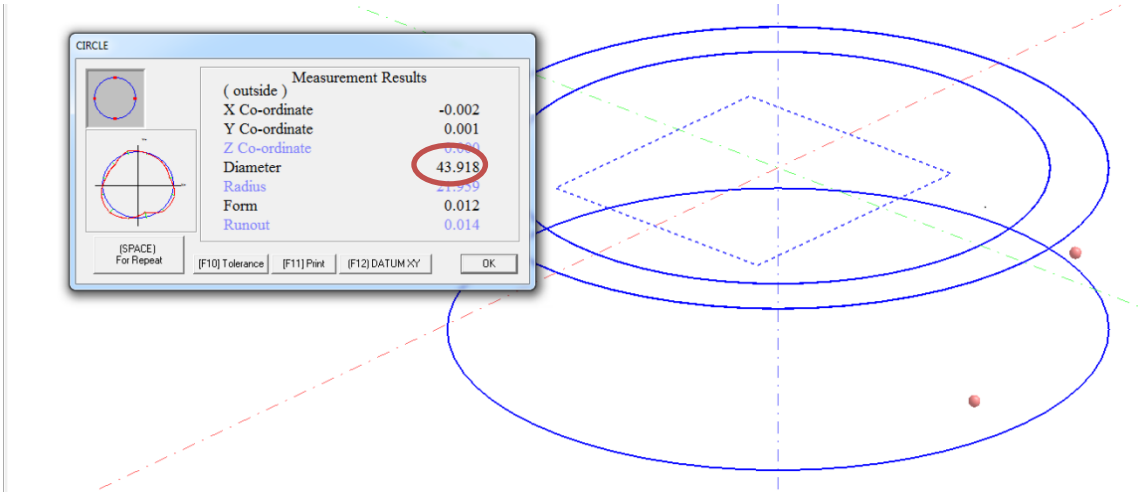

Figure K-10: CMM Results of Right-hand Side Seal Groove of the Piston

Width of Left-hand Side Seal Groove

0007	Point	X	-3.875	Y	-24.791	Z	-11.494
0008	Point	X	22.421	Y	-12.074	Z	-11.505

Width of Right-hand Side Seal Groove

0019	Point	X	1.295	Y	-25.041	Z	-11.442
0020	Point	X	-25.316	Y	0.992	Z	-11.450

Figure K-11: CMM Results of Width of Seal Grooves

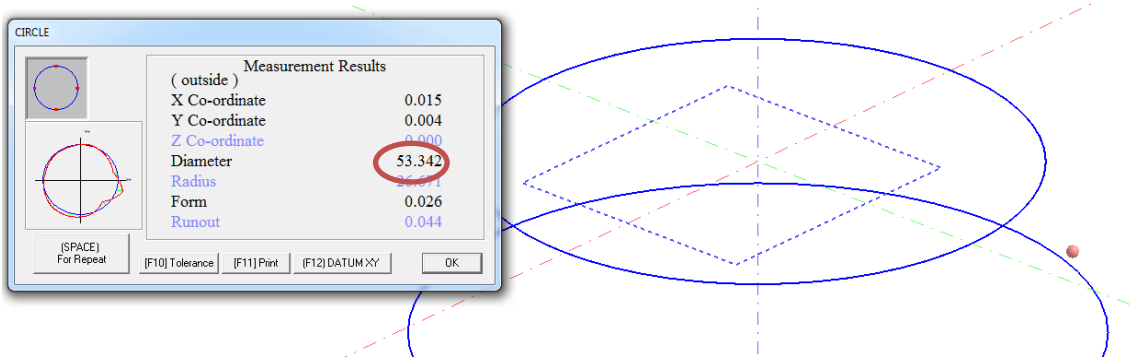

Figure K-12: Outer Diameter of the Piston – 13mm Deep

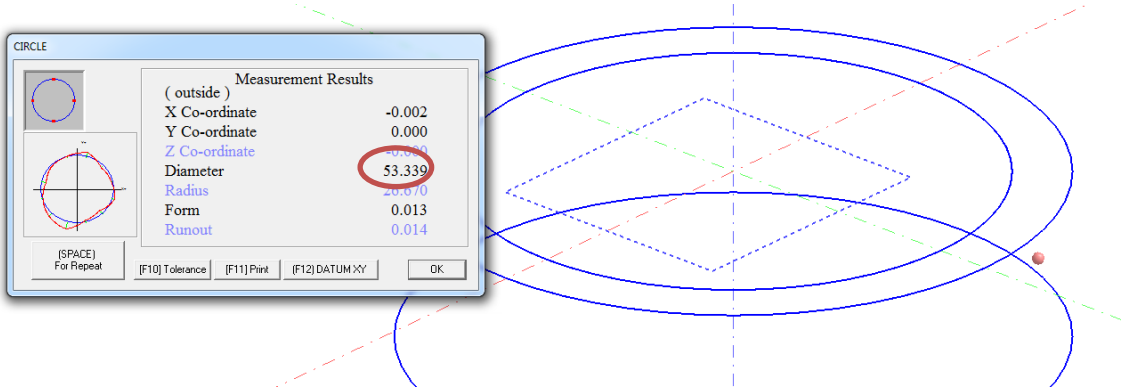

Figure K-13: Outer Diameter of the Piston – 33mm Deep

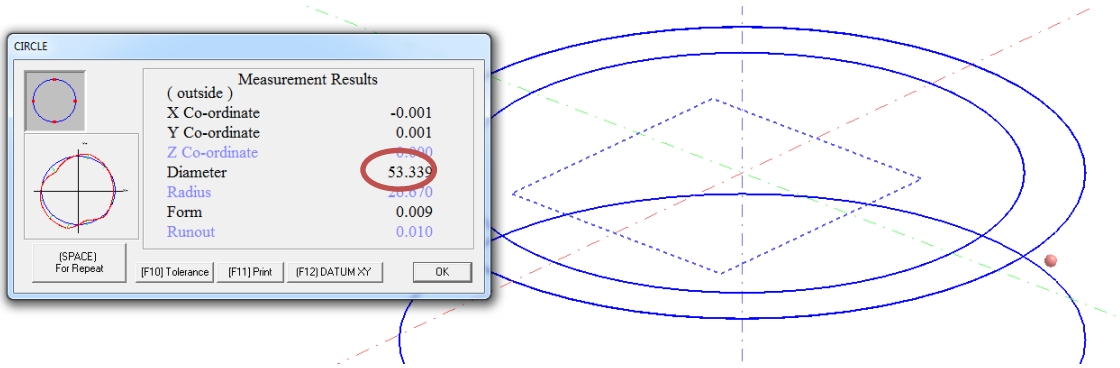

Figure K-14: Outer Diameter of the Piston – 37mm Deep

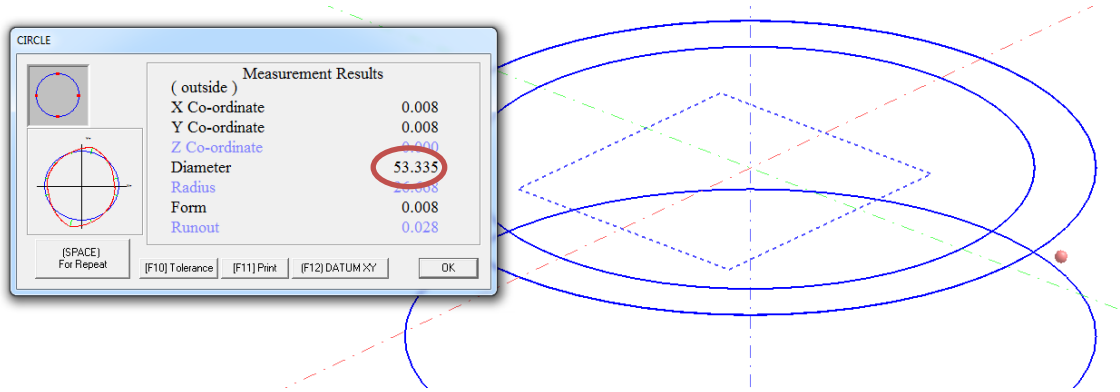

Figure K-15: Outer Diameter of the Piston – 57mm Deep

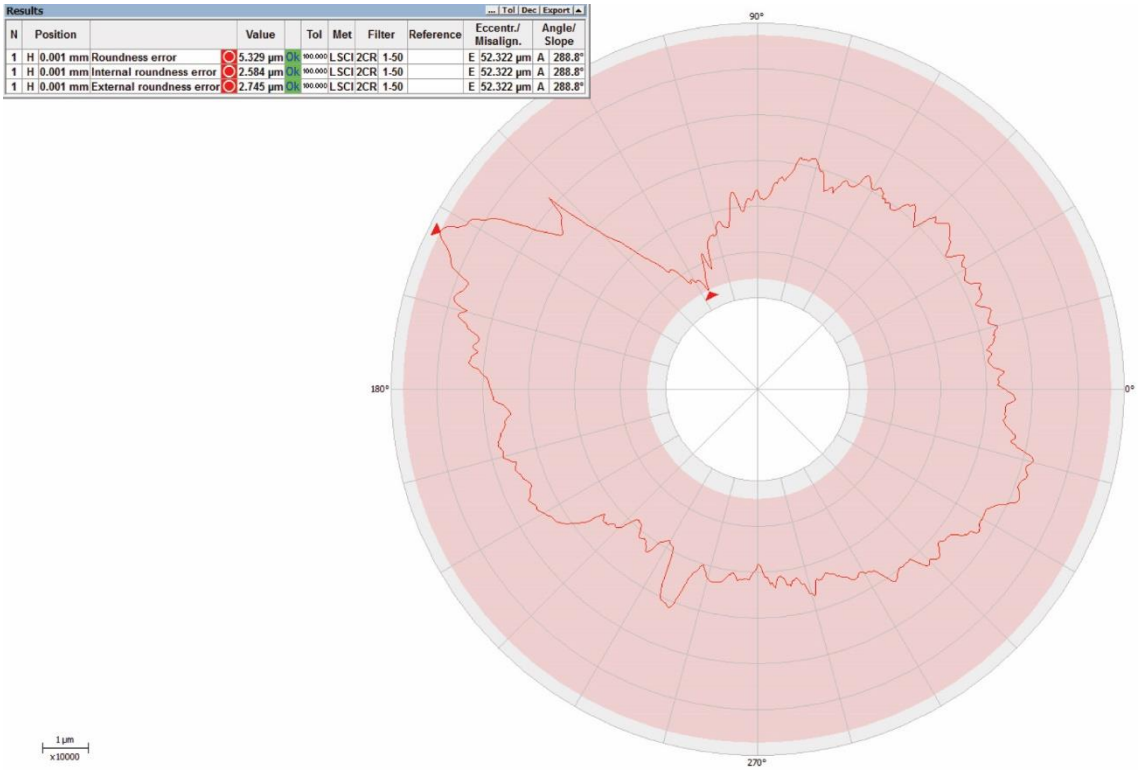

Figure K-16: Roundness of Piston – Left-hand Seal Groove

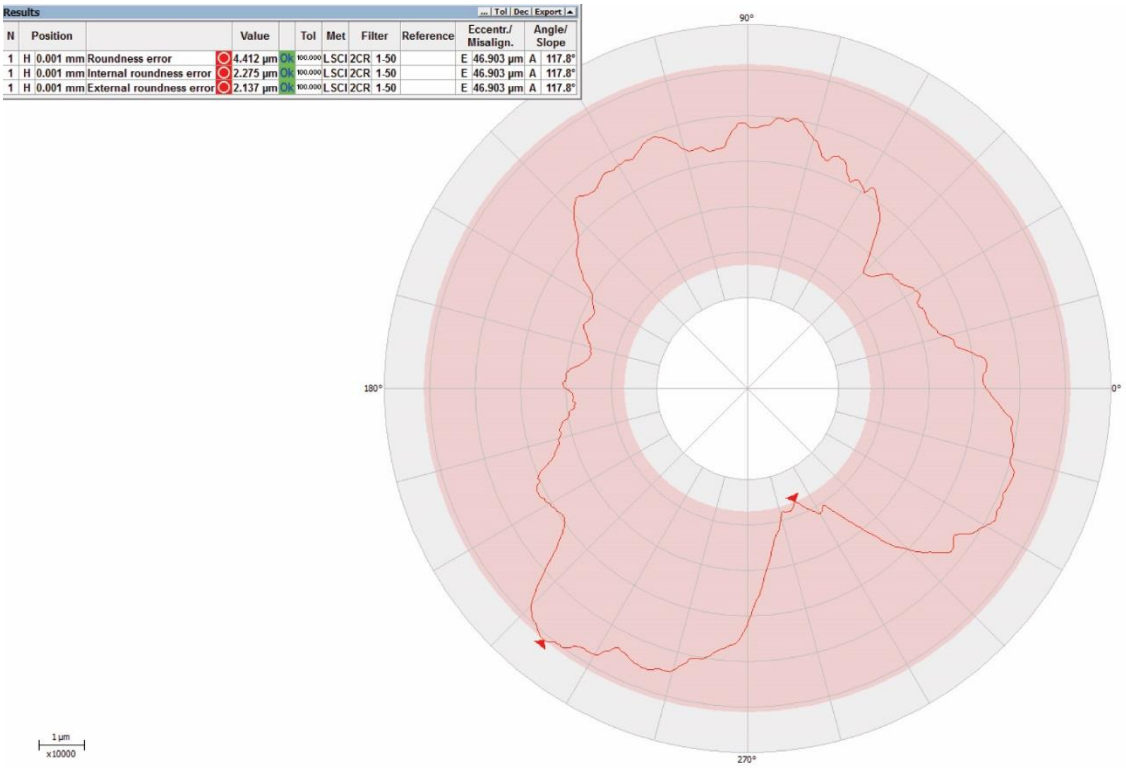

Figure K-17: Roundness of Piston – Right-hand Seal Groove

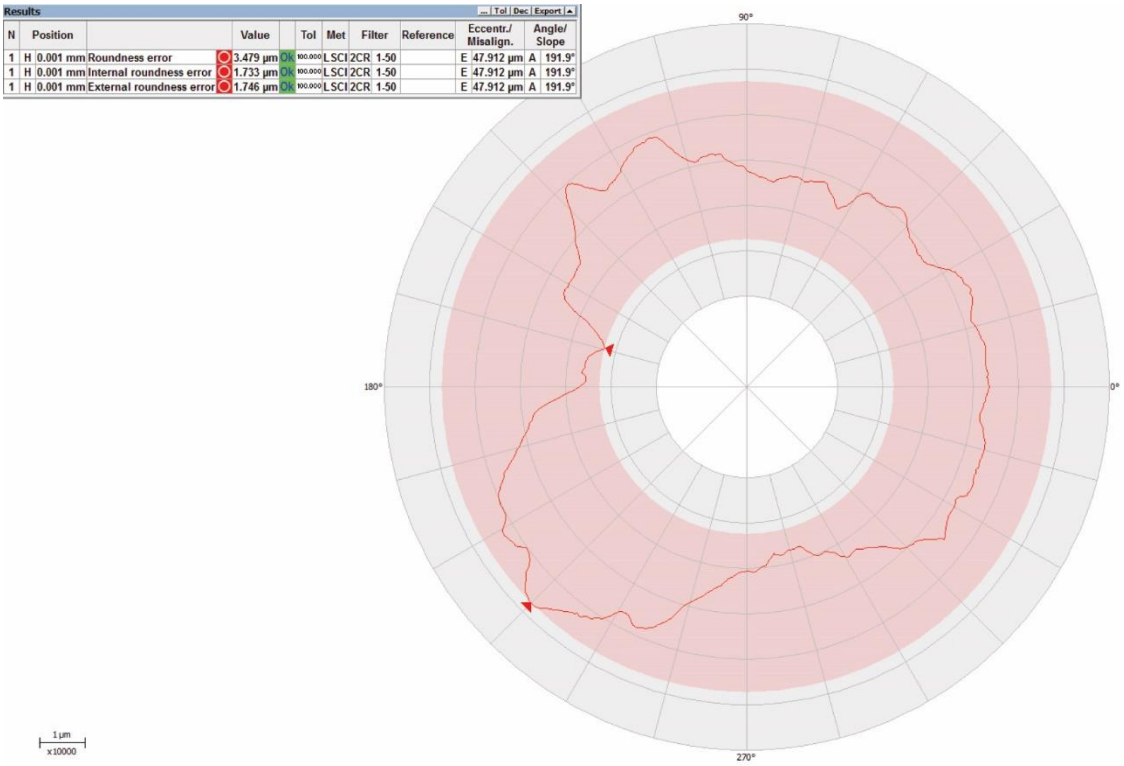

Figure K-18: Roundness of Piston – Outer Diameter

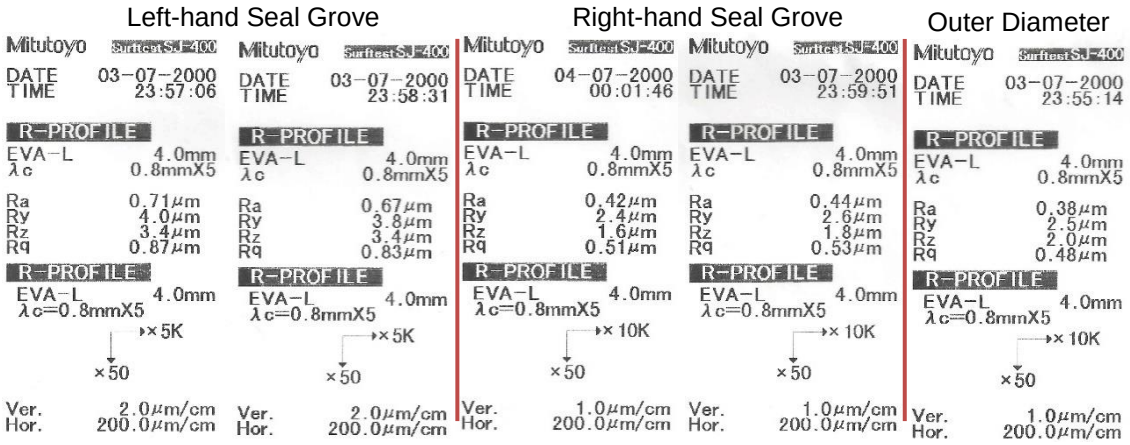

Figure K-19: Unpolished Surface Finish

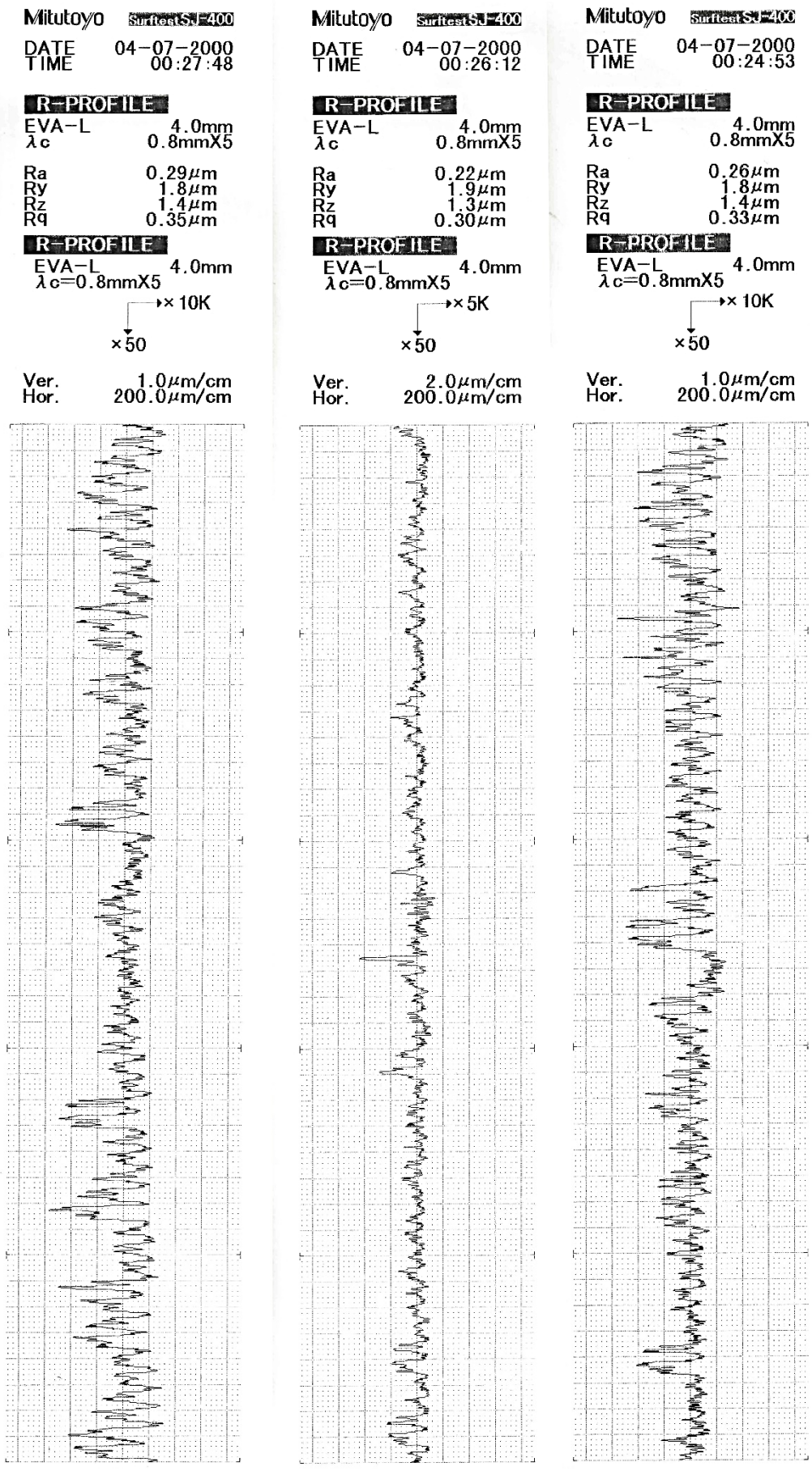

Figure K-20: Surface Finish of Polished Left-hand Side Groove

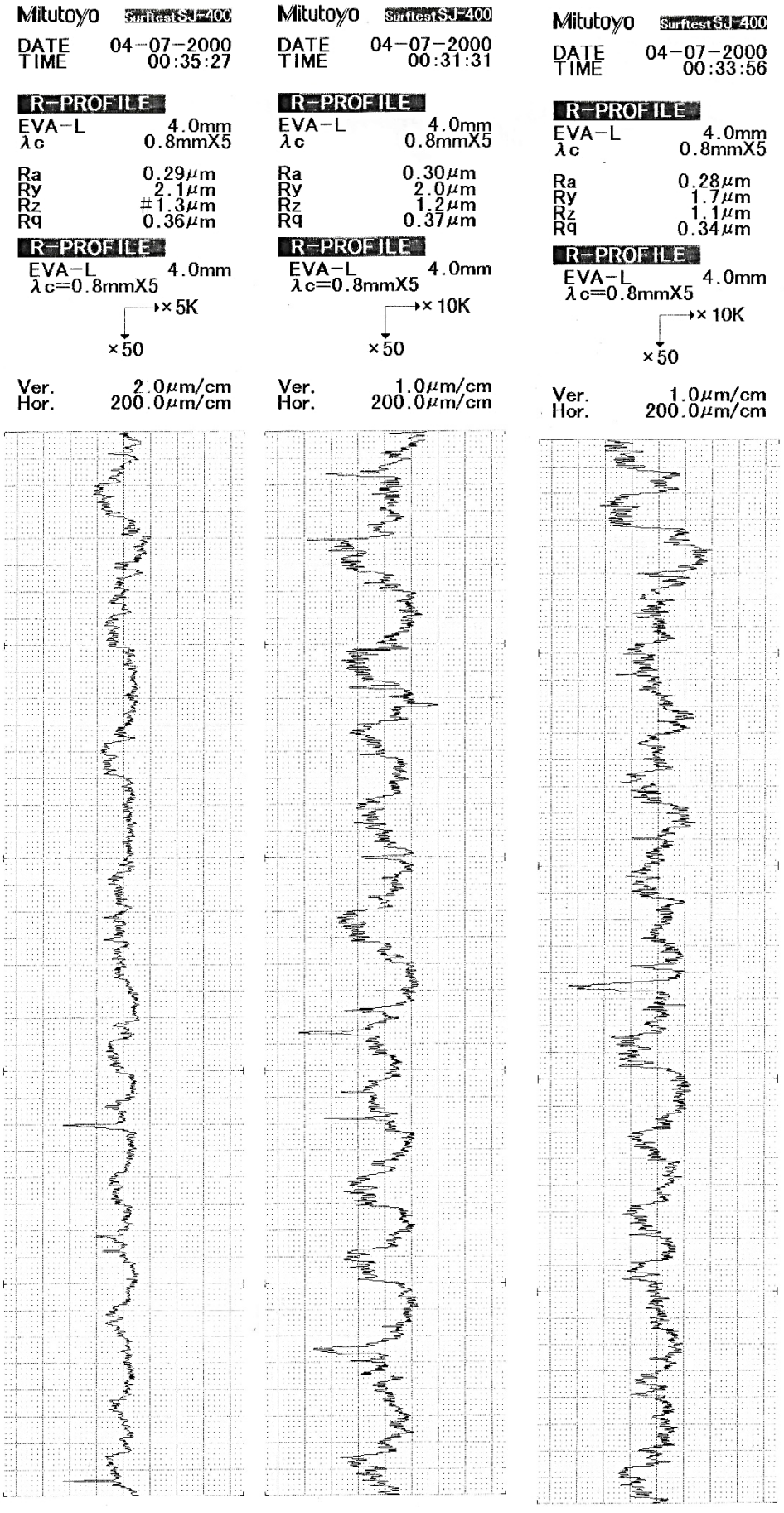

Figure K-21: Surface Finish of Polished Right-hand Side Groove

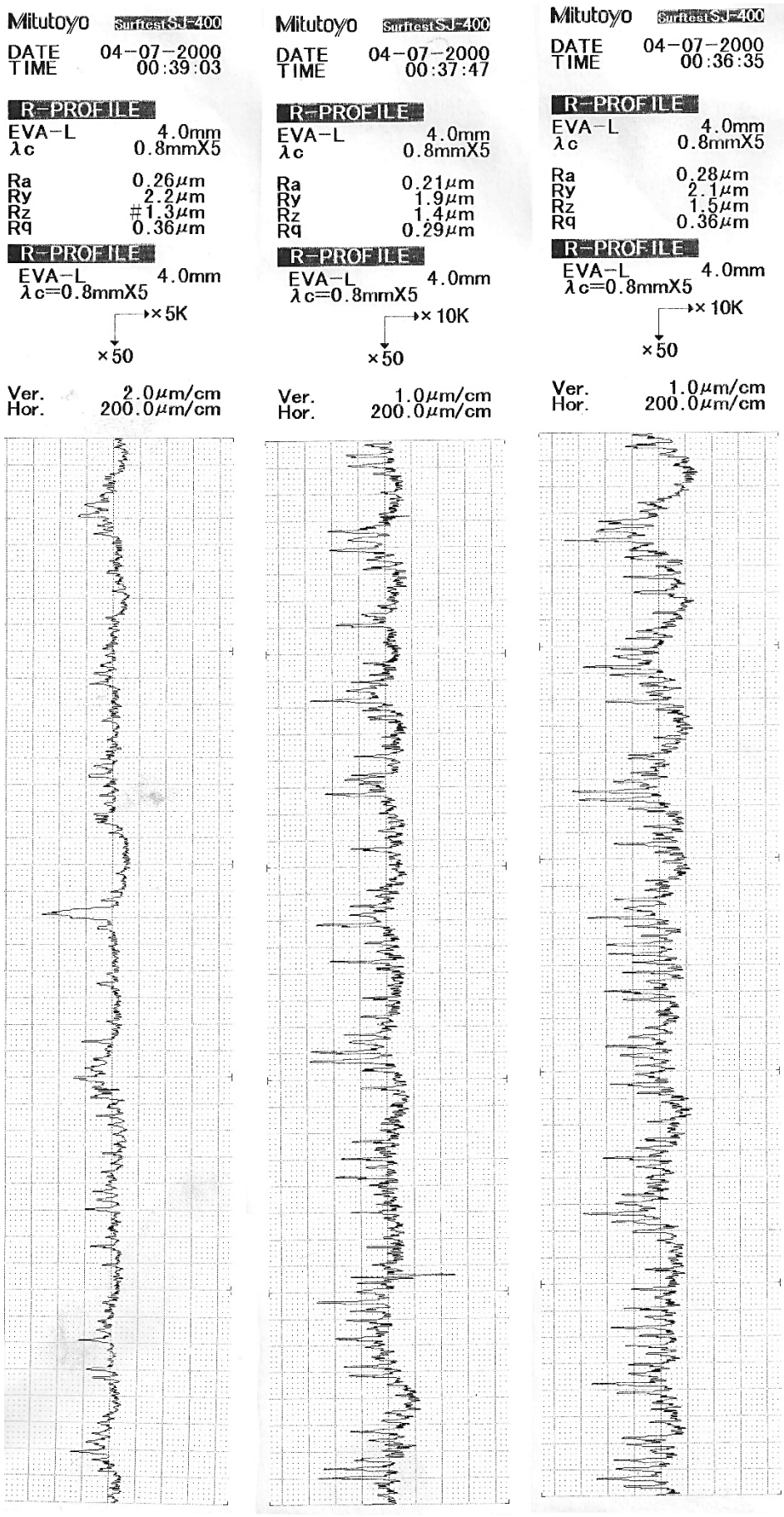

Figure K-22: Surface Finish of Polished Outer Diameter

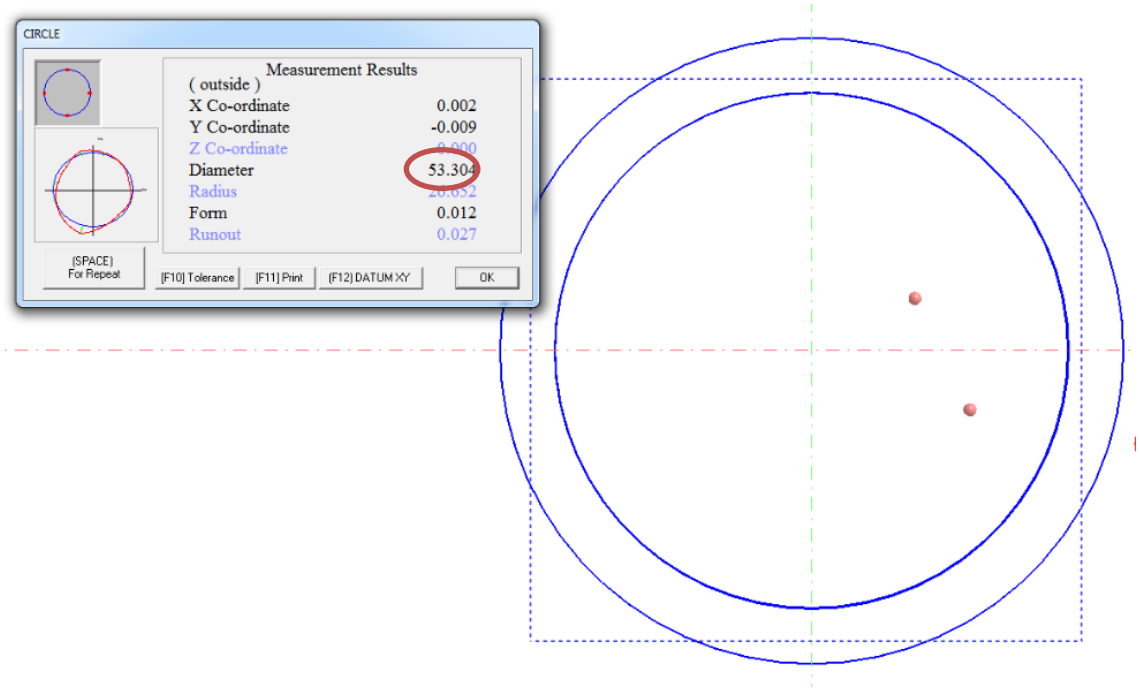

Figure K-23: Outer Diameter of the Left-hand End Cap

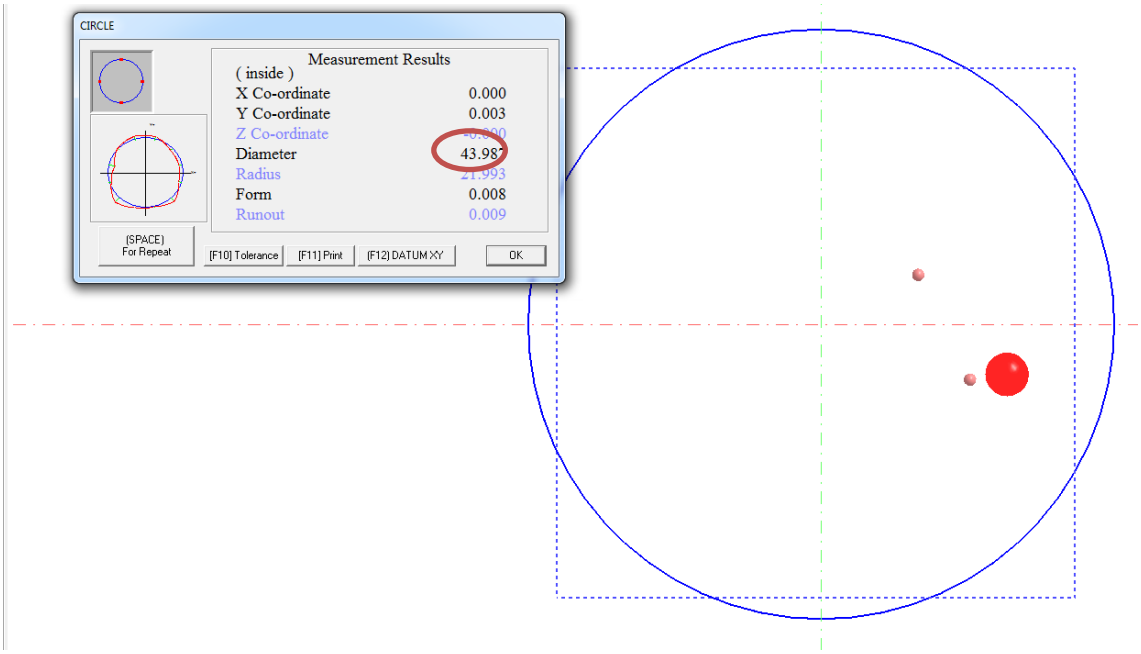

Figure K-24: Bored Diameter of the Left-hand End Cap

0018	Point	X	-227.781	Y	-408.991	Z	-4.296
0019	Point	X	-248.706	Y	-409.019	Z	-4.307

Figure K-25: Bore Depth of the Left-hand End Cap

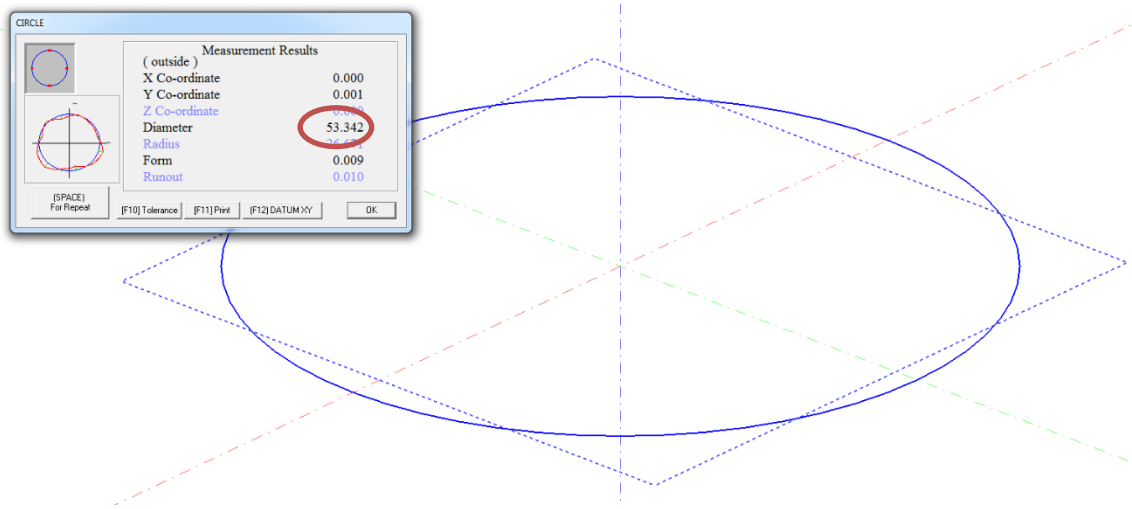

Figure K-26: Outer Diameter of the Right-hand End Cap

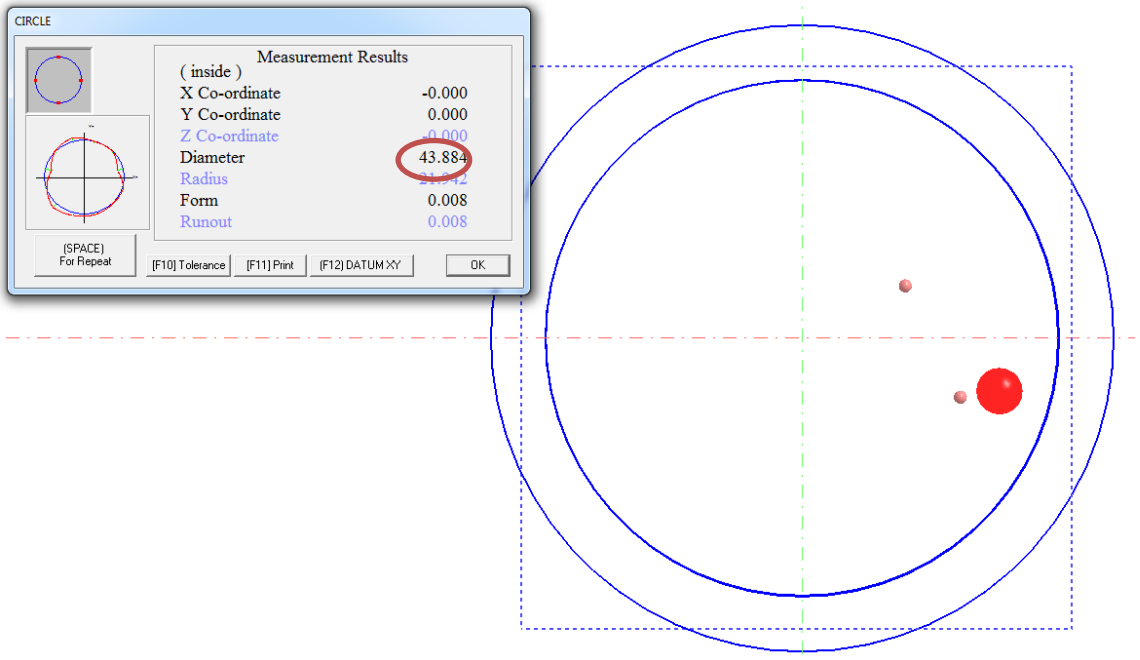

Figure K-27: Bored Diameter of the Right-hand End Cap

0005	Point	X	13.543	Y	-5.019	Z	-4.053
0006	Point	X	8.832	Y	4.468	Z	-4.051

Figure K-28: Bore Depth of the Right-hand End Cap

Results

N		Position		Value		Tol	Met	Filter	Reference	Eccentr./ Misalign.		Angle/ Slope
1	H	0.001 mm	Roundness error	2.638 µm	Ok	100.000	LSCI	2CR 1-50		E 128.840 µm	A	301.3°
1	H	0.001 mm	Internal roundness error	0.862 µm	Ok	100.000	LSCI	2CR 1-50		E 128.840 µm	A	301.3°
1	H	0.001 mm	External roundness error	1.775 µm	Ok	100.000	LSCI	2CR 1-50		E 128.840 µm	A	301.3°

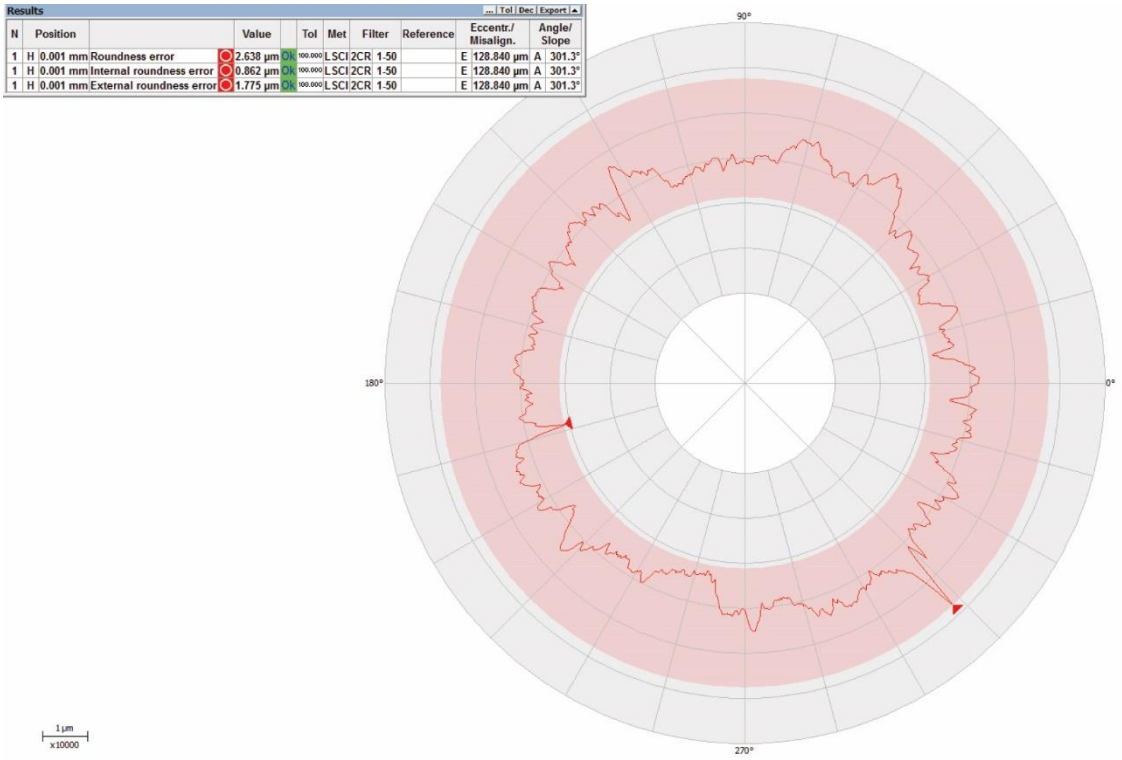

Figure K-29: Outer Diameter Roundness of the Left-hand Cap

Results

N		Position		Value		Tol	Met	Filter	Reference	Eccentr./ Misalign.		Angle/ Slope
1	H	0.001 mm	Roundness error	5.684 µm	Ok	100.000	LSCI	2CR 1-50		E 136.512 µm	A	154.3°
1	H	0.001 mm	Internal roundness error	2.951 µm	Ok	100.000	LSCI	2CR 1-50		E 136.512 µm	A	154.3°
1	H	0.001 mm	External roundness error	2.732 µm	Ok	100.000	LSCI	2CR 1-50		E 136.512 µm	A	154.3°

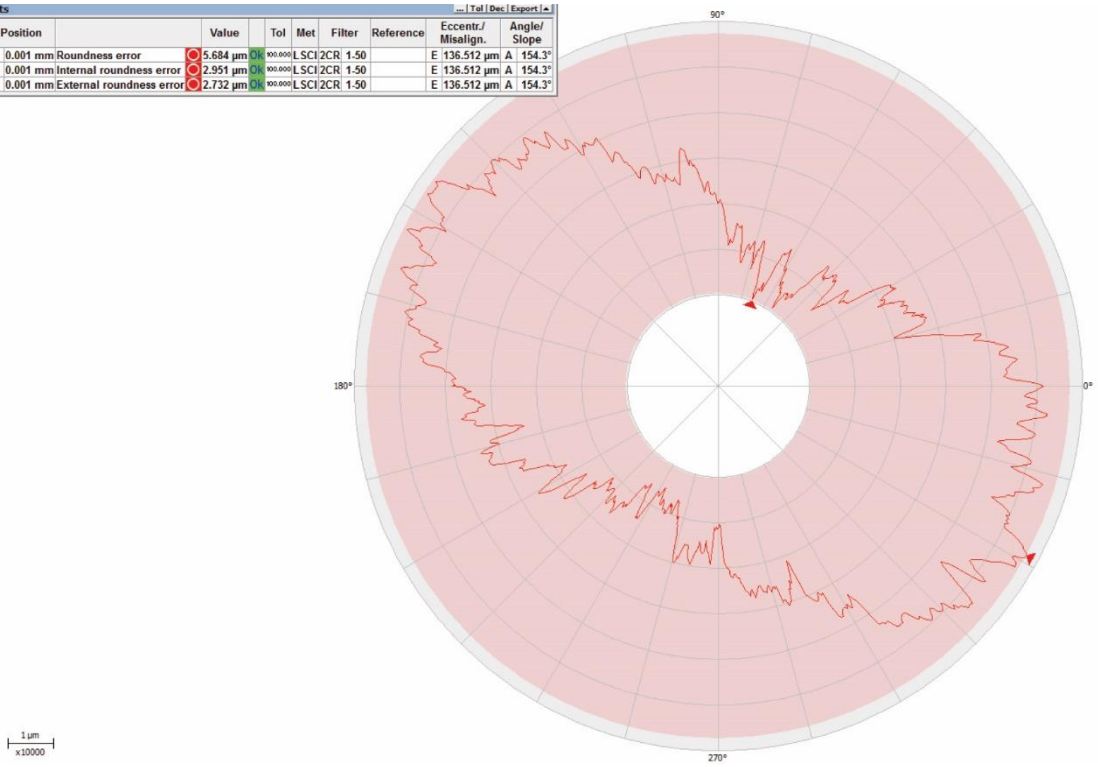

Figure K-30: Outer Diameter Roundness of the Right-hand Cap

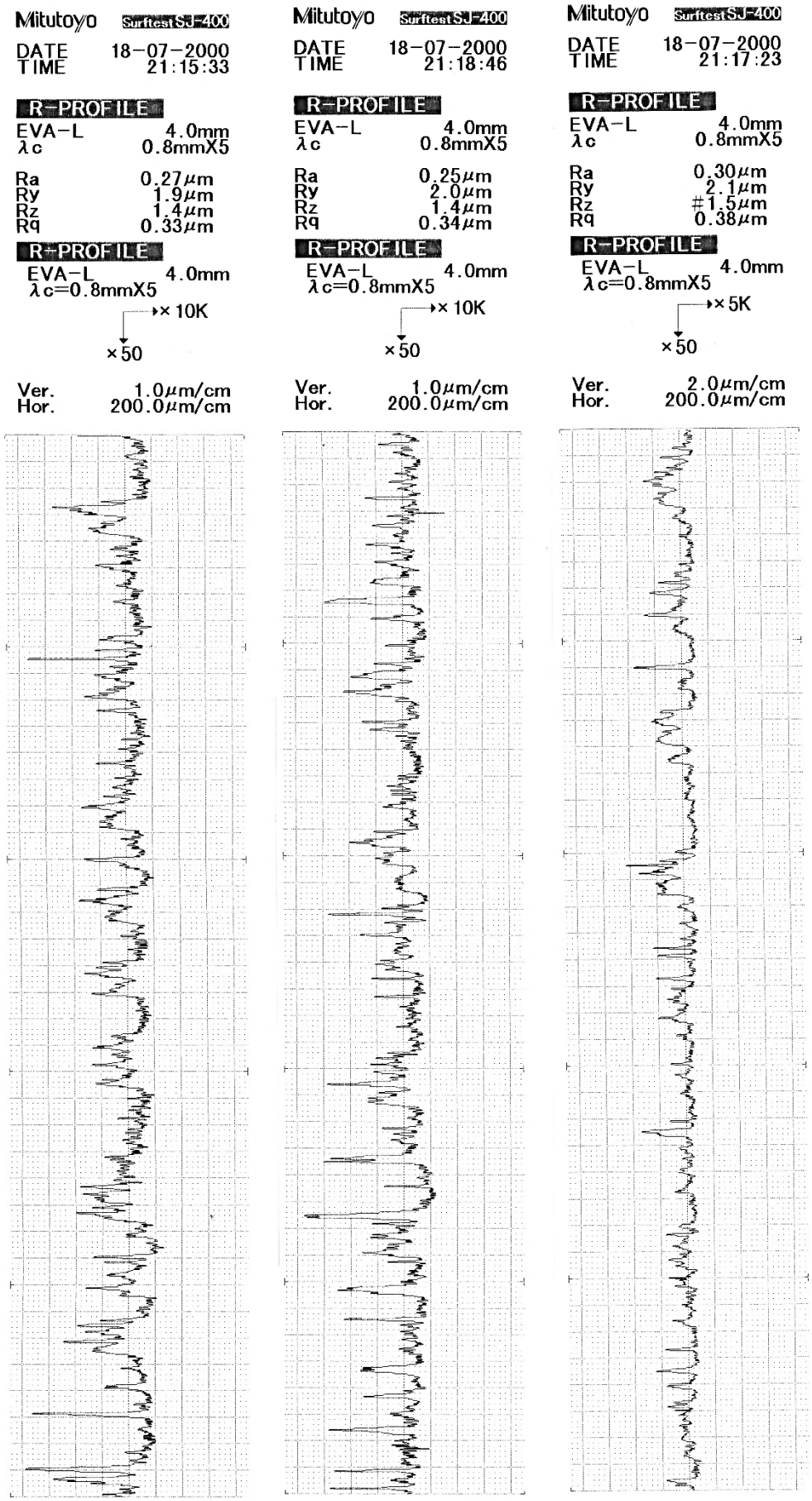

Figure K-31: Outer Diameter Surface Roughness of the Left-hand Cap

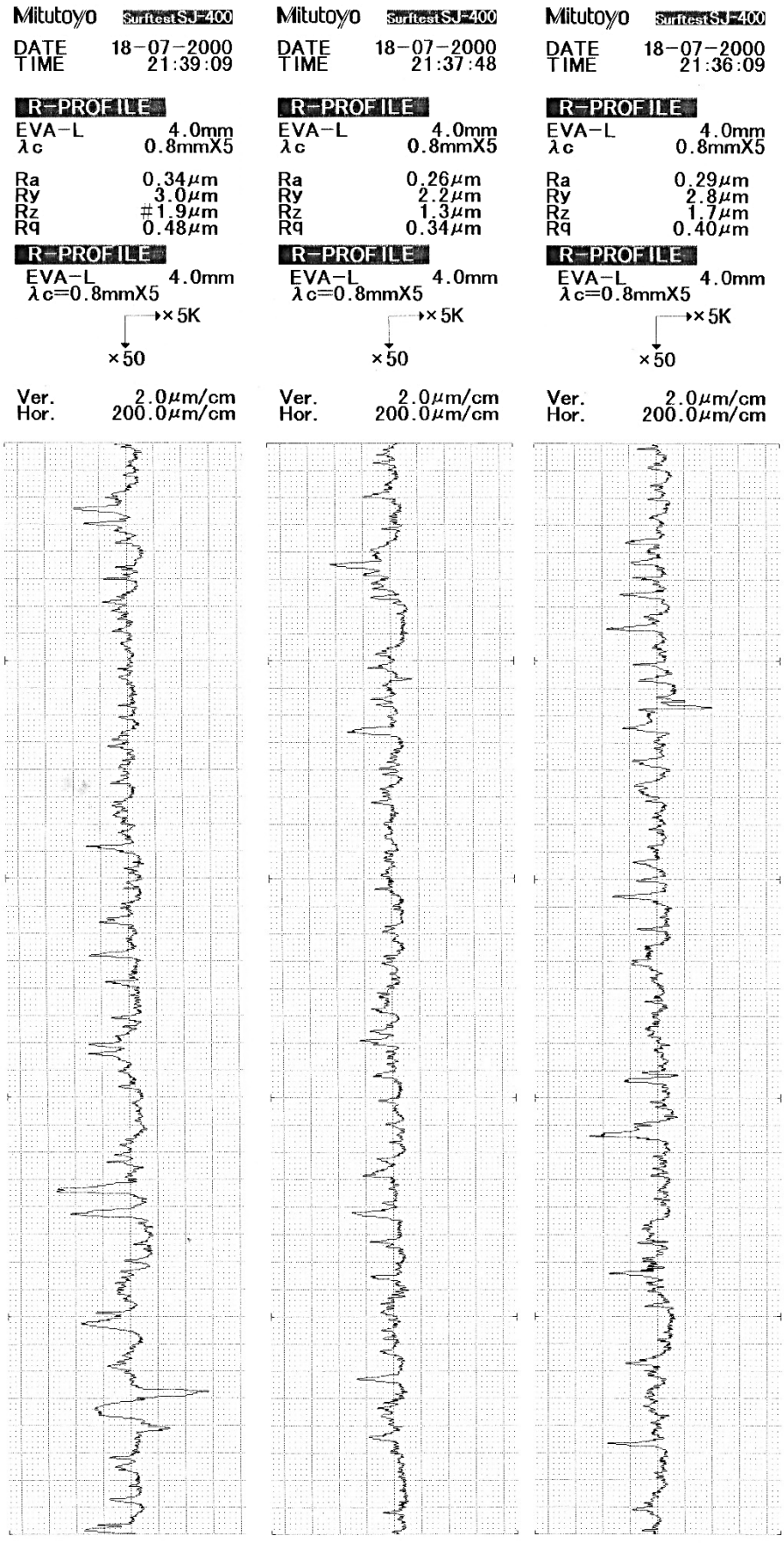

Figure K-32: Outer Diameter Surface Roughness of the Right-hand Cap

L.WinDaq & Thermocouple Sensor Setup

The 4-20mA current loop system is the most common measurement tool used in conjunction with pressure sensors. The system typically consists of a pressure transducer, Data Acquisition Unit (DAU) and DC power supply. The pressure transducer converts the pressure readings into an electrical signal which is then interpreted by the DAU system. To explain how the system works, let's consider a 0-100bar sensor is installed. At 0bar and 100bar, the pressure transducer will send the output values of 4mA and 20mA respectively. There is a linear relationship between pressure and current. It should be noted that the current itself cannot be measured, but by installing a shunt resistor with a known value, the voltage can be calculated using Ohm's Law as shown in Equation L-1.

$$V = I \times R \tag{L-1}$$

Where V – Voltage (V), I – current (A) and R – Resistance (Ω)

For measuring the output pressure (sensor 4, Figure 5-11; pg. 97) a 0-100bar 2-wire pressure transducer was used – the wiring schematic is shown in Figure L-1. A DC power supply is used to power the pressure transducer, which then sends the signal to the DAU system to be interpreted. As shown in this schematic, the WinDaq DI-1100 requires a shunt resistor of 250Ω to calculate the sensor voltage of the signal. It should be noted that if more than one sensor is used, a separate 250Ω shunt resistor must be installed for each sensor.

The pressure reading can be obtained in two ways. 1) By calibrating the engineering units on the WinDaq software, or 2) using the equation of a line (Equation L-2). To determine the accuracy of both methods, the units on the WinDaq software were calibrated against known pressure values. As shown in Figure L-2, a picture was taken of the pressure calibrator and the sensor voltage which then were then recorded as the upper level in the engineering unit settings (Figure L-3). At 0bar, the reading should have shown 1V (250Ω×4mA), but due to system inaccuracy or shifted atmospheric pressure, the DAU system reading was 1.0046V. Thus, this value was set as a lower level limit. It should be noted that the calibration system was only able to go up to around 10bar. The system had a small leak, thus the pictures ensured that the pressure and voltage values were recorded simultaneously. To test the calibration accuracy, the pressure calibrator and the WinDaq readings were compared at various pressures, as shown in Figure L-4 – Figure L-8, and summarised in Table L-1. The comparison revealed that the data obtained by the DAU system was accurate within ≈0.06bar.

$$y = mx + c \tag{L-2}$$

Where m is the gradient of the line and c is a constant.

Table L-1: Pressure Reading Comparison Between Pressure Calibrator and WinDaq Software

Pressure of Pressure Calibrator (bar)	Pressure of WinDaq (bar)	Δ Pressure (bar)
0.957	0.96	0.003
2.326	2.383	0.057
5.956	6.003	0.047

8.943	8.973	0.03
10.173	10.211	0.038

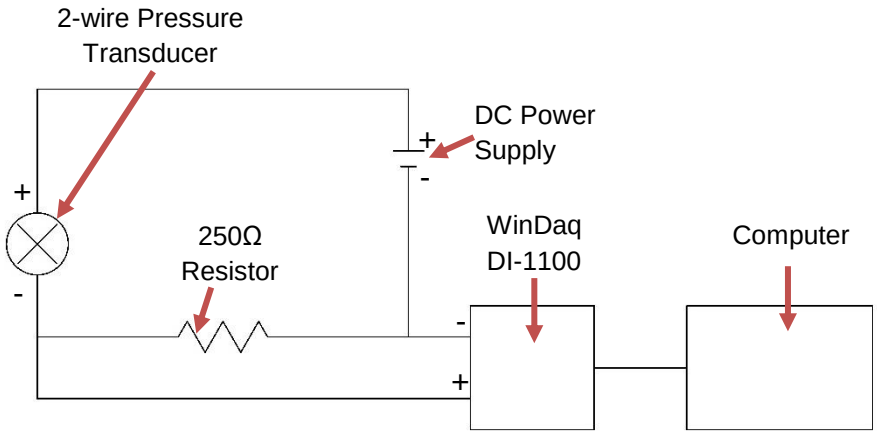

Figure L-1: 2-wire Pressure Connection Graph to WinDaq DI-1100

To compare how these values would vary against the second method, further measurements were taken (Figure L-9 – Figure L-13) to find the correlation between the pressure and voltage. Let y = pressure and x = Voltage, thus two coordinates were derived from these readings – (0.005, 1.006) & (10.554, 1.421). The gradient, m, was calculated using Equation L-3.

$$m = \frac{\Delta y}{\Delta x} \tag{L-3}$$

$$m = \frac{10.554 - 0.005}{1.421 - 1.006} = 25.419\ bar/V$$

The constant, c, was calculated by substituting one of the coordinates to Equation L-2. Thus, the pressure can be calculated from Equation L-4.

$$0.005 = 1.006 \times 25.419 + c$$

$$c = -25.567$$

$$y = 25.419x - 25.567 \rightarrow P = 25.419V - 25.567 \tag{L-4}$$

Where P – pressure (bar) and V – Voltage (V)

To compare the values of voltage at various pressures, readings in Figure L-9 – Figure L-13 were summarised in Table L-2 and converted to pressure using Equation L-4. The results given by this equation are within ≈0.035bar. It should be noted that the WinDaq software uses the same Equation L-2 to calculate the pressure reading, but due to a potential rounding error, it was less accurate than the value estimated by Equation L-4.

Table L-2: Pressure Values Obtain from Pressure vs Voltage Equation Are Compared Against Pressure Calibrator

Pressure of Pressure Calibrator (bar)	Voltage (V)	Pressure (bar)	Δ Pressure (bar)
0.005	1.006	0.005	0
1.902	1.082	1.937	0.0349
3.555	1.145	3.538	-0.0167

7.121	1.287	7.148	0.0268
10.554	1.421	10.554	0

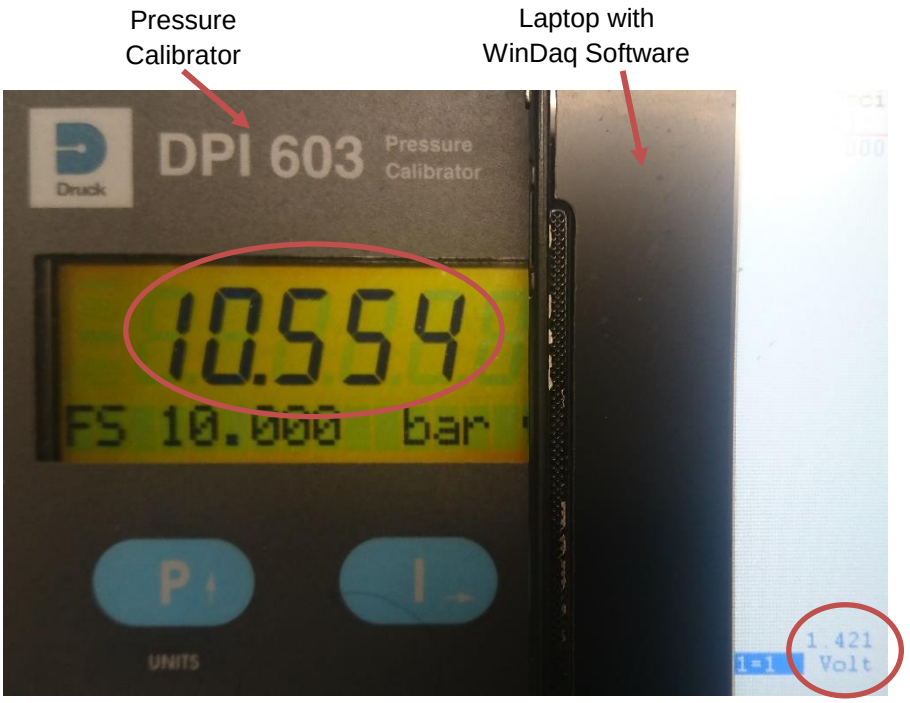

Figure L-2: 2-wire 0-100bar Upper Limit

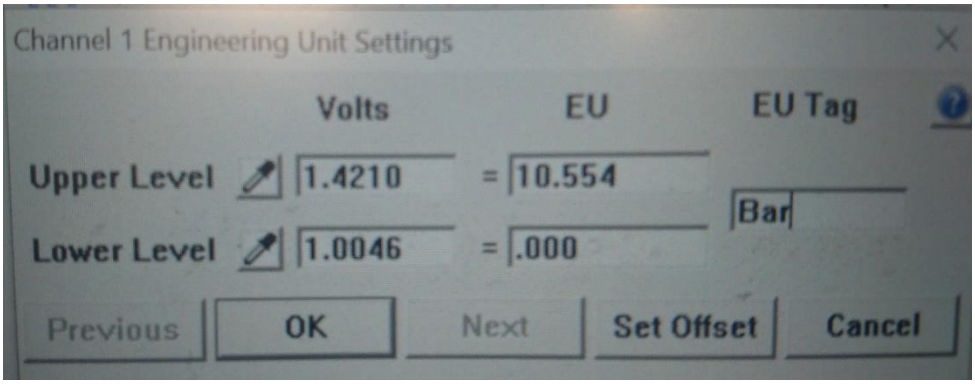

Figure L-3: WinDaq Software Engineering Unit Settings

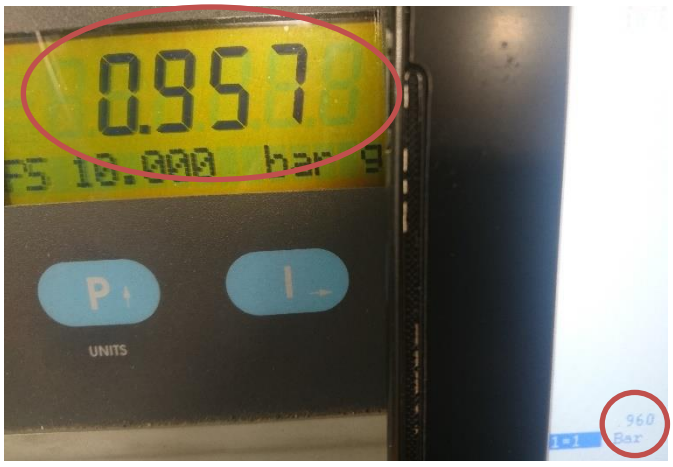

Figure L-4: Pressure Comparison Values at 0.957bar

Figure L-5: Pressure Comparison Values at 2.326bar

Figure L-6: Pressure Comparison Values at 5.956bar

Figure L-7: Pressure Comparison Values at 8.943bar

Figure L-8: Pressure Comparison Values at 10.173bar

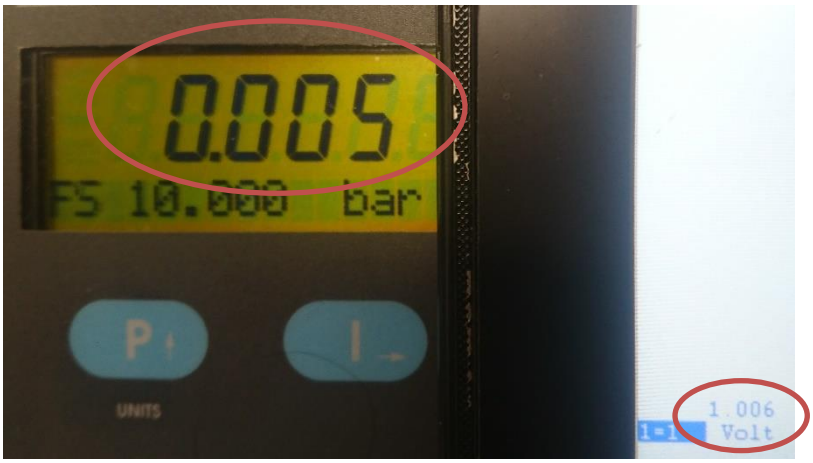

Figure L-9: Pressure vs Voltage – 1.006V

Figure L-10: Pressure vs Voltage – 1.082V

Figure L-11: Pressure vs Voltage – 1.145V

Figure L-12: Pressure vs Voltage – 1.287V

Figure L-13: Pressure vs Voltage – 1.421V

M. Mark II – Seals

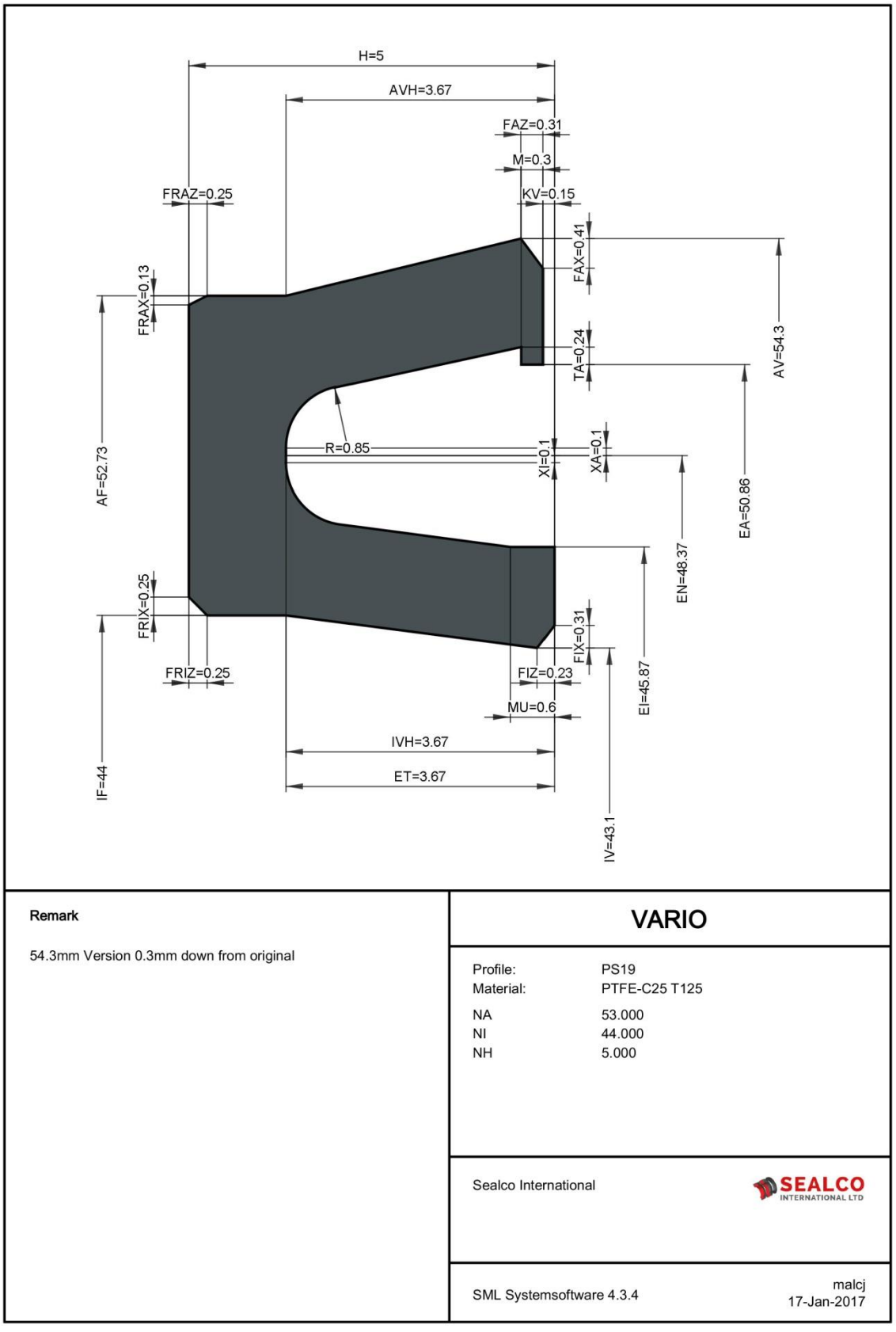

Figure M-1: 75% PTFE and 25% Carbon Seal Drawing with a Cantilever Stiffener

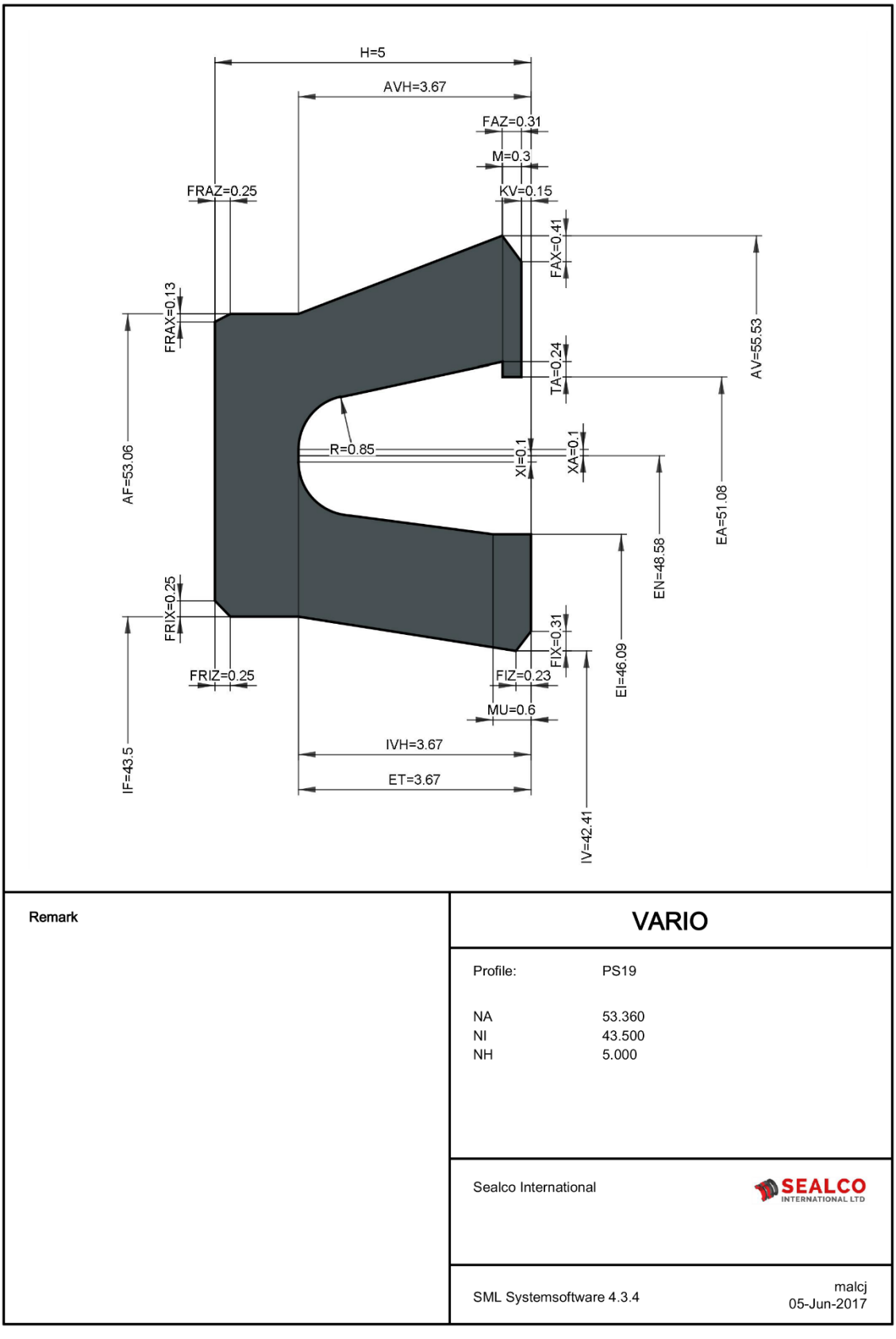

Figure M-2: 75% PTFE, 23% Carbon and 2% Graphite Seal Drawing with a Cantilever Stiffener

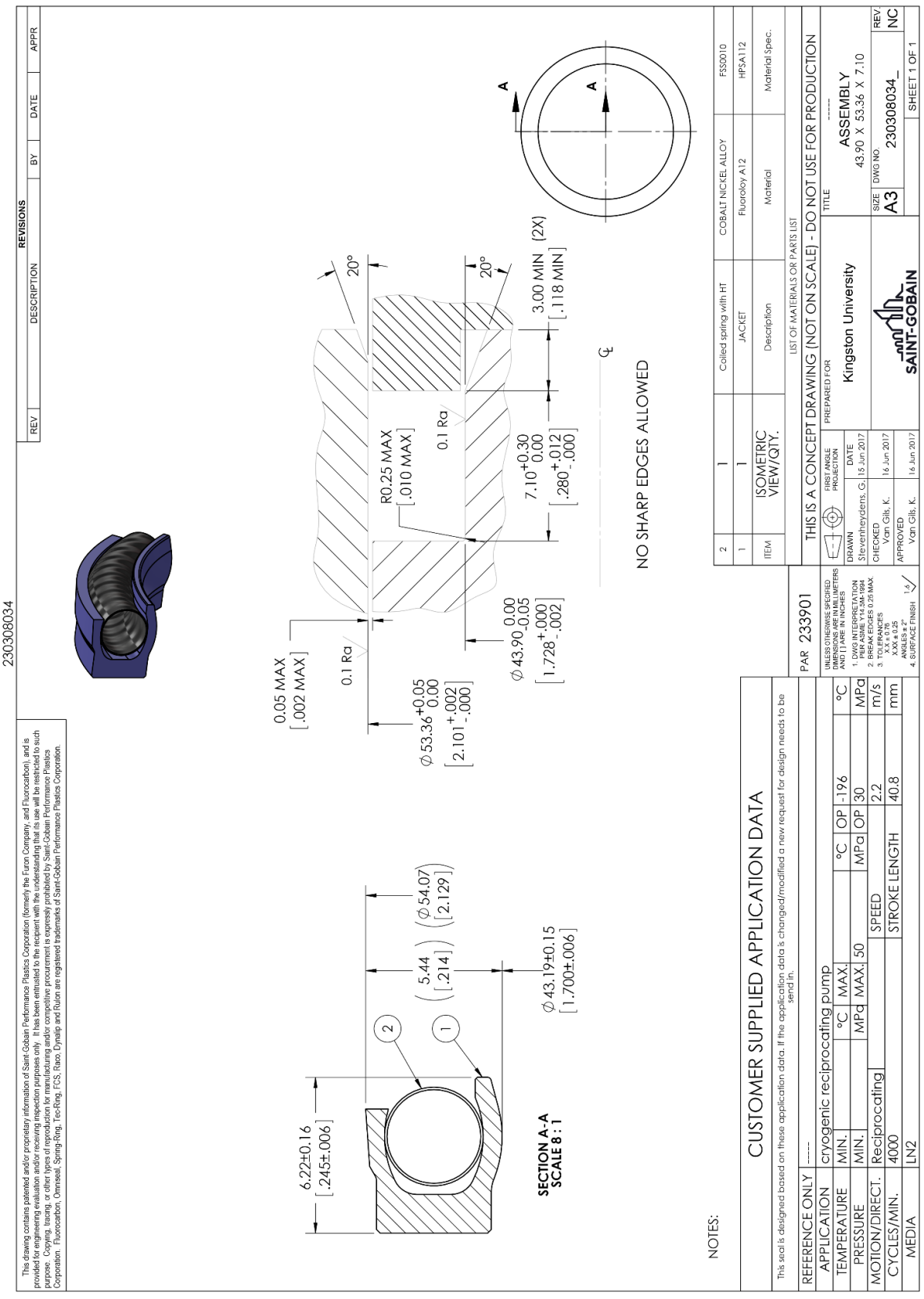

Figure M-3: Fluoroloy A12 Seal Drawing with a Coiled Stiffener

N. LOX Pressure Tests

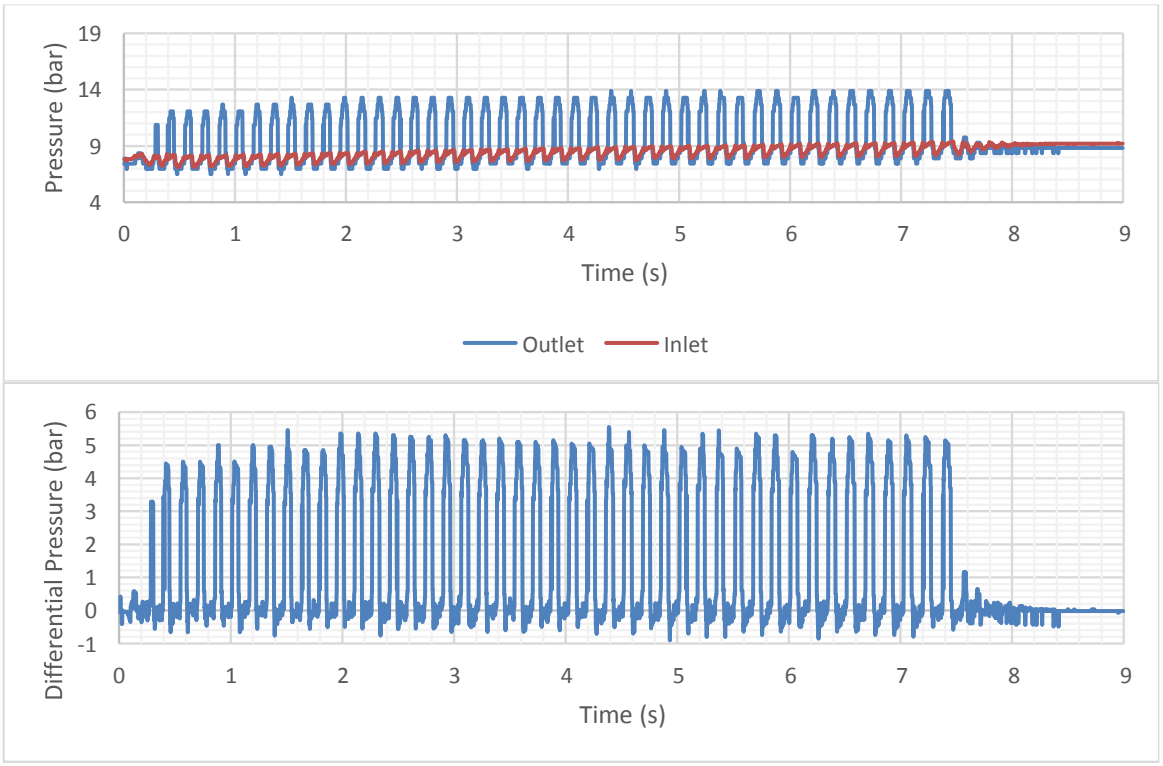

Figure N-1: Pressure Results 1 – Test 1

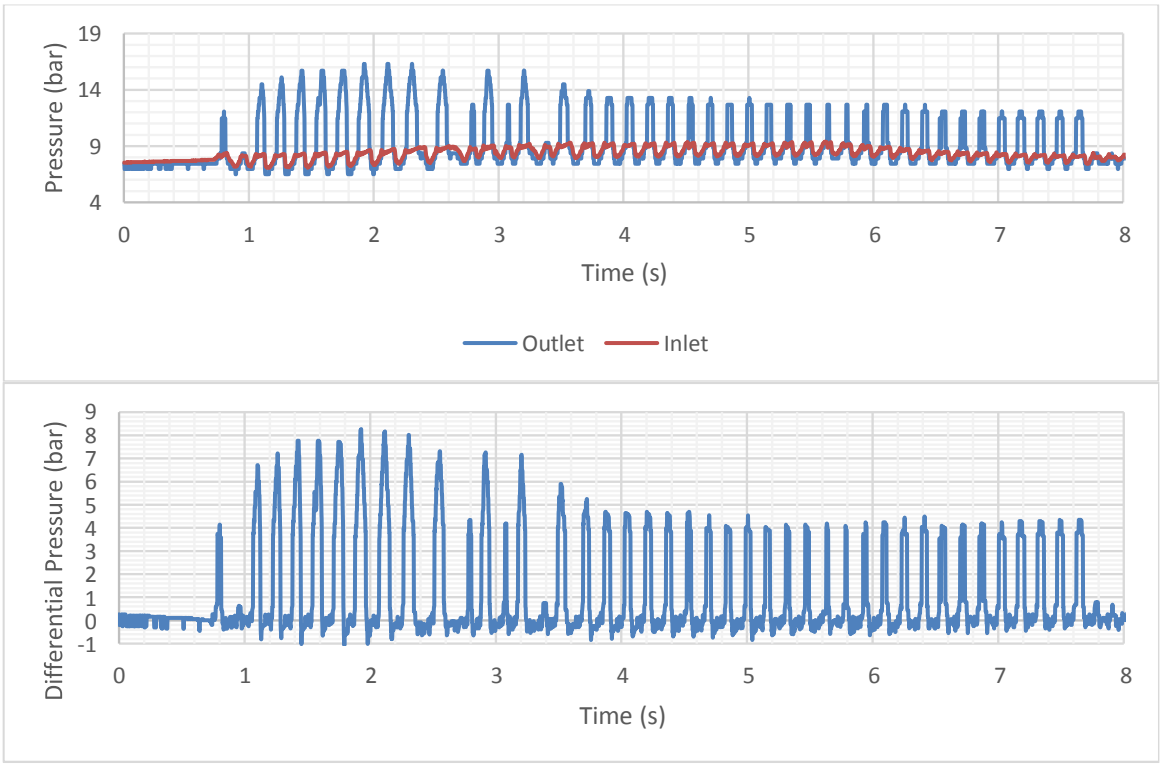

Figure N-2: Pressure Results 2 – Test 1

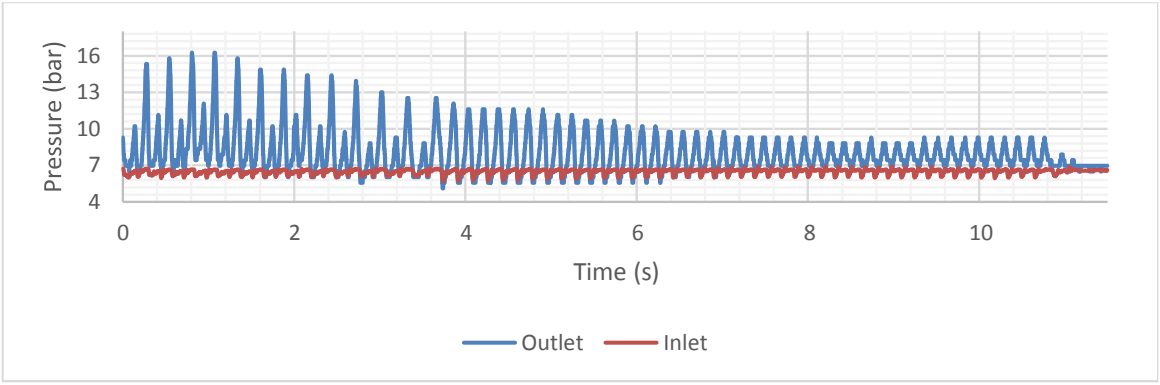

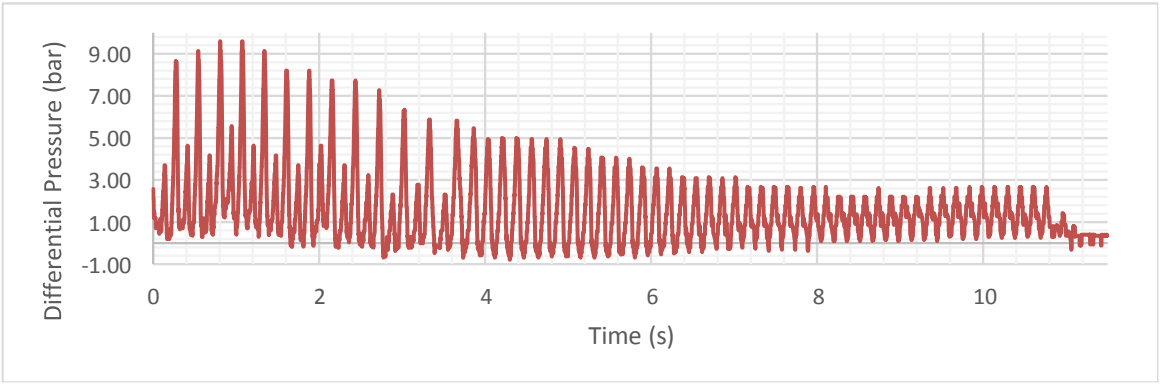

Figure N-3: Pressure Results 5 – Test 2

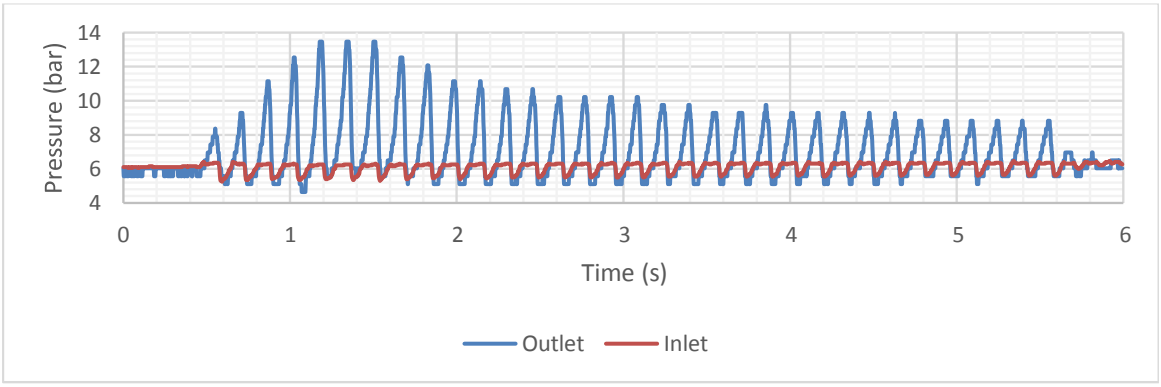

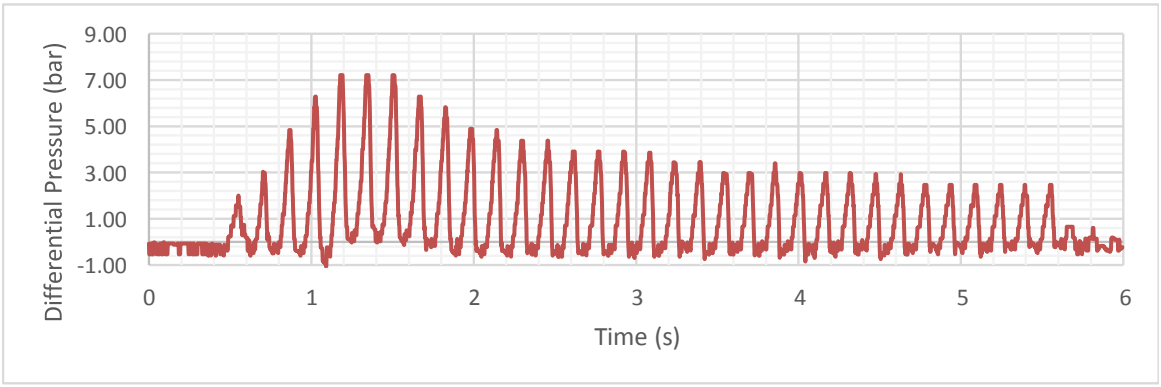

Figure N-4: Pressure Results 6 – Test 2

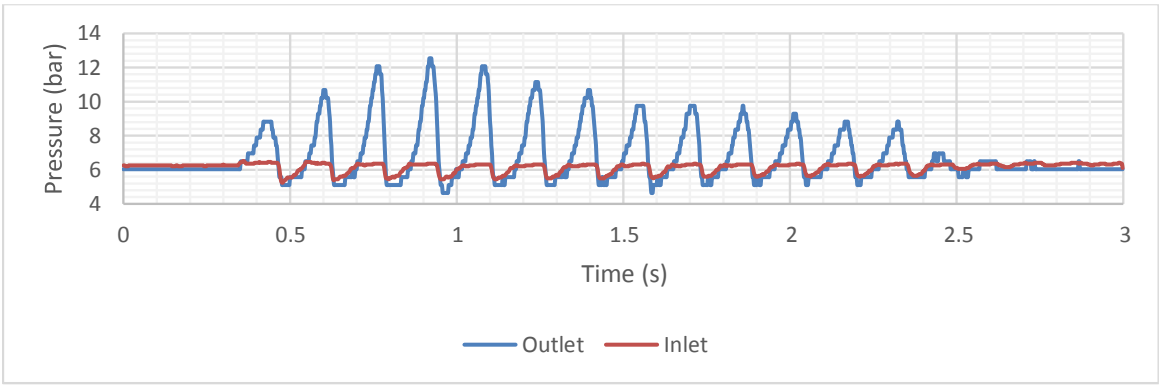

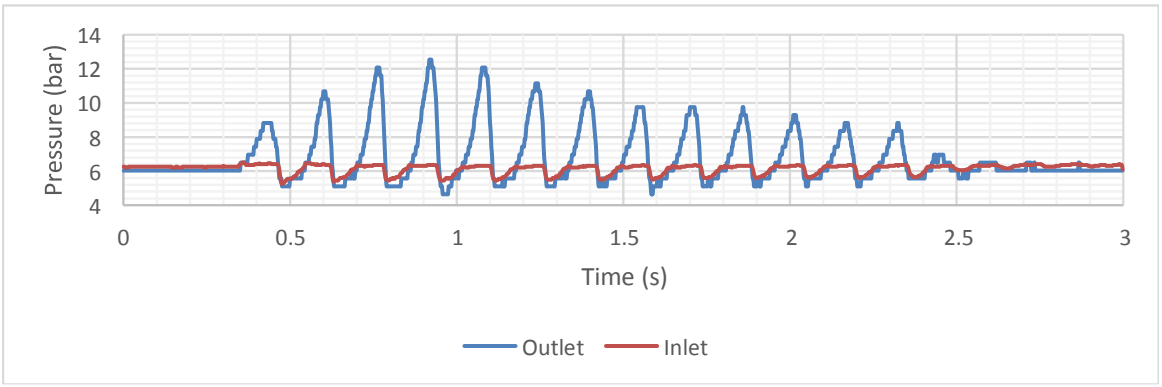

Figure N-5: Pressure Results 7 – Test 2

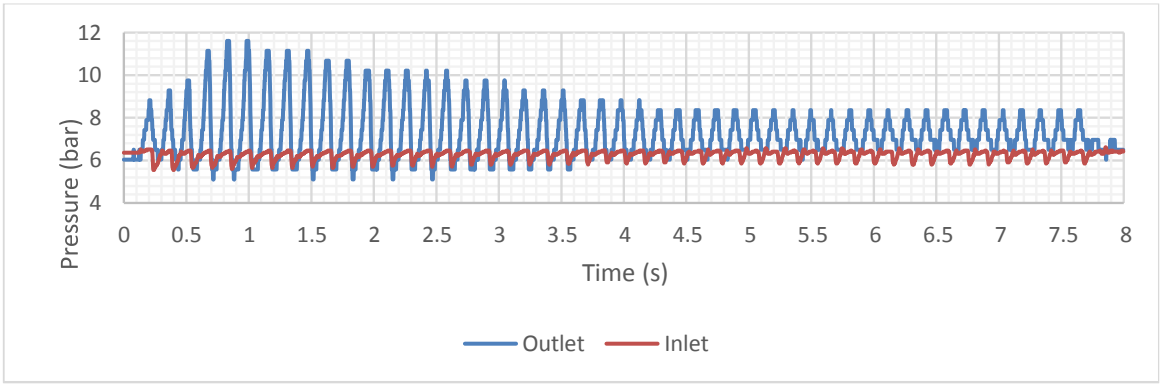

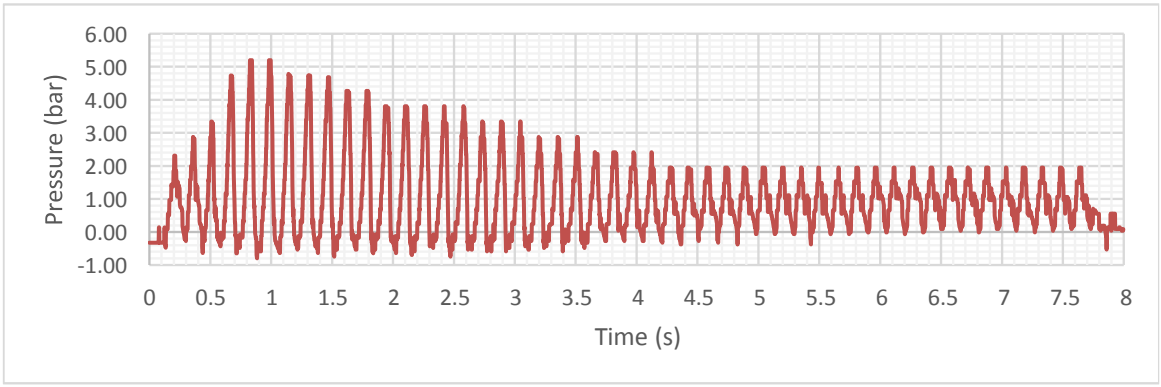

Figure N-6: Pressure Results 8 – Test 2

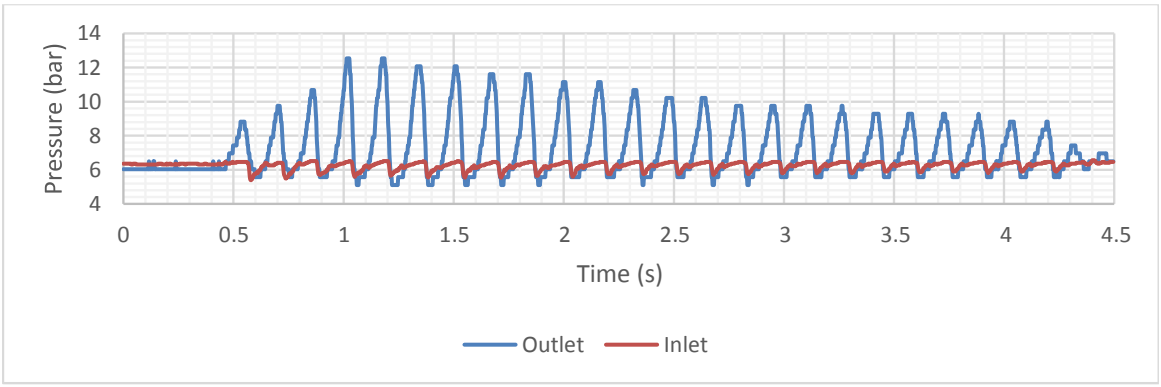

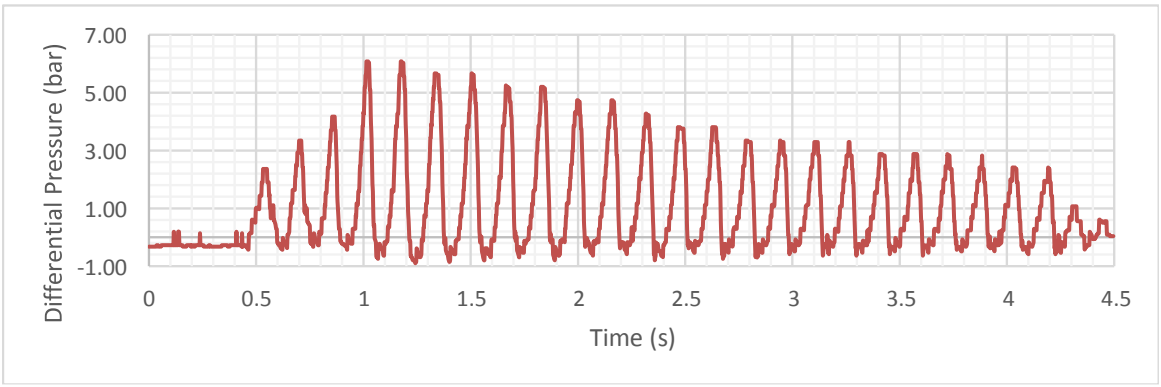

Figure N-7: Pressure Results 9 – Test 2

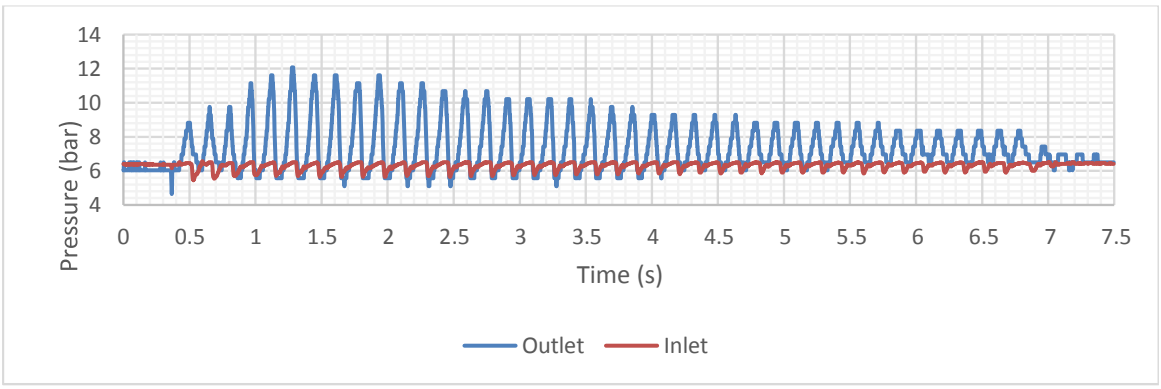

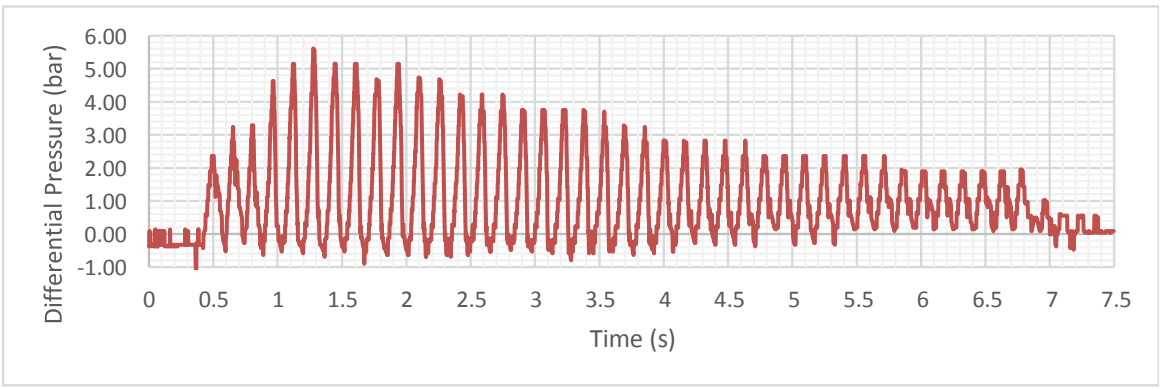

Figure N-8: Pressure Results 10 – Test 2

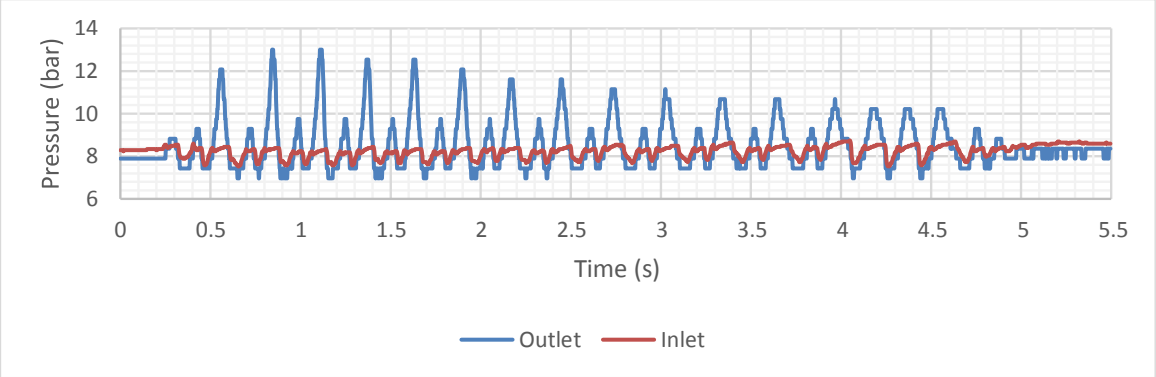

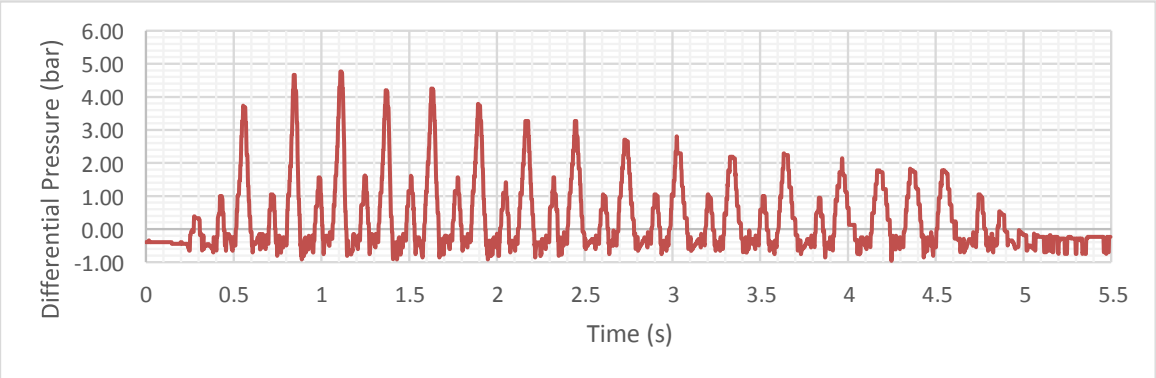

Figure N-9: Pressure Results 11 – Test 2

O. Water Pressure Tests

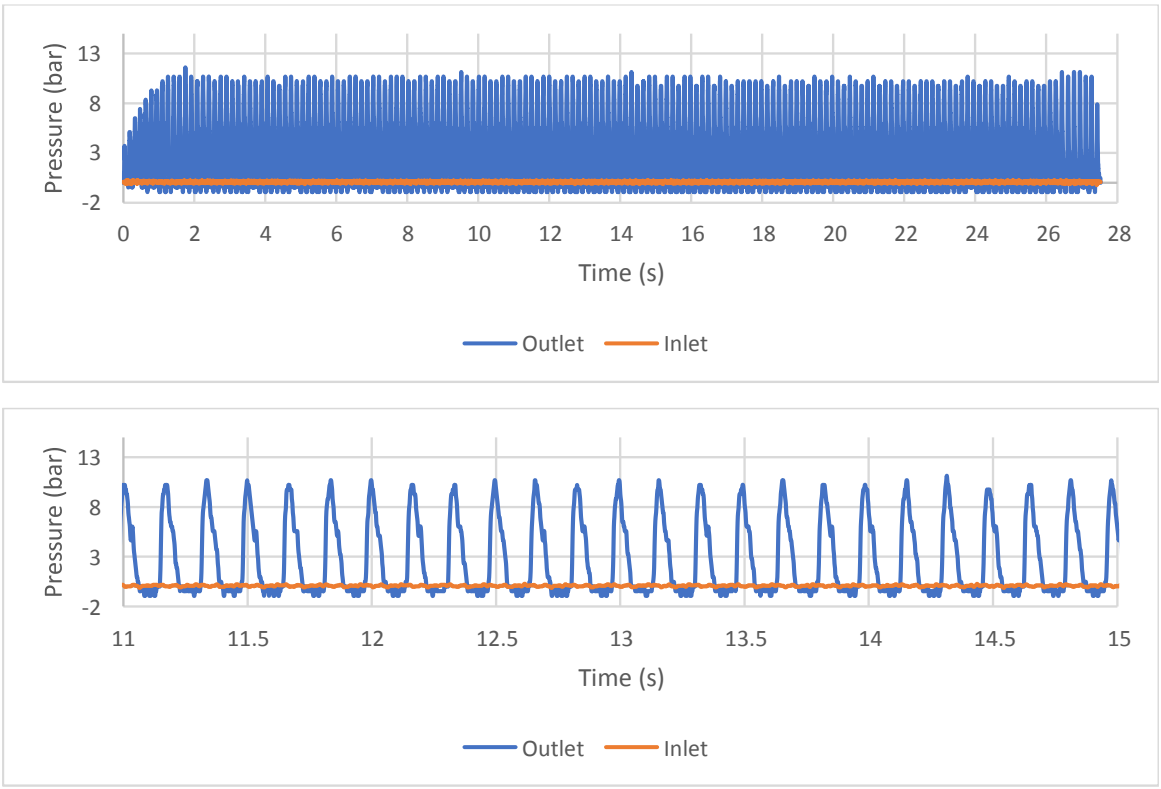

Figure O-1: Water Pressure Test 2 – Outlet Diameter 12.6mm

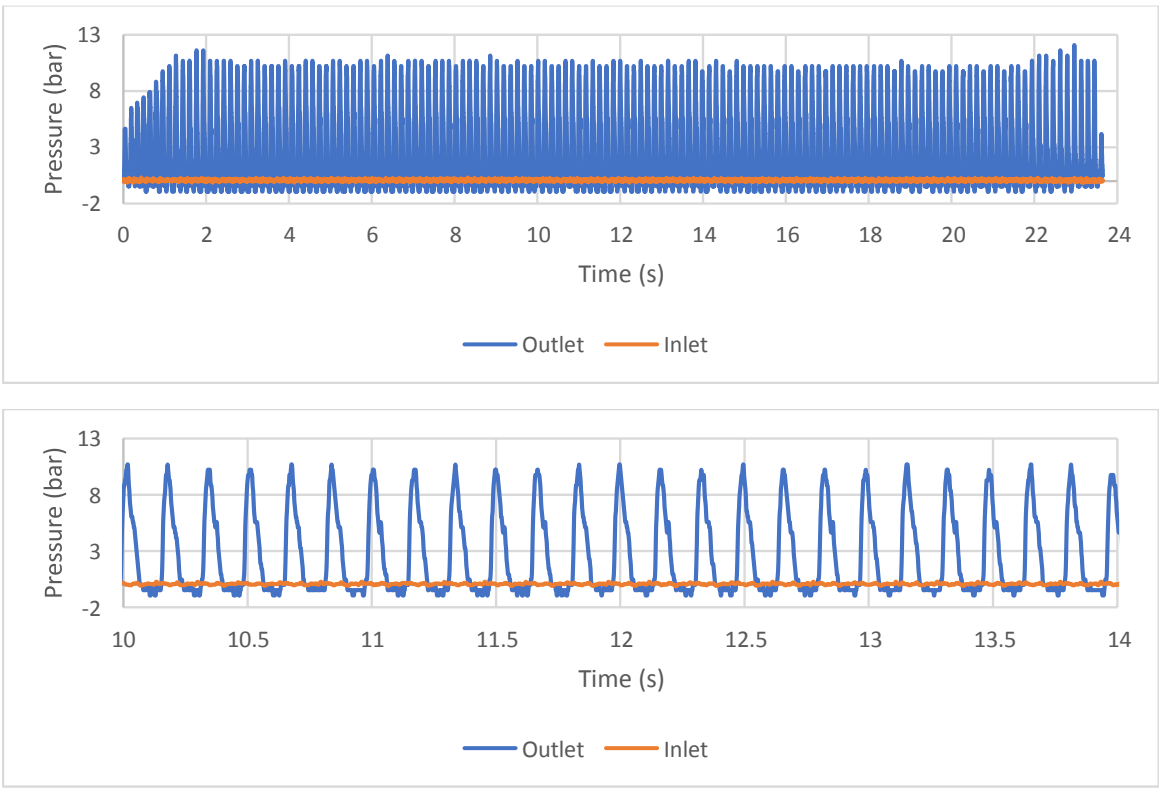

Figure O-2: Water Pressure Test 3 – Outlet Diameter 12.6mm

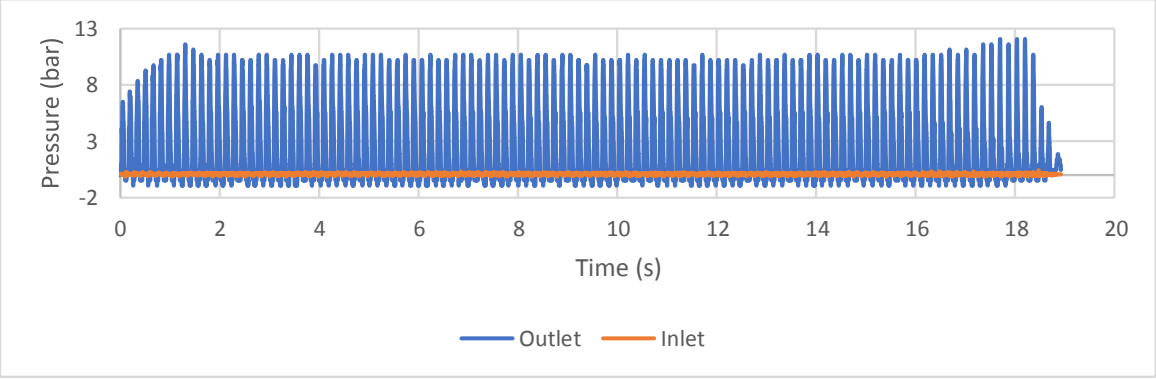

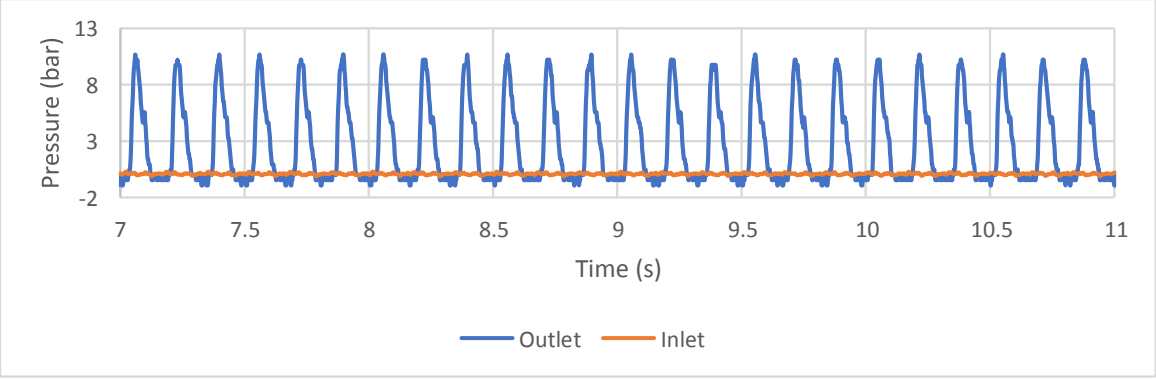

Figure O-3: Water Pressure Test 4 – Outlet Diameter 12.6mm

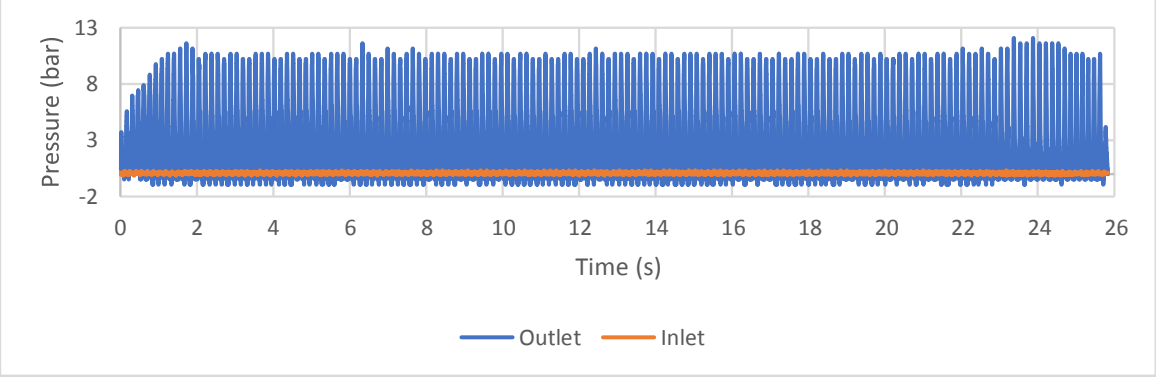

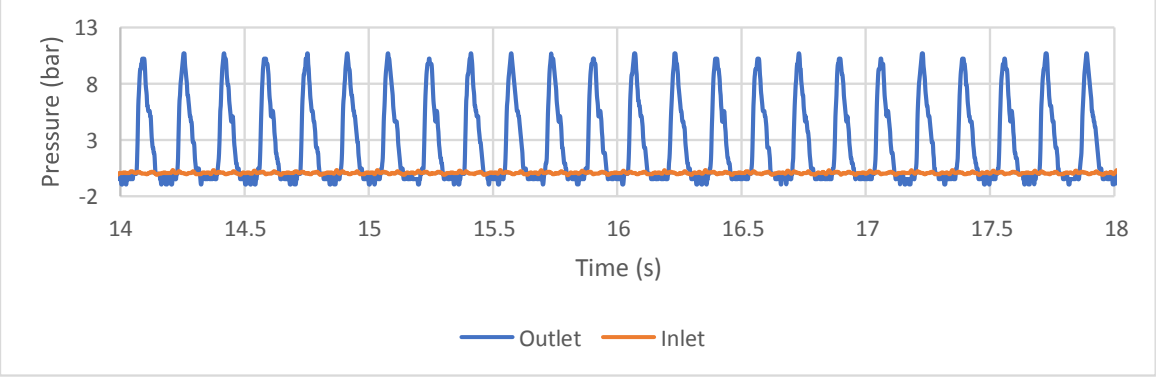

Figure O-4: Water Pressure Test 5 – Outlet Diameter 12.6mm

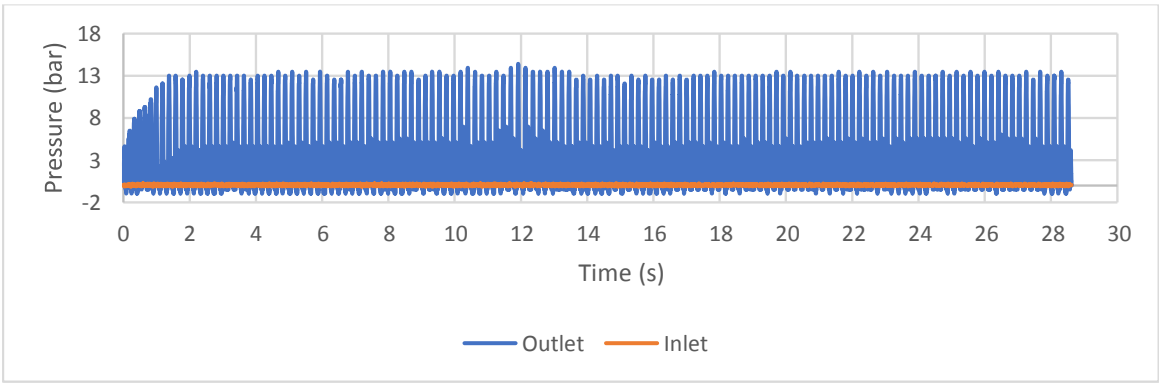

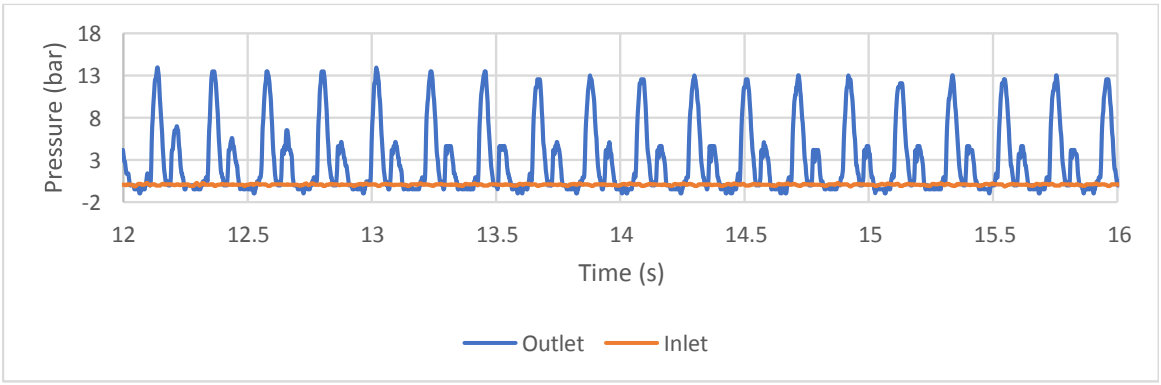

Figure O-5: Water Pressure Test 7 – Outlet Diameter 7mm

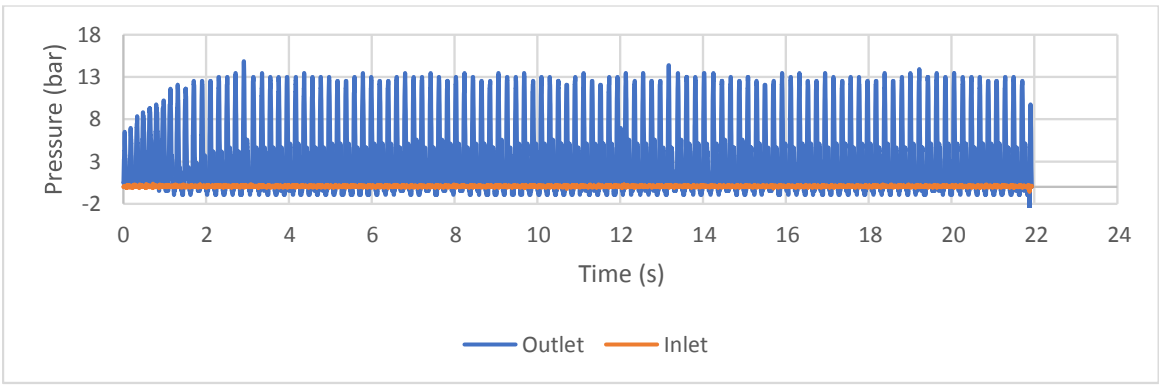

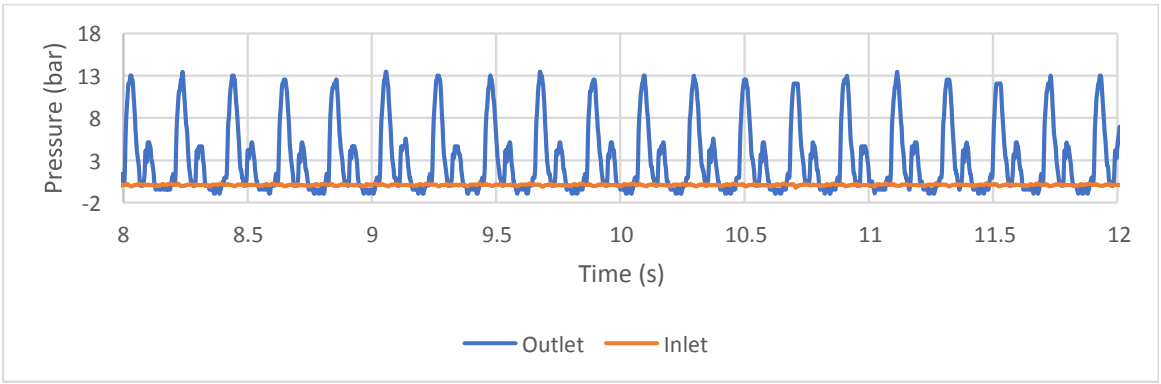

Figure O-6: Water Pressure Test 8 – Outlet Diameter 7mm

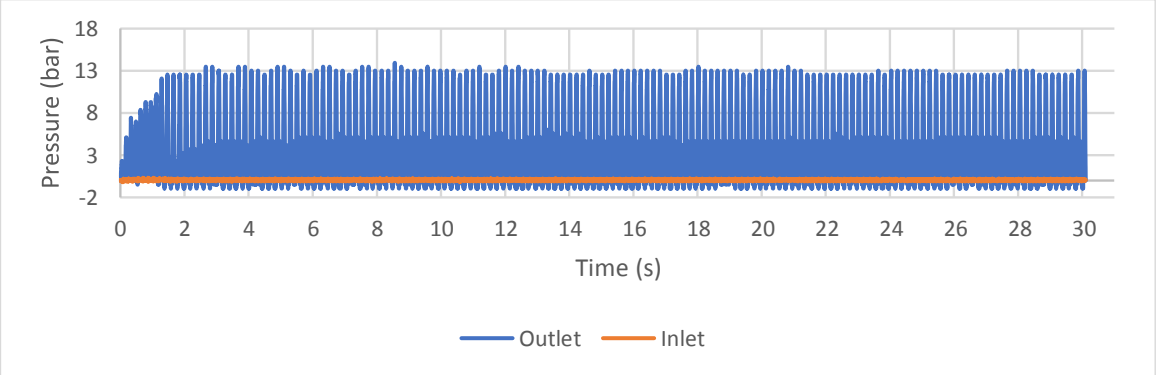

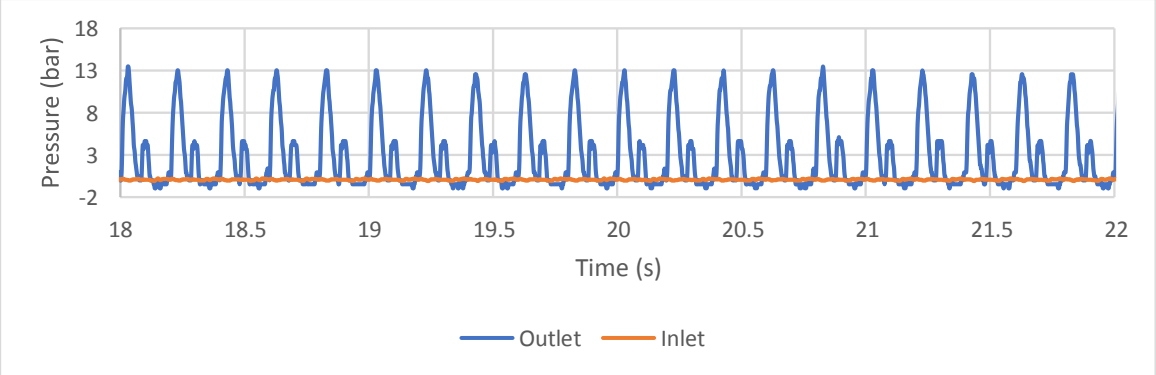

Figure O-7: Water Pressure Test 9 – Outlet Diameter 7mm

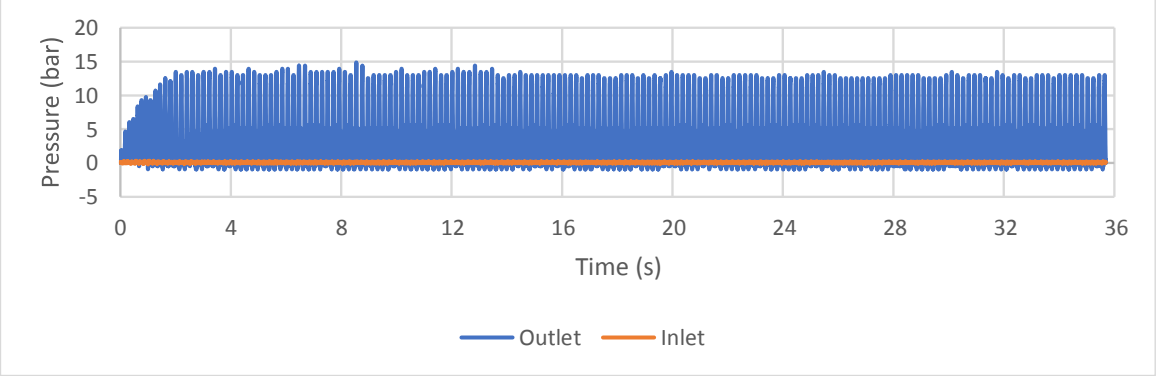

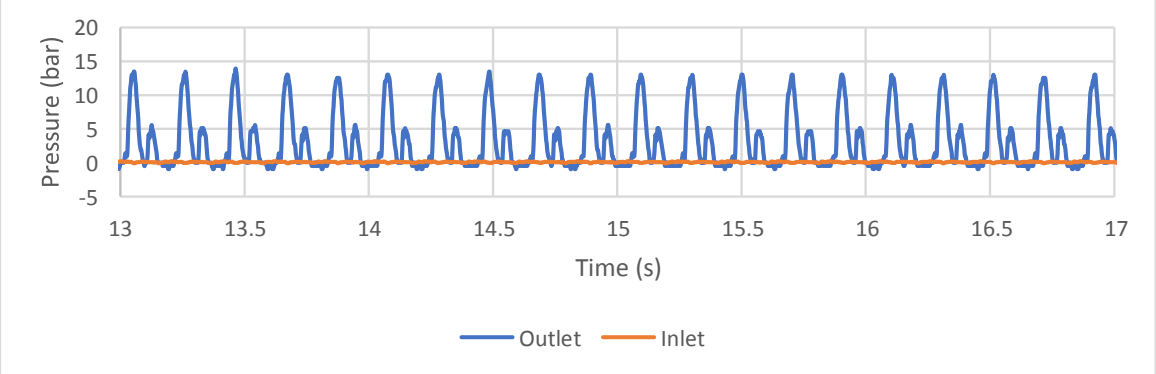

Figure O-8: Water Pressure Test 10 – Outlet Diameter 7mm